Alma Mater Studiorum - Università di Bologna

DOTTORATO DI RICERCA IN

SCIENZE DELLA TERRA, DELLA VITA E DELL'AMBIENTE

Ciclo 35

Settore Concorsuale: 04/A3 - GEOLOGIA APPLICATA, GEOGRAFIA FISICA E GEOMORFOLOGIA

Settore Scientifico Disciplinare: GEO/04 - GEOGRAFIA FISICA E GEOMORFOLOGIA

STRUCTURAL AND STRATIGRAPHIC CONTROL ON HYPOGENE DISSOLUTION IN CARBONATE ROCKS: CASE STUDIES OF CAVE ANALOGUES AND IMPLICATIONS FOR KARST RESERVOIRS

Presentata da: Luca Pisani

Coordinatore Dottorato

Maria Giovanna Belcastro

Supervisore

Jo Hilaire Agnes De Waele

Co-supervisore

Marco Antonellini

Esame finale anno 2023

“Any road followed precisely to its end leads precisely nowhere.
Climb the mountain just a little bit to test that it's a mountain.
From the top of the mountain, you cannot see the mountain.”
(Frank Herbert, Dune, 1965)

ABSTRACT

The main objective of this research is to improve the comprehension of the controlling factors that guide the formation of solutional karst porosity in hypogene settings, contributing to specific geometries and patterns of void-conduit networks.

Subsurface voids created by dissolution may span from few microns in size to decametric tubes providing interconnected conduit systems and forming highly anisotropic permeability domains in many hydrocarbon reservoirs, aquifers, and geothermal fields. Characterizing the spatial-morphological organization of hypogene karst systems is a challenging task that has dramatic implications for the applied geoscience industry, given that only partial data can be acquired from the subsurface by drilling, seismic profiles, or other indirect techniques. At the same time, karst may cause significant engineering and flow management problems, like loss of drill bits and drilling fluids, unexpected fluid breakthrough or total borehole collapse. Because these voids are generally too small to be recognized in seismic profiles and too big to be characterized by well log analyses, there is a great need for studies aiming at predicting their position, geometries, size, and distribution in the subsurface. The genetic interpretation of karstified reservoirs in carbonates affected by silicification, where the relations between diagenesis, silicification processes and hypogene dissolution-precipitation are still poorly understood, is even a more interesting and less studied topic.

To deal with these aspects, we selected two geological case studies where ideal cave systems may represent different settings of hypogene karst reservoirs: the Cavallone-Bove cave system in the Majella Massif (Central Italy), and the karst systems of the Salitre Formation (São Francisco Craton, Northeastern Brazil). In the latter, a peculiar and unusual example of hypogene speleogenesis associated with silicification has been studied, providing an invaluable analogue of many karstified hydrocarbon reservoirs hosted in cherts or cherty carbonates intercalated within mixed sedimentary sequences.

The first part of the thesis is focused on the research about the relationships between fracture patterns, faults and folds architectures, and flow pathways in deformed carbonate sequences in: 1) a fold-and-thrust setting (Majella Massif); 2) a faulted basin in a cratonic block (São Francisco Craton). These two settings represent potential playgrounds for the migration and accumulation of

geofluids, where the development of hypogene karst conduits may affect flow pathways, fluid storage, and reservoir properties.

The main results highlight that localized deformation producing through-going (cross-formational) fracture zones associated with anticline hinges or fault damage zones is critical for the development of solutional karst porosity. The flow pathways and the karst spatial-morphological organization can be predicted by accurate structural analysis. Localized deformation, related to folds or faults, may increase the process of hypogene karstification in the presence of rising aggressive solutions. Furthermore, fault cores of indurated or recrystallized carbonates may represent barriers or combined barrier-conduit domains for fluid flow. Both settings highlight the importance of the structural position and the vertical persistence of fracture and fault zones for the localization of the discharge feeders of the aggressive solutions and consequent hypogene dissolution. In this context detailed structural analyses integrated with an exhaustive interpretation of cave morphologies (implemented with 3D models) represented a first order tool to build conceptual speleogenetic models that may be used for the prediction of hypogene karstification and its spatial organization.

The second part of the thesis deals with the study of hydrothermal silicification and associated hypogene dissolution in a cave in Northeastern Brazil. A multidisciplinary approach involving stratigraphic, structural, petrographic, and geochemical analyses allowed to reconstruct the main diagenetic and speleogenetic events affecting the Neoproterozoic sequence, and the flow pathways that have generated the conduit network. Petrophysical analyses and accurate fracture properties characterization allowed to highlight the presence of high- vs. low-permeability units that controlled the spatial-morphological organization of the conduit system. At the same time, the mineral assemblages and the microthermometric data from fluid inclusions in quartz deposits, combined with silicon and oxygen stable isotope analyses, confirmed that the genesis of the cave system is associated with high temperature hydrothermal solutions rising from the underlying quartzite basement (Chapada Diamantina Group). The novel results obtained from this cave, a site analogue of deeply buried silicified-karstified reservoirs, may shed new light on the close relationship between hydrothermal silicification, hypogene dissolution and the spatial-morphological organization of multistorey cave systems in layered carbonate-siliciclastic sequences, which are controlled by both stratigraphic and structural factors.

Contents

1. Introduction

1.1. Hypogene speleogenesis in carbonate rocks

Karst has been defined as a "*fluid flow system (geo-hydrodynamic system) with a permeability structure evolved as a consequence of dissolutional enlargement of initial preferential flow pathways, dominated by interconnected voids and conduits* […]" (Klimchouk, 2015, p. 306). Several factors may be involved in the genesis of dissolution features, whose morphologies and textures may have variable size, spanning from micron-sized pores (e.g., thin-section scale vuggy porosity), cm-sized cavernous voids and enlarged channels (e.g., in drill cores or hand samples), and macro-scale karst conduits (e.g., proper caves and cave systems).

The process involving the formation of macro-scale solutional conduits is generally referred to as "*speleogenesis*". Speleogenesis is essentially a coupled mass-transfer/mass-transport process, which depends on the aggressiveness of water and flow characteristics. Water flow is governed by head gradients due to hydrodynamic and hydrogeologic processes; aggressiveness results from disequilibrium in the fluid-rock system and is an attribute of the moving groundwater (Huntoon, 1995; Klimchouk, 2015).

Caves in carbonate rocks are the most common on Earth, since limestones and dolostones present the best combination of solubility conditions (at Earth's surface) and distribution. Carbonate minerals dissolve by dissociation, which in pure water is very slow as compared to the dissolution of quartz, for example (D'Angeli, 2019). However, in the presence of acidic solutions, the dissolution of carbonates increases very rapidly (Palmer, 2007 and references therein). The most common acids on Earth are carbonic and sulfuric acid, respectively formed by the reaction of CO_2 or H_2S and water. The source of acidic solutions may derive from: 1) infiltrating waters that slowly percolate through the first meters of subsurface (giving origin to "classic" epigene karst; Palmer, 1991, 2007; Ford and Williams, 2007; Audra and Palmer, 2011, 2015); 2) local (in-situ) chemical reactions between host rock and shallow groundwater (like oxidation of bedrock sulfides producing H_2SO_4, or interaction with hydrocarbons entrapped in the host rock pores; Auler and Smart, 2003; Tisato et al., 2012; Webb et al., 2020); 3) aggressive solutions whose origin is related to deep-seated processes (hypogene speleogenesis, *sensu* Palmer, 2007) and whose upwelling pathways are driven by hydrostatic pressure independent of recharge from the overlying or immediately adjacent surface (*sensu* Klimchouk, 2007). The concept of hypogene speleogenesis has been intensely debated in the last years, and these two main theories have been recently unified and commonly accepted as: *"the formation of solution-enlarged permeability structures by upwelling fluids that recharge the cavernous zone from hydro-stratigraphically lower units, where fluids originate from distant or deep sources, independent of recharge from overlying or immediately adjacent surface"* (Klimchouk, 2017, p.3).

Hypogene speleogenesis is worldwide recognized and is one of the most important processes involved in the genesis of multi-scale karst features in the subsurface. Usually, hypogene voids are formed in deep-seated confined conditions (Klimchouk, 2017). Subsequent events such as uplift, exhumation, and denudation can shift hypogene caves from their native position to shallow environments, where other processes can overprint the original morphologies and deposits (Columbu et al., 2021). Given its nature, accessible hypogene caves certainly represent only a small percentage of their potential distribution. In fact, it must be considered that hypogene caves are formed in crustal domains that are disconnected from the surface, so their discovery is most of the times fortuitous following the exhumation of the hosting rock masses (e.g., by mining, opening of a collapse sinkhole, retreat of a scarp, interception by drilling etc.).

Hypogene speleogenesis may be associated with different diagenetic, hydrogeological, and hydro-chemical settings (Fig.1). Upwelling flow characteristic of discharge regimes can be sourced from deep meteoric flow systems (at the regional scale), or basinal overpressured flow systems (e.g., connate/formation water). Hypogene speleogenesis also tends to be related with interfaces between different flow systems (Klimchouk, 2012). Other sources may be endogenous: juvenile (e.g., magmatic, volcanogenic), metamorphic, hydrothermal, or mixing of different deep geofluids (Mylroie et al., 1995; Dublyansky, 1995; Andreychouk, 2009; Klimchouk, 2012, 2017). Peculiar examples of hypogene speleogenesis may be triggered by the upward migration of H_2S-rich solutions produced by the reduction of sulfate layers at depth (Machel, 2001; Galdenzi and Menichetti, 2017; D'Angeli et al., 2019) or by maturation of organic matter/hydrocarbons (Hill, 1990, 1995; Onac et al., 2011; Klimchouk, 2017). During their upwelling, these deep geofluids undergo changes in pressure and temperature, mix with other fluids and cause the precipitation of different mineralogical suites associated with karstic pore space (Plan et al., 2012; Sauro et al., 2014; Klimchouk, 2017; Klimchouk et al., 2021; Smeraglia et al., 2021). Therefore, studies combining the analysis of conduit morphologies, cave patterns, flow pathways, and associated secondary mineralization are needed to correctly interpret the genesis of hypogene karst features.

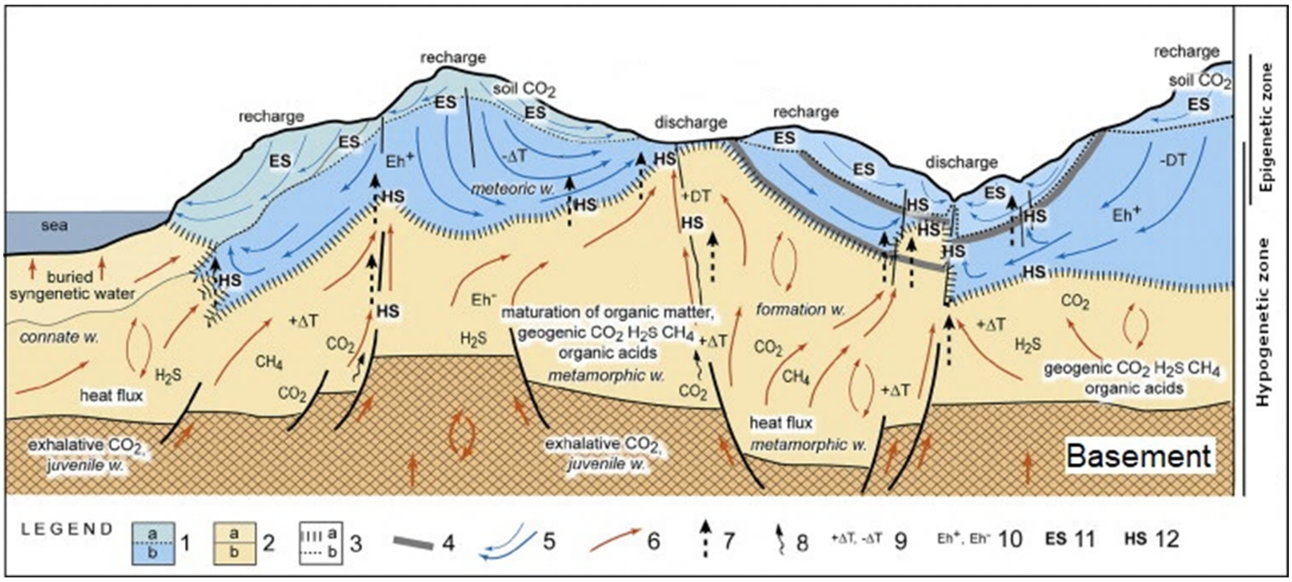

Figure 1. Conceptual diagram of the main speleogenetic zones in relation to groundwater flow regimes. Legend explanation: 1) Meteoric, topography-driven regime: a- local systems (epigene), b- regional systems (confined, hypogene); 2) Basinal regime driven by compaction or tectonic compression: a- in newly deposited sediments, b- in lithified rocks; 3) Interfaces between groundwater regimes and systems: a- meteoric/expulsion regimes, b- local/regional meteoric systems; 4) Low-permeability (buffer/seal) units; 5) Meteoric flow pathways; 6) Deep basinal or endogenous flow pathways; 7) Enhanced cross-formational flow pathways; 8) Intense gas inputs; 9) Temperature and gradient anomaly: positive/negative; 10) Redox conditions: oxidizing or reducing; 11) Epigene speleogenesis; 12) Hypogene speleogenesis. The conceptual diagram is out of scale and the vertical dimension is greatly exaggerated. Modified from Klimchouk (2012).

The occurrence of hypogene speleogenesis has been documented in several lithologies such as carbonates, evaporites, quartzites and skarns (Andreychouk, 2009, Klimchouk, 2019). According to the chemical processes involved, the different types of karstification are related to: sulfuric acid (Jagnow et al., 2000; Audra et al., 2009; D’Angeli et al., 2019; Laurent et al., 2021); carbonic acid (Bakalowicz et al., 1987; Dublyansky, 1995; Andreychouk, 2009; Audra and Palmer, 2015); mixing-corrosion (Mylroie and Carew, 1990; Audra and Palmer, 2015; De Waele and Gutiérrez, 2022); circulation of cooling thermal waters or endogenous fluids with complex composition (Pinneker 1983; Dublyansky, 2013; Klimchouk, 2017, 2019). Other solutional speleogenetic processes may be triggered by organic acids (Kharaka et al., 1986; Klimchouk, 2012; Chen et al., 2021), dissolution of evaporites (Klimchouk et al., 2009; Klimchouk, 2019) or high temperature alkaline aqueous solutions aggressive towards quartz-rich rocks (Andreychouk, 2009; Sauro et al., 2014).

In his comprehensive reviews, Klimchouk (2012, 2019) distinguished three main types of confined hypogene speleogenesis, based on hydrodynamic conditions:

1) Artesian hypogene speleogenesis: related to the upward inter-stratal and inter-formational hydraulic communication in confined multistorey aquifers. Speleogenesis of this type is supported by the meteoric (gravity-driven) regime of groundwater flow and is governed by upward leakages between different aquifers. One of the best studied examples of this type are the giant maze caves in the evaporites of western Ukraine (Klimchouk et al., 2009).
2) Deep-rooted (endogenous) hypogene speleogenesis: related to upwelling cross-formational flow commonly localized along through-going faults and fracture zones. Karstification of this type may occur at substantial depth (likely up to several km) but also within the upper hydrodynamic zone. In the case of hypogene speleogenesis driven by carbonic acid, its occurrence in shallow settings is hindered by a switch to the onset of calcite precipitation caused by the dramatic drop in fluid pressure and CO_2 degassing (Dublyansky, 2013). Deep-rooted hypogene karstification may occur in a variety of geodynamic settings (e.g., from active rift margins to fold-and-thrust belts) and may involve different solutional mechanisms.
3) Combined artesian/deep-rooted hypogene speleogenesis: where deep-sourced fluids ascending along cross-formational discontinuities significantly interact with overlying stratiform aquifers. Karstification of this type is particularly common in intra- and inter-mountain basins, foreland basins, as well as cratonic blocks. Speleogenesis tends to concentrate along major deep-rooted faults and fracture zones, interfaces between different flow regimes, and along basin margins.

Another typology of hypogene speleogenesis is attributed to unconfined aquifers at or close to the water table level (e.g., sulfuric acid speleogenesis; Audra and Palmer, 2011, 2015; De Waele et al., 2016; D'Angeli et al., 2019), or in coastal areas where mixing-corrosion at the sea level can produce large-scale karst porosity (Mylroie and Carew, 1990; Klimchouk, 2017; De Waele and Gutiérrez, 2022).

Hypogene caves formed by different solutional mechanisms, even in different lithologies, demonstrate remarkable similarity in their patterns and shapes, which are determined mainly by the hydrodynamic factors rather than the chemistry of the involved solutions. Hypogene cave patterns usually consist of 2D or 3D (multistorey) maze networks or single-conduit passages (Klimchouk, 2019), most having abrupt endings (Hill, 1995), well-developed cupola-like morphologies on the ceiling of cave conduits, and evidence of ascending discharge and flow (e.g., rift-like feeders, rising wall channels, megacusps) (Klimchouk, 2007; Klimchouk et al., 2016; De Waele and Gutiérrez, 2022). Other typical (but not compelling) features are: spongework pattern, condensation-corrosion cusps, bubble trails, solutional pockets (De Waele and Gutiérrez, 2022). In sulfuric acid caves, one of the most diagnostic morphological features are replacement pockets associated with the precipitation of specific mineral assemblages (De Waele et al., 2016; D'Angeli, 2019).

Thanks to their genesis, hypogene caves are independent of climate, surface topography/hydrology, and do not rely on seepage from CO_2-enriched meteoric water (D'Angeli et al., 2019; De Waele and Gutiérrez, 2022). This explains why many huge hypogene cave systems, such as Carlsbad Caverns and Lechuguilla Cave in the Guadalupe Mountains of New Mexico, USA (Hill, 2000), or Toca da Boa Vista-Toca da Barriguda System in Brazil (Auler and Smart, 2003; Klimchouk et al., 2016), do not occur in high rainfall areas, but are located in semi-arid or dry regions, without connection to any karst topography at the surface. This is even more true for the discovery of deep-seated hypogene void-conduit systems intercepted by boreholes at several km of depth in the Earth's surface, and not related to paleokarstic epigene processes (Andreychouk et al., 2009; Lima et al., 2020).

Other typical attributes of hypogene speleogenesis are the lack of surface solutional features distinctive of the epikarst, such as solutional dolines, sinking streams, and blind valleys, and the absence of underground morphologies, speleogens, and associated transported sediments characteristic of vadose, focused, and fast water flow (Auler and Smart, 2003; Audra and Palmer, 2011). However, many hypogene caves related to the formation of sulfuric acid (e.g., sulfuric acid speleogenesis) are strictly controlled by the reaction between H_2S-rich fluids and oxygenated groundwater; thus, this kind of hypogene setting is strongly controlled by the position and the evolution of the water table in unconfined aquifers (De Waele et al., 2016; D'Angeli et al., 2019). Although the cave development by sulfuric acid dissolution at (and above) the water table may radically give a pronounced sub-horizontal component to the cave pattern, most of the sulfuric hypogene caves still rely on the (channelized) migration of H_2S-rich solutions from depth.

Secondary by-products and mineralizations due to alteration, replacement of host rock, or re-crystallization, are typically abundant in the hypogenic zone (Plan et al., 2012; D'Angeli et al., 2019). Modification of the isotopic composition of cave host rock is a common process which is associated with hypogene speleogenesis (Spötl et al., 2009; Dublyansky et al., 2014; Temovski et al., 2022), whereas it is absent in "classic" epigene caves (Spötl et al., 2021).

It is essential to stress that caves have often a polygenetic history (Hill, 2000; Parise et al., 2018; Columbu et al., 2021; Spötl et al., 2021) and it may be difficult to recognize all the stages of their formation and evolution. For this reason, a multidisciplinary approach combining geomorphological, geochemical, mineralogical, and structural-hydrogeological observations is required to unravel the most reasonable speleogenetic history of karstified carbonate rocks.

1.2. Karstified carbonate reservoirs

Karst networks consisting of open, filled, or collapsed conduits, are complex components that characterize many carbonate reservoirs. Oil and gas deposits in carbonate units constitute a significant percentage of the discovered oil and gas fields worldwide, accounting for an estimated ~60% and ~40% of the world's oil and gas reserves, respectively (Buryakovsky et al., 2012; Nolting et al., 2021). Well-studied examples include the Yates field of West Texas (Craig, 1988; White et al., 1995), the Golden Lane fields in Mexico (Coogan et al., 1972), the Casablanca field in offshore Spain (Lomando et al., 1993), the Kharyaga field in the Russian Arctic (Zempolich and Cook, 2003), the Kashagan field in Kazakhstan (Kaiser and Pulsipher, 2007), the Kirkuk field in Iraq (Trice, 2005), the Tarim Basin in China (Wu et al., 2007; Zhou et al., 2014; Dong et al., 2018; You et al., 2018; Wei et al., 2021), the pre-salt reservoirs in Santos and Campos Basins (Brazil), and in Lower Congo-Kwanza, Africa (De Luca et al., 2017; Girard and San Miguel, 2017; Poros et al., 2017; Teboul et al., 2019; Lima et al., 2020).

Most of the discovered giant and supergiant hydrocarbon reservoirs are hosted in carbonate (both limestones and dolostones) or mixed carbonate-siliciclastic sequences (Fig.2). Among the 345 known fields, 18 sites are characterized by high-porosity cherts or silicified carbonates (see chapter 1.3. for a detailed discussion on unconventional silicified reservoirs).

Although presenting some among the most productive wells in history (Trice et al., 2005), the recovery factor from carbonate reservoirs showing widespread karst features is generally low if compared to conventional carbonate or sandstones reservoirs (Fournillon et al., 2012; Montaron et al., 2014). Some of the biggest challenges for improving reserve estimations are related to volumetric determination and evaluation of karst void geometry and its spatial organization, which directly impact on fluid storage and recovery (Lønøy et al., 2020).

For hydrocarbon exploration activities (but also for geothermal aquifer characterization), karst features not only constitute the most significant reservoir space, but also their logging, testing, and seismic response present critical characteristics that may be useful for identification (Table 1).

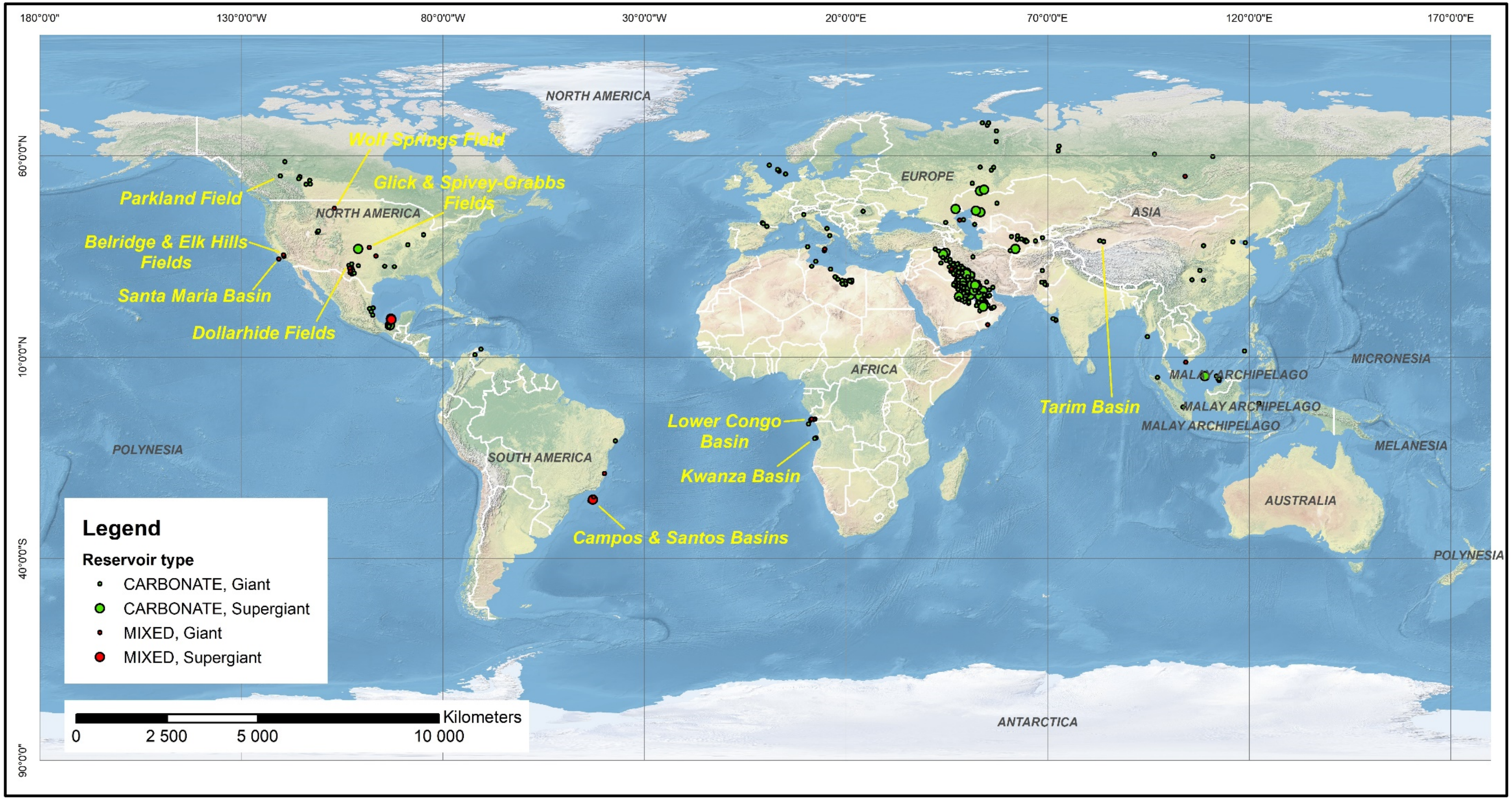

Figure 2. Map of the known giant or supergiant reservoirs hosted in carbonate or mixed lithologies. Yellow labels refer to silicified or chert reservoirs (see chapter 1.3.). The dataset is a compilation modified from the open database from AAPG published for Arcgis online in 2015 (https://worldmap.harvard.edu/data/geonode:giant_oil_and_gas_fields_of_the_world_co_yxz). This dataset complements several AAPG memoirs and series of publications that address giant oil and gas fields.

Table 1. Main geological and technical characteristics of karstified carbonate reservoirs (modified from Baomin and Jingjiang, 2009).

Drilling response characteristics	**Logging response characteristics**	**Macroscopic geological characteristics**	**Drill cores characteristics**	**Seismic response characteristics**
(1) Drilling time is decreased, drilling speed may increase significantly (2) Borehole diameter increases, drilling tool blows off (3) Severe loss of mud or total loss of circulation zones (Fernández-Ibáñez et al., 2022) (4) Mud may be impregnated by hydrocarbons (5) Core recovery may be low or impossible	Three parameters are high: (1) The natural gamma value increases to high levels (2) The value of interval transit time increases to high levels (3) The value of neutron porosity increases to high levels Two parameters are low: (1) The value of resistivity decreases to low levels (2) The value of rock density decreases to low levels	(1) Unconformity surfaces are common (2) Residual overburden can be developed on unconformity surfaces, such as weathering crusts, clay layers or collapse breccia (3) Conduits may be open, partially filled or completely filled (by sediments, collapse breccia, or fluids) (4) From modelling results, conduits filled with fluids within the shallow phreatic realm can remain open to burial depths up to ~10 km. Conversely, open conduits may experience total collapse at depths < 1 km (Nolting et al., 2021)	(1) Solutional pockets, large-mid-small-sized vugs, dissolved holes and macro-scale cavities (up to meter-sized), intergranular and intercrystalline dissolution, solutional holes and pores, various occurrences of dissolved fractures and vuggy cracks (2) Various occurrences and sizes of collapse breccia (3) Dissolved and re-precipitated carbonates (4) Secondary mineral precipitates filling pore space and fractures. They may have variable occurrence, size, and mineralogy	(1) Weak amplitude or dim spot. Strong amplitude or bright spot, discordant reflectors or flat spot (2) Reflectors with lateral amplitude showing elliptic shapes, with abnormalities of ‘catenulate’ or ‘stripe’ forms (3) Caves filled with fluids can form relatively high impedance contrast within dense carbonate rocks, thereby generating a strong reflection interface (Hendry et al., 2021)

Integration of karst features from drill cores, image logs, seismic attributes and dynamic data is compulsory to properly characterize the void-conduit system in this type of reservoirs (Farooq et al., 2020). Incorporating karst conduits into industrial reservoir models commonly relies on statistical modelling methods (Trice, 2005; Borghi et al., 2010; Rongier et al., 2014; Lønøy et al., 2020). However, this approach often fails to capture key aspects of connectivity, geometry, and volume of the karstic void-conduit systems.

In many tight carbonate reservoirs, matrix permeability is very low (Jolley et al., 2007; Giuffrida et al., 2019, 2020). In contrast, karst and fractures contribute to increase secondary permeability and can play a fundamental role in geofluid storage and migration processes (Agar and Geiger, 2015; La Bruna et al., 2021). Karst processes bypass the control exerted by the matrix or fractures, impacting reservoir porosity and permeability at multiple scales (Fig.3) (La Bruna et al., 2021; Fernández-Ibáñez et al., 2022).

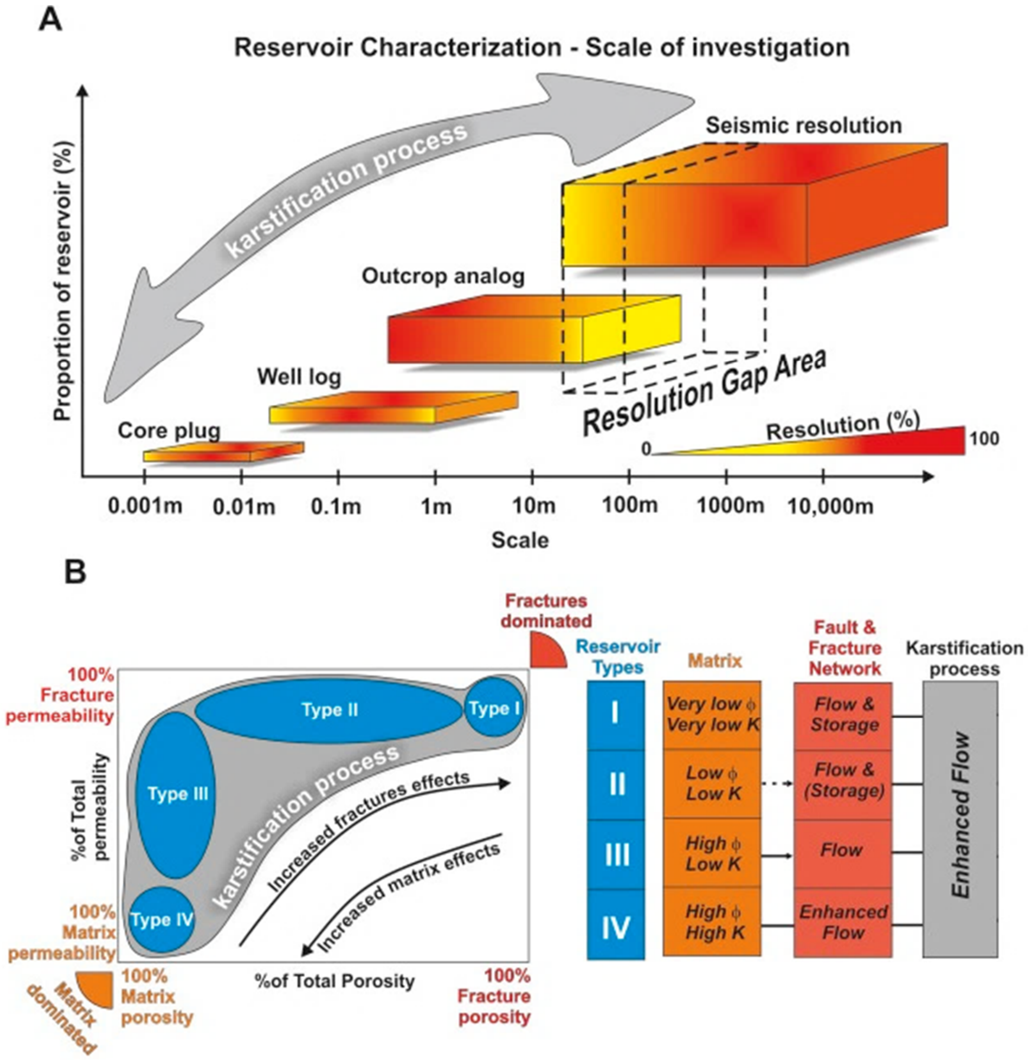

Figure 3. A) Graph showing the resolution of in situ and seismic-scale analyses with respect to the reservoir proportions and karstification (modified after Giuffrida et al., 2020). B) Simplified

conceptual diagram displaying how karstification processes can affect different reservoir types (e.g., fractures- vs. matrix-dominated, and intermediate types) including corrosion of fractures or the contribution of the matrix (modified after Jolley et al., 2007). Panel modified from La Bruna et al. (2021).

In many carbonate reservoirs, the origin of karst porosity has been intensely debated over the past decades. In burial settings, karst porosity is commonly related to past periods of subaerial exposure and epigene speleogenesis (commonly referred to as “paleokarst”) (Esteban and Wilson, 1993; Mylroie et al., 1995; Baomin and Jingjiang, 2009; Fournillon et al., 2017; Tian et al., 2017). The paleokarstic concept presumes that the presence of karst features at depth is explained by the burial of carbonates that were karstified at an earlier time in near-surface continental or island setting (Al-Shaieb and Lynch, 1993; Loucks, 1999; Andreychouk et al., 2009). It is believed that open karst cavities may be preserved from collapse even where pressure increases to lithostatic values, until approximately ~1 km, depending on the shape of the voids (Nolting et al., 2021). Paleokarstic horizons are reliably recognized where they underlie unambiguous stratigraphic unconformities related to subaerial exposure (Klimchouk, 2012; Korneva et al., 2014).

In contrast to karst processes related to the action of acidic meteoric solutions that flow by gravity through carbonate rocks (epigene karst), upwelling corrosive fluids may form vast networks of conduits in deep-seated conditions (hypogene karst). With the recent advancements on the concept of hypogene speleogenesis during the past few decades, features previously interpreted as paleo(epigenic) karst in carbonate reservoirs can be better explained as active or relict products of hypogene alteration processes, commonly ascribed to the circulation of endogenous or basinal fluids (Andreychouk et al., 2009; Klimchouk, 2012, and references therein).

Karst cavities more than 2 m in size in Devonian and Carboniferous carbonates were encountered at depths of 0.5 - 1.5 km in the eastern slope of the Volga-Urals oil and gas basin (Andreychouk et al., 2009). Macro-scale solutional conduits and smaller-scale vugs characterize the offshore pre-salt Aptian reservoirs of Africa and Brazil up to depths of 4-6 km (Lima et al., 2020; Fernández-Ibáñez et al., 2022). Abundant micro-scale cavities and karstified zones were identified up to depths of ca. 5-10 km in many other reservoirs hosted in carbonate rocks, contributing to create incredibly high permeability zones (also defined as “super-K”) (Maximov et al., 1984; Andreychouk et al., 2009).

The preservation of solutional voids and caves until such burial depths depends on the shape of the conduit and the presence of an infilling fluid phase. Numerical modelling reported by Nolting et al.

(2021) proved that if isolated conduits are filled with a fluid (such as water) within the shallow phreatic realm, they can remain open up to burial depths of around 10 km regardless of the geometry. Conversely, during shallow diagenesis until burial depths of 1 km, cave geometry has a great impact on collapse in the presence of air-filled cavities. Later exhumation and removal of the upper sedimentary cover allow to access caves where conduit morphology and pattern are, at least to some extent, the results of solutional processes that may have taken place (or may have undergone burial) at considerable depths.

Many productive oil and gas reservoirs present evidence of hypogene karstification related to the upwelling of geothermal solutions, sometimes in association with silicification and/or dolomitization of the pristine carbonate (Xiao et al., 2018; Souza et al., 2021). The following are among the most studied examples: the Parkland field in Western Canada (Packard et al., 2001), the Tazhong Uplift in Tarim Basin, China (Wu et al., 2007; Zhou et al., 2014; Dong et al., 2018; You et al., 2018; Wei et al., 2021), and the pre-salt reservoirs of Kwanza and Congo Basins, Africa (Girard and San Miguel, 2017; Poros et al., 2017; Teboul et al., 2019) and Campos-Santos Basins, Brazil (Jones and Xiao, 2013; De Luca et al., 2017; Lima et al., 2020; Fernández-Ibáñez et al., 2022). These reservoirs show incredibly complex porosity-permeability heterogeneities, fault- and fracture-controlled conduit systems, secondary mineralization and reactive fronts associated with vuggy pore space.

Because hypogene fluids move upwards through the stratigraphy, their flow is controlled not only by the primary permeability of the carbonate layers, but also by the distribution of fracture-zones, faults, and bed-confined distributed fractures (Cazarin et al., 2019; Balsamo et al., 2020). Large faults and fracture zones or fracture corridors, especially where subvertical, favor the efficient upward movement of aggressive fluids without significant heat loss (Bertotti et al., 2020).

Multidisciplinary research integrating the study of stratigraphy, structures, and hypogene karst features in outcropping reservoir analogues are therefore fundamental to unravel the factors involved in speleogenesis and its development through space and time. Moreover, a better understanding on how stratigraphic, structural, and diagenetic processes influence hypogene speleogenesis is of prime importance for proper genetic interpretations, which are crucial for the development of accurate geological models applicable to the prediction, prospection, and economical development of karstified hydrocarbon or geothermal reservoirs.

1.3. High-permeability zones in unconventional silicified reservoirs

Hydrocarbon accumulations in porous chert or silicified carbonate rocks constitute a poorly studied resource. Yet, many trillions of cubic meters of natural gas and hundreds of millions of oil barrels have been produced from these unconventional reservoirs (Rogers and Longman, 2001). In the geological literature, chert reservoirs are commonly described and classified as "carbonate" reservoirs. This is mostly attributed to the fact that many chert units are the product of calcite (or dolomite) replacement, or because they are intercalated in predominantly carbonate formations. In other cases, chert or silicified reservoirs are inappropriately classified as fine-grained siliciclastic lithologies (Packard et al., 2001).

A preliminary distinction proposed for chert/silicified reservoirs (Rogers and Longman, 2001) is based on the silica source, either primary or secondary. Primary silica has been defined as the product of biogenic sedimentation (or re-mobilization) of sponge spicules (e.g., Glick and Spivey-Grabbs fields in Kansas or Dollarhide & University fields in Texas; Rogers et al., 1995; Montgomery et al., 1998; Ruppel and Barnaby, 2001; Watney et al., 2001), or diatom and radiolarian skeletal grains (e.g., Elk Hills in California; Reid and McIntyre, 2001). Chert of these types has also been defined in the literature as "*porcellanite*", "*spiculites*" or "*chat*" (Rogers and Longman, 2001).

On the contrary, secondary silicification requires an external (endogenous) source of silica to alter the pristine carbonate deposits, like those at Parkland field in British Columbia (Packard et al., 2001), Wolf Springs in Montana (Luebking et al., 2001), Tarim Basin in China (Wu et al., 2007; Zhou et al., 2014; Dong et al., 2018; You et al., 2018; Wei et al., 2021), and in the recently discovered pre-salt reservoirs of offshore Brazil and Africa (Girard and San Miguel, 2017; De Luca et al., 2017; Poros et al., 2017; Teboul et al., 2019; Lima et al., 2020; Fernández-Ibáñez et al., 2022).

Most hydrocarbon production from biogenic chert relates to high porosity lithofacies (Rogers and Longman, 2001) characterized by: 1) moldic porosity in skeletal grains constituted by opal-A or opal-CT (Ruppel and Barnaby, 2001; Watney et al., 2001); 2) preservation of porosity as opal-CT dissolves and micro-quartz precipitates (Graham and Williams, 1985; Chaika et al., 2001; Watney et al., 2001); 3) small vuggy porosity, believed to be the result of both opal or quartz dissolution during diagenesis (Ruppel and Barnaby, 2001); 4) enhanced porosity at clast boundaries (Watney et al., 2001); 5) intraclast micro-fracturing (Watney et al., 2001); 6) intercrystalline microporosity within quartz grains (Ruppel and Barnaby, 2001).

Mississippian and Miocene chert reservoirs of North America exhibit porosities reaching up to 50-70%, and absolute permeabilities from 0.01 to 700 mD (Montgomery et al., 1998; Watney et al., 2001; Chaika et al., 2001; Reid and McIntyre, 2001). On the contrary, silicified carbonate reservoirs resulting from the alteration of pristine carbonate rocks usually present a close association with vuggy porosity-permeability and solutional voids (Fernández-Ibáñez et al., 2022). Recently, a hydrothermal origin for the silicification processes documented in the pre-salt reservoirs have been hypothesized for the Campos and Santos Basins (Alvarenga et al., 2016; De Luca et al., 2017; Lepley et al., 2017; Lima and De Ros, 2019; Lima et al., 2020), its western African counterpart, the Kwanza Basin offshore Angola, (Poros et al., 2017; Girard and San Miguel, 2017; Teboul et al., 2017, 2019), as well as for the Parkland gas field in Canada (Packard et al., 2001) and the Tarim Basin in China (Wu et al., 2007; Zhou et al., 2014; Hu et al., 2018; Wei et al., 2021). In all these basins, silica is present in different phases such as micro- or crypto-crystalline quartz, chalcedony, spherulitic fibrous quartz, and megaquartz cement, with SiO_2 content that can reach up to 50 - 90 wt.% (Packard et al., 2001; You et al., 2018; Lima et al., 2020).

During their tectonic-burial history, the pre-salt and Tarim Basin reservoirs were affected by events that drastically modified the petrophysical properties of the pristine carbonates, generating high porosities (up to 15-20%) and high permeability zones up to 100-200 mD (Wu et al., 2007; You et al., 2018; Hu et al., 2018). These high permeability (cavernous) zones can be partially filled with mineral precipitates (among the most common: quartz, chalcedony, calcite, dolomite, sulfates, sulfides, fluorite, hematite).

Despite the great number of studies regarding the origin of silicification, the interpretation of high-permeability zones has been rarely put in the context of solutional 'karstic' hypogene processes (Wu et al., 2007; Poros et al., 2017). In contrast, most of the secondary porosity and permeability has been generally attributed to fractures (He et al., 2019; Lu et al., 2020), diagenetic (Tosca and Wright, 2018), paleokarstic (Zhou et al., 2014; Lu et al., 2020), and replacement or alteration/metasomatic processes (Packard et al., 2001; Lima et al., 2020).

With the recent advancements in hypogene karst studies, deep-seated dissolution in almost pure quartz lithologies has been reported in several sites worldwide. Cavities enlarged by dissolution in quartzites were described in Kirghizstan (Leven, 1961; Kornilov, 1978), in Ukraine (Tsykin, 1989), in Colorado (Lovering et al., 1978), and in Russia (Dublyansky, 1990). Proper caves and vast karst systems were also reported in the silicified carbonates of Sardinia, Italy (Sauro et al., 2014) and in Northeastern Brazil (Bertotti et al., 2020; La Bruna et al., 2021; Souza et al., 2021). As reported in these examples, dissolution voids may span from small size vugs/channels to macro-scale karst conduits like in Corona 'e Sa Craba Cave, Italy (Sauro et al. 2014) or Crystal Cave, Brazil (Souza et al., 2021).

Despite being generally considered unusual, the formation of void-conduit systems in quartz lithologies is possible under specific geochemical and hydrodynamic conditions (Andreychouk et al., 2009; Sauro, 2014). The solubility of silica is low in the conditions normally prevailing at the Earth's surface (Mitsiuk, 1974); in fact, values of quartz solubility calculated in pure water at 25°C with experimental tests vary between 6 and 14 mg/L (De Waele and Gutiérrez, 2022). pH exerts a significant control on silica dissolution rate and solubility, which is low and nearly constant at pH < 8-9, and significantly increases at more alkaline values (Fig. 4) (Mitsiuk, 1974; Bennet et al., 1988; Andreychouk et al., 2009; Mecchia et al., 2019; Pan et al., 2021). However, it is well known that silica solubility exponentially increases with temperature (Fig.4A) (Siever, 1962; Rimstidt, 1997; Dove, 1999; Gunnarsson and Arnórsson, 2000; Marin-Carbonne et al., 2014; Sauro et al., 2014). Some authors reported also that the presence of cations transported in solution (e.g., Ba^{2+}, Ca^{2+}) could have a significant enhancing effect on quartz solubility (Dove and Nix, 1997). The solubility of amorphous silica glass, opal-A, and opal-CT is up to one order of magnitude greater than the solubility of quartz and may reach tens and hundreds of mg/L (Andreychouk et al., 2009; Sauro et al., 2014; Mecchia et al., 2019; Pan et al., 2021) (Fig.4). The dissolution rate for both quartz and amorphous silica increases up to four orders of magnitude at values of pH higher than 8-9 (Sauro, 2014).

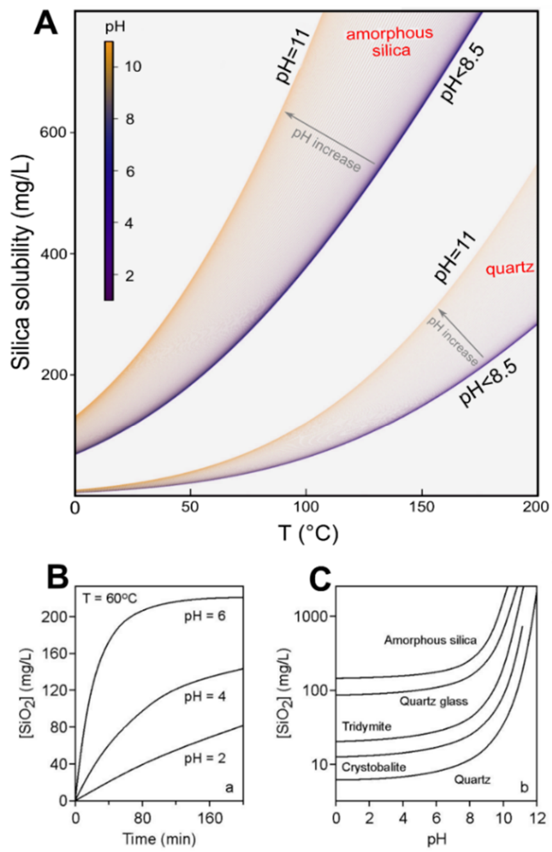

Figure 4. A) Solubility curves of amorphous silica (left) and quartz (right) at varying temperature and pH (modified from Pan et al., 2021 and calculated from the equations for quartz and amorphous silica given in Dove, 1995 and Gunnarsson and Arnórsson, 2000). B) Dissolution rate of amorphous silica at T=60°C and varying pH (from Andreychouk et al., 2009 after Mitsiuk, 1974). C) Solubility of different varieties of SiO_2 in pure water at different pH in standard conditions (from Andreychouk et al., 2009 after Mitsiuk, 1974).

High temperature and high pH conditions may be characteristic of hydrothermal systems in the deep-seated hypogenic zone (Dublyansky, 1990; Andreychouk et al., 2009; Klimchouk, 2017), where solubility of silica is increased, and becomes comparable to that of gypsum or anhydrite in near-surface conditions (Klimchouk, 2012; De Waele and Gutiérrez, 2022).

Considering these factors, it is important to take in consideration the potential of hydrothermal hypogene processes in deep carbonate reservoirs where silicification, dissolution, and mineral precipitation are intimately linked. Given that many silicified reservoirs are in close association with carbonate rocks or residual calcite/dolomite, this may be true not only for the generation of solutional porosity in silica, but also in carbonate lithofacies. At low or moderate pressures, calcite and dolomite are extremely soluble in acidic solutions, whereas silica dissolves more readily in alkaline conditions (De Waele and Gutiérrez, 2022). At the same time, temperature has an opposite effect respect to quartz and calcite solubility, being the lower temperatures most favorable for calcite dissolution whereas high temperatures favor silica dissolution (Cui et al., 2017). This duality may be characteristic of evolving hydrothermal (hypogene) speleogenesis (Dublyansky, 1995) and may have significant implications for carbonate and silicified/chert reservoirs, which are currently under-evaluated.

1.4. Geological controls on hypogene karst development

There is a large gap to fill in the understanding of dissolution mechanisms and karstification processes over geological time scales investigated by means of laboratory experiments, numerical modelling, and field data (De Waele and Gutiérrez, 2022). This is commonly attributed to spatial and temporal scale problems (Viles, 2001). Analogical experiments, simulations, and numerical modelling lack in depicting the real complexity of the multi-scale local and regional geological controls that exert a critical role on karst development. In contrast, multi- and inter-disciplinary field data acquired in caves accessible to scientists and speleologists can represent a first-order tool to study and expand our comprehension on the relation between background geological factors, karst initiation, and speleogenesis.

Among the main factors that steer speleogenesis in carbonate rocks, primary diagenetic and sedimentary features are of crucial importance. The proportion of soluble minerals and impurities in the stratigraphic successions is among the most important factors involved in the feasibility of karstification. Poorly soluble grains inhibit dissolution and may even prevent karst development. In the case of carbonate rocks, it is widely accepted that karst is mostly favored in rocks with almost pure bulk composition (e.g., > 80-90 wt.% of $CaCO_3$ or $CaMg(CO_3)_2$), like pure limestones, dolostones or marbles (Bögli, 1980; Klimchouk and Ford, 2000; Ford and Williams, 2007). Heterolith layers or carbonates with a high percentage of dispersed siliciclastic grains (e.g., marls and marly limestones), on the contrary, may be unsuitable for karst development. Furthermore, grain size, grain textures, and their roughness strongly impact fluid-rock interactions and dissolution rates, given that they influence the water-rock reactive area available for dissolution (Rauch and White, 1977; Walter and Morse, 1984; Ford and Williams, 2007; De Waele and Gutiérrez, 2022).

The stratigraphic and hydrological setting play a primary role in determining the size, shapes, and spatial distribution of karst voids in carbonate rocks (Lowe, 1997; Klimchouk and Ford, 2000; Palmer, 2000, 2007; Cazarin et al., 2019). In layered sedimentary units, the vertical variation of petrophysical properties such as porosity and permeability may present strong heterogeneity, greatly impacting fluid flow and storage (Klimchouk et al., 2009; Klimchouk et al., 2016; Balsamo et al., 2020). Moreover, because of the low primary porosity and permeability typical of tight carbonates, especially if subjected to severe burial diagenesis, the potential of karstification is generally controlled by secondary non-fabric selective pores, which are largely represented by stratigraphic or structural discontinuities.

The occurrence, geometrical properties, and preferential orientation of tectonic discontinuities and their networks play an important role in guiding the trends of cave systems, both epigene and hypogene (Palmer, 1989, 1991; Shanov and Kostov, 2015; Wang et al., 2017; Antonellini et al., 2019; Pisani et al., 2019). Since hypogene speleogenesis relies on ascending discharge, initial variations of the vertical permeability across layered sedimentary sequences are critically important (Gross and Eyal, 2007; Cazarin et al., 2019; Klimchouk, 2019; Balsamo et al., 2020). These variations are mainly subject to controls imposed by lithostratigraphy and related differences in: rock composition (and solubility), primary porosity, cementation, diagenetic re-crystallization, mechanical properties, and fracture patterns (e.g., distribution, geometry, connectivity, and hierarchy). Bed-confined (strata-bound) fracture networks, which largely depend on mechanical properties, determine the hydro-stratigraphic compartmentalization of rock units, whereas the vertical connectivity and discharge relies mainly on the presence of cross-formational structures (e.g., through-going faults, fractures, and fault/fracture zones; Antonellini and Aydin, 1994; Lavenu et al., 2014; Klimchouk et al., 2016; Rustichelli et al., 2016; Klimchouk, 2019; Balsamo et al., 2020).

Structures of enhanced permeability that cross barriers and interfaces between hydro-stratigraphic units are usually comprised of segments aligned within narrow zones of localized deformation.

Combinations of several major fractures variously linked by splay fracture systems and joints (Myers and Aydin, 2004) produce connectivity that is essential for upwelling fluid migration from deep-seated sources (Klimchouk, 2012; Audra and Palmer, 2015). Speleogenetic pathways along deep-rooted structures is strictly controlled by the relative permeability of the different hydro-stratigraphic storeys, where vertical flow may diverge laterally in presence of high-permeability beds or low-permeability barriers (e.g., buffer zones, seals, aquitards) that can confine the flow pathways. If significant permeability difference exists between two storeys, vast maze networks are usually found in the more permeable beds and below the low-permeability aquitards, with conduits controlled mainly by the most conductive fracture systems (Klimchouk, 2012; Audra and Palmer, 2015; Klimchouk, 2019). The presence of cross-formational structures allowing discharge and hydro-stratigraphic interfaces within predominantly soluble carbonates, commonly produce 3D multistorey cave patterns (Audra and Palmer, 2015; De Waele and Gutiérrez, 2022), which are typical of deep-rooted hypogene speleogenesis in layered sequences.

Large, deep, and complex fault zones supporting cross-formational upwelling flow are commonly long-lived structures, even if periods of intense and quiescent fluid activity may alternate (Tartaglia et al., 2020). Various geochemical scenarios that can change over geological time scales may favor dissolution and produce the generation of void-conduit systems, as well as promoting alternating dissolution and precipitation conditions (Michie, 2015; Bertotti et al., 2020; Cazarin et al., 2021; Vignaroli et al., 2021).

Since many tectonic and diagenetic features that govern the relative permeability of rock units are below seismic resolution (e.g., bed-confined joints, pressure solution seams, bed interfaces), exhumed hypogene cave patterns that reflect paleo fluid flow pathways are excellent laboratories to study the relation between structures, stratigraphy, and speleogenesis (Bertotti et al., 2020; La Bruna et al., 2021). Despite the increasing amount of research developed in recent time on this topic, a detailed understanding on the influence of stratigraphic and structural factors in controlling hypogene cave patterns and speleogenesis is still requiring attention. Therefore, the correct recognition and characterization of structural, diagenetic, and speleogenetic features is key to fill the existing gap between the in-situ and the seismic resolution analyses (Fig. 3) in reservoirs, aquifers, and geothermal fields.

1.5. Objectives and outline of the thesis

The main objective of this thesis is to improve the comprehension of the controlling factors that guide the formation of solutional (karst) porosity in hypogene settings, highlighting the speleogenetic mechanisms and their implications for karst reservoirs in carbonate and silicified rocks. To attempt these goals, we selected two case studies where accessible (fossil) caves represent ideal analogues of deep-seated hypogene conduit networks that may be encountered in different reservoir settings.

During the thesis I realized the following fieldwork and research activities in laboratories at the University of Bologna (IT), University of Natal (BR), University of Innsbruck (AT), and University of Genova (IT):

- Sampling of bedrock, fault rocks and secondary mineralizations in caves and outcrops
- Geological, structural, and geomorphological surveys in caves and outcrops
- Elaboration and morphological observations of 3D cave models and topographic surveys
- Quantitative structural surveys and fracture properties characterization
- Petrographic observations and interpretation of rock textures at optical microscope
- SEM-EDS analyses of cave bedrock and secondary mineralizations
- Petrophysical properties analyses (porosity-permeability) with a N_2-gas porosimeter on rock core plugs
- Microthermometry and Raman spectroscopy of fluid inclusions in silica samples

I also supervised other laboratory analyses performed by collaborators from external facilities or Universities:

- $\delta^{30}Si$ and $\delta^{18}O$ stable isotope measurements on silica samples (Nord-SIMS Lab, Sweden)
- XRD-XRF analyses of rocks and mineral samples (University of São Paulo, Brazil)
- U-Th-Pb dating of monazite grains with electron-microprobe (University of Graz, Austria)
- FTIR spectroscopy and $\delta^{13}C$ stable isotope measurements on carbonaceous material trapped in speleothems and host rock samples (University of Almería, Spain)

This PhD dissertation is organized as a collection of four scientific articles that are presented in two sections: the first is focused on the relationships between fracture patterns, faults and folds architectures, and flow (dissolution) pathways in deformed carbonate sequences of the Majella Massif (Cavallone-Bove cave system, Italy) and in the Salitre Formation (São Francisco Craton, Brazil); the second section is focused on the study of a peculiar cave system in Brazil where

silicification and hydrothermal alteration produced solutional features like those characterizing many hydrocarbon reservoirs in chert lithology and silicified carbonates.
The main outline of the thesis and my contribution for each article are summarized below:

SECTION: Hypogene karst dissolution in fractured carbonates

Paper 1 (chapter 2.1.)

Structurally controlled development of a sulfuric hypogene karst system in a fold-and-thrust belt (Majella Massif, Italy) *First author and corresponding author. Author contribution: conceptualization, methodology, investigation, formal analyses, validation, data curation, writing original draft-review-editing.*

In this paper, we described the formation of a sulfuric hypogene karst system in the Majella anticline (Central Italy). The analyzed karst features represent potential analogues of hypogene voids typically found in oil and gas reservoirs associated with deformed fold-and-thrust belts in carbonate host rocks. We documented the relationship between tectonic structures, lithology and fluid flow pathways observed in the southeastern domain of the Majella anticline. Our findings suggest that deep-rooted, sub-vertical strike-slip fault zones reaching the H_2S source rocks were the main vehicle for ascending acidic fluid flow. Linkage and intersection of these faults by splays in extensional stepovers and pre-orogenic normal faults allowed ascending fluids to reach multiple recharge points (feeders) near the paleo water-table. In proximity of the oxygenated groundwater, where H_2SO_4 was produced, lateral dissolution focused along bedding planes and zones of localized deformation (e.g, fracture clusters, fracture corridors) characterizing the hinge of the anticline. We conclude that the structural position in the anticline and vertically extended strike-slip fault zones control the localization of efficient permeability pathways and represent first order controlling features for fluid flow in the fold-and-thrust belt. Finally, we discuss the time-space evolution, geometry, and patterns of hypogene karst systems in other folded carbonates, highlighting the importance of conceptual speleogenetic models that may help for accurate conduit-system characterization in fractured and karstified reservoirs.

Paper 2 (chapter 2.2.)

Flow pathways in multiple-direction fold hinges: Implications for fractured and karstified carbonate reservoirs *Co-author. Author contribution: investigation, validation, writing review-editing.*

In this paper, we studied four caves located in the São Francisco Craton (Brazil) to determine the relationships between fracture and fold patterns and the development of hypogene karst conduits, like those that may form in deep carbonate reservoirs. We performed structural field investigations, petrographic analyses, and geometric-geomorphological characterization using Light Detection and Ranging (LIDAR). We found that the conduit shape, usually with an ellipsoidal cross-section, reflects the tectonic features and stratigraphic-textural variations in the sedimentary sequence. Carbonate layers containing pyrite and low terrigenous mineral contents are generally more karstified and appear to act as favorable flow pathways. Our results indicate that the development of the karst features is related to persistent fracture corridors formed along parallel and orthogonal sets of fold hinges, which represented preferential pathways for fluid flow and contributed to the development of enhanced dissolution zones. This study provides insights into the prediction of subseismic-scale voids in folded carbonate reservoirs, with direct application for the hydrocarbon and hydrogeology industry.

SECTION: Silicification and high-permeability zones produced by hydrothermal alteration in mixed carbonate-siliciclastic sequences

Paper 3 (chapter 3.1.)

Silicification, flow pathways, and deep-seated hypogene dissolution controlled by structural and stratigraphic variability in a carbonate-siliciclastic sequence (Brazil) *First author and corresponding author. Author contribution: conceptualization, methodology, investigation, formal analyses, validation, data curation, writing original draft-review-editing.*

In this paper, we documented the relationships between lithology, structural patterns, silicification, and the spatial-morphological organization of a multistorey cave system developed in a mixed carbonate-siliciclastic sequence in Brazil (Neoproterozoic age). Our results indicate that the interplay between lithology, silicification, fracture patterns (influenced by lithostratigraphic variability), and petrophysical properties control the formation of high- or low-permeability zones. We propose a deep-seated hydrothermal origin for the fluids involved in the main phases of karst formation. Warm and alkaline hydrothermal fluids caused silica dissolution, followed by chalcedony and quartz reprecipitation in pore space and fractures at varying pH or temperature. Rising hydrothermal solutions concentrated along through-going vertical fracture zones in the lower storey, whereas sub-horizontal bedding-parallel fluid flow was focused along sedimentary packages containing highly silicified dolostones (SiO_2 > 80 wt.%) characterized by high permeability. The Calixto Cave is an enlightening example for the complex speleogenetic history affecting a mixed carbonate-siliciclastic succession where the combined effect of silicification and hypogene karst dissolution can potentially generate high-quality reservoirs. In fact, this cave represents an analogue of layered carbonate-siliciclastic units where diagenetic processes and hydrothermal (karst) alteration may drastically modify the petrophysical properties of the host rock, generating multistorey conduit systems.

Paper 4 (chapter 3.2.)

Hydrothermal silicification and hypogene dissolution of an exhumed Neoproterozoic carbonate sequence in Brazil: Insights from fluid inclusion microthermometry and silicon-oxygen isotopes

First author and corresponding author. Author contribution: conceptualization, methodology, investigation, formal analyses, validation, data curation, writing original draft-review-editing.

In this paper, we studied a hypogene cave system in northeastern Brazil (Calixto Cave) to unravel the origin of silicification and hypogene dissolution in the silicified carbonates. The study followed a multidisciplinary approach combining petrography, fluid inclusion microthermometry and Raman spectroscopy, silicon-oxygen stable isotope analyses, and U-Th-Pb dating of monazite grains. Our results point to a high-temperature hydrothermal origin (T > 160-210 °C) for the emplacement of megaquartz cement that partially fills vuggy pore space and fractures in the cave. The $\delta^{30}Si$ and $\delta^{18}O$ isotopes modelling rules out the possibility of a pure diagenetic origin, confirming the source of Si-rich hydrothermal fluids in the underlying Mesoproterozoic basement units (Chapada Diamantina quartzites). U-Th-Pb dating of monazite crystals associated with the silicified layers in quartz-rich hydraulic breccias points to a detrital origin. A new maximum depositional age for the Salitre Formation has been calculated (617±26 Ma). However, some crystals appear to have been hydrothermally altered, giving unreliable (younger) results with high uncertainties. We interpreted our results in their regional context, suggesting that the Cambrian tectono-thermal events associated with the latest phases of the Brasiliano orogeny, responsible for large-scale hydrothermal fluids circulation in the basin, promoted the alteration of the carbonate sequence and dissolution. Despite the high variability of silica sources in sedimentary basins, integrating geochemical, petrographic, and field observations in caves representing analogues of deep-seated conduits, is a first-order tool to expand our knowledge on hypogene speleogenetic and minerogenetic processes. The research conducted in Calixto Cave may help to clarify the origin of silica dissolution-precipitation processes in other carbonate reservoirs where silicification and high-permeability zones are closely associated.

References

Agar, S.M., Geiger, S., 2015. Fundamental controls on fluid flow in carbonates: current workflows to emerging technologies. Geol. Soc. London Spec. Publ. 406, 1–59.

Al-Shaieb, Z., M. Lynch, 1993. Paleokarst Features and Thermal Overprints Observed in Some of the Arbuckle Cores in Oklahoma. In: Fritz, R.D., Wilson, J.L., Yurewicz, D.A. (Eds.), Paleokarst Related Hydrocarbon Reservoirs. SEMP Spec. Pub., Vol. 18, 11−59.

Alvarenga, R.S., Iacopini, D., Kuchle, J., Scherer, C.M.S., Goldberg, K., 2016. Seismic characteristics and distribution of hydrothermal vent complexes in the Cretaceous offshore rift section of the Campos Basin, offshore Brazil. Mar. Pet. Geol. 74, 12–25.

Andreychouk, V., Dublyansky, Y., Ezhov, Y., Lisenin, G., 2009. Karst in the Earth's Crust: Its Distribution and Principal Types. University of Silezia — Ukrainian Institute of Speleology and Karstology, Sosnovec–Simferopol, 72 pp.

Antonellini, M., Aydin, A., 1994. Effect of Faulting on Fluid Flow in Porous Sandstones: Petrophysical Properties. AAPG Bulletin 78, 355–377.

Antonellini, M., Nannoni, A., Vigna, B., De Waele, J., 2019. Structural control on karst water circulation and speleogenesis in a lithological contact zone: the Bossea cave system (Western Alps, Italy). Geomorphology 345, 106832.

Audra, P., Mocochain, L., Bigot, J.Y., Nobecourt, J.C., 2009. Hypogene cave patterns. In: Klimchouk, A.B., Ford, D.C. (Eds.), Hypogene speleogenesis and karst hydrogeology of artesian basins. Ukrainian Institute of Speleology and Karstology, Special Paper 1, 17-22.

Audra, P., Palmer, A.N., 2011. The pattern of caves: controls of epigenic speleogenesis. Géomorphologie Relief Processus Environnement 17, 359–378.

Audra, P., Palmer, A.N., 2015. Research frontiers in speleogenesis. Dominant processes, hydrogeological conditions and resulting cave patterns. Acta Carsologica 44 (3), 315–348.

Auler, A.S., Smart, P.L., 2003. The influence of bedrock-derived acidity in the development of surface and underground karst: evidence from the Precambrian carbonates of semi-arid northeastern Brazil. Earth Surf. Proc. Landf. 28, 157–168.

Baomin, Z., Jingjiang, L., 2009. Classification and characteristics of karst reservoirs in China and related theories. Pet. Explor. Dev. 36, 12–29.

Bakalowicz, M.J., Ford, D.C., Miller, T.E., Palmer, A.N., Palmer, M.V., 1987. Thermal genesis of dissolution caves in the Black Hills, South Dakota. Geol. Soc. Am. Bull. 99, 729–738.

Balsamo, F., Bezerra, F.H.R., Klimchouk, A.B., Cazarin, C.L., Auler, A.S., Nogueira, F.C., Pontes, C., 2020. Influence of fracture stratigraphy on hypogene cave development and fluid flow anisotropy in layered carbonates, NE Brazil. Mar. Pet. Geol. 114, 104207.

Bennett, P.C., Melcer, M.E., Siegel, D.I., Hassett, J.P., 1988. The dissolution of quartz in dilute aqueous solutions of organic acids at 25°C. Geochim. Cosmochim. Acta 52, 1521–1530.

Bertotti, G., Audra, P., Auler, A., Bezerra, F.H., de Hoop, S., Pontes, C., Prabhakaran, R., Lima, R., 2020. The Morro Vermelho hypogenic karst system (Brazil): Stratigraphy, fractures, and flow in a carbonate strike-slip fault zone with implications for carbonate reservoirs. AAPG Bull. 104, 2029–2050.

Bögli, 1980. Karst Hydrogeology and Physical Speleology. Springer-Verlag, Berlin, 304 pp.

Borghi, A., Renard, P., Jenni, S., 2010. How to model realistic 3D karst reservoirs using a pseudo-genetic methodology–example of two case studies. In: Andreo B., Carrasco, F., Durán, J.J., LaMoreaux, J.W. (Eds.), Advances in Research in Karst Media, Springer, New York, 251–255.

Buryakovsky, L., Chilingar, G.V., Rieke, H.H., Shin, S., 2012. Petrophysics: Fundamentals of the petrophysics of oil and gas reservoirs. Hoboken, New Jersey, John Wiley & Sons, 369 pp.

Cazarin, C.L., Bezerra, F.H.R., Borghi, L., Santos, R.V., Favoreto, J., Brod, J.A., Auler, A.S., Srivastava, N.K., 2019. The conduit-seal system of hypogene karst in Neoproterozoic carbonates in northeastern Brazil. Mar. Pet. Geol. 101, 90–107.

Cazarin, C.L., van der Velde, R., Santos, R.V., Reijmer, J.J.G., Bezerra, F.H.R., Bertotti, G., La Bruna, V., Silva, D.C.C., de Castro, D.L., Srivastava, N.K., Barbosa, P.F., 2021. Hydrothermal activity along a strike-slip fault zone and host units in the São Francisco Craton, Brazil – Implications for fluid flow in sedimentary basins. Precambrian Res. 106365.

Craig, D.H., 1988. Caves and Other Features of Permian Karst in San Andres Dolomite, Yates Field Reservoir. In: James, N.P., Choquette, P.W. (Eds.), Paleokarst. Springer, New York, 342–363.

Chaika, C., Williams, L.A., 2001. Density and Mineralogy Variations as a Function of Porosity in Miocene Monterey Formation Oil and Gas Reservoirs in California. AAPG Bulletin 85, 149–167.

Chen, J., Xu, J., Wang, S., Sun, Z., Li, Z., Jia, W., Peng, P., 2021. Dissolution of different reservoir rocks by organic acids in laboratory simulations: Implications for the effect of alteration on deep reservoirs. Geofluids 2021, 6689490.

Columbu, A., Audra, P., Gázquez, F., D'Angeli, I.M., Bigot, J.Y., Koltai, G., Chiesa, R., Yu, T.L., Hu, H.M., Shen, C.C., Carbone, C., Heresanu, V., Nobécourt, J.C., De Waele, J., 2021. Hypogenic speleogenesis, late stage epigenic overprinting and condensation-corrosion in a complex cave system in relation to landscape evolution (Toirano, Liguria, Italy). Geomorphology 376, 107561.

Coogan, A.H., Maggio, C., Bebout, D.G., 1972. Depositional environments and geologic history of golden Lane and poza rica trend, Mexico, an alternative view. AAPG Bulletin 56, 1419–1447.

Cui, H., Kaufman, A.J., Xiao, S., Zhou, C., Liu, X.M., 2017. Was the Ediacaran Shuram Excursion a globally synchronized early diagenetic event? Insights from methane-derived authigenic carbonates in the uppermost Doushantuo Formation, South China. Chem. Geol. 450, 59–80.

D'Angeli, I.M., 2019. Speleogenesis of sulfuric acid caves in Southern Italy. PhD thesis, University of Bologna, 296 pp.

D'Angeli, I.M., Parise, M., Vattano, M., Madonia, G., Galdenzi, S., De Waele, J., 2019. Sulfuric acid caves of Italy: a review. Geomorphology 333, 105–122.

De Luca, P.H.V., Matias, H., Carballo, J., Sineva, D., Pimentel, G.A., Tritlla, J., Esteban, M., Loma, R., Alonso, J.L.A., Jiménez, R.P., Pontet, M., Martinez, P.B., Vega, V., 2017. Breaking barriers and paradigms in presalt exploration: The Pão de Açúcar discovery (Offshore Brazil). AAPG Memoir 113, 177–193.

De Waele, J., Audra, P., Madonia, G., Vattano, M., Plan, L., D'Angeli, I. M., Bigot, J.Y., Nobécourt, J. C., 2016. Sulfuric acid speleogenesis (SAS) close to the water table: examples from southern France, Austria, and Sicily. Geomorphology 253, 452-467.

De Waele, J., Gutiérrez, F., 2022. Karst Hydrogeology, Geomorphology and Caves. John Wiley & Sons, 888 pp.

Dong, S., You, D., Guo, Z., Guo, C., Chen, D., 2018. Intense silicification of Ordovician carbonates in the Tarim Basin: constraints from fluid inclusion Rb–Sr isotope dating and geochemistry of quartz. Terra Nova 30, 406–413.

Dove, P.M., 1995. Kinetic and thermodynamic controls on silica reactivity in weathering environments. In: White A. F., Brantley S. L. (Eds.), Reviews in Mineralogy 31, Chemical Weathering Rates of Silicate Minerals, Berlin, De Gruyter & Co., 235-291.

Dove, P.M., Nix, C.J., 1997. The influence of the alkaline earth cations, magnesium, calcium, and barium on the dissolution kinetics of quartz. Geochimica et Cosmochimica Acta 61(16), 3329–3340.

Dublyansky, Y.V., 1990. Zakonomernosti formirovaniya i modelirovaniye gidrotermokarsta (Particularities of the development and modeling of hydrothermal karst). Nauka, Novosibirsk, 151 pp.

Dublyansky, Y.V., 1995. Speleogenetic history of the Hungarian hydrothermal karst. Environmental Geology 25, 24–35.

Dublyansky, Y.V., 2013. Karstification by geothermal waters. In: Shroder, J., Frumkin, A. (Eds.), Treatise on geomorphology, Vol. 6, Karst Geomorphology. Academic Press, San Diego, 57–71.

Dublyansky, Y.V., Klimchouk, A., Spötl, C., Timokhina, E.I., Amelichev, G.N., 2014. Isotope wallrock alteration associated with hypogene karst of the Crimean piedmont, Ukraine. Chemical Geology 377, 31–44.

Esteban, M., Wilson, J.L., 1993. Introduction to Karst Systems and Paleokarst Reservoirs. In: Fritz, R.D., Wilson, J.L., Yurewicz, D.A. (Eds.), Paleokarst Related Hydrocarbon Reservoirs. SEMP Spec. Pub., Vol. 18, 1-9.

Farooq, U., Meyer, A., Al Obeidli, A.K., Maroof, M. Ben, Ali Baloch, S., Dey, S.K., Almarzooqi, M.J., 2020. Characterization of karst development using an integrated workflow in an upper cretaceous carbonate reservoir from onshore field, United Arab Emirates. Soc. Pet. Eng., Abu Dhabi Int. Pet. Exhib. Conf. 2020, ADIP 2020.

Fernández-Ibáñez, F., Jones, G.D., Mimoun, J.G., Bowen, M.G., Simo, J.A.T., Marcon, V., Esch, W.L., 2022. Excess permeability in the Brazil pre-Salt: Non matrix types, concepts, diagnostic indicators, and reservoir implications. AAPG Bulletin 106, 701–738.

Ford D.C., Williams P.W., 2007. Karst hydrogeology and geomorphology. John Wiley & Sons, 562 pp.

Fournillon, A., Abelard, S., Viseur, S., Arfib, B., Borgomano, J., 2012. Characterization of karstic networks by automatic extraction of geometrical and topological parameters: comparison between observations and stochastic simulations. Geological Society of London Special Publications 370, 247–264.

Fournillon, A., Bellentani, G., Moccia, A., Jumeaucourt, C., Terdich, P., Siliprandi, F., Peruzzo, F., 2017. Characterization of a Paleokarstic Oil Field (Rospo Mare, Italy): Sedimentologic and Diagenetic Outcomes, and Their Integration in Reservoir Simulation, 47–55.

Galdenzi, S., Menichetti, M., 2017. Hypogenic Caves in the Apennine Mountains (Italy). In: Klimchouk, A.B., Audra, P., Palmer, A.N., De Waele, J., Auler, A. (Eds.), Hypogene Karst Regions and Caves of the World. Springer International Publishing, Cham, 127-142.

Girard, J.P., San Miguel, G., 2017. Evidence of high temperature hydrothermal regimes in the pre-salt series, Kwanza Basin, offshore Angola. In: American Association of Petroleum Geologists Annual Convention and Exhibition (Houston, Texas, USA, Abstracts).

Giuffrida, A., La Bruna, V., Castelluccio, P., Panza, E., Rustichelli, A., Tondi, E., Giorgioni, M. Agosta, F., 2019. Fracture simulation parameters of fractured reservoirs: Analogy with outcropping carbonates of the Inner Apulian Platform, southern Italy. J. Struct. Geol. 123, 18-41.

Giuffrida, A., Agosta, F., Rustichelli, A., Panza, E., La Bruna, V., Eriksson, M., Torrieri, S., Giorgioni, M., 2020. Fracture stratigraphy and DFN modelling of tight carbonates, the case study of the Lower Cretaceous carbonates exposed at the Monte Alpi (Basilicata, Italy). Mar. Pet. Geol. 112, 104045.

Graham, S.A., Williams, L.A., 1985. Tectonic, depositional and diagenetic history of Monterey Formation (Miocene), central San Joaquin basin, California. AAPG Bulletin 69, 385–411.

Gross, M.R., Eyal, Y., 2007. Throughgoing fractures in layered carbonate rocks. Bull. Geol. Soc. Am. 119, 1387–1404.

Gunnarsson, I., Arnórsson, S., 2000. Amorphous silica solubility and the thermodynamic properties of $H_4SiO_4^{\circ}$ in the range of 0°to 350°C at P(sat). Geochim. Cosmochim. Acta 64, 2295–2307.

He, J., Ding, W., Huang, W., Cao, Z., Chen, E., Dai, P., Zhang, Y., 2019. Petrological, geochemical, and hydrothermal characteristics of Ordovician cherts in the southeastern Tarim Basin, NW China, and constraints on the origin of cherts and Permian tectonic evolution. J. Asian Earth Sci. 170, 294–315.

Hendry, J., Burgess, P., Hunt, D., Janson, X., Zampetti, V., 2021. Seismic characterization of carbonate platforms and reservoirs: An introduction and review. Geol. Soc. Spec. Publ. 509, 1–28.

Hill, C.A., 1990. Sulfuric acid speleogenesis of Carlsbad Cavern and its relationship to hydrocarbons, Delaware Basin, New Mexico and Texas. AAPG Bulletin 74, 1685–1694.

Hill, C.A., 1995. Sulfur redox reactions: hydrocarbons, native sulfur, Mississippi Valley-type deposits, and sulfuric acid karst in the Delaware Basin, New Mexico and Texas. Environmental Geology 25, 16–23.

Hill, C.A., 2000. Overview of the geologic history of cave development in the Guadalupe Mountains, New Mexico. Journal of Cave and Karst Studies 62 (2), 60–71.

Hu, W., Wang, X., Zhu, D., You, D., Wu, H., 2018. An overview of types and characterization of hot fluids associated with reservoir formation in petroliferous basins. Energy Exploration & Exploitation 36, 1359–1375.

Huntoon, P.W., 1995. Is it appropriate to apply porous media groundwater circulation models to karstic aquifers? In: El-Kadi, Ali (ed.), Groundwater models for resources analysis and management. Lewis Publishers, Boca Raton, pp. 339−358.

Jagnow, D.H., Hill, C.A., Davis, D.G., DuChene, H.R., Cunningham, K.I., Northup, D.E., Queen, J.M., 2000. History of the sulfuric acid theory of speleogenesis in the Guadalupe Mountains, New Mexico. Journal of Cave and Karst Studies 62 (2), 54–59.

Jones, G.D., Xiao, Y., 2013, Geothermal convection in South Atlantic subsalt lacustrine carbonates: Developing diagenesis and reservoir quality predictive concepts with reactive transport models. AAPG Bulletin 97, 1249–1271.

Kaiser, M.J., Pulsipher, A.G., 2007. A review of the oil and gas sector in Kazakhstan. Energy Policy 35, 1300–1314.

Kharaka Y.K., Law, L.M., Carothers, W.W., Goerlitz, D.F., 1986. Role of organic species dissolved in formation waters from sedimentary basins in mineral diagenesis. In: Gautier, D.L. (Ed.), Roles of Organic Matter During Sediment Diagenesis. SEPM Spec. Pub., Vol. 38, 111-122.

Klimchouk, A., 2007. Hypogene speleogenesis: hydrogeological and morphometric perspective. Carlsbad, National Cave and Karst Research Institute: 106 pp.

Klimchouk, A., 2012. Speleogenesis, hypogenic. In: White, W.B., Culver, D.C. (Eds.), Encyclopedia of Caves, 2nd edition. Academic Press, New York, 748–764.

Klimchouk, A., 2015. The karst paradigm: changes, trends and perspectives. Acta Carsologica 44, 289–313.

Klimchouk, A., 2017. Types and Settings of Hypogene Karst. In: Klimchouk, A., Palmer, A.N., De Waele, J., Auler, A.S., Audra, P. (Eds.), Hypogene Karst Regions and Caves of the World, Cave and Karst Systems of the World, Springer International Publishing, Cham, 1-39.

Klimchouk, A., 2019. Speleogenesis, hypogene. In: White, W.B., Culver, D.C., Pipan, T. (Eds.), Encyclopedia of Caves, 3rd edition. Academic Press, New York, pp. 974–988.

Klimchouk, A., Ford, D.C., 2000. Lithologic and structural controls of dissolutional cave development. In: Klimchouk, A., Ford, D.C., Palmer, A.N., Dreybrodt, W. (Eds.), Speleogenesis: Evolution of Karst Aquifers, 54-64.

Klimchouk, A., Andreychouk, V.N., Turchinov, I.I., 2009. The structural prerequisites of speleogenesis in gypsum in the Western Ukraine, 2nd edition. University of Silesia - Ukrainian Institute of Speleology and Karstology, Sosnowiec-Simferopol, 96 pp.

Klimchouk, A., Auler, A.S., Bezerra, F.H.R., Cazarin, C.L., Balsamo, F., Dublyansky, Y., 2016. Hypogenic origin, geologic controls, and functional organization of a giant cave system in Precambrian carbonates, Brazil. Geomorphology 253, 385–405.

Klimchouk, A., Amelichev, G.N., Chervyatsova, O.Y., Tokarev, S.V., Kiseleva, D.V., Potapov, S.S., 2021. Ferruginous accumulations in hypogene karst conduits of Crimean Piedmont: Evidence for a deep iron source for the Kerch-Taman iron-ore province, north Black Sea region. Mar. Pet. Geol. 127, 104954.

Korneva, I., Tondi, E., Agosta, F., Rustichelli, A., Spina, V., Bitonte, R., Di Cuia, R., 2014. Structural properties of fractured and faulted Cretaceous platform carbonates, Murge Plateau (southern Italy). Mar. Pet. Geol. 57, 312–326.

Kornilov, V.F., 1978. The temperature regime of formation of the mercury–antimony mineralization (Southern Kirghizia). In: Ermakov, N.P. (Ed.), Thermobarogeochemistry of the Earth's Crust. Nauka, Moscow, pp. 155–161.

La Bruna, V., Bezerra, F.H.R., Souza, V.H.P., Maia, R.P., Auler, A.S., Araújo, R.E.B., Cazarin, C.L., Rodrigues, M.A.F., Vieira, L.C., Sousa, M.O.L., 2021. High-permeability zones in folded and faulted silicified carbonate rocks – Implications for karstified carbonate reservoirs. Mar. Pet. Geol. 128, 105046.

Laurent, D., Durlet, C., Barré, G., Sorriaux, P., Audra, P., Cartigny, P., Carpentier, C., Paris, G., Collon, P., Rigaudier, T., Pironon, J., Gaucher, E.C., 2021. Epigenic vs. hypogenic speleogenesis governed by H2S/CO2 hydrothermal input and Quaternary icefield dynamics (NE French Pyrenees). Geomorphology 387, 107769.

Lavenu, A.P.C., Lamarche, J., Salardon, R., Gallois, A., Marié, L., Gauthier, B.D.M., 2014. Relating background fractures to diagenesis and rock physical properties in a platform-slope transect. Example of the Maiella Mountain (central Italy). Marine and Petroleum Geology 51, 2–19.

Lepley, S., Piccoli, L., Chitale, V., Kelley, I., Quest, M., 2017. The Importance of Understanding Diagenesis for the Development of Pre-salt Lacustrine Carbonates. American Association of Petroleum Geologists Annual Convention and Exhibition, Houston, Texas, USA, Abstracts.

Leven, J.A., 1961. Problems of origin of optical-quality fluorite from deposits of the Zeravshan–Gissar Mountains. Trans. Samarkand Univ. 16, 35–51.

Lima, B.E.M., De Ros, L.F., 2019. Deposition, diagenetic and hydrothermal processes in the Aptian Pre-Salt lacustrine carbonate reservoirs of the northern Campos Basin, offshore Brazil. Sediment. Geol. 383, 55–81.

Lima, B.E.M., Tedeschi, L.R., Pestilho, A.L.S., Santos, R.V., Vazquez, J.C., Guzzo, J.V.P., De Ros, L.F., 2020. Deep-burial hydrothermal alteration of the Pre-Salt carbonate reservoirs from northern Campos Basin, offshore Brazil: Evidence from petrography, fluid inclusions, Sr, C and O isotopes. Mar. Pet. Geol. 113, 104143.

Lomando, A.J., Harris, P.M., Orlopp, D.E., 1993. Casablanca Field, Tarragona Basin, Offshore Spain: A Karsted Carbonate Reservoir. In: Fritz, R.D., Wilson, J.L., Yurewicz, D.A. (Eds.), Paleokarst Related Hydrocarbon Reservoirs. SEPM Spec. Pub., Vol. 18, 201-205.

Lønøy, B., Tveranger, J., Pennos, C., Whitaker, F., Lauritzen, S.E., 2020. Geocellular rendering of cave surveys in paleokarst reservoir models. Mar. Pet. Geol. 122, 104652.

Loucks, R. G., 1999. Paleocave carbonate reservoirs: Origins, burial-depth modifications, spatial complexity, and reservoir implications. AAPG Bulletin 83, 1795–1834.

Lovering, T.S., Tweto, O., Loweing, T.G., 1978. Ore deposits of the Gilman District, Eagle Country, Colorado. U.S. Geological Survey Professional Paper 1017. 90 pp.

Lowe, D.J., Gunn, J., 1997. Carbonate speleogenesis: an inception horizon hypothesis. Acta Carsologica 26(2), 457-488.

Lu, X., Wang, Y., Yang, D., Wang, X., 2020. Characterization of paleo-karst reservoir and faulted karst reservoir in Tahe Oilfield, Tarim Basin, China. Advances in Geo-Energy Research 4, 339-348.

Machel, H.G., 2001. Bacterial and thermochemical sulfate reduction in diagenetic setting: old and new insights. Sedimentary Geology 140, 143-175.

Marin-Carbonne, J., Robert, F., Chaussidon, M., 2014. The silicon and oxygen isotope compositions of Precambrian cherts: A record of oceanic paleo-temperatures? Precambrian Research 247, 223–234.

Maximov, S.P., Zolotov, A.N., Lodzhevskaya, M.I., 1984. Tectonic conditions for oil and gas generation and distribution on ancient platforms. J. Pet. Geol. 7(3), 329-340.

Mecchia, M., Sauro, F., Piccini, L., Columbu, A., De Waele, J., 2019. A hybrid model to evaluate subsurface chemical weathering and fracture karstification in quartz sandstone. J. Hydrol. 572, 745–760.

Michie, E.A.H., 2015. Influence of host lithofacies on fault rock variation in carbonate fault zones: A case study from the Island of Malta. J. Struct. Geol. 76, 61–79.

Mitsiuk, B.N., 1974. Vzaimodeistvie kremnezema s vodoy v hydrotermalnych usloviach (Interaction between silica and water in hydrothermal conditions). Naukova Dumka. Kiev, 86 pp.

Montaron, B.A., Xue, F.J., Tian, W., Han, R., Ray, P., 2014. Cave Geomorphology and its Effects on Oil Recovery Factors in Tarim Karst Reservoirs, West China. International Petroleum Technology Conference. Kuala Lumpur, Malaysia, pp. 13.

Montgomery, S.L., Mullarkey, J.C., Longman, M.W., Colleary, W.M., Rogers, J.P., 1998, Mississippian "chat" reservoirs, south Kansas: low-resistivity pay in a complex chert reservoir. AAPG Bulletin 82, 187–205.

Myers, R., Aydin, A., 2004. The evolution of faults formed by shearing across joint zones in sandstone. J. Struct. Geol. 26, 947–966.

Mylroie, J.E., Carew, J.L., 1990. The flank margin model for dissolution cave development in carbonate platforms. Earth Surface Processes and Landforms 15(5), 413-424.

Mylroie, J.E., Carew, J.L., Vacher, H.R., 1995. Karst development in the Bahamas and Bermuda, Geological Society of America Special Paper 300, 251-267.

Nolting, A., Moore, P.J., Homburg, J., Fernández-Ibáñez, F., 2021. The preservation of water-table caves at depth: Observations from subsurface data and numerical modeling. AAPG Bulletin 105, 135–155.

Onac, B.P., Wynn, J.G., Sumrall, J.B., 2011. Tracing the sources of cave sulfates: a unique case from Cerna Valley, Romania. Chemical Geology 288 (3–4), 105–114.

Packard, J.J., Al-Aasm, I., Samson, I., 2001. A Devonian hydrothermal chert reservoir: The 225 bcf Parkland field, British Columbia, Canada. AAPG Bulletin 85(1), 51–84.

Palmer, A.N., 1989. Stratigraphic and structural control of cave development and groundwater flow in the Mammoth Cave region. In: White, W.B., White, E.L. (Eds.), Karst Hydrogeology, Concepts from the Mammoth Cave Area, Von Nostrand Reinhold, New York, 293-316.

Palmer, A.N., 1991. Origin and morphology of limestone caves. Geological Society of America Bulletin 103(1), 1–21.

Palmer, A.N., 2000. Hydrogeologic control of cave patterns. In: Klimchouk, A., Ford, D.C., Palmer, A.N., Dreybrodt, W. (Eds.), Speleogenesis: Evolution of Karst Aquifers, Vol. 240, 145–146.

Palmer, A.N., 2007. Cave Geology. In: Cave Books, Dayton, Ohio, 454 pp.

Pan, L., Carter, J., Quantin-Nataf, C., Pineau, M., Chauviré, B., Mangold, N., Le Deit, L., Rondeau, B., Chevrier, V., 2021. Voluminous silica precipitated from martian waters during late-stage aqueous alteration. Planet. Sci. J. 2, 65.

Parise, M., Gabrovsek, F., Kaufmann, G., Ravbar, N., 2018. Recent advances in karts research: from theory to fieldwork and applications. Geological Society of London Special Publications 466, 1-24.

Pinneker, E.V., 1983. General hydrogeology. Cambridge University Press, Cambridge, 141 pp.

Pisani, L., Antonellini, M., De Waele, J., 2019. Structural control on epigenic gypsum caves: evidences from Messinian evaporites (Northern Apennines, Italy). Geomorphology 332, 170–186.

Plan, L., Tschegg, C., De Waele, J., Spötl, C., 2012. Corrosion morphology and cave wall alteration in an alpine sulfuric acid cave (Kraushöhle, Austria). Geomorphology 169-170, 45-54.

Poros, Z., Jagniecki, E., Luczaj, J., Kenter, J., Gal, B., Correa, T.S., Ferreira, E., McFadden, K.A., Elifritz, A., Heumann, M., Johnston, M., Matt, V., 2017. Origin of silica in pre-salt carbonates, Kwanza Basin, Angola. In: American Association of Petroleum Geologists Annual Convention and Exhibition (Houston, Texas, USA).

Rauch, H.W, White, W.B., 1977. Dissolution kinetics of carbonate rocks. Effects of lithology on dissolution rate. Water Resources Research 13, 381-394.

Reid, S.A., McIntyre, J.L., 2001. Monterey Formation Porcelanite Reservoirs of the Elk Hills Field, Kern County, California. AAPG Bulletin 85, 169–189.

Rimstidt, J.D., 1997. Quartz solubility at low temperatures. Geochimica et Cosmochimica Acta 61, 2553–2558.

Rogers, J.P., Longman, M.W., Lloyd, R.M., 1995. Spiculitic chert reservoir in Glick field, south-central Kansas. The Mountain Geologist 32, 1–22.

Rogers, J.P., Longman, M.W., 2001. An introduction to chert reservoirs of North America. AAPG Bulletin 1, 1–5.

Rongier, G., Collon-Drouaillet, P., Filipponi, M., 2014. Simulation of 3D karst conduits with an object-distance based method integrating geological knowledge. Geomorphology 217, 152–164.

Ruppel, S.C., Barnaby, R.J., 2001. Contrasting Styles of Reservoir Development in Proximal and Distal Chert Facies: Devonian Thirtyone Formation, Texas. AAPG Bulletin 85, 7–33.

Rustichelli, A., Torrieri, S., Tondi, E., Laurita, S., Strauss, C., Agosta, F., Balsamo, F., 2016. Fracture characteristics in Cretaceous platform and overlying ramp carbonates: An outcrop study from Maiella Mountain (central Italy). Marine and Petroleum Geology 76, 68–87.

Sauro, F., De Waele, J., Onac, B.P., Galli, E., Dublyansky, Y., Baldoni, E., Sanna, L., 2014. Hypogenic speleogenesis in quartzite: The case of Corona ’e Sa Craba Cave (SW Sardinia, Italy). Geomorphology 211, 77–88.

Shanov, S., Kostov, K., 2015. Dynamic Tectonics and Karst. Springer, Berlin, Heidelberg, pp. 123.

Siever, R., 1962. Silica solubility, 0°C - 200°C, and the diagenesis of siliceous sediments. Journal of Geology 70, 127-150.

Smeraglia, L., Giuffrida, A., Grimaldi, S., Pullen, A., La Bruna, V., Billi, A., Agosta, F., 2021. Fault-controlled upwelling of low-T hydrothermal fluids tracked by travertines in a fold-and-thrust belt, Monte Alpi, southern apennines, Italy. J. Struct. Geol. 144, 104276.

Souza, V.H.P., Bezerra, F.H.R., Vieira, L.C., Cazarin, C.L., Brod, J.A., 2021. Hydrothermal silicification confined to stratigraphic layers: Implications for carbonate reservoirs. Mar. Pet. Geol. 124, 104818.

Spötl, C., Dublyansky, Y.V., Meyer, M., Mangini, A., 2009. Identifying low-temperature hydrothermal karst and palaeowaters using stable isotopes: A case study from an alpine cave, Entrische Kirche, Austria. Intern. J. Earth Sci. 98, 665–676.

Spötl, C., Dublyansky, Y., Koltai, G., Cheng, H., 2021. Hypogene speleogenesis and paragenesis in the Dolomites. Geomorphology 382, 107667.

Tartaglia, G., Viola, G., van der Lelij, R., Scheiber, T., Ceccato, A., Schönenberger, J., 2020. “Brittle structural facies” analysis: A diagnostic method to unravel and date multiple slip events of long-lived faults. Earth Planet. Sci. Lett. 545, 116420.

Teboul, P.A., Kluska, J.M., Marty, N.C.M., Debure, M., Durlet, C., Virgone, A., Gaucher, E.C., 2017. Volcanic rock alterations of the Kwanza Basin, offshore Angola - insights from an integrated petrological, geochemical and numerical approach. Mar. Pet. Geol. 80, 394–411.

Teboul, P.A., Durlet, C., Girard, J.P., Dubois, L., San Miguel, G., Virgone, A., Gaucher, E.C., Camoin, G., 2019. Diversity and origin of quartz cements in continental carbonates: Example from the Lower Cretaceous rift deposits of the South Atlantic margin. Applied Geochemistry 100, 22–41.

Temovski, M., Rinyu, L., Futó, I., Molnár, K., Túri, M., Demény, A., Otoničar, B., Dublyansky, Y., Audra, P., Polyak, V., Asmerom, Y., Palcsu, L., 2022. Combined use of conventional and clumped carbonate stable isotopes to identify hydrothermal isotopic alteration in cave walls. Scientific Reports 2022, 12112.

Tian, F., Lu, X., Zheng, S., Zhang, H., Rong, Y., Yang, D., Liu, N., 2017. Structure and Filling Characteristics of Paleokarst Reservoirs in the Northern Tarim Basin, Revealed by Outcrop, Core and Borehole Images. Open Geosci. 9, 266–280.

Tisato, N., Sauro, F., Bernasconi, S. M., Bruijn, R. H., De Waele, J., 2012. Hypogenic contribution to speleogenesis in a predominant epigenic karst system: a case study from the Venetian Alps, Italy. Geomorphology 151, 156-163.

Tosca, N.J., Wright, V.P., 2018. Diagenetic pathways linked to labile Mg-clays in lacustrine carbonate reservoirs: A model for the origin of secondary porosity in the Cretaceous pre-salt Barra Velha Formation, offshore Brazil. Geol. Soc. Spec. Publ. 435, 33–46.

Tsykin, R.A., 1989. Paleokarst of the Union of Soviet Socialistic Republics. In: Bosák, P., Ford, D.C., Głazek, J., Horáček, I. (Eds.), Paleokarst: A Systematic and Regional Review. Vidala Academia, Praha, 253–295.

Trice, R., 2005. Challenges and insights in optimising oil production form middle eastern karst reservoirs. In: SPE Middle East Oil and Gas Show and Conference. Society of Petroleum Engineers.

Vignaroli, G., Viola, G., Diamanti, R., Zuccari, C., Garofalo, P.S., Bonini, S., Selli, L., 2020. Multistage strain localisation and fluid-assisted cataclasis in carbonate rocks during the seismic cycle: Insights from the Belluno Thrust (eastern Southern Alps, Italy). J. Struct. Geol. 141, 104216.

Walter, L.M., Morse, J.W., 1984. Reactive surface of skeletal carbonates during dissolution: effect of grain size. Journal of Sedimentary Petrology 54, 1081-1090.

Wang, X., Lei, Q., Lonergan, L., Jourde, H., Gosselin, O., Cosgrove, J., 2017. Heterogeneous fluid flow in fractured layered carbonates and its implication for generation of incipient karst. Adv. Water Resour. 107, 502–516.

Watney, W.L., Guy, W.J., Byrnes, A.P., 2001. Characterization of the Mississippian Chat in South-Central Kansas. AAPG Bulletin 85, 85–113. https://doi.org/10.1306/8626C767-173B-11D7-8645000102C1865D

Webb, J.A., 2020. Supergene sulphuric acid speleogenesis at the origin of hypogene caves: evidence from the Northern Pennines, UK. Earth Surface Process and Landforms 46, 455-464.

Wei, D., Gao, Z., Fan, T., Niu, Y., Guo, R., 2021. Volcanic events-related hydrothermal dolomitisation and silicification controlled by intra-cratonic strike-slip fault systems: Insights from the northern slope of the Tazhong Uplift, Tarim Basin, China. Basin Research 33, 2411–2434.

White, W.B., Culver, D.C., Herman, J.S., Kane, T.C., Mylroie, J.E., 1995. Karst lands. American Scientist 83 (5), 450–459.

Wu, M.B., Wang, Y., Zheng, M.L., Zhang, W.B., Liu, C.Y., 2007. The hydrothermal karstification and its effect on Ordovician carbonate reservoir in Tazhong uplift of Tarim Basin, Northwest China. Science in China Series D: Earth Science, 50(2), 103-113.

Xiao, D., Zhang, B., Tan, X., Liu, H., Xie, J., Wang, L., Yang, X., Ma, T., 2018. Discovery of a shoal-controlled karst dolomite reservoir in the Middle Permian Qixia Formation, northwestern Sichuan Basin, Southwest China. Energy Explor. Exploit. 36, 686–704.

Xu, X., Chen, Q., Chu, C., Li, G., Liu, C., Shi, Z., 2017. Tectonic evolution and paleo- karstification of carbonate rocks in the Paleozoic Tarim Basin. Carb. & Evap. 32, 487–496.

You, D., Han, J., Hu, W., Qian, Y., Chen, Q., Xi, B., Ma, H., 2018. Characteristics and formation mechanisms of silicified carbonate reservoirs in well SN4 of the Tarim Basin. Energy Explor. Exploit. 36, 820–849.

Zempolich, W.G., Cook, H.E., 2003. Paleozoic carbonates of the Commonwealth of Independent States (CIS): Subsurface Reservoirs and Outcrop Analogues. SEPM Spec. Pub., Vol. 74, pp.243.

Zhao, X., Jin, F., Zhou, L., Wang, Q., Pu, X., 2018. Re-exploration Programs for Petroleum-Rich Sags in Rift Basins. Gulf Professional Publishing, 642 pp.

Zhang, J.J., 2019. Rock physical and mechanical properties, in: Applied Petroleum Geomechanics. Elsevier, pp. 29–83.

Zhou, X., Chen, D., Qing, H., Qian, Y., Wang, D., 2014. Submarine silica-rich hydrothermal activity during the earliest Cambrian in the Tarim basin, northwest China. Int. Geol. Rev. 56, 1906–1918.

2. Hypogene karst dissolution in fractured carbonates

This section of the thesis is focused on the research carried out in the Majella Massif (Central Italy) and in Northeastern Brazil (São Francisco Craton), where several caves have been selected as case studies to highlight the relationship between hypogene karst development and deformation patterns in layered carbonate sequences. The section is organized in two articles published in Journal of Structural Geology during 2021. The first paper involves me as first author and corresponding author, whereas I contributed as co-author for the second paper.

2.1

Published in Journal of Structural Geology 145 (2021)

https://doi.org/10.1016/j.jsg.2021.104305

Structurally controlled development of a sulfuric hypogene karst system in a fold-and-thrust belt (Majella Massif, Italy)

Luca PISANI[1*], Marco ANTONELLINI[1], Ilenia M. D'ANGELI[1], Jo DE WAELE[1]

1 University of Bologna, Department of Biological, Geological and Environmental Sciences

* Corresponding author

Abstract

We documented the deformation in the southeastern domain of the Majella anticline (Central Apennines, Italy) to highlight timing and structural characteristics of different fracture sets affecting the outcropping Cretaceous-Miocene ramp carbonates. An isolated and inactive hypogene karst system produced by sulfuric acid (Cavallone-Bove cave system) was studied following a multidisciplinary approach. Our findings suggest that deep-rooted, sub-vertical strike-slip fault zones reaching the H_2S source rocks were the main vehicle for ascending acidic fluid flow. Linkage and intersection of these faults by splays in extensional stepovers and pre-orogenic normal faults permitted ascending fluids to reach multiple recharge points (feeders) near the paleo water-table. In proximity to the oxygenated groundwater, where H_2SO_4 was produced, lateral dissolution focused along bedding planes and zones of localized deformation (fracture clusters) characterizing the hinge of the anticline. We conclude that structural position in the anticline and large-offset, vertically extended strike-slip fault zones control the localization of efficient permeability pathways and represent first order controlling features for fluid flow in the fold-and-thrust belt. This study provides insights into the understanding of time-space evolution, geometry, and pattern of sulfuric hypogene karst systems in folded carbonates, whose prediction is critical for fractured and karstified reservoirs.

Key Words

Fluid flow; sulfuric acid speleogenesis; karst porosity; fractured carbonates; fault zones

2.1.1. Introduction

Karst macro-scale porosity, deriving from dissolution of soluble rocks, is represented by underground cavities with an average diameter larger than 0.5 m (Curl, 1986; Albert et al., 2015). On a regional scale (tens to hundreds of km^2), karst macro-scale porosity is usually less than 3% (Worthington et al., 2000; Albert et al., 2015). Despite this low value, it represents extremely efficient (and localized) permeability pathways for sub-surface fluid flow (Palmer, 2000; Ford and Williams, 2007; Ennes-Silva et al., 2016; Klimchouk et al., 2016; Boersma et al., 2019; Pisani et al., 2019; Antonellini et al., 2019).

Chemical dissolution in carbonate rocks generally produces disconnected micro-scale voids (vuggy porosity) whereas the development of interconnected macro-scale cave passages requires the presence of permeable structural anisotropies and suitable climate, geochemical and hydrogeological conditions.

Dissolution in deep-seated environments not directly connected to the surface (hypogene speleogenesis) is of primary interest for many applied fields such as those concerning subsurface characterization, modeling for oil, geothermal, or groundwater production, and sinkhole formation (Gutiérrez et al., 2014; Cazarin et al., 2019; Bagni et al., 2020; Balsamo et al., 2020; Bertotti et al., 2020). During the last decades, recognition of hypogene speleogenesis as a diffuse form of natural weathering has raised renewed interest in karst science. In contrast to epigene karst, hypogene caves result from dissolution of soluble rocks by rising fluids, whose dissolution efficiency is not dependent on processes taking place at the surface (Klimchouk, 2007). Hypogene karst systems are among the longest known on Earth (Audra et al., 2009; Stafford et al., 2009; Klimchouk, 2009; 2012; De Waele et al., 2014; D'Angeli et al., 2019a). Their large morphological diversity is the result of a complex interplay between geological framework, dissolution processes, and their spatial and temporal variations. Furthermore, karst porosity development in deep-seated environments may be the result of various processes reflecting variations in geochemistry and migration paths of fluids (Palmer, 2007).

Sulfuric acid (H_2SO_4) is very aggressive, and it can be produced both in hypogene and supergene conditions (D'Angeli et al., 2019a; Webb, 2020). This strong acid usually forms abundantly when ascending H_2S-rich fluids mix with oxygenated groundwater. The greatest rock dissolution occurs in the mixing zone at (or close to) the water table, and the resultant karst porosity tends to decrease away from the outlets (feeders) of the rising fluids (Hill, 1990; Auler and Smart, 2003; De Waele et al., 2016). A typical byproduct of the reaction between H_2SO_4 and the calcite of carbonate rocks is gypsum (Hill, 1995; Polyak and Provencio, 2001; Galdenzi and Maruoka, 2003; D'Angeli et al., 2018). This cave-forming process is called sulfuric acid speleogenesis (SAS).

Besides direct input of H_2S-rich fluids in hydrothermal or volcanic environments (Palmer, 1991; Ford and Williams, 2007), H_2S may also form in a wide range of sedimentary basins due to hydrocarbon maturation (Palmer, 1990; Hill, 1990, 1995) and sulfate reduction in evaporitic sediments (Egemeier, 1981; Machel, 2001; DuChene et al., 2017; Galdenzi and Menichetti, 2017; D'Angeli et al., 2019a). In shallow confined aquifers, the oxidation of sulfide minerals (i.e., pyrite, chalcopyrite) present in the host rock may generate H_2S and increase the acidity of the water (Ball and Jones, 1990; Auler and Smart, 2003; Tisato et al., 2012; Webb, 2020).

Understanding the speleogenetic mechanisms and the structural discontinuities allowing fluid movement is of primary importance, especially for carbonate reservoirs, which host up to 60% of the global hydrocarbon reserves and between 25% and 50% of world's water supply (Ford and Williams, 2007; Montaron, 2008; Klimchouk et al., 2016; Balsamo et al., 2020; Farooq et al., 2020). New challenges in the understanding of fractured and karstified carbonate reservoirs require integrating karst features into the modeling efforts, given that interconnected cave passages strongly affect fluid circulation, drilling operations, and porosity-permeability at the scale of the reservoir.

At a regional-seismic scale (tens to hundreds of km^2), sub-surface fluid flow is strongly conditioned by fault zone architecture and associated structures. Opening-mode fractures usually represent conduits (Pollard and Aydin, 1988; Ford and Williams, 2007; Peacock et al., 2017) whereas pressure solution features containing residual clay-rich material may form either barriers or conduits (Fletcher and Pollard, 1981; Graham-Wall et al., 2006; Tondi et al., 2006; Bruna et al., 2019; Araújo et al., 2021). These structures often characterize fault damage zones, which consist of fractured or fragmented rocks with an intensity above the background of the host rock. In contrast, fault cores characterized by comminution, brecciation, dissolution-recrystallization, and cataclasis lose the original host rock fabric and petrophysical properties (Sibson, 1977). Therefore, fault zones architectures and textures exert a strong control on fluid flow, and may either act as conduits, barriers, or as combined barrier-conduit permeability structures (Antonellini and Aydin, 1994; Caine et al., 1996; Agosta et al., 2009; Matonti et al., 2012).

The Majella Massif (Italy) offers the possibility to investigate an isolated complex of connected hypogene conduits produced by SAS, the Cavallone-Bove cave system (CBS). This karst system opens on the eastern flanks of the Taranta Valley, exposing highly faulted carbonate rocks. Furthermore, several sites in the Majella are characterized by accumulation and production of hydrocarbons (Tondi et al., 2006; Antonellini et al., 2008; Agosta et al., 2009; Brandano et al., 2013; Lipparini et al., 2018). In this context, structurally controlled hypogene conduits are proxies of paleo fluid flow pathways and focused high hydraulic conductivity.

We performed a detailed geological mapping as well as a structural and geomorphological analysis of the Taranta Valley and CBS, to reconstruct the deformation history and identify those geological structures controlling sub-surface fluid flow and the resultant hypogenic karst system. Our work aims to offer first order predictive tools to characterize localization, spatial organization, and patterns of hypogene systems formed by sulfuric acid within fold-and-thrust belts. Our case study may be compared to similar setting elsewhere to improve the understanding of hypogene karst systems and migration paths of fluids in potential sulfuric-acid environments.

2.1.2. Geological setting

The CBS opens along the eastern cliffs of the Taranta Valley (Majella Massif, Central Apennines, Italy). The Majella Massif is the easternmost outcropping thrust sheet of the Central Apennines fold-and-thrust belt (Ghisetti and Vezzani, 1997; Aydin et al., 2010). The most prominent first-order structure is an elongated, curvilinear, and open anticline with a steeply inclined eastern forelimb (Fig. 1A). The axis of this double plunging fold rotates from NW-SE (in the northern domain) to NE-SW (in the southern domain), and is roughly N–S in its central area (Roure et al., 1991; Casabianca et al., 2020). In the study area, the projected trace at the surface of the buried basal thrust separates the carbonate platform-ramp succession of the Majella series (upper Jurassic – upper Miocene) from the syn-tectonic foredeep deposits (Messinian - lower Pliocene) (Ori et al., 1986; Festa et al., 2014). This sedimentary sequence overlies a deeply-buried Triassic-Jurassic sequence predominantly composed of carbonates and evaporites, which is assumed (based on seismic data) to extend down to a depth of about 2 km (Fig. 1C) (Ghisetti and Vezzani, 2002; Masini et al., 2011; Casabianca et al., 2020).

According to the literature, five distinct deformation phases affected the carbonate units of the Majella series: (i) extensional syn-sedimentary tectonics until upper Cretaceous (Accarie et al., 1986; Casabianca et al., 2002; 2020; Lavenu et al., 2014); (ii) Miocene - lower Pliocene pre-thrusting flexural extension (Scisciani et al., 2002; Di Cuia et al., 2009); (iii) middle-upper Pliocene thrusting and folding (Graham et al., 2003; Tondi et al., 2006; Antonellini et al., 2008; Agosta et al., 2009; Aydin et al., 2010; Rustichelli et al., 2016); (iv) lower-middle Pleistocene regional uplift (Ghisetti and Vezzani, 2002; Pizzi, 2003); (v) upper Pleistocene – Holocene active extensional tectonics in the internal (western) sector of the thrust sheet (Pizzi et al., 2010; Di Domenica and Pizzi, 2017).

The main structural features described in the Majella anticline consist of pre-tilting normal faults, strike-slip faults, and reverse faults associated with a roughly E-W direction of maximum contraction related to the Central Apennines orogeny. Aside from the contractional structures with an eastward vergence, a wide range of recent normal or oblique-slip faults (Ghisetti and Vezzani, 1997; 1998; 2002; Agosta et al., 2009) affect the internal architecture of the massif. Among these, the Caramanico Fault, consisting of nearly 30 km-long interconnected segments, marks the western boundary of the thrust sheet (Calamita et al., 2002; Ghisetti and Vezzani, 2002; Scisciani et al., 2002; Tondi and Cello, 2003).

The outcropping Majella series is characterized by an upper Jurassic to upper Miocene carbonate sequence typical of a platform-ramp-basin sedimentary setting (Fig. 1B) (Cornacchia et al., 2018). In the study area, upper Cretaceous to upper Miocene ramp carbonates from Orfento (ORF), Santo Spirito (SS), and Bolognano (BOL) Formations (Fm) crop out extensively (Festa et al., 2014).

The ORF Fm (upper Cretaceous) is characterized by deposits of variable thickness (ranging from 50 m to 300 m), composed of porous bioclastic grainstones, often presenting a completely recrystallized fabric, and chaotic rudist-rich rudstones/floatstones interpreted as channel-fill facies (Rustichelli et al., 2016; Eberli et al., 2019). The middle Paleocene to lower Oligocene SS Fm stands above this unit, and is composed of discontinuous bodies of calcareous turbidites and sedimentary breccias (lower part, here named “SS1”) and thick-layered bioclastic packstones and wackestones alternating with marly limestones (upper part, named “SS2”) for a total thickness ranging from 100 m to 350 m (Crescenti et al., 1969; Vecsei et al., 1998; Festa et al., 2014; Cornacchia et al., 2018). The SS Fm is the main lithotype hosting the CBS karst conduits (Di Domenica and Pizzi, 2017). The uppermost ramp carbonates outcropping in the Majella Massif are represented by the upper Oligocene to upper Miocene limestones and hemipelagic marls of the BOL Fm (Rustichelli, 2010; Brandano et al., 2013).

The evolution of this upper Cretaceous – upper Miocene carbonate ramp ended in the Messinian with the deposition of re-sedimented gypsum-arenites, marls, and siliciclastic turbidites of the

Gessoso-Solfifera, Lago-Mare and Majella Flysch Fm (Cosentino et al., 2005; Festa et al., 2014), which crop out at the southeastern margin of the study area, in the Aventino river valley.

From the end of early Pliocene to late Pliocene, the described sequence was affected by folding and thrusting associated with the Apennine orogeny (Bally et al., 1988; Ghisetti and Vezzani, 2002; Agosta et al., 2009; Masini et al., 2011; Casabianca et al., 2020). Ghisetti and Vezzani (2002), and Pizzi (2003) reported a second distributed uplifting phase, which involved the regional doming of the Majella anticline. As discussed by Pizzi (2003), in the anticline culmination the net uplift rate is up to 3.0 mm/y (during Pliocene contractional phases), and up to 1.0 mm/y since middle-upper Pleistocene (post 0.7 Ma ago). Further analyses based on dating of CBS secondary minerals (D'Angeli et al., 2019b) suggest that the sulfuric acid processes were active at least until 1.52 ± 0.28 Ma ago, additionally constraining the recent uplift rate to 0.55–0.80 mm/y since lower-middle Pleistocene.

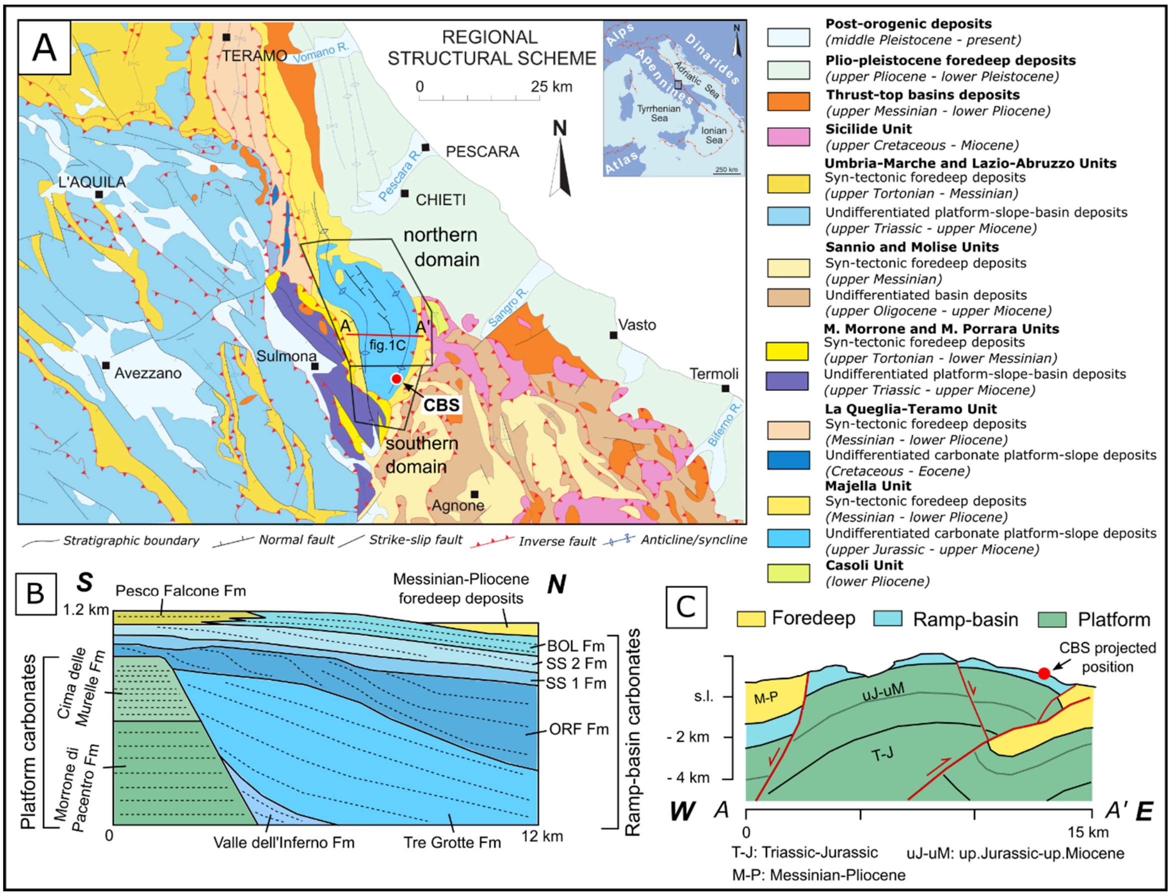

Figure 1: A) Simplified regional structural scheme of the Central Apennine fold-and-thrust belt (modified from Festa et al., 2014). The red dot marks the CBS study area location. The red line A-A' is the trace of the geological section of Fig. 1C; B) schematic stratigraphic section of the upper Jurassic - upper Miocene Majella series (after Vecsei, 1991; and Lampert et al., 1997); C) Schematic geologic section A-A' (see trace on Fig. 1A) of the central area of Majella Massif. Red lines show the main faults with relative sense of shear.

2.1.3. Material and methods

The geological mapping in the study area was performed using a multidisciplinary approach integrating a preliminary remote sensing investigation (by Google Earth Pro, ArcGis software and satellite images) and field-based geological and structural surveys.

We used high resolution orthophoto images (1 m spatial resolution) provided by the WMS regional database system (Geoportale Regione Abruzzo, http://geoportale.regione.abruzzo.it/Cartanet) and displayed in the ArcGis software to identify the main structural lineaments of the study area. Digital terrain models (DTM) at 10 m spatial resolution, extracted from the 1:5000 topographic maps of the Regione Abruzzo, were processed to obtain shaded relief models that highlight the structural lineaments and landscape morphology. Google Earth Pro high-resolution satellite images (< 1 m spatial resolution) and the digital "relief" view were used to inspect the outcrops of the whole valley and to establish a preliminary interpretation for the mapped structures.

Furthermore, a new topographic survey of the main branches of the caves (Fig. 2) was acquired by using a laser-based digital technology, with an average standard deviation of ±1.1° for direction measurements and ±1 cm for distances after device calibration (Heeb, 2009). The two surveys of the Cavallone and Bove caves were linked by an external polygonal trace acquired with the same digital surveying method to reduce the errors of multiple GPS acquisitions of CBS entrances. The CBS topography dataset was further processed using the cSurvey software (https://www.csurvey.it/) to obtain a tridimensional, geographically referenced model corrected for the 2019 magnetic declination. cSurvey allows reconstructing the volumes of the cave by interpolation of splay points collected during the acquisition with the laser device and the manually edited sketches drafted by the surveyor. The topographic survey of the cave system was processed in ArcGis to manually extract the conduits' preferential direction of development, normalized by the length of each cave segment (same method described in Pisani et al., 2019 and Sauro et al., 2020). This approach permits to have quantitative data for CBS main trends of development and compare them with the detailed structural datasets collected during the geological survey.

The geological mapping and detailed structural analysis were performed using classical tools (compass, clinometer, GPS, laser distance-meter) to create an original geological map (scale 1:25000) of the Taranta Valley integrating new surface and cave observations with previous datasets of the surrounding areas from available geological maps (ISPRA geological map 1:100000; Festa et al., 2014). Detailed structural observations permit deciphering the nature, attitude, geometrical relations, mechanical aperture, and kinematics of individual features characterizing the carbonate rocks, and reconstructing timing and different deformation events that affect the outcropping sequence of ORF and SS Fm. All structures were classified after fieldwork observations and statistical analysis with the Stereonet software (Allmendinger et al., 2012). Fracture apertures were calculated using the comparator proposed by Ortega et al. (2006) and relative age of fractures is interpreted following the crosscutting and abutting relationships discussed by Peacock et al. (2018) and Peacock and Sanderson (2018).

The geometric, spatial, and physical properties of the structures were integrated with a geomorphological analysis of the conduit system to build conceptual genetic models for CBS development and its spatial and morphological organization in the fold-and-thrust belt.

Petrographic optical microscopy observations on 26 polished thin sections (stained with blue epoxy) from fresh samples collected in cave walls and surface outcrops were performed to investigate the lithological and structural textures of the carbonate sequence. Calculation of the total optical 2D porosity with the ImageJ software (Schneider et al., 2012) was performed following the same approach described by Grove and Jerram (2011). Thin sections were scanned with a high-resolution commercial photographic scanner at 4800 dpi, and total optical porosity was extracted by image analysis involving threshold application, binary conversion, and segmentation. Optical 2D porosity only represents the resolvable estimation of the total pore volume at the thin-section scale, as defined by Grove and Jerram (2011). Issues related to the upscaling of petrophysical properties were not considered in this paper, but they are extensively dealt with in recent works (Ma et al., 2019; Proctor et al., 2019).

The petrographic analysis of carbonate rocks followed the classifications proposed by Dunham (1962) and Embry and Klovan (1971); fault rocks micro-structural analysis adopted the terminology used by Higgins (1971), Braathen et al. (2004), Michie (2015) and Peacock et al. (2016).

2.1.4. Results

2.1.4.1. Satellite images and cave topography analysis

The detailed GIS-based analysis allowed us to map structural lineaments and recognize different sets of structures in the Taranta Valley. Numerous continuous linear features are formed by preferential erosion along steep to sub-vertical fractures that show systematic trends and consistent geometric relationships. Structural lineaments range from several tens of meters to 3–4 km in length. Four systems of structures were mapped: N–S (system *a*), E-W (system *b*), NW-SE (system *c*) and WNW-ESE (system *d*), as shown on Fig. 2.

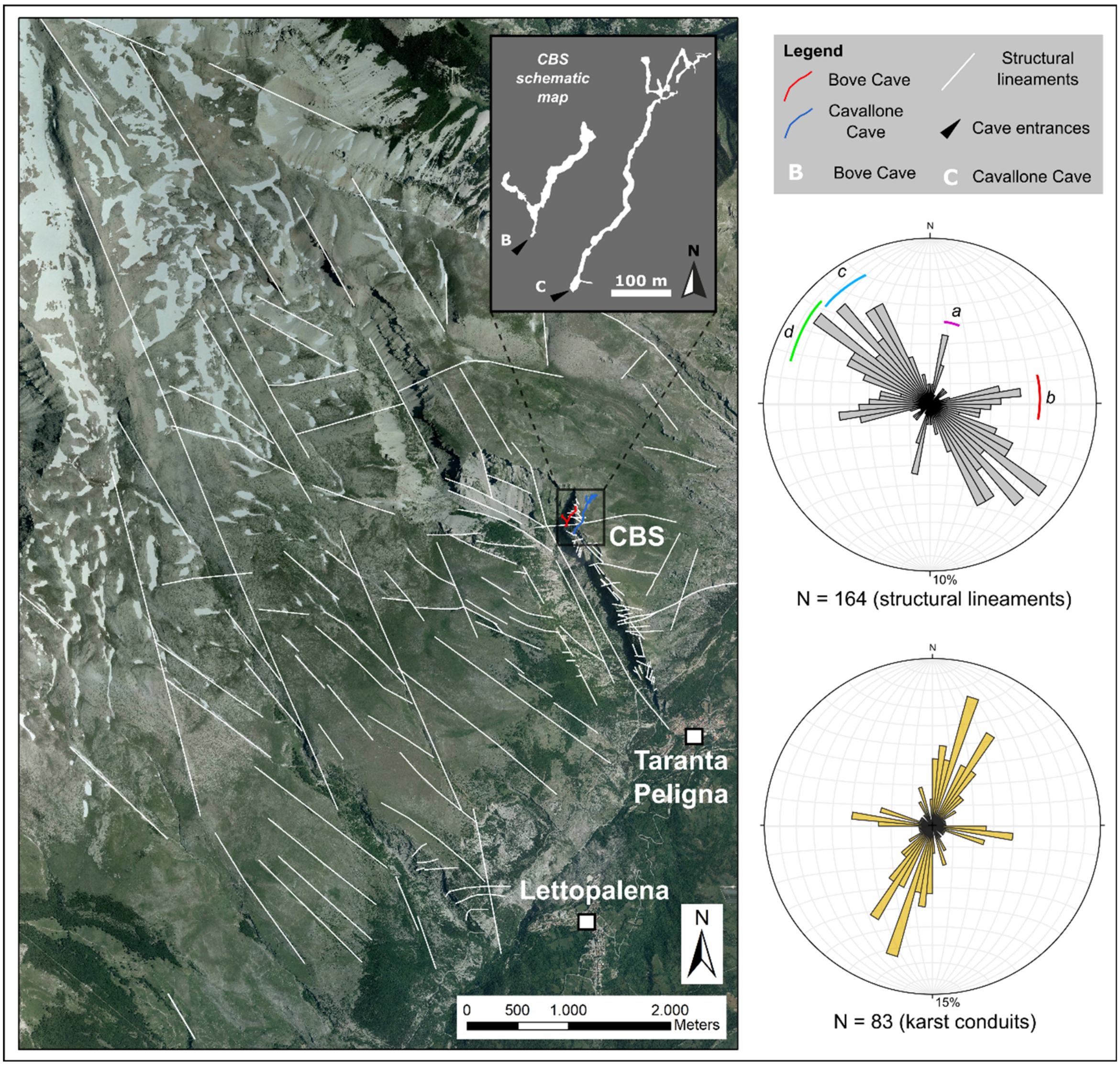

Figure 2. Left: map showing structural lineaments and the CBS survey (base map: 1 m resolution orthophoto image from the Geoportale Regione Abruzzo, http://geoportale.regione.abruzzo.it/Cartanet). Right: rose diagrams of structural lineaments (up) and CBS conduits (down), normalized by length. Structural lineament clusters are named 'a' (N–S); 'b' (E–W); 'c' (NW-SE) and 'd' (WNW-ESE).

From a preliminary analysis, it is not possible to infer genetic or kinematic information for the N15 striking system *a*. System *b*, on the other hand, is consistent with a conjugate system of normal faults (mean value striking N85E) passively rotated with increasing bedding dip towards the thrust front. The longest structures (striking N150E-N160E) are associated with system *c*, interpreted as strike-slip sub-vertical faults. System *d* consists of second order short faults, which show a variety of orientations between N105E and N130E. These structures are mainly observed at the tips or in the overlap region in between left stepping segments of the strike-slip faults grouped in system *c*.

The CBS hosts wide sub-horizontal conduits developed with an elongated and angular pattern (following the classification proposed by Palmer, 1991), and rare secondary branches that diverge from the main conduits. The entire system has gentle elevation variability (total depth is < 90 m). The direction of cave conduits with a linear planimetric development (> 1 m) are shown in the normalized rose diagram of Fig. 2. The CBS conduits show three main trends, in order of decreasing magnitude: NNE-SSW (N10E), NE-SW (N35E) and E-W (N100E). A subordinate trend strikes NW-SE (N160E).

2.1.4.2. Geomorphological observations

The CBS is more than 1 km long and includes two disconnected caves, which are about 60 m from each other in map view (Fig. 2). The Cavallone Cave is the longest one and its entrance is at ca. 1480 m asl on the eastern cliffs of the Taranta Valley. The Bove Cave entrance is located to the NW, on the same cliffs at ca. 1460 m asl.

Three different sub-horizontal master levels (large and continuous interconnected conduits mostly developed with gentle elevation differences) were identified in the whole cave system. These levels are at around 1490 m, 1470 m, and 1450 m, respectively (Fig. 3). The Bove Cave represents the lower and intermediate levels, and the Cavallone Cave is mainly developed in the upper and intermediate levels with vertical rising shafts connecting with the lower one.

The whole system is mainly developed within the lower (SS1) and upper (SS2) units of the SS Fm. The ORF Fm is exposed at the entrance and in the lowermost portion of the Bove Cave whereas the Cavallone Cave is entirely developed in the SS Fm. The lower level of Cavallone Cave presents short branches with drippings, speleothems, lakes, and sumps formed by surface water infiltration. Progressive enlargement of sub-horizontal conduits, whose apertures are generally decreasing away from the sulfuric recharge points (discharge feeders of rising acidic fluids), may have produced roof collapses and coalescence of distinct genetic levels at variable elevation.

The original shape and volume of the sub-horizontal conduits are often difficult to recognize due to frequent collapses and rockfalls. The internal morphology of the caves (Fig. 4) includes rounded or trapezoidal-shaped tunnels (Fig. 4A) connected by inclined rising conduits (ca. 40°–45°, Fig. 4F) or narrow sub-vertical fissures (Fig. 4C).

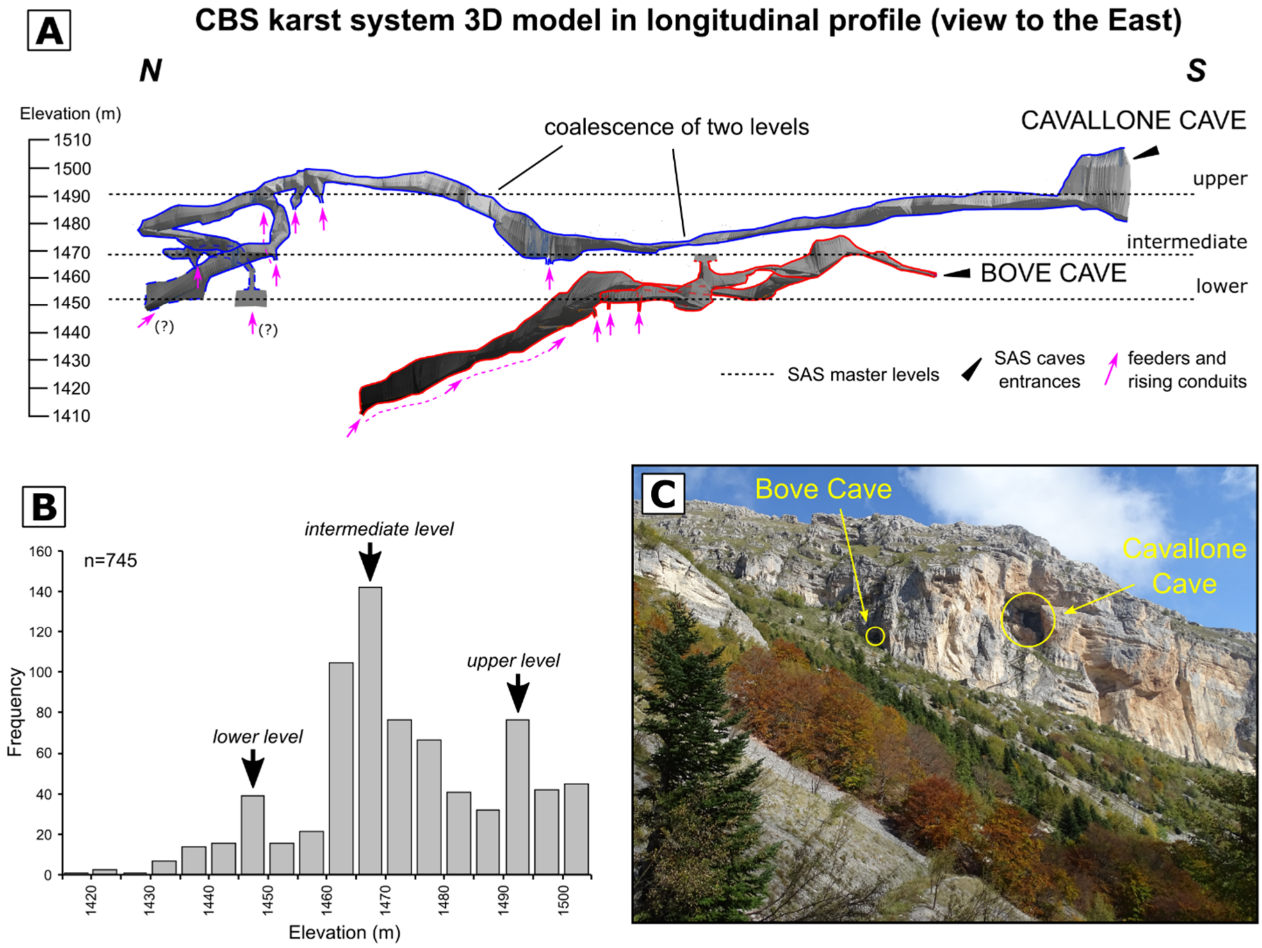

Figure 3. A) New original topographic survey of the CBS displayed in a N–S longitudinal view, highlighting the present-day position of the three main speleogenetic levels; B) histogram of survey points elevation, as extracted by cSurvey software. The distribution of elevation variability clearly indicates three distinct speleogenetic levels, which are more or less sub-horizontal; C) picture of the east walls of the Taranta Valley, where the entrances of the karst system are located.

Other macro-scale morphological features are replacement pockets (Fig. 4B), stacking mega-cusps (Fig. 4A), rising channels, and cupolas (Fig. 4D). These features, together with the complete absence of clastic sediments or traces of turbulent flowing waters, and the occurrence of peculiar by-products such as gypsum, alunite, jarosite, and gibbsite (Fig. 4A and E), are usually associated with hypogenic SAS (Audra et al., 2009; D'Angeli et al., 2018, 2019b).

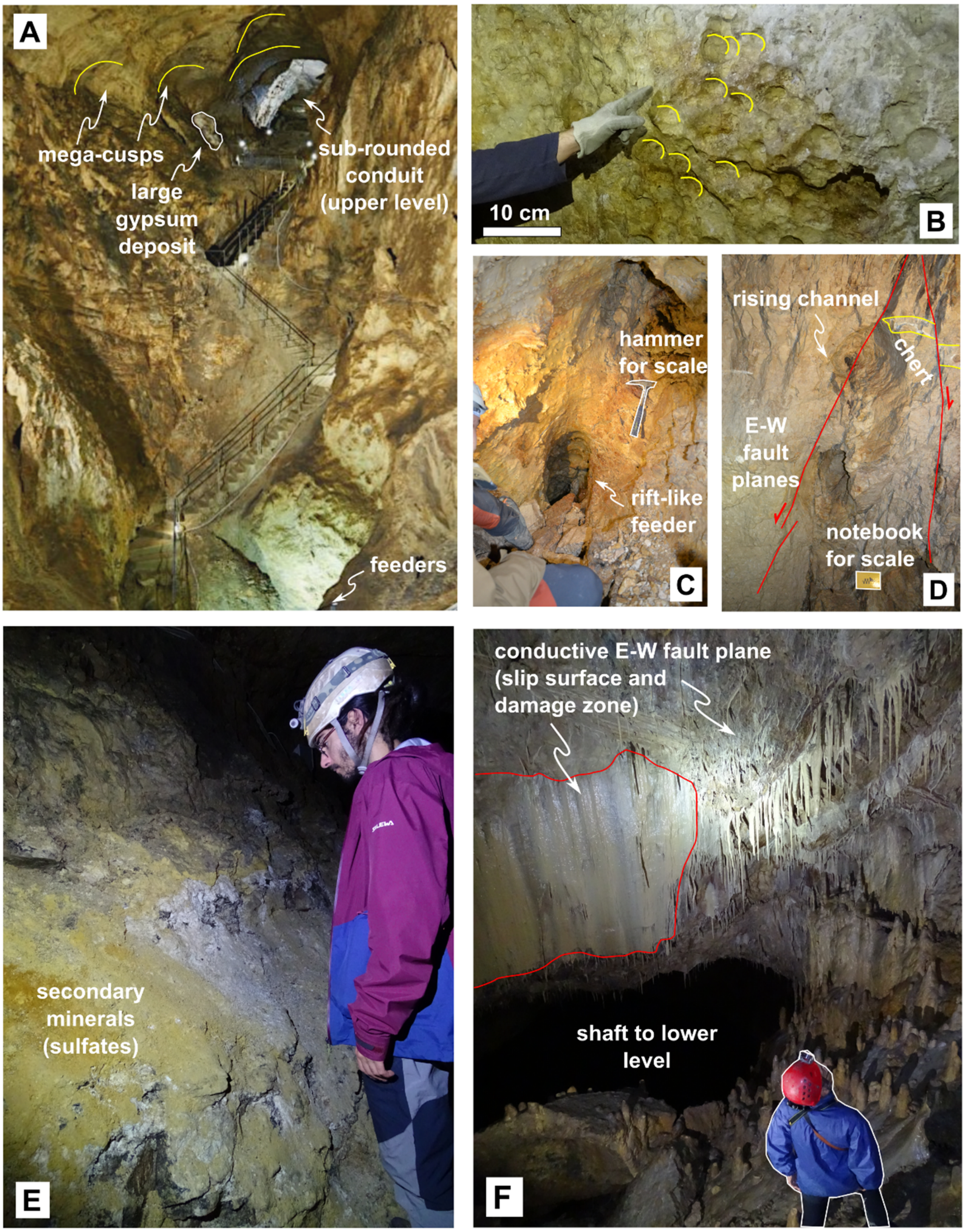

Figure 4. A) Mega-cusps characterizing the upper level of Cavallone Cave, where large gypsum deposits are observed; the lower part of this chamber (named 'Bolgia Dantesca') hosts rift-like feeders; B) replacement pockets (some examples are highlighted with yellow lines); C) example of a rift-like feeder in Bove Cave; D) rising channel elongated on a normal fault; E) secondary by-products of calcite dissolution (mainly sulfates) nearby a feeder (Cavallone Cave); F) shaft (rising-conduit type) connecting two levels in Cavallone Cave, developed along a fault zone with speleothems from percolating water.

Speleothems related to meteoric water percolation are abundant in the most external part of both caves (50–100 m from the entrance) and in the lower level of Cavallone Cave. Flowstones and dripstones usually grew (or are still growing) from highly fractured zones in fault damage zones and are almost always associated with impregnations of black organic material both inside the calcite crystals or as a fluid viscous paste that are both interpreted as tar/bitumen manifestations. Other deposits are associated with secondary fine-grained minerals (i.e., gypsum, alunite, jarosite) in the nearby feeders (Fig. 4A and E). Fault slip surfaces and the highly fractured associated damage zones are the main conductive discontinuities for recent percolation of fluids from the surface and correlated growth of speleothems (Fig. 4F).

2.1.4.3. Geological mapping and structural analysis

The detailed geologic mapping and structural analysis at macro- and meso-scale permit the recognition of different structures and the reconstruction of the deformation phases in the carbonate sequence of the southeastern Majella anticline. The field-based analysis improved the satellite images interpretation and allowed us to prepare a detailed geological map and cross-section (Fig. 5).

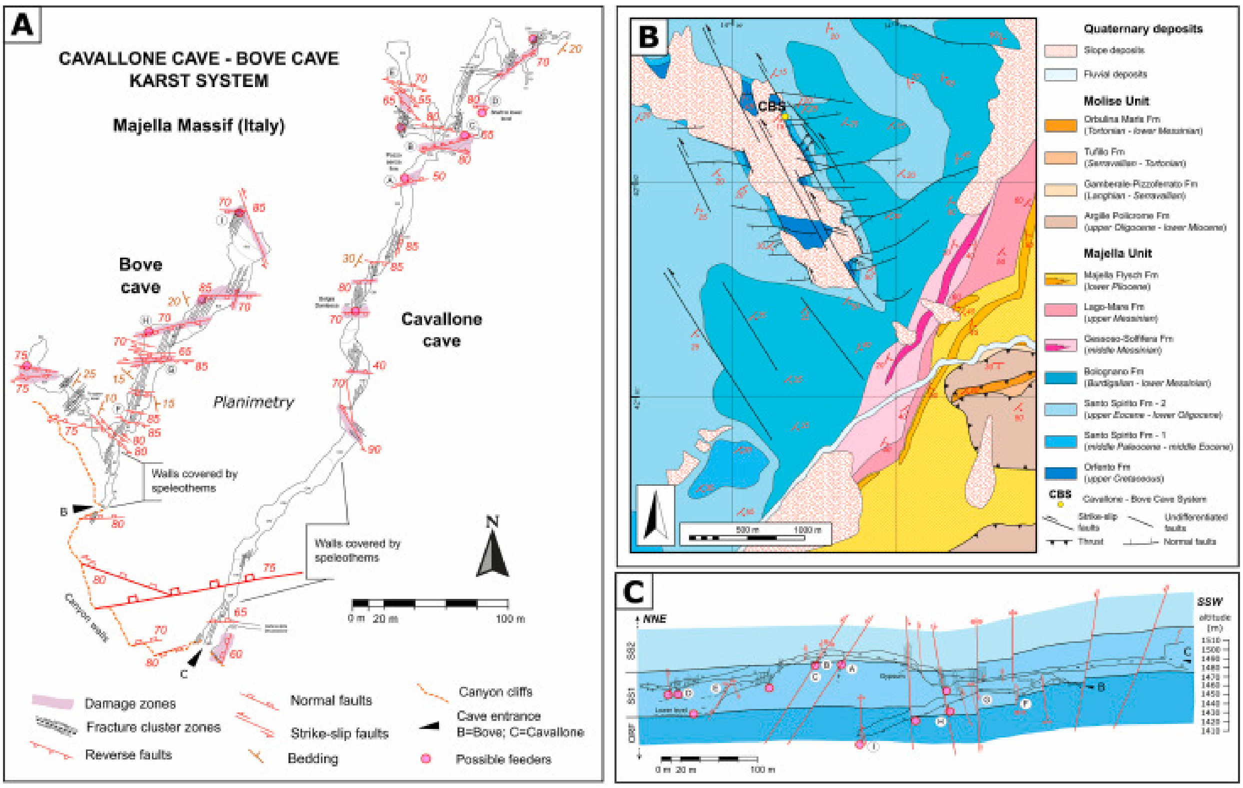

Figure 5. A) Structural map drafted on the new topographic survey of the CBS; B) schematic geological map of the Taranta Valley (original data have been integrated with those from Festa et al. (2014); C) geological cross-section along a NNE-SSW longitudinal profile of the cave system.

The ORF and SS outcrops along the Taranta Valley flanks are cut by several faults and have a high density (and variability) of fractures (Fig. 6). Integrating the surface and subsurface datasets, fracture characteristics and their geometric relationships, we recognized three structural assemblages, which are described and summarized below:

i) PRE-OROGENIC – Cretaceous and Miocene extensional phases:

1. ~N-S extensional syn-sedimentary faults and shear bands with an anastomosing pattern (F1 set)
2. Burial-related, bedding-parallel pressure solution seams (PSS1 set)
3. E-W bedding-normal joints/calcite veins (JV1 set)
4. E-W conjugate normal faults, passively rotated with bedding at present position (F2 set)

ii) EARLY OROGENIC – beginning of contraction and thrusting:

5. ~N-S (normal to bedding dip) pressure solution seams (PSS2a set) and less common ~E-W (parallel to bedding dip) pressure solution seams (PSS2b set)
6. oblique to bedding splay pressure solution seams (PSS3 set)
7. N130E sub-vertical joints/calcite veins (JV2 set)
8. NW-SE sub-vertical strike-slip faults with left-lateral kinematics (F3 set) and reactivation of F2 set in strike-slip or oblique-slip faults
9. WNW-ESE dip-slip or oblique-slip faults (F4 set)

iii) LATE OROGENIC – growth of the Majella anticline and Pleistocene doming of the overthickened thrust wedge:

10. linkage between PSS3 and PSS2, with possible reactivation in shearing and formation of high-angle normal faults striking parallel to bedding (F5 set)
11. N-S or NE-SW through-going joints (rarely filled by calcite) and fracture cluster zones (FCZ) in the anticline hinge region (J3 set)

In the following discussion, we refer to ‘background’ structures as those developed during the first two deformation phases and pervasively distributed in the whole study area. Through-going fractures refer to highly persistent, non-strata bound (cross-layering) structures (Giuffrida et al., 2020).

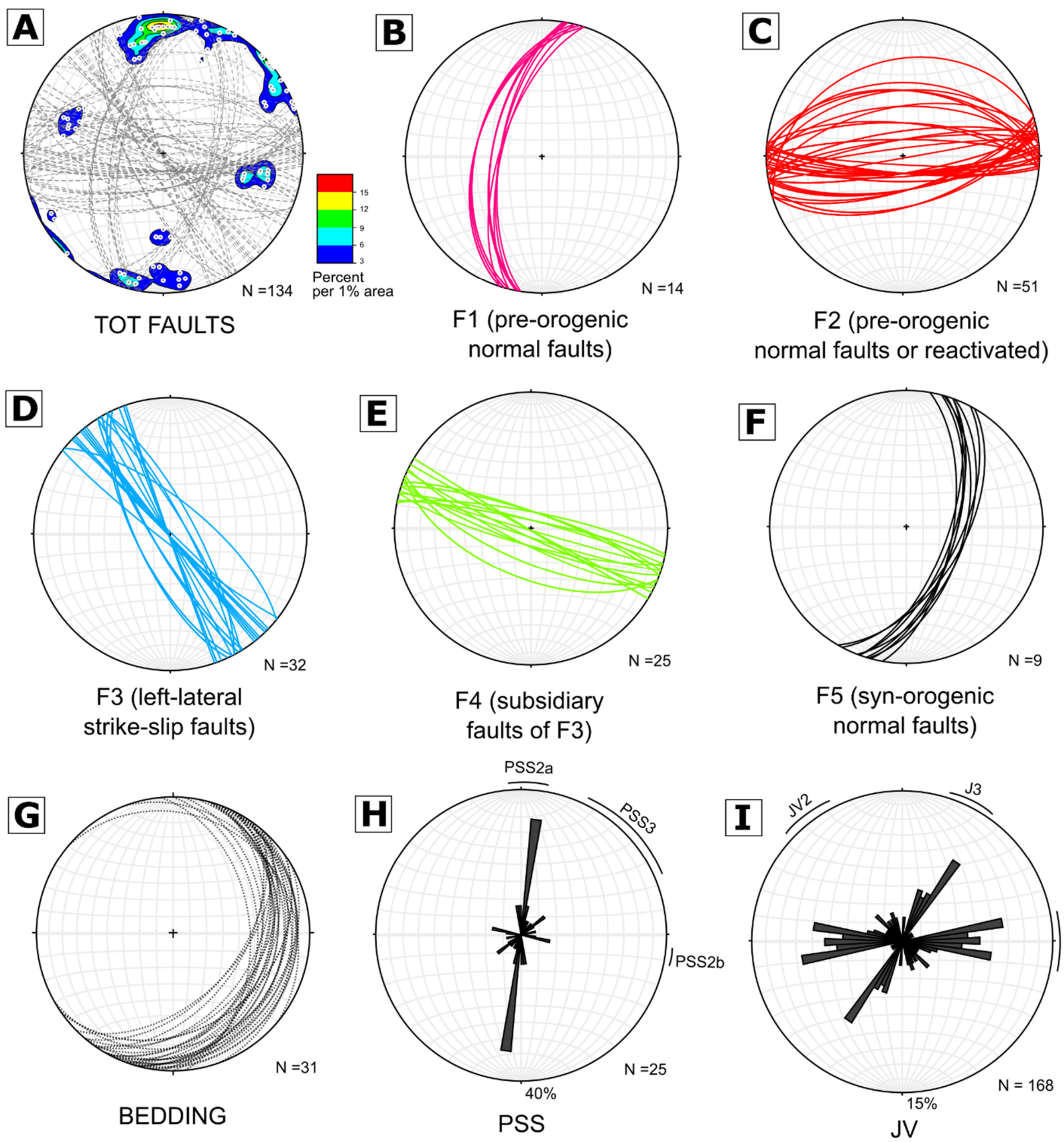

Figure 6: A) Equal area stereonet projection showing the density of all mapped fault poles; B-G) equal area stereonet projection showing great circles representation of the classified fault sets after contour, statistical and field-based analyses; B) F1 set: pre-orogenic, syn-sedimentary normal faults; C) F2 set: pre-orogenic normal faults passively rotated with tilted beds towards the thrust front; rotation axis is roughly E-W (106°-110°N) and the calculated average angle of rotation is about 20°–25°; some F2 faults were reactivated as strike-slip or oblique-slip faults during the contraction phases; D) F3 set: left-lateral strike-slip faults; E) F4 set: splays or subsidiary faults of F3 interacting segments; these faults show dip-slip or oblique-slip kinematics; F) F5 set: syn-orogenic normal faults, striking parallel to bedding; G) bedding measurements; H) rose diagram representation of pressure

solution seams frequency; PSS2 consist in bedding-normal orthogonal structures whereas PSS3 are oblique to bedding; I) rose diagram representation of joints/veins frequency classified by set; JV1 set: pre-orogenic opening-mode fractures; JV2 set: early-orogenic opening-mode fractures; J3 set: late-orogenic opening-mode fractures.

2.1.4.3.1. Joints, veins, and pressure solution seams

Opening-mode fractures, such as joints or veins usually filled by calcite (JV) and closing-mode fractures such as pressure solution seams and stylolites (PSS), are the main distributed structures in the study area.

PSS are quite abundant in the carbonate rocks of the Majella series (Agosta et al., 2009; Lavenu et al., 2014). In the study area, burial-related PSS1 (bedding-parallel) are common and define the mechanical layering. In ORF the average layer spacing is 10–15 cm except in the upper part of the unit characterized by thick massive horizons of floatstones or rudstones; SS1 shows an alternation of thin (3–5 cm) to medium layers (10–20 cm) of calcareous turbidites (mainly packstones, floatstones, wackestones and sedimentary breccias); in SS2 the layers' thickness is variable from thin marly limestone interlayers (3–5 cm) to thick bioclastic packstone/wackestone beds (30–40 cm). PSS1 are often sheared (with bedding-parallel slip demonstrated by slickenlines), and intensely weathered due to karst dissolution processes.

Besides PSS1, E-W veins filled with calcite (JV1) are other early burial-related structures. JV1 are bed-perpendicular and generally stratabound or shorter than single layer thickness (Fig. 7A and B). The original mechanical aperture and roughness of these fractures are variable and difficult to measure due to intense weathering. Typical joint apertures and vein fillings are < 0.2 mm where not karstified.

During the early contraction phase, N–S striking pressure solution seams developed normal to bedding (PSS2a). PSS2a are not so common in the study area and of difficult identification because of the intense weathering that make them like opening-mode fractures; their identification was therefore confirmed by thin sections analysis. Rare E-W bedding-normal, dip-parallel, pressure solution seams were also observed (PSS2b). The last set of pressure solution seams is observed at oblique-angle (~ 40°) respect to bedding and oriented parallel to the layers' strike (PSS3) (Fig. 7B).

A younger set of structures strikes NW-SE (JV2). JV2 consists of steeply inclined stratabound or occasionally through-going bedding-normal joints or calcite veins (Fig. 7B) with mechanical apertures and fillings around 0.4–0.5 mm. This set is the least common in the study area.

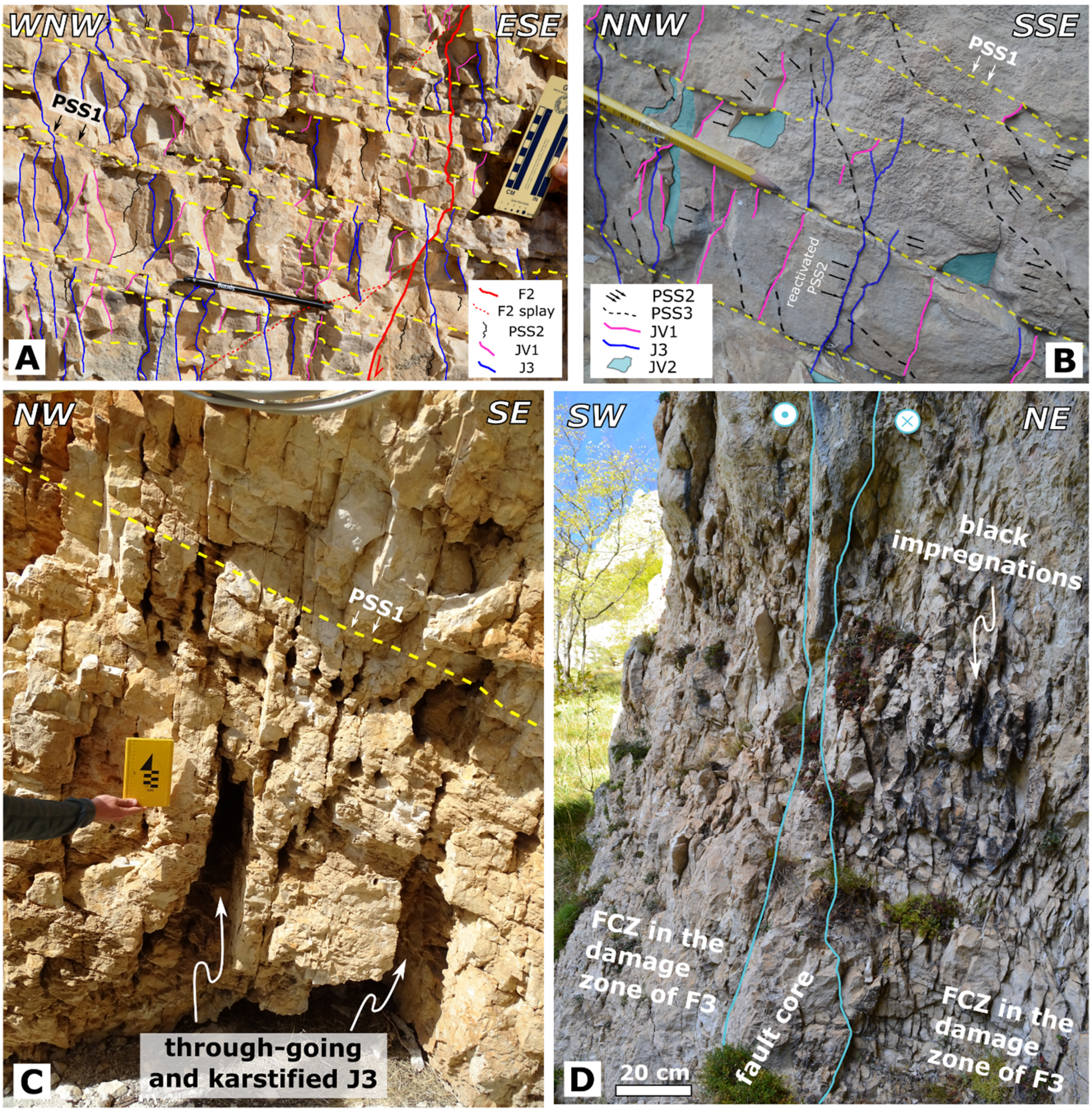

Figure 7. A) Fracture assemblages observed in porous recrystallized grainstones of ORF Fm; different examples of structures are highlighted by a line drawing; B) detail of fractures highlighted by a line drawing in a SS Fm outcrop with layered fine-grained bioclastic wackestones and packstones; C) through-going, closely-spaced and highly karstified J3 structures observed near the Cavallone Cave entrance; D) left-lateral F3 fault with a cataclasite core and through-going fracture cluster zones (FCZ) in the damage zone; note also the black tar/bitumen impregnations within the FCZ.

The last set of documented structures (J3) is represented by tensile fractures striking N–S or NE-SW, which can be the product of PSS2a reactivation in opening-mode (Fig. 7B). J3 localization occurred mainly in the anticline hinge culmination and produced through-going persistent fractures (Fig. 7C) and fracture cluster zones with large apertures (up to 1 cm), high connectivity, and small spacing (< 4–5 cm). We used the definition of "fracture-cluster-zones" (FCZ) to refer to volumes of localized deformation characterized by a dense array of clustered fractures, with high persistence and lateral continuity with respect to surrounding background structures. Sub-vertical J3 are sometimes connected via oblique-angle PSS3 developed during folding from sheared PSS1 (Fig. 7B).

Opening-mode fractures are predominant in fault damage zones, producing through-going splay joints organized in FCZ (Fig. 7D) or pervasive fragmentation (average fracture spacing < 4 cm), with formation of 'breccia-like' pockets (Fig. 8). This leads to a weak and erodible fabric, as observed in some outcrops of the Taranta Valley's eastern flank and nearby the CBS entrances. Opening-mode fractures in the damage zones present large apertures (0.4 mm–1 cm), excellent connectivity, and usually signs of karst dissolution and black tar/bitumen impregnations (Fig. 7, Fig. 8C).

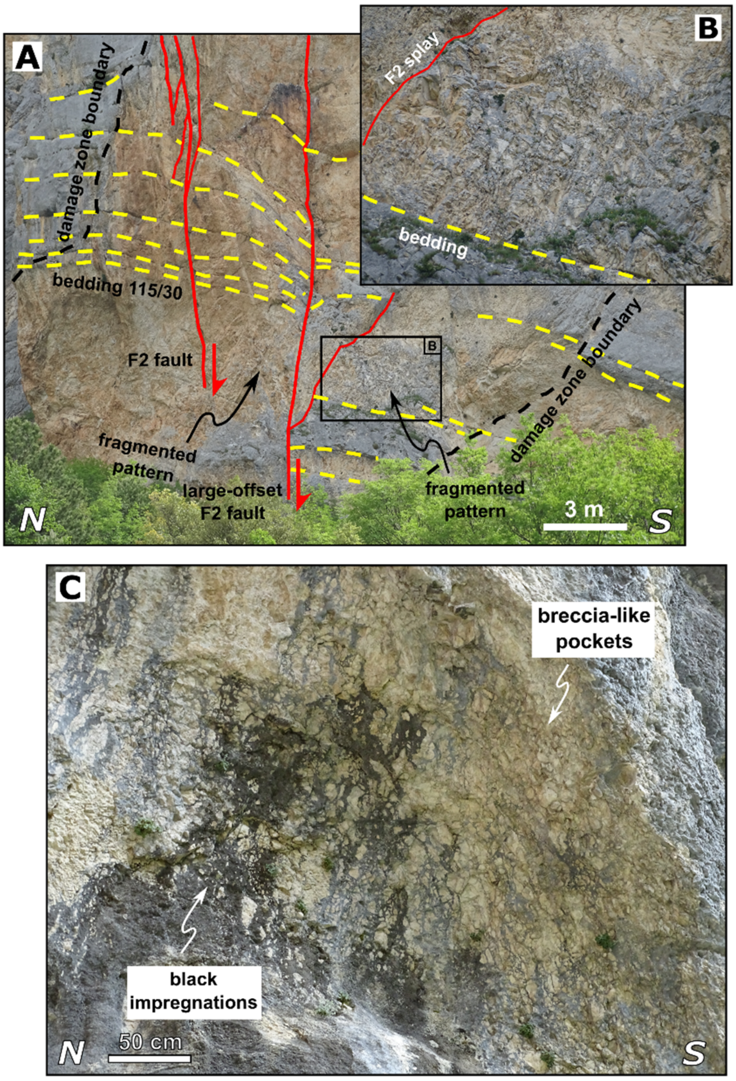

Figure 8. A) Picture showing an outcrop on the eastern flank of Taranta Valley and line drawing of the observed structures (large-offset F2 fault zone and associated damage zone). The damage zone is characterized by a pervasively fragmented rock; B) detail of the pervasively fragmented rock characterizing the damage zone of the F2 fault (red line); C) pervasive fragmentation and breccia-like pockets in a F3 fault damage zone (note also the black tar/bitumen impregnations).

2.1.4.3.2. Pre-thrusting normal faults (F1 and F2)

Structures related to pre-orogenic deformation include two systems of normal faults, which have passively rotated with the general increase of bedding dip towards the thrust front. The first set (F1, Fig. 6B) consists of W-dipping high angle syn-sedimentary normal faults (Fig. 9A) and shear bands with an anastomosing pattern. The second set consists of conjugate normal faults oriented ~ E-W (F2, Fig. 6C) with classical Mohr-Coulomb cut-off angles with respect to bedding (~ 50°–60°); they are common in the entire Taranta Valley (Fig. 8, Fig. 9A and C).

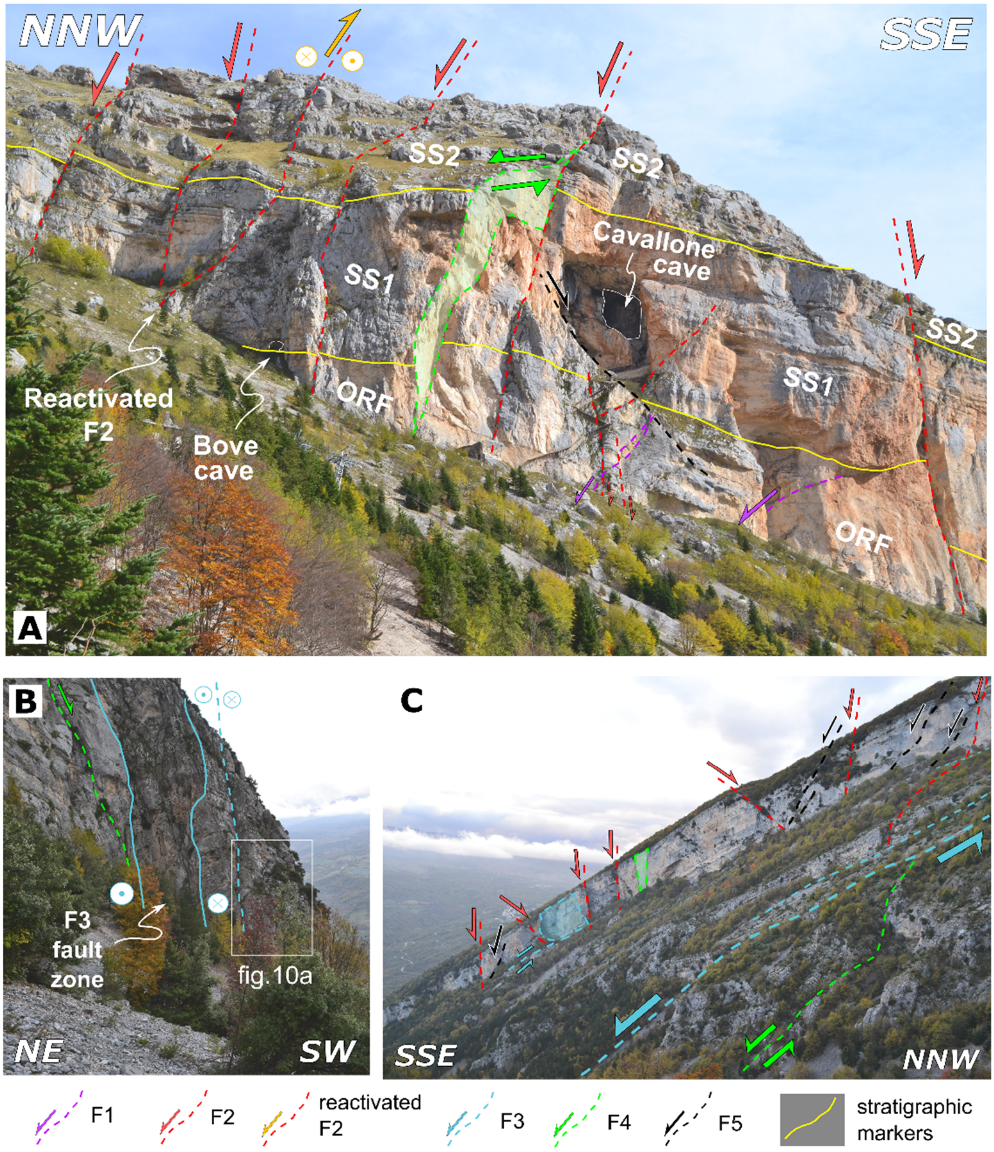

Figure 9. A) Faults and lithostratigraphic units at the entrances of the CBS; B) southeastward view along the Taranta Valley, with outcropping F3 fault zones; C) southward view along the western flank of the Taranta Valley. F2 faults are in conjugate sets, passively rotated with the increase of bedding dip towards the thrust front (average rotation angle around 20°–25°). Arrows represent the sense of shear on the faults.

F2 faults are associated with subsidiary splay faults and joints and they often show evidence of reactivation as strike-slip or transpressional structures (Fig. 5, Fig. 10A and C), testified by several generations of striae and kinematic indicators on slip surfaces. F2 faults in the CBS consist of sharp planes with one or multiple sub-parallel polished slip surfaces, and thin to thick fault cores (1–30 cm) with cataclasite or indurated matrix-supported fault breccia. Large-offset fault zones (offset > 10 m) generally have cores with composite chaotic breccias characterized by rotated cataclasite clasts.

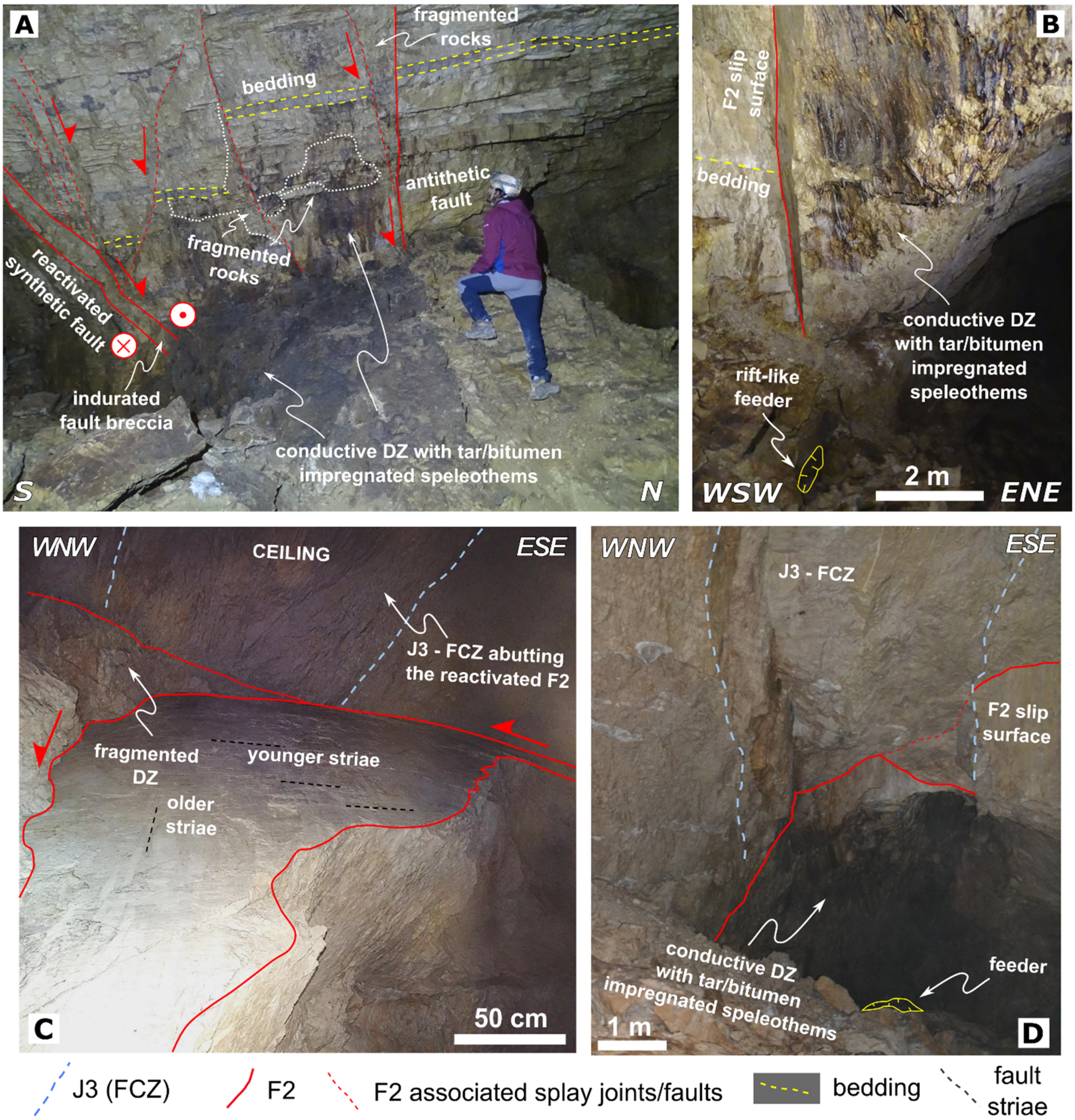

Figure 10. A) Conjugate set of E-W normal faults (F2) and their associated splay fractures in the CBS. Note the distribution of black hydrocarbon impregnations in the damage zone of the faults (Cavallone Cave, point 'B' on Fig. 5A); B) active percolation shown by black speleothems in the damage zone of a F2 fault. Also note the presence of a rift-like feeder under collapsed blocks near

the main slip surface; C) E-W fault zone (F2) showing a sharp polished slip surface with two generations of kinematic indicators, suggesting reactivation in strike-slip during syn-orogenic contraction. On the ceiling, there is the trace of a J3 fracture cluster zone (FCZ) abutting against F2 (Bove Cave, west side of point 'G' on Fig. 5A); D) F2 fault zone with conductive damage zone characterized by growth of black hydrocarbon-impregnated speleothems. A rift-like feeder is observed in the damage zone of the same fault (Bove Cave, point 'I' on Fig. 5A). Arrows represent the sense of shear of the faults. Key words and labels explanation; DZ: damage zone.

The damage zones of F2 faults are wide (between ca. 1 m to 7–8 m) and show closely spaced fault-parallel splay fractures or pervasive fragmentation. Inside the CBS, black tar/bitumen-impregnated speleothems are observed in some F2 damage zones (Fig. 10A and B, Appendix A). Fractures in the damage zones and opening along the slip surfaces bounding the fault cores are also the main conduits for recent epigenic water infiltration (Fig. 3F).

The sub-vertical J3 set abut or crosscut the F2 faults, which are truncated by F3, F4, and F5, confirming the relative younger age of J3 and associated FCZ.

The F2 set is the most common in the CBS and strike orthogonal to the main karst conduits. Faults in the caves expose slip surfaces forming sharp planes and jutting scarps in the conduit's walls. Such prominent planes often localize recent opening cracks, which break the continuity of the nearby blocks and cause gravitative collapses. Offsets of F2 faults are generally < 10 m but a few of them, with offsets up to 20–30 m, crosscut the entire valley.

2.1.4.3.3. Strike slip and associated faults (F3 and F4)

A N150-160E striking sub-vertical set of faults with a left-lateral strike-slip kinematics (F3, Fig. 6D) is also observed in the Taranta Valley. Canyon walls expose these NW-trending fault planes and fault cores surrounded by damage zones characterized by closely spaced fragmentation or FCZ (average fracture spacing ~ 4–5 cm) (Fig. 7, Fig. 8, Fig. 9B).

F3 strike-slip faults consist of long segments, which often cluster or interact, producing linkage via WNW-ESE subsidiary faults (F4, Fig. 6E). These structures cut across the entire anticline forelimb; abutting/cross-cutting relationships suggest that they are younger than F1 and F2, older than F5 and synchronous with F4. F3 and F4 faults have apparent throws in the range of 1–10 m and intense karstification in their fractured damage zones (Fig. 11).

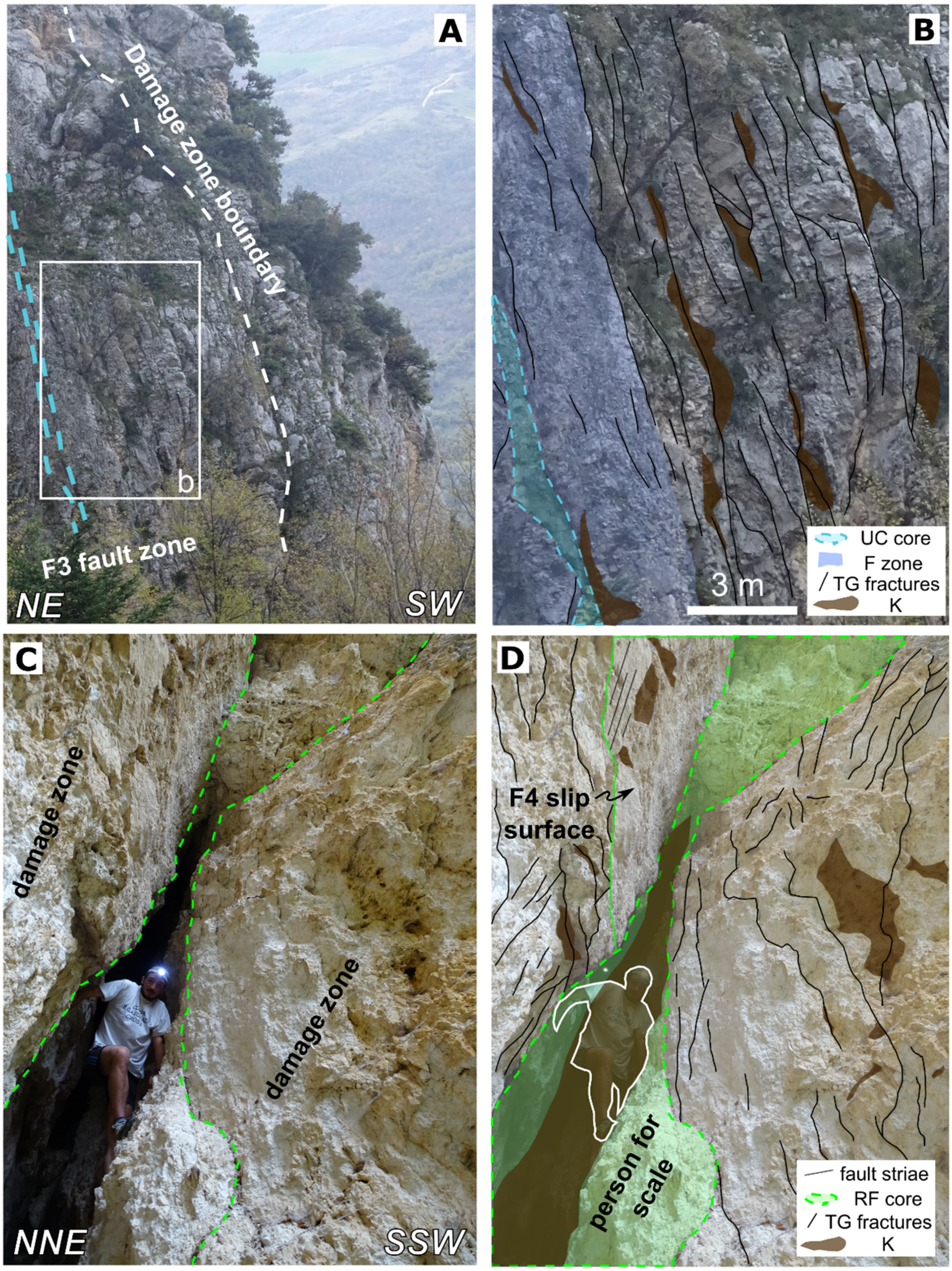

Figure 11. Outcrops and line drawing of F3 (A–B) and F4 (C–D) fault architectures and their relationships with karst inception. A) N160E left-lateral strike-slip fault outcropping in the eastern walls of the Taranta Valley (see Fig. 9B for location). Karst dissolution is significant in the damage zone (B). C) N120E oblique-normal fault with a short cave passage. Karst dissolution is concentrated mostly in the fault core and in the damage zone (D). Key words and labels explanation; F: pervasive fragmented zone with fracture clusters, UC: ultra-cataclasite (fault core), RF: recrystallized and fragmented (fault core), TG: through-going, K: karst solutional cavities.

Fault cores in small offset (displacement < 10 m) F3 and F4 faults have a thickness ranging from a few dm-to 1 m; they usually consist of indurated fault breccia, cataclasite or ultra-cataclasite (Fig. 11A and B). Mature fault zones (displacement > 10 m) are characterized by wide damage zones with through-going splay fractures forming FCZ and highly fragmented rock volumes (Fig. 11B). Evidence of focused fluid flow and karst dissolution are widespread in these pervasively fractured domains of the fault zones.

Occasionally, some fault cores in F3 and F4 faults present a recrystallized and highly fragmented fabric without cataclasis (Fig. 11C and D), and short epigenic cave passages and meso-scale cavities inside the fault cores.

One last set of secondary subsidiary structures, observed once in the CBS and in two spots of the Taranta Valley eastern flank, are NE-SW-striking reverse or oblique-slip high angle faults (with main reverse component); they are associated with right contractional stepping interaction of left-lateral F3 fault segments.

2.1.4.3.4. Folding-related normal faults (F5)

The normal fault set striking parallel to bedding and dipping ESE (F5, Fig. 6F) have an oblique cut-off angle at 40°–45° with respect to bedding (Fig. 12), and cut across all other fault sets documented in the study area.

Based on their attitude and on the model proposed by Graham et al. (2003), F5 faults form from shearing of splay oblique-to-bedding pressure solution seams (PSS3) during the progressive folding of the carbonate layers. PSS3 splay structures start from sheared PSS1 and they abut against the uppermost mechanical layer boundary (Fig. 7, Fig. 12C). Progressive shear causes first the formation of splay joints at the termination of the PSS3, and then linkage with bedding-normal PSS2 leading to breccia formation and incipient faulting (Fig. 12D).

Mature faults show normal or oblique-slip kinematics (normal component always prevalent) with formation of highly fragmented rock volumes showing an incohesive brecciated texture. F5 offsets mainly range from 1 to 2 m, but they can be up to 10–15 m. Finally, we observed that F5 structures are more common approaching the thrust front and decrease in density moving towards the hinge zone of the anticline.

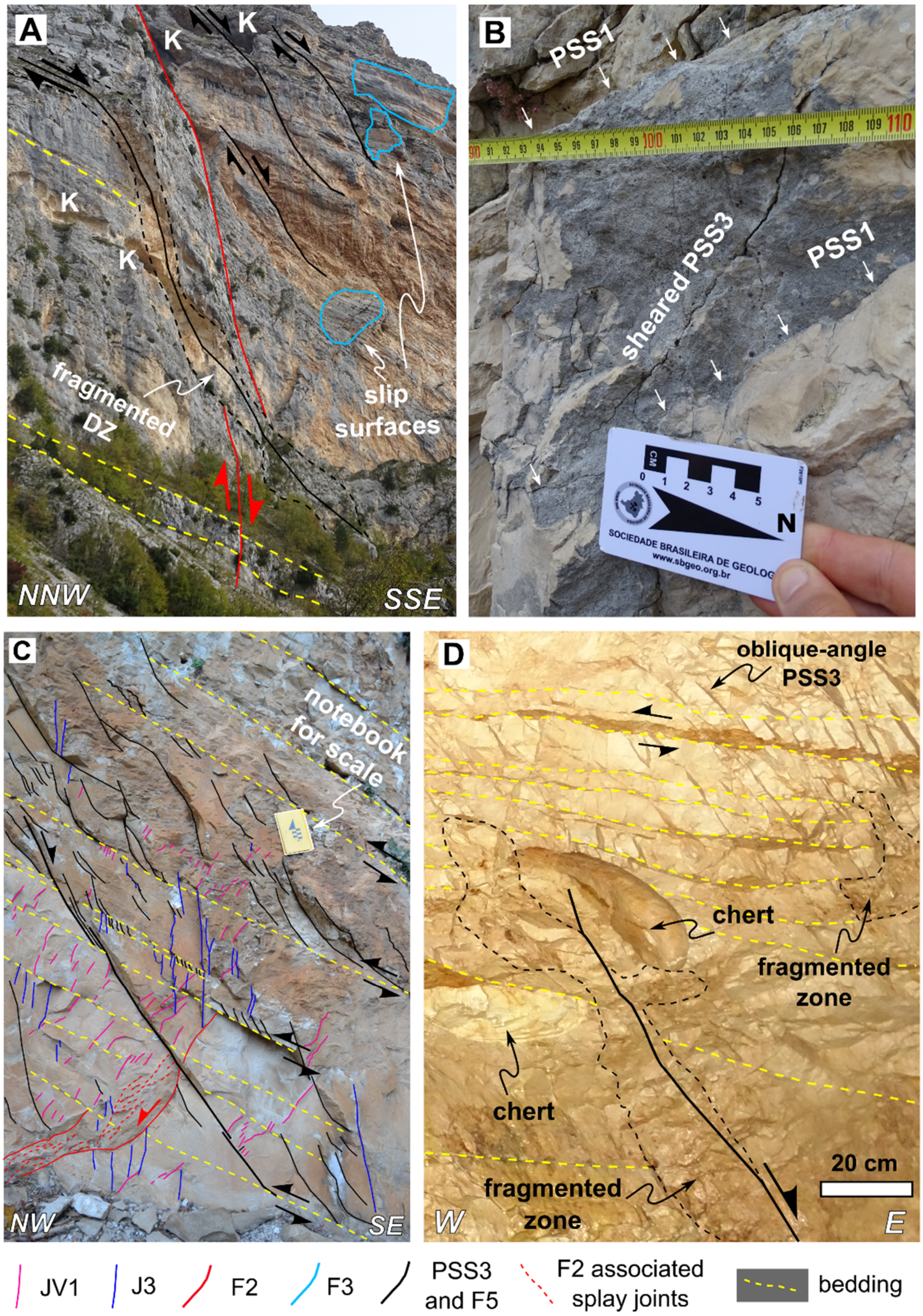

Figure 12. A) Eastern flank of Taranta Valley with examples of F2, F5, and F3 faults. Karst dissolution is focused in the pervasive fragmented damage zone of F5 faults and along bedding interfaces; B) sheared PSS1 and PSS3 in a thick bioclastic packstone layer; C) fracture assemblage in an outcrop of layered bioclastic wackestones. Note the development of splay oblique-angle to bedding pressure solution seams (PSS3) and their shearing and linkage forming F5 faults; D) PSS3 developed from sheared PSS1 and small-offset F5 fault with formation of fragmented incohesive breccia (Bove Cave). Arrows represent the sense of shear of the faults. Key words and labels explanation; DZ: damage zone, K: karst solutional cavities.

2.1.4.4. Microstructural observations

Twenty-six blue-stained polished thin sections were analyzed with optical microscopy to recognize lithological variability and the microstructural textures of fault rocks. Examples of ORF and SS Fm lithofacies and fault rocks types are illustrated in Fig. 13. Fault rock textures and the total optical porosity values measured in the thin sections are summarized in Table 1.

Table 1. List of samples analyzed by optical microscopy with measured total optical porosity (Φ) in main lithofacies and fault rock types. Key words explanation: ND, fault core not sampled, because of material characteristics.

	Formation - lithofacies	mean optical *Φ* (%)	Fault rocks	fault rocks optical *Φ* (%)	fault set
ORF	Crystalline limestones (n° samples = 5)	6.2	Ultra-cataclasite	2.3	F4
			Ultra-cataclasite	0.2	F3
	Bioclastic floatstones/rudstones (n = 2)	4.4			
SS1	Bioclastic chaotic floatstones (n = 1)	4.8	Recrystallized and fragmented	3.7	F4
			Ultra-cataclasite	0.8	reactivated F2
	Bioclastic fine-grained wackestones (n = 1)	3.3	Cataclasite	3.2	F2
			Cataclasite	3.7	F2
			Composite chaotic breccia	11.2	reactivated F2
	Bioclastic fine-grained packstones (n = 2)	5.6	Composite chaotic breccia	17.7	reactivated F2
			Indurated matrix-supported breccia	0.6	F1
SS2	Bioclastic wackestones (n = 3)	< 0.1	Indurated fault breccia	0.1	F2
			Indurated fault breccia	0.2	F3
	Bioclastic packstones (n = 1)	0.9	Incohesive mosaic breccia	ND	F5

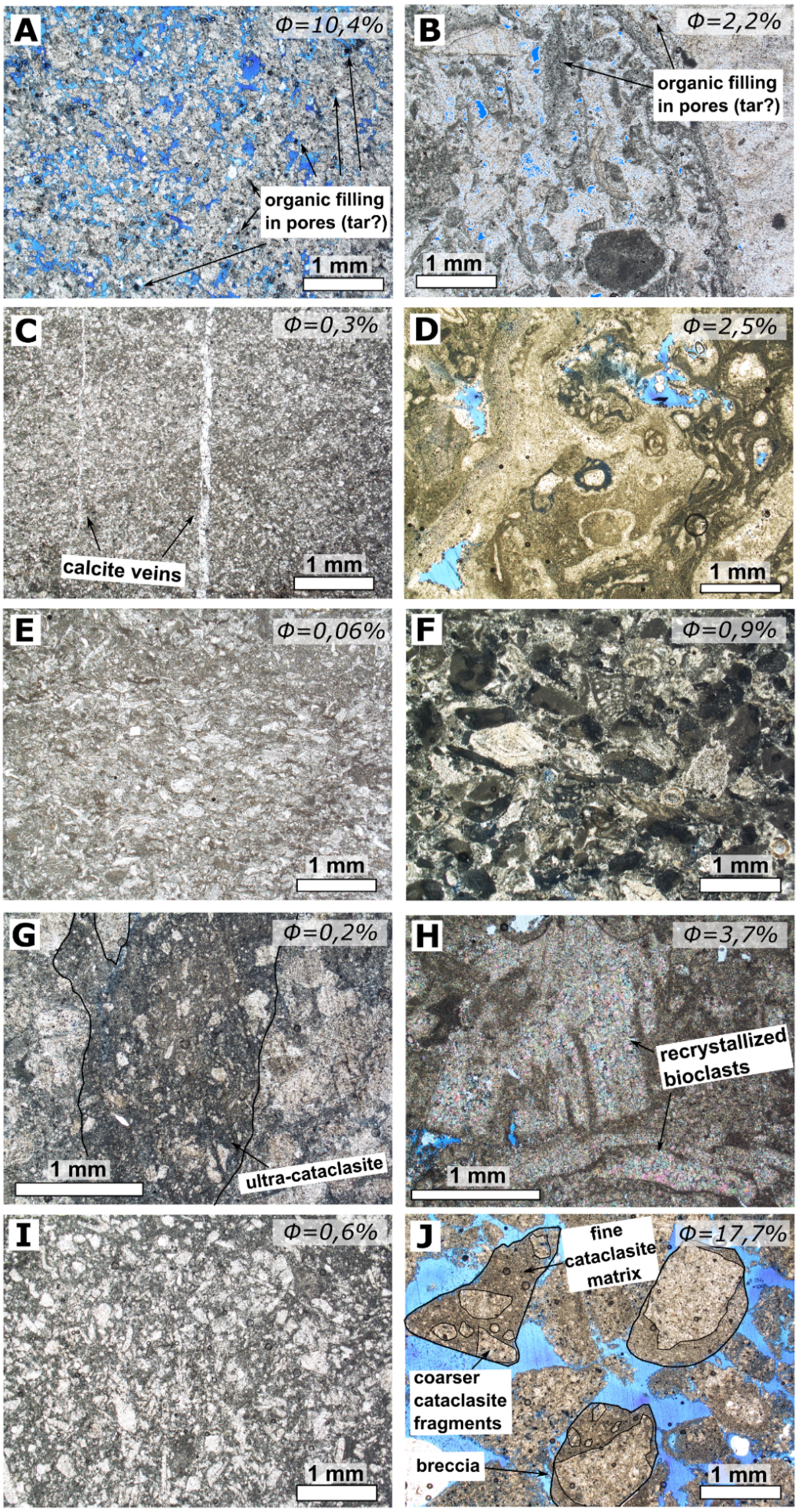

Figure 13. Microphotographs of blue-stained thin sections under plane-polarized light (except 'H'). A) porous recrystallized limestone (grainstone texture) (ORF); B) bioclastic, partially recrystallized, floatstone (ORF); C) bioclastic fine-grained wackestone with JV1 calcite veins (SS1); D) bioclastic chaotic floatstone (SS1); E) bioclastic wackestone (SS2); F) bioclastic packstone (SS2); G) cataclastic fault rock with an ultra-cataclasite band (ORF); H) microphotograph under cross-polarized light; recrystallized fault rock from the same layer of the bioclastic floatstone in 'D' (SS1); I) matrix-supported indurated fault breccia (SS1); J) porous composite chaotic breccia with angular cataclasite fragments (SS1). Optical porosity values reported in each microphotograph refer to those computed from the high-resolution scanned images of the whole thin section.

Samples from the ORF Fm are mainly porous recrystallized limestones with grainstone or packstone textures and grain size ranging from silt to fine sand (Fig. 13A). Samples from the upper part of the unit, where lenticular channel deposits have been observed, show floatstone and rudstone textures with coarser grains (Fig. 13B). Bioclastic and detrital grains (mainly rudists, coral fragments, and sporadic orbitoides) show intense recrystallization and variable porosity (vuggy, fracture, intergranular, and intragranular) with a mean of 6% and maximum values around 10%. Samples with the highest porosity have been collected near the CBS entrances.

Most of the SS1 unit rocks are fine-grained (mud-silt grain size) packstones and wackestones (Fig. 13C) composed of bioclastic skeletal grains of planktonic foraminifera, algal crusts, echinoids, rotalids, and large benthonic foraminifera (alveolinids and miliolids). Coarse-grained packstones and chaotic floatstones (with coarser clasts > 2 mm, Fig. 13D) are also observed. Total optical porosity is variable, with a mean around 5% for packstones and floatstones, and <1% for micrite-dominated wackestones.

Samples from the SS2 unit are bioclastic wackestones (Fig. 13E) and packstones (Fig. 13F). Grain size ranges from silt to medium sand. Skeletal bioclastic grains are large benthonic foraminifera (nummulitids, miliolids, alveolinids), mollusca, peloids, algae, and planktonic foraminifera. Optical matrix porosity is < 0.1%, in the form of intragranular and moldic voids.

Fault rocks from medium to large offset faults (offset > 2 m) inside the ORF Fm contain cataclasites or ultra-cataclasites (Fig. 13G), often with evidence of calcite precipitation in pore space. In the SS Fm, fault rocks present different microstructures controlled by the primary textural properties (micrite- or grain-dominated facies), fault offset, and type. Samples from fault cores of small-offset faults (< 2 m) developed in the chaotic floatstones of the SS1 unit show recrystallized textures and no evident cataclastic or brecciated textures (Fig. 13H). Pervasive open fractures are often present inside these fault cores, causing an increase in optical porosity. Indurated matrix-supported breccias (Fig. 13I) developed in the fine micrite-dominated carbonates of SS1 and in relatively small fault zones, whereas cataclastic rocks were observed in the packstone facies and more mature faults (offset > 2 m). Cataclastic rocks from large-offset (> 10 m) or reactivated faults show composite chaotic cataclasite breccia (as described also in Michie, 2015). The reactivation process is associated with opening of new voids and an increase in porosity up to 17% (mean around 14%) (Fig. 13J). Cataclastic (Fig. 13G), recrystallized (Fig. 13H) or indurated (Fig. 13I) fault rocks present a reduction in total optical porosity compared to the surrounding protolith (see also values in Table 1). Another type of fault rock is an incohesive, highly fragmented mosaic breccia, occasionally observed in F5 fault cores and not sampled because of material characteristics.

2.1.5. Discussion

The occurrence of well-developed sulfuric acid hypogene karst systems in a fold-and-thrust belt requires the presence of: i) soluble rocks with high permeability; ii) source of aggressive (H_2S-rich) fluids; iii) vertically extended structures focusing rising fluid flow. The main objectives of this research were to unravel the fundamental structures able to focus H_2S flow from depth and the development of vast sub-horizontal interconnected conduits in the subsurface of Majella Massif. Therefore, understanding the timing of deformation, the relative chronology of fractures, and their association to paleo fluid flow (and karst dissolution) is crucial.

In the next sections we will interpret the observed structures in their regional tectonic setting, constraining timing of deformation, fluid conductive structures, and fluid-rock interaction (with associated resultant morphology of the karst system). Finally, we briefly discuss the importance of sulfuric acid karst systems developed in fold-and-thrust belts, and the issues related to their prediction in carbonate reservoirs.

2.1.5.1. Structural interpretation

The southeastern portion of the Majella anticline contains a great variety of structures organized in a complex network illustrated in Fig. 14. Our interpretations of the structural assemblages are consistent with the most recent literature (Graham et al., 2003; Marchegiani et al., 2006; Tondi et al., 2006; Antonellini et al., 2008; Agosta et al., 2009; Aydin et al., 2010; Rustichelli et al., 2016; Torabi et al., 2019) and provide new detailed data on the deformation pattern characterizing the anticline hinge, where the CBS is located.

Syn-sedimentary N–S normal faults (F1), E-W joints/veins (JV1), and conjugate E-W normal faults (F2) formed during the pre-orogenic extensional phases since Cretaceous time (Di Cuia et al., 2009; Casabianca et al., 2020). These structures are observed at present day tilted within bedding towards the thrust front and they are occasionally reactivated during strike-slip Pliocene tectonics (Fig. 5, Fig. 9, Fig. 10C).

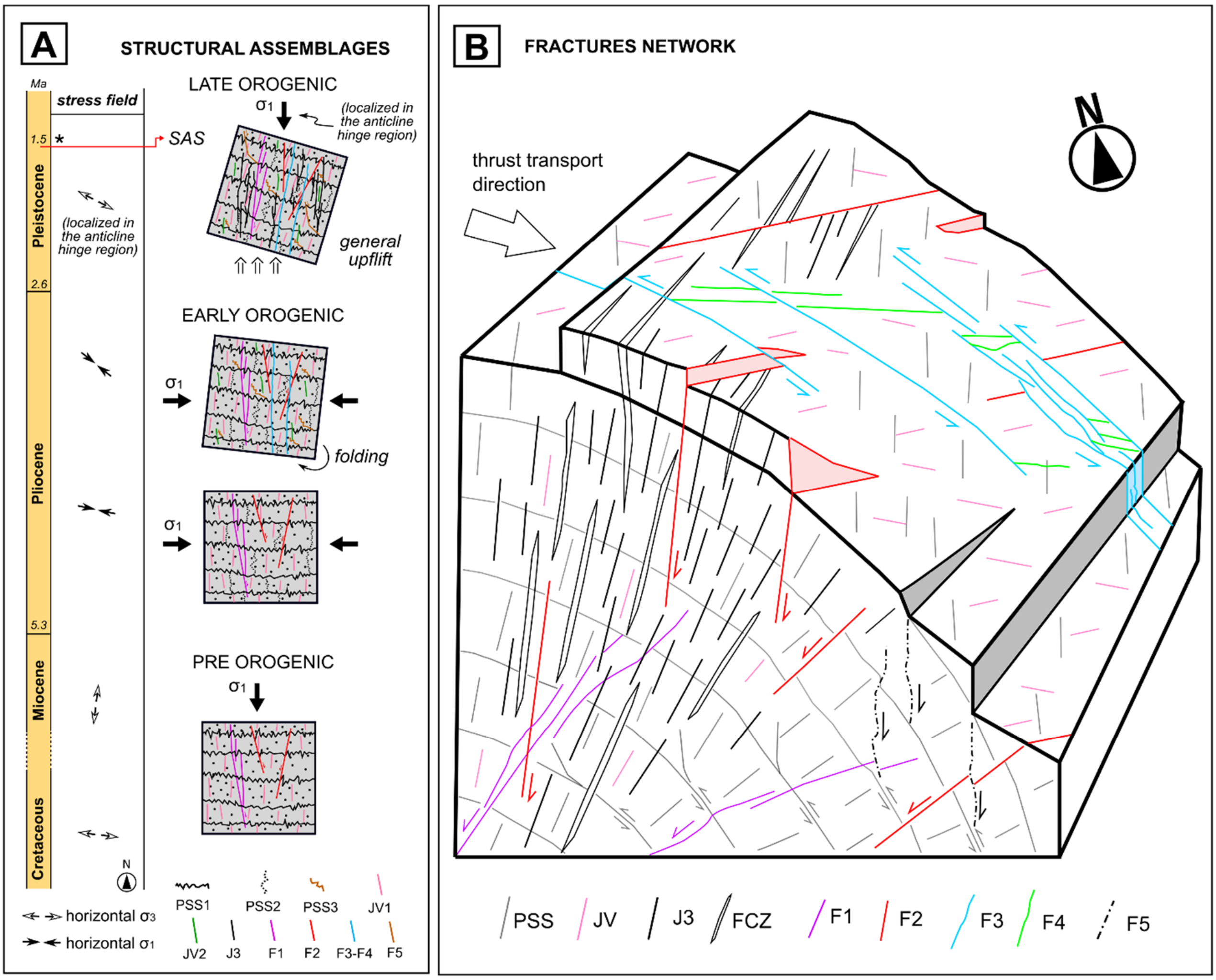

*Figure 14. A) Conceptual model illustrating the deformation events and associated structural assemblages in the southeastern Majella ramp carbonates. *: dating of alunite deposits from D'Angeli et al. (2019b); B) conceptual schematic 3D box illustrating the fracture network in the study area and their spatial, geometric, and kinematic characteristics. Illustrated structures are: burial-related bedding-parallel pressure solution seams (PSS1); pre-orogenic syn-sedimentary N–S normal faults (F1) and pre-orogenic E-W conjugate normal faults (F2); burial-related and early-orogenic joints/veins (JV1-JV2); early-orogenic bedding-normal (PSS2) and oblique to bedding (PSS3) pressure solution seams; NW-SE left-lateral strike-slip faults (F3) and associated splay/subsidiary faults (F4); late-orogenic oblique to bedding normal faults developed on sheared PSS3 (F5); N–S or NE-SW opening-mode fractures (J3) associated with extension in the anticline hinge region and forming fracture cluster zones (FCZ).*

The early stage of contraction in the Central Apennines, with an average σ_1 striking ~ E-W (Ghisetti and Vezzani, 1997, Ghisetti and Vezzani, 1998), caused the formation of bedding-normal pressure solution seams (PSS2) in the carbonates. Both PSS2a and PSS2b abut against PSS1 and show mutual cross-cutting relationships. For this reason, we consider the two orthogonal PSS2a and PSS2b sets contemporaneous. We explain their coeval development with a penecontemporaneus reversal in the greatest and least principal stress axes during the early contractional stages (Agosta et al., 2009). Progressive deformation during thrusting and folding of the carbonate units produced flexural slip (Graham et al., 2003) with formation of splay PSS at oblique-angle with respect to bedding (PSS3). This interpretation is based on models proposed by Rispoli (1981) and Fletcher and Pollard (1981) regarding the formation of splay closing-mode fractures in the compressional quadrant of a sheared mechanical discontinuity in carbonate rocks.

Younger ~ N130E striking opening-mode fractures filled with calcite (JV2) indicate a progressive clockwise rotation of the direction of maximum principal stress (σ_1) moving towards the southern portion of the anticline. This is also consistent with the rotation from N–S to NE-SW of the fold-and-thrust belt front and its associated structures (Fig. 1, Fig. 5B). The switch of the fundamental failure modes from pressure solution (closing-mode, plastic deformation) to jointing (opening-mode, brittle deformation) may have taken place during the exhumation of the Majella Massif (Ghisetti and Vezzani, 2002; Agosta et al., 2009).

~ N130E striking contraction also produced NW-SE strike-slip sub-vertical faults with a left-lateral component of movement (F3 set). Progressive deformation caused the growth of F3 faults segments and linkage by splay or subsidiary faults (F4 set), developed at F3 extensional stepovers and tips (Cooke, 1997; Florez-Niño et al., 2005; De Joussineau et al., 2017; Schultz, 2019). JV2, F3, and F4 fault orientations and kinematics are consistent with σ_1 striking ~ N130E, and we suggest that the same stress field also determined the reactivation in strike-slip or oblique-slip (transpressional) kinematics of some of the F2 faults observed in the caves and in the Taranta Valley.

The late orogenic phase was characterized by the formation of normal faults (F5) developed on sheared PSS3 splays linked by bedding-normal PSS2, as previously observed by several authors (Graham et al., 2003; Agosta et al., 2009), and N–S or NE-SW striking opening-mode fractures (J3 set).

J3 structures are interpreted as the consequence of uplift due to the regional doming of the overthickened thrust wedge since lower-middle Pleistocene (Ghisetti and Vezzani, 2002; Pizzi, 2003) that caused extension along the hinge of the Majella anticline. The same deformation mechanism is observed in other settings worldwide (Avouac et al., 1992; Tavani et al., 2012; 2014; Watkins et al., 2015; Gholipour et al., 2016) with late-thrusting uplift-induced extension in the anticline hinges of fold-and-thrust belts. We documented pre-existent N–S-striking PSS2a reactivated in opening-mode by this process, whereas new joints developed with a strike parallel to the anticline hinge (NE-SW).

The network of structures in the hanging wall of the thrust also affects the evolving landscape of the area. In particular, the Taranta Valley is elongated in two morpho-structural lineaments following the same strike of F3 and F4 segments (Fig. 2). There is a general increase in frequency of F3 faults and associated splays (F4) towards the center of the valley, suggesting the presence of a large damage zone with weak (more prone to erosion) fragmented rocks. This damage zone may belong to a major strike-slip tear fault buried in the valley.

2.1.5.2. Fluid flow pathways and structural control on hypogene karst development

The occurrence of hypogene karst macro-scale porosity formed by rising aggressive fluids is an excellent proxy for paleo (or possibly still active) fluid flow. Hypogene caves generally show fracture-controlled conduits and a strong structural guidance (Klimchouk, 2007). The case study of CBS represents a peculiar example of an inactive SAS system developed close to the paleo water-table (De Waele et al., 2016; D'Angeli et al., 2019b), formed in a structurally complex setting where different deformation events produced a large variety of structures.

Water-table caves are characterized by bi-dimensional (horizontally-developed) patterns, which can become tri-dimensional (extended also vertically) if the position of the paleo water-table has changed over time (Audra et al., 2009). This is the case of the multi-level system of sub-horizontal conduits in the CBS, which reflects the evolving positions of the sulfuric acid water-table through time (Fig. 3). For each single genetic stage, second order fluctuations of the water-table level generated a zone of enhanced dissolution by oxidation of H_2S, which produces aggressive H_2SO_4 and karst macro-scale porosity formation.

Narrow rift-like passages in the CBS (Fig. 4, Fig. 10D) often with sulfate deposits in their surroundings, were the main discharge feeders of ascending H_2S-rich solutions. Feeders and rising solutional features inside the caves occur mainly within F2 damage zones and, subordinately, J3 organized in FCZ, suggesting a strong control on rising fluids by localized fracture permeability.

Fault zone permeability is significant in the open fractures of the damage zones and along the polished slip surfaces bounding the fault cores (Figs. 10 and 11), as suggested by the speleothems growth and black tar/bitumen impregnations (see Appendix A). Fault cores characterized by cataclastic rocks or indurated fault breccias (optical porosity < 3%) are, on the other hand, low-permeability domains, especially if they are laterally continuous along the fault. The presence of fragmented fault cores (Fig. 11C) or composite chaotic breccias (Fig. 13J) in large-offset (> 10 m) and/or reactivated fault zones, on the other hand, may represent conduits for fluid flow (optical porosity > 10%).

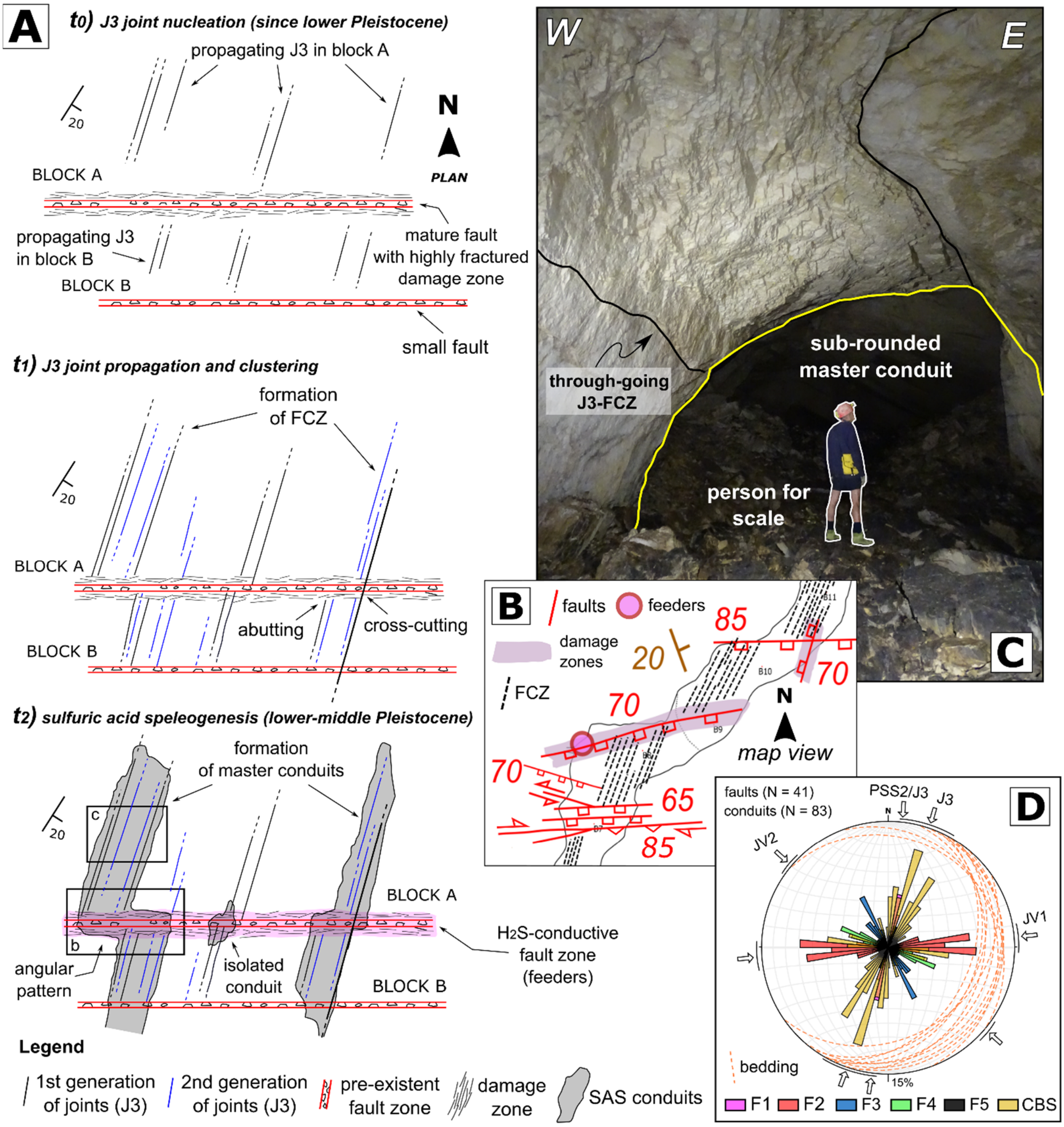

Figure 15. A) Conceptual model of the lower-middle Pleistocene time-space evolution of J3 fracture sets and SAS development. The conceptual model highlights J3 set propagation and abutting/crosscutting relationships with pre-orogenic F2 normal faults; sulfuric acid speleogenesis (active at least until 1.5 Ma) along F2 and J3-FCZ produced sub-horizontal master conduits with an

angular pattern in map view; B) detail of the CBS structural map, with J3-FCZ abutting against F2 fault zones, and their control on master conduit formation, forced to step laterally (see also the whole topographic survey in Fig. 4A); C) example of a sub-rounded master conduit imposed on J3-FCZ in the Bove Cave; D) relationships between normalized trends of the master conduits in CBS, bedding, and geological structures mapped in the caves. The diagram shows strong relations between karst conduit directions and, in order of frequency: J3, bedding strike, and F2 fault zones.

In the CBS, master conduits are elongated following the trend of the main sub-vertical FCZ localized along the hinge zone of the anticline. Because of their properties and spatial distribution, they characterize structural domains with higher fracture permeability with respect to surrounding rock volumes. Therefore, the nucleation of J3-FCZ was crucial to provide efficient permeability pathways in rocks with low primary porosity and permeability.

The geometrical relationships between FCZ and H_2S-conductive fault zones strongly control the cave pattern and conduits' spatial organization, as illustrated in Fig. 15. In the CBS, J3-FCZ abut against (or crosscut) the F2 faults, which are usually characterized by fault cores with indurated breccia or cataclasite. These mechanically hard zones likely acted as barriers segmenting the progressive in-plane propagation of J3, creating a "stepping" angular pattern in map view (Fig. 10, Fig. 15B). Where J3 are longer and cluster into high-persistent FCZ, they may crosscut the pre-orogenic normal faults. Recent sulfur stable isotopes analyses from D'Angeli et al. (2019b) were carried out on secondary sulfate minerals collected in the CBS, in Triassic and Messinian evaporites from southern Italy, and in tar/bitumen impregnations from the Majella's abandoned mines (Table 2). Their results suggest that the origin of H_2S-rich fluids was triggered by bacterial-mediated reduction of buried Triassic evaporites interacting with different mixtures of hydrocarbons over time.

Even if the source rocks are not well known, hydrocarbon generation and migration in the subsurface of the Majella Massif is indicated by diffuse tar and bitumen manifestations in the outcropping carbonates (Lipparini et al., 2018). Such hydrocarbon manifestations are predominant in the BOL Fm, especially in the damage zones of faults characterized by a high frequency of opening-mode fractures or fragmentation (Agosta et al., 2009).

Table 2. Results of sulfur stable isotope analysis ($\delta^{34}S$‰), modified from D'Angeli et al. (2019b). $\delta^{34}S$ values indicate a SAS origin of the sulfates and, in general, of the whole CBS. H_2S derives from the bacterial-mediated reduction of deep-seated Triassic evaporites interacting with hydrocarbons.

Sample	**$\delta^{34}S$ ‰**	**Description and location**
Bove Cave		
BOV1	1.4	Sulfates, lower level
BOV2	0.5	Sulfates, lower level
BOV7	4.7	Sulfates, lower level
BOV10	3.6	Sulfates, lower level
BOV11	4.2	Sulfates, lower level
BOV13	−1.4	Sulfates, bottom feeder
BOV16	−8.9	Sulfates, intermediate level (nearby entrance)
BOV17	−6.0	Sulfates, intermediate level (nearby entrance)
Cavallone Cave		
CAV2	8.5	Sulfates, intermediate level
CAV3	9.1	Sulfates, intermediate level
CAV6	8.7	Sulfates, intermediate level
CAV8	9.3	Sulfates, intermediate level
CAV9	6.2	Sulfates, intermediate level
CAV11	8.7	Sulfates, intermediate level
CAV13	8.2	Sulfates, upper level
CAV14	8.1	Sulfates, upper level
CAV21	8.9	Sulfates, upper level
Gypsum bedrock		
G1	23.6	Messinian gypsum (Sicily)
PN1	15.1	Triassic gypsum (Apulia)
Bitumen from Majella mines		
P1	−17.2	Bitumen, Pilone Mine (Majella)
P3	−17.8	Bitumen, Pilone Mine (Majella)
PM1	−17.5	Bitumen, Piana dei Monaci Mine (Majella)
SL1	−18.9	Bitumen, Santa Liberata Mine (Majella)

As reported by Lipparini et al. (2018) and documented by our findings, also ORF and SS Fm manifest hydrocarbon impregnations both in the matrix (Fig. 13E and F) and fracture porosity (Fig. 7, Fig. 8, Fig. 10). Black organic impregnations interpreted as tar/bitumen manifestations were observed in the matrix porosity of the studied thin sections and inside the CBS, in isolated spots or encased in black speleothems always occurring in the highly fractured/fragmented damage zones of the faults. These hydrocarbon manifestations represent the evidence of active fluid circulation controlled by fault zone permeability. The BOL Fm has been the target for oil exploration in the area since the early 20th century, and almost all viable economic accumulations have been exploited (Gerali and Lipparini, 2018). Late-stage hydrocarbon migration occurred (and still takes place) as downward percolation from the BOL Fm outcrops on the plateau above the caves downwards through the cave vaults.

In the regional context of the Majella Massif, vertical upward migration of H_2S-rich fluids from deep-buried Triassic evaporites must have been driven by vertically extended structures acting as permeability pathways. Our geological mapping, detailed structural analysis, together with geomorphological observations (cave topography, localization, pattern) and evidences of fracture conductivity and dissolution, suggest that the complex system of faults in the study area represents a network of barrier-conduit structures for fluid flow. Deep-rooted, sub-vertical tear faults (F3) may reach the base of the thrust sheet becoming the principal vehicle for vertical cross-formational H_2S flow. The damage zones of the wider faults, with through-going FCZ or fragmented rocks formed high-permeability domains for fault-parallel fluid flow. Linkage and intersection of these faults by F4 splays in extensional step overs and pre-orogenic normal faults (F2), with pervasively fractured damage zones, permit ascending fluids to reach multiple recharge points getting close to the paleo water-table.

As illustrated in the conceptual model of Fig. 16, sulfuric acid speleogenesis in the fold-and-thrust belt occurred predominantly at the intersection of the multiple feeders with the oxygenated water-table level. In the anticline hinge, dissolution focused laterally along fracture cluster zones and bedding interfaces, forming huge interconnected conduits. During progressive uplift, the paleo water-table shifted to lower elevations, with the creation of different speleogenetic levels.

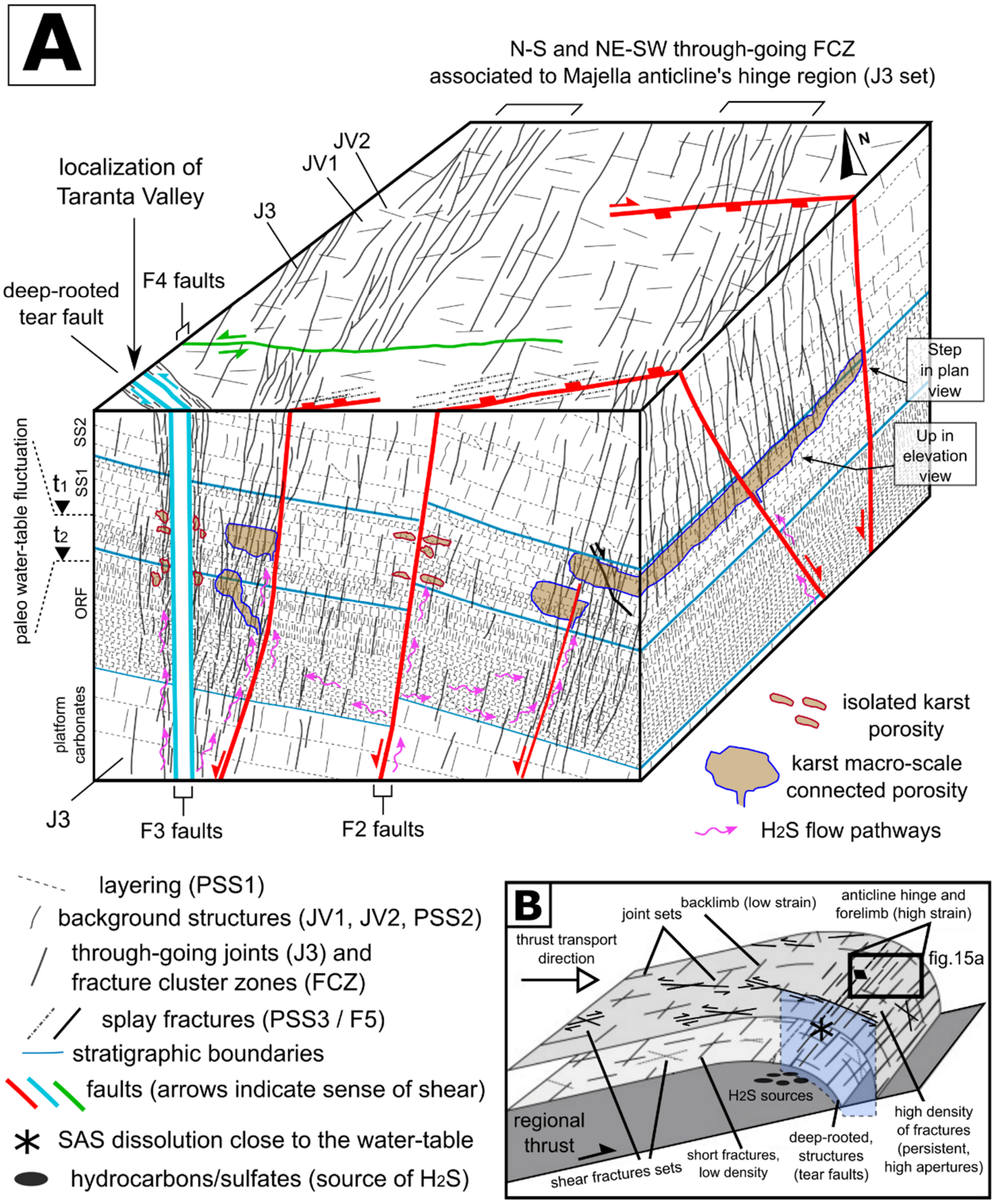

Figure 16. Conceptual genetic model for SAS localization in the Majella anticline. A) at the cave scale (hundreds of meters long passages), karst conduits are developed close to the paleo water-table levels, taking advantage of the most persistent, open, and well-connected fractures (FCZ in the anticline hinge); karst geometries and pattern are controlled by the geometric relationships between fault zones associated with H_2S recharge points (feeders) and through-going FCZ; B) at the scale of the fold-and-thrust belt, localization of sulfuric acid speleogenesis is controlled by the presence of buried H_2S sources, deep-rooted permeability pathways (like tear fault zones), and their connectivity with the highly-persistent fracture networks along the anticline hinge. Diagram in box 'B' modified after Watkins et al. (2015).

2.1.5.3. Prediction of sulfuric hypogene caves in fold-and-thrust belts: implications for carbonate reservoirs

The issues regarding predictive models for karst features in the subsurface are a main (and yet poorly investigated) problem for the oil industry and, in general, for the whole applied geoscience community. Karst features in carbonate reservoirs provide multiple storage space with variable geometry, and this causes strong heterogeneity in porosity distribution and complex flow characteristics (Lyu et al., 2020). Furthermore, their prediction is usually critical, because of their sub-seismic scale.

Hypogene caves in carbonate units, generated by deep fluids rising along steep cross-formational fractures, have been described in other settings (Klimchouk, 2007; Audra et al., 2009; Klimchouk, 2017; Balsamo et al., 2020; Bertotti et al., 2020), and especially in fold-and-thrust belts of the Central and Northern Apennines (Galdenzi and Menichetti, 1995; Galdenzi et al., 2010; Galdenzi and Menichetti, 2017; D'Angeli et al., 2019a). Such caves highlight the local development of karst macro-scale porosity focused along the guiding subvertical discontinuities where deep fluids are mixing with oxygenated shallow aquifers.

Migration of rising aggressive fluids towards the upper crust, with the associated possibility of hypogene speleogenesis, has been commonly observed associated with deep-rooted structures like strike-slip or reverse faults (Nosike, 2009; Hobléa et al., 2010). These structural elements represent ideal features that can connect different reservoirs, promoting vertical flow, and, thereby, the localization of karstification (Bertotti et al., 2020). In the Taranta Valley, we found that strike-slip fault zones segmenting the thrust front were the main guiding features for paleo fluid flow and, therefore, their occurrence is a first order prerequisite (and consequently a prediction element) for hypogene cave development in the Majella Massif. However, the susceptibility to develop this kind of caves also requires available aggressive H_2S sources and sufficient time for mixing with oxygenated water.

The structural and geological setting observed in several thrust sheets of the Apennines, with buried sources of hydrocarbons and/or evaporitic units (Triassic anhydrites) that can contribute to the formation of H_2S-rich solutions, make this region a perfect site for SAS (D'Angeli et al., 2019a). Examples of numerous and different sulfuric hypogene caves in the Apennine chain strengthen the results discussed in this paper, and the predictive power of fracture networks typically found in fold-and-thrust belts to localize hypogene karstification.

In the Frasassi gorge, Rio Garrafo and Mt. Cucco areas, more than 50 km of sulfuric hypogene cave passages have been carved following fracture networks in hinge zones and forelimbs of thrust-related anticlines developed during Pliocene-Pleistocene (Galdenzi and Menichetti, 1995; Galdenzi et al., 2010). As in the CBS, inlets of sulfidic fluids (feeders) are concentrated along steep fault zones, which channelized H_2S towards the shallow groundwater, where it oxidizes into H_2SO_4 tending immediately to corrode carbonate and produce typical water-table cave levels. The main passages of these caves are sub-horizontal conduits whose dimension is controlled by: (1) duration of the water-table remaining stable at the same elevation, which is directly influenced by the general geomorphic evolution of the area; and (2) the intensity of corrosion, which depends on the location (feeder) of the rising flow, the relative distance from the rising points, and the time scale when such fluids were active. The pattern of these caves is usually maze or ramiform (Palmer, 1991), with networks of individual conduits following bedding planes and open fractures in a fashion similar to what described in many places worldwide (Klimchouk, 2009; Ennes-Silva et al., 2016; Klimchouk et al., 2016; Balsamo et al., 2020).

In low primary porosity and permeability units, like tight limestones or dolostones, open fracture networks are expected to be the most significant permeability pathways for rising fluids from the subsurface. Our results suggest that identification of fault zones characterized by highly deformed damage zones (high permeability domains), vertically connected with deep-rooted H_2S-conductive structures, may be used to predict the presence of multiple feeders of corrosive geofluids (Fig. 16). In order to assess the hydraulic conductivity of fault zones, however, a detailed structural analysis, which helps to identify high-vs. low-permeability domains within the same fault's architecture, is required (Billi et al., 2003; Agosta et al., 2009; Matonti et al., 2012). Scaling-laws and models to quantify the intensity and distribution of open fractures associated to fault growth mechanisms (Billi et al., 2003; La Bruna et al., 2018; Torabi et al., 2019) are needed to predict the hydraulic conductivity of fault zones in carbonate reservoirs, and could be integrated with the structural and geomorphological field evidence we documented in the Majella Massif to evaluate the susceptibility to karstification at a regional-scale.

At the same time, the stratigraphic setting may hamper or boost fracture development, with significant changes controlled by mechanical stratigraphy (Balsamo et al., 2020), which should be taken into consideration for characterizing the spatial and functional organization of caves, and for the detailed prediction of conduits geometry.

Finally, we stress that clustering of open and through-going fractures (FCZ) strongly affect permeability and fluid circulation with consequent sub-horizontal karstification at each specific water-table level. In the CBS, this localized fracture-controlled dissolution model guided the development of an elongated pattern of single master conduits (Figs. 15 and 16) rather than maze or ramiform networks. Although with a possible degree of specificity and local variability, the CBS pattern and spatial-morphological organization represent an analog that can be implemented in carbonate reservoirs models to predict sulfuric acid hypogene karstification in fold-and-thrust belts with deep H_2S sources.

2.1.6. Conclusions

Detailed structural analysis and geological mapping allowed us to reconstruct the deformation phases affecting the southeastern sector of the Majella Massif. Reconstructing the deformation events and associated structural assemblages is crucial to evaluate timing of nucleation (and spatial organization) of the potential permeable pathways allowing flow of acidic fluids and consequent fluid-rock interaction (speleogenesis).

Our results can be summarized as follow:

1. The structural assemblages in the southeastern Majella consist of a complex network of pre-orogenic normal faults (F1 and F2), strike-slip faults and their associated splays (F3 and F4), and late-orogenic normal faults (F5) developed on pre-existent fractures formed during flexural slip. Pre-existing pressure solution seams (PSS) played a critical role for layering definition and opening-/shearing-mode fracturing during the contractional phases.
2. Fault networks consist of barrier-conduit structures with high-permeability domains localized in the pervasively fractured damage zones and along slip surfaces. Fault cores characterized by indurated fault breccia or recrystallized/cataclastic fault rocks acted as low-permeability domains (barriers) for fluid flow. Cores with pervasive fragmentation or composite chaotic breccia may represent conduits for fluid flow.
3. Sulfuric acid speleogenesis was triggered by cross-formational H_2S flow from depth (Triassic evaporites interacting with hydrocarbons). Ascending acidic fluids were channelized in the damage zones of deep-rooted tear faults linked with pre-orogenic normal faults, that acted as multiple discharge feeders.
4. Sulfuric acid speleogenesis generated a network of sub-horizontal conduits with an elongated and angular pattern. Lateral dissolution close to the water-table was focused on bedding interfaces and through-going fracture cluster zones (FCZ) formed along the anticline hinge. Localized deformation producing high-apertures and

through-going fracture clusters, rather than background structures (strata bound veins and pressure solution seams), exert the main control on flow pathways and karst dissolution.

5. Detailed structural analysis integrated with an exhaustive interpretation of cave morphologies represent a first order tool for prediction of hypogene karstification and its spatial organization in fold-and-thrust belts.

Acknowledgements

We sincerely thank "*Parco Nazionale della Majella*", "Cooperativa Majella" and the municipalities of Taranta Peligna and Lama dei Peligni for the access to the caves and the special permission for taking rock samples. We also thank Giuseppe (Pino) Antonini, Leonardo Del Sole, Maria Nagostinis, Alessandro Marraffa, Samuele Curzio, and Nevio Preti for their help during field work and logistics; Claudio Busi for the use of the high-resolution photographic scanner; Paolo Forti and Fernando Gázquez for the useful discussions about the organic-impregnated black speleothems; Giulio Viola and Paolo Garofalo for the access to the optical microscopy laboratory (University of Bologna); Fabio Gamberini for thin sections preparation. Finally we thank Arthur Lavenu and one anonymous reviewer for their helpful suggestions that permit to improve the final version of the manuscript.

This research did not receive any specific grant from funding agencies in the public, commercial, or not-for-profit sectors.

References

Accarie, H., Beaudoin, B., Cussey, R., Joseph, P., Triboulet, S., 1986. Dynamique sédimentaire et structurale au passage plate-forme/bassin. Les faciès carbonatés Cretacés du massif de la Maiella (Abruzzes, Italie). Memorie della Società Geologica Italiana 36, 217–231.

Agosta, F., Alessandroni, M., Tondi, E., Aydin, A., 2009. Oblique normal faulting along the northern edge of the Majella Anticline, central Italy: Inferences on hydrocarbon migration and accumulation. Journal of Structural Geology 31, 674–690.

Albert, G., Virág, M., Erőss, A., 2015. Karst porosity estimations from archive cave surveys studies in the Buda Thermal Karst System (Hungary). International Journal of Speleology 44, 151–165.

Allmendinger, R.W., Cardozo, N., Fisher, D., 2012. Structural Geology Algorithms: Vectors and Tensors in Structural Geology. Cambridge University Press, UK.

Antonellini, M., Aydin, A., 1994. Effect of faulting on fluid flow in porous sandstones: petrophysical properties. AAPG Bulletin 78, 355–377.

Antonellini, M., Tondi, E., Agosta, F., Aydin, A., Cello, G., 2008. Failure modes in deep- water carbonates and their impact for fault development: Majella Mountain, Central Apennines, Italy. Marine and Petroleum Geology 25 (10), 1074–1096.

Antonellini, M., Nannoni, A., Vigna, B., De Waele, J., 2019. Structural control on karst water circulation and speleogenesis in a lithological contact zone: The Bossea cave system (Western Alps, Italy). Geomorphology 345, 106832.

Araújo, R.E.B., La Bruna, V., Rustichelli, A., Bezerra, F.H.R., Xavier, M.M., Audra, P., Barbosa, J.A., Antonino, A.C.D., 2021. Structural and sedimentary discontinuities control the generation of karst dissolution cavities in a carbonate sequence, Potiguar Basin, Brazil. Marine and Petroleum Geology 123, 104753.

Audra, P., Mocochain, L., Bigot, J.Y., Nobecourt, J.C., 2009. Hypogene cave patterns. In: Klimchouk, A.B., Ford, D.C. (Eds.), Hypogene speleogenesis and karst hydrogeology of artesian basins. Ukrainian Institute of Speleology and Karstology, Special Paper 1, 17-22.

Auler, A.S., Smart, P.L., 2003. The influence of bedrock-derived acidity in the development of surface and underground karst: evidence from the Precambrian carbonates of semi-arid northeastern Brazil. Earth Surface Processes and Landforms 28, 157–168.

Avouac, J.P., Meyer, B., Tapponnier, P., 1992. On the growth of normal faults and the existence of flats and ramps along the El-Asnam active fold-and-thrust. Tectonics 11, 1–11.

Aydin, A., Antonellini, M., Tondi, E., Agosta, F., 2010. Deformation along the leading edge of the Maiella thrust sheet in central Italy. Journal of Structural Geology 32, 1291–1304.

Bagni, F.L., Bezerra, F.H., Balsamo, F., Maia, R.P., Dall'Aglio, M., 2020. Karst dissolution along fracture corridors in an anticline hinge, Jandaíra Formation, Brazil: Implications for reservoir quality. Marine and Petroleum Geology 115, 104249.

Ball, C.K., Jones, J.C., 1990. Speleogenesis in the limestone outcrop north of the South Wales Coalfield: the role of microorganisms in the oxidation of sulphides and hydrocarbons. Cave Science 17, 3–8.

Bally, A.W., Burbi, L., Cooper, C., Ghelardoni, R., 1988. Balanced sections and seismic reflection profiles across the central Apennines. Memorie della Società Geologica Italiana 35, 257–310.

Balsamo, F., Bezerra, F.H.R., Klimchouk, A.B., Cazarin, C.L., Auler, A.S., Nogueira, F.C., Pontes, C., 2020. Influence of fracture stratigraphy on hypogene cave development and fluid flow anisotropy in layered carbonates, NE Brazil. Marine and Petroleum Geology 114, 104207.

Bertotti, G., Audra, P., Auler, A., Bezerra, F.H., de Hoop, S., Pontes, C., Prabhakaran, R., Lima, R., 2020. The Morro Vermelho hypogenic karst system (Brazil): Stratigraphy, fractures, and flow in a carbonate strike-slip fault zone with implications for carbonate reservoirs. AAPG Bulletin 104, 2029–2050.

Billi, A., Salvini, F., Storti, F., 2003. The damage zone - fault core transition in carbonate rocks: Implications for fault growth, structure and permeability. Journal of Structural Geology 25, 1779–1794.

Boersma, Q., Prabhakaran, R., Bezerra, F.H., Bertotti, G., 2019. Linking natural fractures to karst cave development: a case study combining drone imagery, a natural cave network and numerical modelling. Petroleum Geoscience 25 (4), 454-469.

Braathen, A., Osmundsen, P.T., Gabrielsen, R.H., 2004. Dynamic development of fault rocks in a crustal-scale detachment: An example from western Norway. Tectonics 23, 1–21.

Brandano, M., Scrocca, D., Lipparini, L., Petracchini, L., Tomassetti, L., Campagnoni, V., Meloni, D., Mascaro, G., 2013. Physical stratigraphy and tectonic settings of Bolognano Formation (Majella): A potential carbonate reservoir. Journal of Mediterranean Earth Sciences 5, 151–176.

Bruna, P.O., Lavenu, A.P.C., Matonti, C., Bertotti, G., 2019. Are stylolites fluid-flow efficient features? Journal of Structural Geology 125, 270–277.

Caine, J.S., Evans, J.P., Forster, C.B., 1996. Fault zone architecture and permeability structure. Geology, 24, 1025-1028.

Calamita, F., Scisciani, V., Montefalcone, R., Paltrinieri, W., Pizzi, A., 2002. L'ereditarietà del paleomargine dell'Adria nella geometria del sistema orogenico centro-appenninico: l'area abruzzese esterna. Memorie della Società Geologica Italiana 57, 355-368.

Casabianca, D., Bosence, D., Beckett, D., 2002. Reservoir potential of Cretaceous platform margin breccias, central Italian Apennines. Journal of Petroleum Geology 25 (2), 179–202.

Casabianca, D., Auzemery, A., Barrier, A., Ricciato, A., Borello, S., Lecardez, A., Di Cuia, R., 2020. Latest fold and thrust tectonics conceals extensional structures inherited from Cretaceous syn-sedimentary deformation: insights for exploration in fold-and-thrust belts from the Maiella Mountain. Geological Society of London Special Publication 490.

Cazarin, C.L., Bezerra, F.H.R., Borghi, L., Santos, R. V., Favoreto, J., Brod, J.A., Auler, A.S., Srivastava, N.K., 2019. The conduit-seal system of hypogene karst in Neoproterozoic carbonates in northeastern Brazil. Marine and Petroleum Geology 101, 90–107.

Cooke, M.L., 1997. Fracture localization along faults with spatially varying friction, Journal of Geophysical Research 102 (22), 425–434.

Cornacchia, I., Brandano, M., Raffi, I., Tomassetti, L., Flores, I., 2018. The Eocene–Oligocene transition in the C-isotope record of the carbonate successions in the Central Mediterranean. Global and Planetary Change 167, 110–122.

Cosentino, D., Cipollari, P., Lo Mastro, S., Giampaolo, C., 2005. High-frequency cyclicity in the latest Messinian Adriatic foreland basin: Insight into palaeoclimate and palaeoenvironments of the Mediterranean Lago-Mare episode. Sedimentary Geology 178, 31–53.

Crescenti, U., Crostella, A., Donzelli, G., Raffi, G. 1969. Stratigrafia della serie calcarea dal Lias al Miocene nella regione Marchigiano Abruzzese. (Parte II – Litostratigrafia, biostratigrafia, paleogeografia). Memorie della Società Geologica Italiana 9, 343–420.

Curl, R., 1986. Fractal dimensions and geometries of caves. Mathematical Geology 18, 765-783.

D'Angeli, I.M., Carbone, C., Nagostinis, M., Parise, M., Vattano, M., Madonia, G., De Waele, J., 2018. New insights on secondary minerals from Italian sulfuric acid caves. International Journal of Speleology 47 (3), 271–291.

D'Angeli, I.M., Parise, M., Vattano, M., Madonia, G., Galdenzi, S., De Waele, J., 2019a. Sulfuric acid caves of Italy: a review. Geomorphology 333, 105–122.

D’Angeli, I.M., Nagostinis, M., Carbone, C., Bernasconi, S.M., Polyak, V.J., Peters, L., McIntosh, W.C., De Waele, J., 2019b. Sulfuric acid speleogenesis in the Majella Massif (Abruzzo, Central Apennines, Italy). Geomorphology 333, 167–179.

De Joussineau, G., O. Mutlu, A. Aydin, D.D. Pollard, 2007. Characterization of strike-slip fault–splay relationships in sandstone. Journal of Structural Geology 29, 1831–1842.

De Waele, J., Audra, P., Madonia, G., Vattano, M., Plan, L., D'Angeli, I. M., Bigot, J.-Y., Nobécourt, J. C., 2016. Sulfuric acid speleogenesis (SAS) close to the water table: examples from southern France, Austria, and Sicily. Geomorphology 253, 452-467.

De Waele, J., Galdenzi, S., Madonia, G., Menichetti, M., Parise, M., Piccini, L., Sanna, L., Sauro, F., Tognini, P., Vattano, M., Vigna, B., 2014. A review on hypogene caves in Italy. In: Klimchouk, A.B., Sasowsky, I.D., Mylroie, J.R., Summers Engel, A., Engel, A.S. (Eds.), Hypogene Cave Morphologies. Karst Waters Institute Special Publication 18. Leesburg, Virginia, 28–30.

Di Cuia, R., Shakerley, A., Masini, M., Casabianca, D., 2009. Integrating outcrop data at different scales to describe fractured carbonate reservoirs: example of the Maiella carbonates, Italy. First Break 27, 45–55.

Di Domenica, A., Pizzi, A., 2017. Defining a mid-Holocene earthquake through speleoseismological and independent data: Implications for the outer Central Apennines (Italy) seismotectonic framework. Solid Earth 8, 161–176.

DuChene, H., Palmer, A.N., Palmer, M.V., Queen, J.M., Polyak, V.J., Decker, D.D., Hill, C.A., Spilde, M., Burger, P.A., Kirkland, D.W., Boston, P., 2017. Hypogene Speleogenesis in the Guadalupe Mountains, New Mexico and Texas, USA. In: Klimchouk, A.B., Audra, P., Palmer, A.N., De Waele, J., Auler, A. (Eds.), Hypogene Karst Regions and Caves of the World, 511-530. Springer: Cham (Switzerland).

Dunham, R., 1962. Classification of carbonate rocks according to depositional textures. In: In: Ham, W.E. (Ed.), Classification of Carbonate Rocks, vol. 1. American Association of Petroleum Geologists, 108–121.

Eberli, G.P., Bernoulli, D., Vecsei, A., Sekti, R., Grasmueck, M., Lüdmann, T., Anselmetti, F.S., Mutti, M., Della Porta, G., 2019. A Cretaceous carbonate delta drift in the Montagna della Maiella, Italy. Sedimentology 66, 1266–1301.

Egemeier, S.J., 1981. Cavern development by thermal waters. NSS Bulletin 43, 31–51.

Embry, A.F., Klovan, J.E., 1971. A late Devonian reef tract on northeastern Banks Insland, Bulletin of Canadian Petroleum Geology 19 (4), 730–781.

Ennes-Silva, R.A., Bezerra, F.H., Nogueira, F.C., Balsamo, F., Klimchouk, A., Cazarin, C.L., Auler, A.S., 2016. Superposed folding and associated fracturing influence hypogene karst development in Neoproterozoic carbonates, São Francisco Craton, Brazil. Tectonophysics 666, 244–259.

Festa, A., Accotto, C., Coscarelli, F., Malerba, E., Palazzin, G., 2014. Geology of the Aventino River Valley (eastern Majella, central Italy). Journal of Maps 10, 584–599.

Fletcher, R.C., Pollard, D.D., 1981. Anticrack model for pressure solution surfaces. Geology 9, 419–424.

Florez-Niño, J.M., Aydin, A., Mavko, G., Antonellini, M., Ayaviri, A., 2005. Fault and fracture systems in a fold and thrust belt. An example from Bolivia. AAPG Bulletin 89 (4), 471–493.

Ford, D.C., Williams, P.W., 2007. Karst Hydrogeology and Geomorphology. John Wiley and sons, Chichester.

Galdenzi, S., Cocchioni, F., Filipponi, G., Morichetti, L., Scuri, S., Selvaggio, R., Cocchioni, M., 2010. The sulfidic thermal caves of Acquasanta Terme (central Italy). Journal of Cave and Karst Studies 72 (1), 43–58.

Galdenzi, S., Maruoka, T., 2003. Gypsum deposits in the Frasassi Caves, central Italy. Journal of Cave and Karst Studies 65 (2), 111-125.

Galdenzi, S., Menichetti, M., 1995. Occurrence of hypogenic caves in a karst region: examples from central Italy. Environmental Geology 26, 39-47.

Galdenzi, S., Menichetti, M., 2017. Hypogenic Caves in the Apennine Mountains (Italy). In: Klimchouk, A.B., Audra, P., Palmer, A.N., De Waele, J., Auler, A. (Eds.), Hypogene Karst Regions and Caves of the World, 127-142. Springer: Cham (Switzerland).

Gerali, F., Lipparini, L., 2018. Maiella, an oil massif in the Central Apennines ridge of Italy: Exploration, production and innovation in the oil fields of Abruzzo across the nineteenth and twentieth centuries. Geological Society of London Special Publication 465, 275–303.

Ghisetti, F., Vezzani, L. 1997. Interfering paths of deformation and development of arcs in the fold-and-thrust belt of the central Apennines (Italy). Tectonics 16, 523-536.

Ghisetti, F. Vezzani, L. 1998. Segmentation and tectonic evolution of the Abruzzi-Molise thrust belt (central Apennines, Italy). Annales Tectonicae 12, 97-112.

Ghisetti, F., Vezzani, L., 2002. Normal faulting, extension and uplift in the outer thrust belt of the central Apennines (Italy): Role of the Caramanico fault. Basin Research 14, 225–236.

Giuffrida, A., Agosta, F., Rustichelli, A., Panza, E., La Bruna, V., Eriksson, M., Torrieri, S., Giorgioni, M., 2020. Fracture stratigraphy and DFN modelling of tight carbonates, the case study of the Lower Cretaceous carbonates exposed at the Monte Alpi (Basilicata, Italy). Marine and Petroleum Geology 112, 104045.

Gholipour, A.M., Cosgrove, J.W., Ala, M., 2016. New theoretical model for predicting and modelling fractures in folded fractured reservoirs. Petroleum Geoscience 22 (3), 257-280.

Graham, B., Antonellini, M., Aydin, A., 2003. Formation and growth of normal faults in carbonates within a compressive environment. Geology 31, 11-14.

Graham-Wall, B., Girgacea, R., Mesonjesi, A., Aydin, A., 2006. Evolution of fluid pathways through fracture controlled faults in carbonates of the Albanides fold-thrust belt. American AAPG Bulletin 90, 1227–1249.

Grove, C., Jerram, D.A., 2011. JPOR: An ImageJ macro to quantify total optical porosity from blue-stained thin sections. Computers and Geosciences 37, 1850–1859.

Gutiérrez, F., Parise, M., De Waele, J., Jourde, H., 2014. A review on natural and human-induced geohazards and impacts in karst. Earth-Science Reviews 138, 61-88.

Heeb, B., 2009. An all-in-one electronic cave surveying device. Cave Radio & Electronics Group Journal 72, 8–10.

Higgins, M.W., 1971. Cataclastic rocks. U.S. Geol. Surv. Prof. Pap. 687, 1-97.

Hill, C.A., 1990. Sulfuric acid speleogenesis of Carlsbad Cavern and its relationship to hydrocarbons, Delaware Basin, New Mexico and Texas. AAPG Bulletin 74, 1685–1694.

Hill, C.A., 1995. Sulfur redox reactions: hydrocarbons, native sulfur, Mississippi Valley-type deposits, and sulfuric acid karst in the Delaware Basin, New Mexico and Texas. Environmental Geology 25, 16–23.

Hobléa, F., Gallino-Josnin, S., Audra, P., 2010. Genesis and functioning of the Aix-les-Bains hydrothermal karst (Savoie, France): past research and recent advances. Bulletin de la Société Géologique de France 181, 315−326.

Jolley, S.J., Barr, D., Walsh, J.J., Knipe, R.J., 2007. Structurally complex reservoirs: an introduction. Geol. Soc. London Spec. Publ. 292, 1–24.

Klimchouk, A.B., 2007. Hypogene speleogenesis. Hydrogeological and morphogenetic perspective. NCKRI Special Paper Series, 1, National Cave and Karst Research Institute, 77.

Klimchouk, A.B., 2009. Morphogenesis of hypogenic caves. Geomorphology 106, 100–117.

Klimchouk, A.B., 2012. Speleogenesis, hypogenic. In: White, W.B., Culver, D.C. (Eds.), Encyclopedia of Caves, 2nd edition Elsevier, Academic Press, Chennai, 748–765.

Klimchouk, A.B., 2017. Type and settings of hypogene karst. In: Palmer, A.N., De Waele, J., Auler, A., Audra, P. (Eds.), Hypogene karst region and caves of the world, 1-39.

Klimchouk, A.B., Auler, A.S., Bezerra, F.H., Cazarin, C.L., Balsamo, F., Dublyansky, Y., 2016. Hypogenic origin, geologic controls and functional organization of a giant cave system in Precambrian carbonates, Brazil. Geomorphology 253, 385–405.

La Bruna, V., Agosta, F., Lamarche, J., Viseur, S., Prosser, G., 2018. Fault growth mechanisms and scaling properties in foreland basin system: The case study of Monte Alpi, Southern Apennines, Italy. Journal of Structural Geology, 116. 94–113.

Lampert, S.A., Lowrie, W., Hirt, A.M., Bernoulli, D., Mutti, M., 1997. Magnetic and sequence stratigraphy of redeposited upper Cretaceous limestones in the Montagna della Maiella, Abruzzi, Italy. Earth and Planetary Sciences Letters 150, 79–93.

Lavenu, A.P.C., Lamarche, J., Salardon, R., Gallois, A., Marié, L., Gauthier, B.D.M., 2014. Relating background fractures to diagenesis and rock physical properties in a platform-slope transect. Example of the Maiella Mountain (central Italy). Marine and Petroleum Geology 51, 2–19.

Lipparini, L., Trippetta, F., Ruggieri, R., Brandano, M., Romi, A., 2018. Oil distribution in outcropping carbonate-ramp reservoirs (Maiella Mountain, Central Italy): Three-dimensional models constrained by dense historical well data and laboratory measurements. AAPG Bulletin 102 (7), 1273-1298.

Lyu, X., Zhu, G., Liu, Z., 2020. Well-controlled dynamic hydrocarbon reserves calculation of fracture–cavity karst carbonate reservoirs based on production data analysis. Journal of Petroleum Exploration and Production Technology 10, 2401–2410.

Ma, L., Dowey, P. J., Rutter, E., Taylor, K. G., Lee, P. D., 2019. A novel upscaling procedure for characterising heterogeneous shale porosity from nanometer-to millimetre-scale in 3D. Energy 181, 1285–1297.

Machel, H.G., 2001. Bacterial and thermochemical sulfate reduction in diagenetic setting: old and new insights. Sedimentary Geology 140, 143-175.

Marchegiani, L., Van Dijk, J.P., Gillespie, P.A., Tondi, E., Cello, G., 2006. Scaling properties of the dimensional and spatial characteristics of fault and fracture systems in the Majella Mountain, central Italy. Geological Society of London Special Publication 261, 113-131.

Masini, M., Bigi, S., Poblet, J., Bulnes, M., Di Cuia, R., Casabianca, D., 2011. Kinematic evolution and strain simulation, based on cross-section restoration, of the Maiella Mountain: an analogue for oil fields in the Apennines (Italy). Geological Society of London Special Publication 349, 25–44.

Matonti, C., Lamarche, J., Guglielmi, Y., Marié, L., 2012. Structural and petrophysical characterization of mixed conduit/seal fault zones in carbonates: example from the Castellas fault (SE France). Journal of Structural Geology 39, 103-121.

Michie, E.A.H., 2015. Influence of host lithofacies on fault rock variation in carbonate fault zones: A case study from the Island of Malta. Journal of Structural Geology 76, 61–79.

Montaron, B., 2008. Confronting carbonates. Oil Review Middle East 5, 132–135.

Nosike, L., 2009. Relationship between tectonics and vertical hydrocarbon leakage: a case study of the deep off-shore Niger Delta. PhD thesis, University of Nice-Sophia Antipolis, 281.

Ori, G.G., Roveri, M., Vannoni, F., 1986. Plio-Pleistocene sedimentation in the Apennine–Adriatic foredeep (central Adriatic Sea, Italy). In: Allen, P.A., Homewood, P. (Eds.), Foreland Basins. Blackwell, Oxford, 183–198.

Ortega, O.J., Marrett, R.A., Laubach, S.E., 2006. A scale-independent approach to fracture intensity and average spacing measurement. AAPG Bulletin 90, 193–208.

Palmer, A.N., 1990. Ground water processes in karst terranes. In: Higgins, C.G., Coates, D.R. (Eds). Groundwater Geomorphology. Geological Society of America Special Publication 252, 177–209.

Palmer, A.N., 1991. Origin and morphology of limestone caves. Geological Society of America Bulletin 103, 1–21.

Palmer, A.N., 2000. Hydrogeologic control of cave patterns. In: Klimchouk, A., Ford, D.C., Palmer, A.N., Dreybrodt, W. (Eds.), Speleogenesis: Evolution of Karst Aquifers, 77-90. National Speleological Society: Huntsville (AL).

Palmer, A.N., 2007. Cave Geology. In: Cave Books, Dayton, OH, 454.

Peacock, D.C.P., Nixon, C.W., Rotevatn, A., Sanderson, D.J., Zuluaga, L.F., 2016. Glossary of fault and other fracture networks. Journal of Structural Geology 92, 12–29.

Peacock, D.C.P., Dimmen, V., Rotevatn, A., Sanderson, D.J., 2017. A broader classification of damage zones. Journal of Structural Geology 102, 179-192.

Peacock, D.C.P., Sanderson, D.J., 2018. Structural analyses and fracture network characterisation: seven pillars of wisdom. Earth-Science Reviews 184, 13-28.

Peacock, D.C.P., Sanderson, D.J., Rotevatn, A., 2018. Relationships between fractures. Journal of Structural Geology 106, 41-53.

Pisani, L., Antonellini, M., De Waele, J., 2019. Structural control on epigenic gypsum caves: evidences from Messinian evaporites (Northern Apennines, Italy). Geomorphology 332, 170–186.

Pizzi, A. 2003. Plio-Quaternary uplift rates in the outer zone of the central Apennine fold-and-thrust belt, Italy. Quaternary International 101-102 (1), 229-237.

Pizzi, A., Falcucci, E., Gori, S., Galadini, F., Messina, P., Di Vicenzo, M., Esestime, P., Giaccio, B., Pomposo, G., Sposato, A., 2010. Active faulting in the Maiella Massif (central Apennines, Italy). GeoActa Special Publication 3, 57–73.

Pollard, D., Aydin, A., 1988. Progress in understanding jointing over the past century. Geological Society of America Bulletin 100, 1181–1204.

Polyak, V. J., Provencio, P., 2001. By-product materials related to H_2S-H_2SO_4 influenced speleogenesis of Carlsbad, Lechuguilla, and other caves of the Guadalupe Mountains, New Mexico. Journal of Cave and Karst Studies 63 (1), 23-32.

Proctor, J. M., Droxler, A. W., Derzhi, N., Hopson, H. H., Harris, P.M., Khanna, P., Lehrmann, D. J., 2019. Upscaling lithology and porosity-type fractions from the micro- to the core-scale with thin-section petrography, dual-energy computed tomography, and rock typing: creation of diagenesis and porosity-type logs. Interpretation 7 (1), 9-32.

Rispoli, R., 1981. Stress field about strike-slip faults inferred from stylolites and tension gashes. Tectonophysics 75, 29–36.

Roure, F., Casero, P., Vially, R., 1991. Growth-processes and mélange formation in the southern Apennines accretionary wedge. Earth and Planetary Sciences Letters 102, 395–412.

Rustichelli, A. 2010. Mechanical stratigraphy of carbonate rocks: examples from the Maiella Mountain (Central Italy) and the Granada Basin (Southern Spain). PhD thesis, Università degli Studi di Camerino, 185.

Rustichelli, A., Torrieri, S., Tondi, E., Laurita, S., Strauss, C., Agosta, F., Balsamo, F., 2016. Fracture characteristics in Cretaceous platform and overlying ramp carbonates: An outcrop study from Maiella Mountain (central Italy). Marine and Petroleum Geology 76, 68–87.

Sauro, F., Mecchia, M., Tringham, M., Arbenz, T., Columbu, A., Carbone, C., Pisani, L., De Waele, J., 2020. Speleogenesis of the world's longest cave in hybrid arenites (Krem Puri, Meghalaya, India). Geomorphology 359, 107160.

Schneider, C. A., Rasband, W. S., Eliceiri, K.W., 2012. NIH Image to ImageJ: 25 years of image analysis. Nature Methods 9, 671–675.

Schultz, R., 2019. Geologic Fracture Mechanics. Cambridge: Cambridge University Press.

Scisciani, V., Tavarnelli, E., Calamita, F., 2002. The interaction of extensional and contractional deformation in the outer zones of the Central Apennines, Italy. Journal of Structural Geology 24, 1647–1658.

Sibson, R.H., 1977. Fault rocks and fault mechanisms. Journal of the Geological Society of London 133, 191–213.

Stafford, K. W., Klimchouk, A., Land, L., Gary, M. O., 2009. The Pecos River hypogene speleogenetic province: a basin-scale karst paradigm for eastern New Mexico and west Texas, USA. In: Land, L., Stafford, K. W., Veni, G. (Eds.). Advances in Hypogene Karst Studies, 121-135. National Cave and Karst Research Institute: Carlsbad (NM).

Tavani, S., Storti, F., Bausà, J., Muñoz, J.A., 2012. Late thrusting extensional collapse at the mountain front of the Northern Apennines (Italy). Tectonics 31, TC4019.

Tavani, S., Snidero, M., Muñoz, J.A., 2014. Uplift-induced residual strain release and late-thrusting extension in the Anaran mountain front anticline, Zagros (Iran). Tectonophysics 636, 257-269.

Tisato, N., Sauro, F., Bernasconi, S. M., Bruijn, R. H., De Waele, J., 2012. Hypogenic contribution to speleogenesis in a predominant epigenic karst system: a case study from the Venetian Alps, Italy. Geomorphology 151, 156-163.

Tondi, E., Cello, G., 2003. Spatiotemporal evolution of the central Apennines fault system (Italy). Journal of Geodynamics. 36, 113–128.

Tondi, E., Antonellini, M., Aydin, A., Marchegiani, L., Cello, G., 2006. The roles of de- formation bands and pressure solution seams in fault development in carbonate grainstones in the Majella Mountain. Journal of Structural Geology 28, 376–391.

Torabi, A., Ellingsen, T.S.S., Johannessen, M.U., Alaei, B., Rotevatn, A., Chiarella, D., 2019. Fault zone architecture and its scaling laws: where does the damage zone start and stop? Geological Society of London Special Publication 496, 99-124.

Vecsei, A., 1991. Aggradation und Progradation eines karbonatplatform-Randes: Kreide bis Mittleres Tertiar der Montagna della Maiella. In: Mitt. Geol. Inst. Eidg. Techn. Hochsch. Univ. Zürich, Abruzzen, Neue Folge, 294.

Vecsei, A., Sanders, D., Bernoulli, D., Eberli, G., Pignatti, J.S., 1998. Evolution and sequence stratigraphy of the Maiella platform margin, Late Jurassic to Miocene, Italy. In: De Graciansky, P.Ch. Hardebol, J., Jacquin, Th., Vail, P.R. (Eds.), Mesozoic-Cenozoic Sequence Stratigraphy of Western European Basins. Society of Economic Paleontologists and Mineralogists, 121–135.

Watkins, H., Butler, R.W.H., Bond, C.E., Healy, D., 2015. Influence of structural position on fracture networks in the Torridon Group, Achnashellach fold and thrust belt, NW Scotland. Journal of Structural Geology 74, 64–80.

Webb, J.A., 2020. Supergene sulphuric acid speleogenesis and the origin of hypogene caves: evidence from the Northern Pennines, UK. Earth Surf. Process. Landforms 46, 455–464.

Worthington, S.R.H., Ford, D.C., Beddows, P.A., 2000. Porosity and permeability enhancement in unconfined carbonate aquifers as a result of solution. In: Klimchouk, A., Ford, D., Palmer, A., Dreybrodt, W. (Eds.). Speleogenesis: evolution of karst aquifers. Huntsville, National Speleological Society, 463-472.

2.2

Published in Journal of Structural Geology (2021)

https://doi.org/10.1016/j.jsg.2021.104324146

Flow pathways in multiple-direction fold hinges: Implications for fractured and karstified carbonate reservoirs

---

Cayo C.C. PONTES[1*], Francisco H.R. BEZERRA[1], Giovanni BERTOTTI[2], Vincenzo LA BRUNA[1], Philippe AUDRA[3], Jo DE WAELE[4], Augusto S. AULER[5], Fabrizio BALSAMO[6], Stephan DE HOOP[2], Luca PISANI[4]

1 Department of Geology, Federal University of Rio Grande do Norte, Natal, Brazil

2 Department of Geoscience and Engineering, Delft University of Technology, Delft, The Netherlands

3 Polytech'Lab EA 7498, University Côte d'Azur, France

4 Bologna University, Department of Biological, Geological and Environmental Sciences, Via Zamboni 67, 40126 Bologna, Italy

5 Instituto do Carste, Carste Ciência e Meio Ambiente, Belo Horizonte, Brazil

6 Department of Chemistry, Life Sciences and Environmental Sustainability, University of Parma, Italy

* Corresponding author

Abstract

Caves developed in carbonate units have a significant role in fluid flow, but most of these subsurface voids are below seismic resolution. We concentrated our study on four caves to determine the roles of fractures and folds in the development of karst conduits that may form flow pathways in carbonate reservoirs. We performed structural field investigations, petrographic analyses, and geometric characterization using Light Detection and Ranging (LIDAR) for caves in Neoproterozoic carbonates of the Salitre Formation, central part of the São Francisco Craton, Brazil. We found that the conduit shape, usually with an ellipsoidal cross-section, reflects the tectonic features and textural variations. Carbonate layers containing pyrite and low detritic mineral contents are generally karstified and appear to act as favorable flow pathways. Our results indicate that the development of the karst system is related to fracture corridors formed along parallel and orthogonal sets of fold hinges, which provide preferential pathways for fluid flow and contribute to the development of super-K zones. This study provides insights into the prediction of subseismic-

scale voids in carbonate reservoirs, with direct application for the hydrocarbon and hydrogeology flow and storage.

Key Words

Fracture corridors; Hypogene karst conduits; Salitre Formation; Carbonate reservoir

2.2.1. Introduction

Fractured and karstified carbonate rocks host significant hydrocarbon and groundwater reservoirs (Xu et al., 2017). Karst systems are formed where the dissolution of these rocks by an aqueous fluid is the dominant process (De Waele et al., 2009). Karst features are mainly controlled by structural heterogeneities such as bedding planes, faults, and fractures, which affect fluid flow by providing preferential pathways for geofluids with the development of secondary porosity (e.g., Balsamo et al., 2016; Ennes-Silva et al., 2016, and references therein). This may influence the production and exploitation of oil reservoirs (Ogata et al., 2012; Frumkin, 2013; Klimchouk et al., 2017).

An accurate characterization of karst systems, essential in carbonate reservoirs, requires special attention given that this type of reservoir represents 60% of the world's oil and 40% of the world's gas reserves (Montaron, 2008), with approximately the 25% of the world population that depend on drinking karst water (Chen et al., 2017). Therefore, they have high economic and social importance. Understanding the time-space evolution, geometry, and size of karst porosity is fundamental in modeling and predicting fluid flow in carbonate aquifers and oil reservoirs (Popov et al., 2007; Agar and Geiger, 2015Agar; Gholpoiur et al., 2016; Xu et al., 2017; Lyu et al., 2020).

The main mechanisms controlling karst distribution are chemical processes (meteoric CO_2, oxidation of sulfides and/or hypogenic biogenic CO_2), hydrothermalism, recharge patterns, regional flow, and regional and local structural and stratigraphical control (Auler and Smart, 2003; Palmer, 2007; De Waele et al., 2009; Ennes-Silva et al., 2016). Dissolution of carbonate rocks can occur by fluids enriched in CO_2 coming from the surface (epigenic karst, e.g., Audra and Palmer, 2011) or when ascending flow brings thermal CO_2-rich water (Dublyansky, 2012) or sulfidic fluids (Pisani et al., 2021). Fluids can also acquire their dissolutional aggressivity by mixing processes (for example, in coastal areas, Mylroie, 2012), or by localized oxidation of sulfides (e.g., pyrite) (Auler and Smart, 2003; Tisato et al., 2012). Dissolution zones and karst features of carbonate rocks are closely related to geological structures, hydrogeological conditions, and lithology (Antonellini et al., 2019; Araújo et al., 2021). The dissolution rate is mostly affected by the chemical and mineral composition

(Klimchouk and Ford, 2000; Frumkin, 2013). Still, discontinuities, such as fractures and faults, may facilitate flow in rocks with higher dissolution resistance (Smeraglia et al., 2021).

Folds may concentrate the highest strain in the fold hinge zone (Cosgrove, 2015), where fractures and fracture corridors occur. The term fracture corridor will be used to describe persistent subparallel fractures with consistent continuity (Ogata et al., 2014).

The presence of karstified zones can cause problems such as loss of fluid circulation and well collapse in the exploited oil field (Xu et al., 2017). Therefore, decisions about reservoir prospecting and exploration are carried out amid many uncertainties arising from a poor understanding of karst systems (Ogata et al., 2014; Klimchouk et al., 2016). On the other hand, karstified zones, marked by intense dissolution, could enhance the capacity of the fluid flow in carbonate reservoirs (Pantou, 2014), forming very high-permeability (super-K) zones, representing an important factor assessed in oil reservoir (Questiaux et al., 2010; Ogata et al., 2012, 2014). Several studies have applied new methodologies combined with seismic data to optimize the prediction of karst, such as thin section analyses and C/O isotope ratios of core samples, borehole images, 3D delineation methods (Tian et al., 2015 and references therein), and well-seismic inversion (Zhao et al., 2015).

Even with the recent advances in knowledge about karst and fractures connecting different parts of rock masses (Pollard and Aydin, 1988; Matthäi and Belayneh, 2004; Narasimhan, 2005; Balsamo et al., 2020; Araújo et al., 2021), several parameters such as karst evolution, karst geometry, structural control, and their influence on carbonate reservoirs have not been fully clarified through conventional exploration techniques, like seismic surveys or wells, because they are too small and remain undetected (Tian et al., 2017). Hence, the use of carbonate outcrop analogues (Guerriero et al., 2010, 2011; Santos et al., 2015; Giuffrida et al., 2019, 2020; 2020; La Bruna et al., 2017, La Bruna et al., 2018, La Bruna et al., 2020; Balsamo et al., 2020) could provide insights about karst systems, supplying an interesting explanation of the close relation between caves, depositional, diagenetic, and structural properties, to minimize errors in development and production in carbonate reservoirs and allow for more reliable reservoir or aquifer reconstruction.

This contribution focuses on the reconstruction of paleo-flow pathways below seismic resolution (less than 10 m) by analyzing subseismic-scale fractures and folds in four hypogenic karst systems developed within the carbonate succession of the Salitre Formation (Fig. 1 a, b), an analog of fractured and karstified reservoirs within the São Francisco Craton (SFC, Almeida et al., 2000) and adjacent areas.

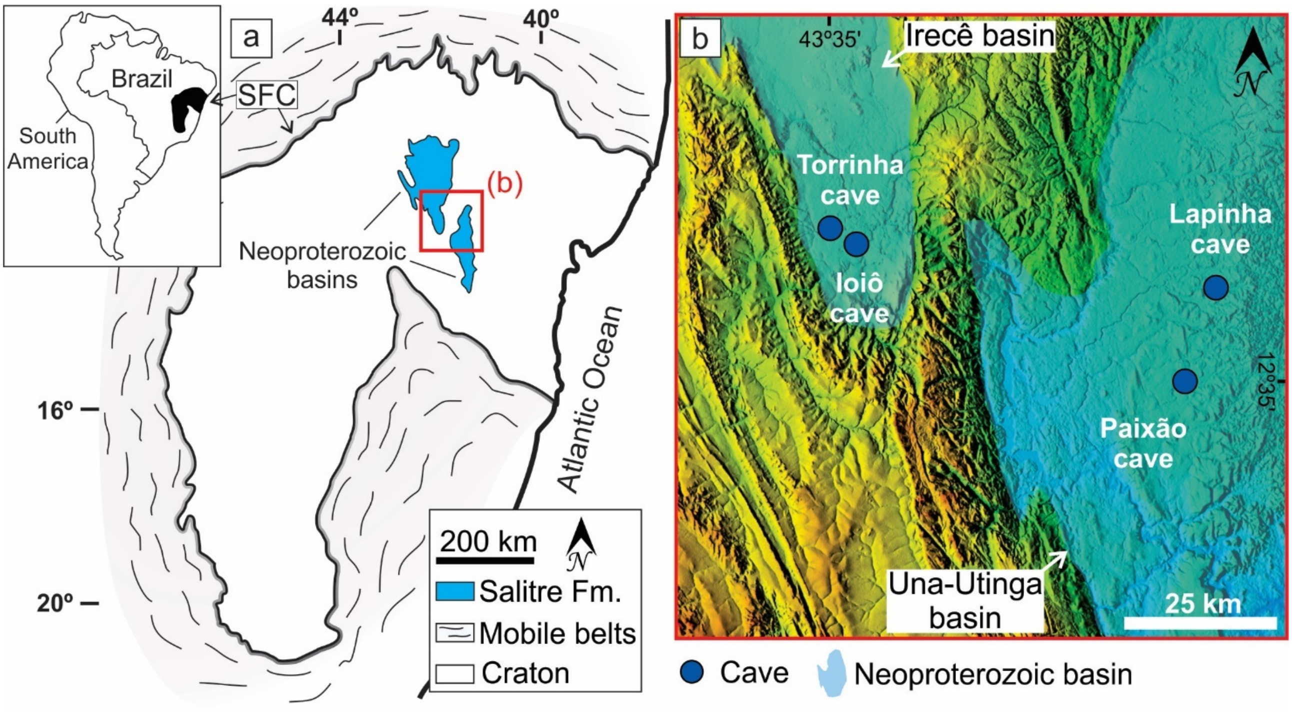

Figure 1. (a) Sketch map of the São Francisco Craton Salitre formation; (b) zoom and location of the studied sites.

In this study, we employed a multiscale and multidisciplinary approach involving petrographic characterization, qualitative and quantitative structural analysis, and high-resolution Light Detection and Ranging (LiDAR) imagery. LiDAR analysis was performed to provide predictions on the occurrence and geometry of karst features and to better understand the relationship between diffuse or localized deformation on the development of high dissolution zones that acted as flow pathways. We present a first-order prediction of the occurrence and geometrical attributes in karstified carbonate rocks to shed new light on the role played by karst systems localized along faults, fracture corridors, and fractured fold hinges, forming an orthogonal network of high-permeability zones.

2.2.2. Geological and speleological settings

The São Francisco Craton (Almeida et al., 2000) (Fig. 1 a) corresponds to the western portion of a large cratonic area together with the Congo Craton in Africa, which were segmented during the Pangea breakup and opening of the South Atlantic Ocean in the Late Jurassic and Early Cretaceous (Alkmim and Martins-Neto, 2012; Cazarin et al., 2019). The most recent part of the SFC is composed of Meso- and Neoproterozoic sedimentary units: the Una Group, which overlaps both Paleoproterozoic and Archean basement units.

Within the SFC, the Irecê and Una-Utinga basins were formed by rifting that occurred during the fragmentation of the Rodinia supercontinent (c. 950–600 Ma) (Condie, 2002; Guimarães et al., 2011). The presence of normal faults in the Una Group indicates that the extensional tectonic regime continued until the sedimentation of these Neoproterozoic basins (Misi and Veizer, 1998; Guimarães et al., 2011). A later deformation stage occurred during the Brasiliano orogeny (~650–500 Ma) (Misi and Veizer, 1998). Two main phases of deformation, marked respectively by folds and thrusts that strike NNE-SSW and E-W, are related to collisional events on the margin of the SFC during the Brasiliano orogeny (Guimarães et al., 2011; Ennes-Silva et al., 2016; Boersma et al., 2019). The Salitre Formation, mostly composed of carbonate units (Misi and Veizer, 1998), represents an excellent natural laboratory to investigate the relationship between karst systems and fractured carbonate reservoirs. This unit occurs at the top of the approximately 500-m thick Una Group.

The Salitre Formation hosts hundreds of caves, including the longest cave systems in South America, with a combined length of over 140 km of passages (Auler et al., 2017). Most caves were developed in deep-seated confined conditions, formed by a combination of rising flow that migrated upward through the basal units and then spread laterally (Klimchouk et al., 2016), and oxidation of sulfide-rich beds in shallow aquifers (Auler and Smart, 2003). Bertotti et al. (2020) highlighted the local development of caves formed along strike-slip faults, displaying clear evidence of the interaction between silica-rich fluids and carbonate rocks during cave formation that is rarely observed in other settings worldwide. In almost all cave systems, folds and related fractures control the planimetric development of the passages (Auler and Smart, 2003). The development of a huge number of caves in the Salitre Formation mostly occurred along fold hinges (Ennes-Silva et al., 2016; Boersma et al., 2019). The deformation features visible in the caves include bed-parallel and tectonic stylolites, fold hinges, strike-slip faults, conjugate shear fractures, and open-mode fractures (joints and veins). The open mode fractures were classified in (i) stratabound fractures (SB), confined within a mechanical unit, and (ii) non strata-bound fractures (NSB), smaller and greater than the mechanical unit. The folds display a basin-dome configuration (Ramsay, 1967). Two contractional phases were also documented by previous research conducted by Cruz and Alkmim (2006), Guimarães et al. (2011), Ennes-Silva et al. (2016), Klimchouk et al. (2016), D'Angelo et al. (2019), and Balsamo et al. (2020).

D'Angelo et al. (2019) proposed two contractional phases that affected the Neoproterozoic sedimentary cover, with ENE-WSW and N–S shortening direction. Based on geophysical models, they proposed a parallelism between the structures in the Neoproterozoic sedimentary cover, and

N–S and E-W normal faults in the crystalline basement, suggesting a control of strain distribution during sedimentary cover deformation.

The stratigraphic features of the caves in the northern part of the Irecê basin were described by Cazarin et al. (2019). They identified five units from the bottom to the top: (1) grainstones with cross-bedded stratification, (2) fine grainstones with chert nodules, (3) microbial carbonates, (4) fine siliciclastic layers and marls, and (5) crystalline grainstone interfingered with chert layers. The compositional difference in these units is related to the variable degrees of diagenesis and provides these rocks with different petrophysical properties. Some units concentrate fluid flow, whereas others act as sealing units, preventing fluid flow and intensifying the dissolution in the underlying layers (Cazarin et al., 2019; Balsamo et al., 2020).

2.2.3. Methods

In this study, four caves were selected: Ioiô, Torrinha, Lapinha, and Paixão caves (Fig. 1b). All caves are interpreted as displaying features associated with confined flow/hypogenic conditions (Auler, 1999), although epigenic features may also occur. Data integration allowed for clarifying the relationship between the physical properties of the host rocks and both fracturing and karstification processes. We describe the petrographic, lithostratigraphic, structural and LiDAR analyses in the following sections.

2.2.3.1. Petrographic and lithostratigraphic analyses

The laboratory work included the petrographic analysis of 22 oriented thin sections obtained from fresh samples collected in the caves. The petrographic analysis was carried out using a Leica DMLP optical microscope under planar and cross-polarized lights. Based on their texture, carbonate rocks were described according to Dunham (1962). This analysis allowed us to define the composition, sedimentary facies, and texture of the karstified carbonates. Four stratigraphic columns, one for each cave, were reconstructed and sampled in key sectors. This approach was employed to understand which units had the highest degree of dissolution, based on the distribution of facies and mineral composition.

2.2.3.2. Structural analysis

Deformation features in the Salitre Formation caves were measured and sorted into different types: mode I fractures (joints and veins), bed-parallel stylolites, conjugate shear fractures and fold hinges.

Joints and veins include both stratabound (SB) and non-stratabound (NSB) structures. Bedding attitude and dip variations were also measured systematically. Detailed qualitative and quantitative structural analyses were carried out at each site. The qualitative analysis aimed at deciphering the nature, kinematics, relative timing, and attitude of individual features affecting the carbonate rock multilayers. In total, 603 fractures were measured and analyzed with stereonet software (Allmendinger et al., 2011)

Moreover, fracture attributes were constrained by means of 14 linear scanlines (Marrett et al., 1999; Ortega et al., 2006; Miranda et al., 2014; Giuffrida et al., 2019; Pontes et al., 2019). These analyses were performed along the sub-vertical walls at the external portion of cave entrances. At each site analyzed, the 5-m-long parallel-to-bedding scanlines were located orthogonally to the main fracture striking-sets (N–S and E-W directions) to be as representative as possible of all the structural features present. For each fracture, we measured the following parameters: attitude, height, distance from the origin of the scanline, type (joint, shear joint, fault), aperture, and infill (if present). The aperture was measured using a comparator developed by Ortega et al. (2006). The real spacing between fractures was calculated with trigonometric equations using the azimuthal angle formed by the scanline plunge/dip and the main strike/dip of each set (Terzaghi, 1965). The Coefficient of variation (Cv) was calculated; it consists of the ratio between the σ1 standard deviation and the mean value of fracture spacing of individual fracture sets (Zambrano et al., 2016; Giuffrida et al., 2019). Furthermore, the best-fit equations were calculated for the recognized individual fracture striking-sets. This distinction among fracture striking-sets was determined by plotting the mean fracture spacing and their cumulative number (cn), in bi-logarithmic plots (Gillespie et al., 1993; Railsback, 1998; Odonne et al., 2007).

2.2.3.3. LiDAR survey

The caving club "*Grupo Bambui de Pesquisas Espeológicas*" provided the cave maps with topographic data from the caves. Using these maps, it was possible to formulate data acquisition strategies for LiDAR, boundary outlines, and the structural maps of caves. The purpose of this technique was to understand the karst geometry and the relation with the fracture patterns. We carried out laser scanning with a terrestrial LiDAR system (TLS) using a Leica Scanstation P40 scanner from ViGeA (Reggio Emilia, Italy) and a mobile LiDAR system (MLS), a ZEB-Revo GeoSLAM scanner. The MLS shows better results for the cave morphology and irregularities in the passages. In addition, the user could move through complex cave passages with the MLS during the acquisition of the 3D point clouds without defining fixed stations, which provided quick and better results to cover the whole cave morphology. On the other hand, the TLS can provide more accuracy and precision due to the series of additional sensors such as an inclinometer, an electronic compass, and a dual-axis compensator (Jacquemyn et al., 2012; Fabbri et al., 2017; De Waele et al., 2018). At least 35 millions of points were acquired for each cave studied.

We processed the point clouds with the open-source software Cloud Compare using the raw file from the LIDAR data. Cloud Compare offers several tools to improve the analysis of cave morphology and geometry (Fabbri et al., 2017; De Waele et al., 2018). MLS data were loaded to plot the intensity values of the scalar field using grayscale. For a good visualization of the structural features, we used the "Eye-dome Lighting" filter. We created 3D model slices of several parts to visualize the cave geometry using the "Cross Section" tool. Approximately 1.4 km of cave passages were surveyed, being 350 m in the Ioiô cave, 500 m in the Torrinha cave, 240 m in the Lapinha cave, and 200 m in the Paixão cave.

2.2.4. Results

2.2.4.1. Lithostratigraphy of cave systems

In the area of the four investigated caves, the carbonate rocks of the Salitre Formation are arranged in millimeter-to centimeter-thick tabular layers. Stratigraphic analysis indicates three main lithologies, from the base to the top: (a) microbial carbonates, (b) microbial carbonates with intercalations of siltstone levels, and (c) sedimentary breccia (Fig. 2a).

The microbial carbonate layers display chert nodules or dark *boudin* concretions in some portions (Fig. 2a.). The thin section analysis indicates that the texture of these carbonate layers are mudstones affected by an intensive process of dolomitization. The primary porosity of lithologies that compose the Salitre Formation was reduced mostly by mesodiagenesis cementation (Cazarin et al., 2019). The secondary porosity was mostly represented by fractures. The mudstone interval shows a smaller grain size, with a particle-size distribution classified as silt, with frequent chert nodules and presence of pyrite crystals (Fig. 2 b, c).

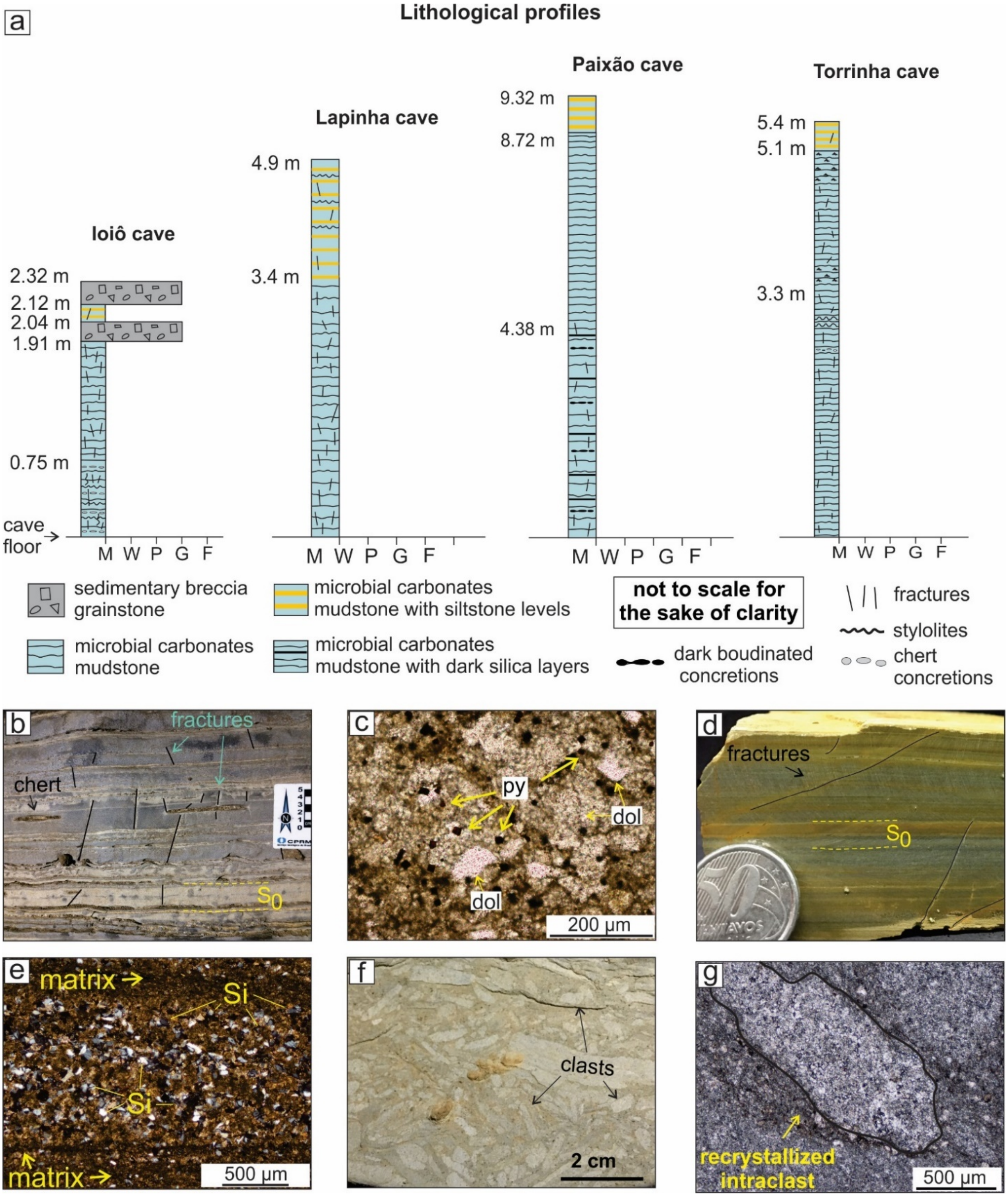

Figure 2. (a) Schematic stratigraphic column of the study area from Ioiô, Lapinha, Torrinha, and Paixão caves. (b) Close up view of a grainstone; (c) photomicrograph of a representative mudstone with the pervasive occurrence of pyrite. (d) Hand sample of mudstone with siltstone levels; (e) photomicrograph of mudstone that shows siliciclastic grains; (e) close up view of mudstone with chert nodules; (g) photomicrograph of a representative grainstone; Key: Un: stratigraphic unit described in the text, M: Mudstone, W: Wackestone, P: Packstone, G: Grainstone, F: Floatstone, Py: pyrite, Si: Silica, dol: dolomite, S_0: bedding.

The microbial carbonate with siltstone levels is a mudstone (Fig. 2 d, e) affected by dolomitization and characterized by detritic minerals that correspond to 10–20% of their composition. The sedimentary breccia (Fig. 2 f, g) corresponds to grainstone characterized by coarse grain size (sands). Specific layers display less significant dissolution than others, forming high relief zones (prominent layers) that vary according to rock texture and composition (Fig. 3). Usually, the mudstone with siltstone levels and the grainstone are more prominent in relief inside the caves than the mudstone layers (Fig. 3). Occasionally within the mudstone layers, we identified darker intercalations composed of organic material and/or pyrite (Fig. 2 c), which indicate a reducing deposition environment.

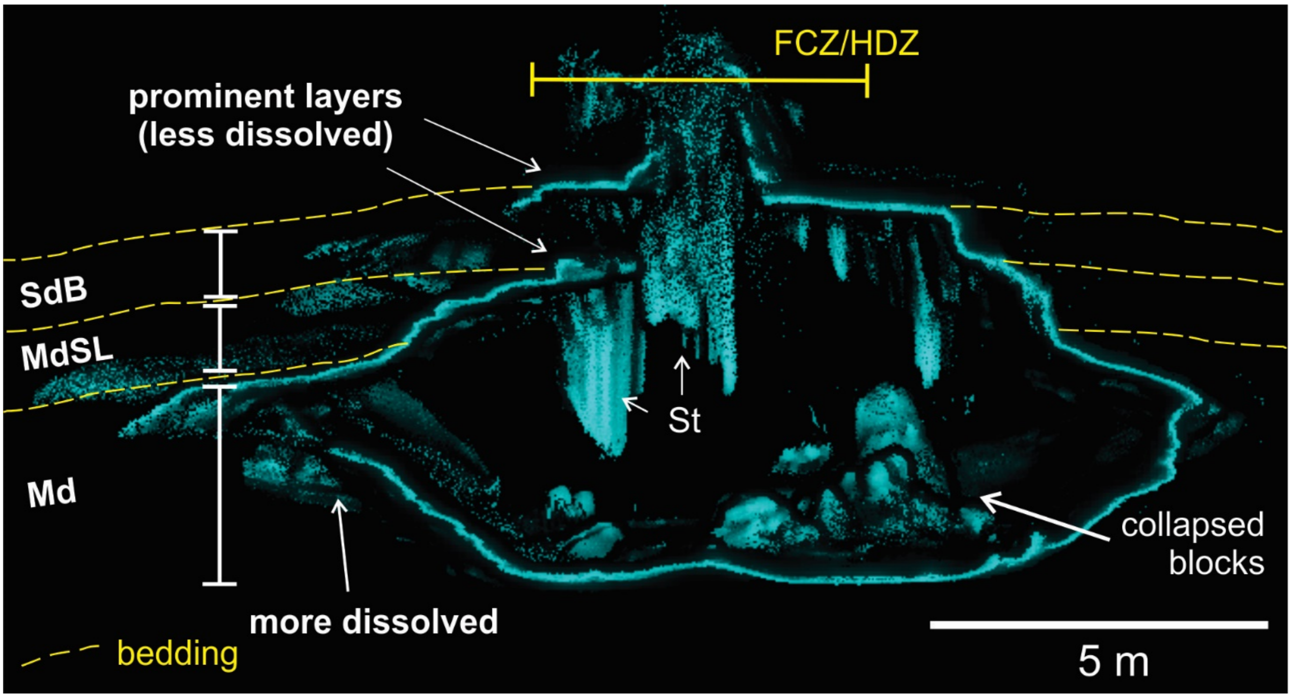

Figure 3. 3D model slice orthogonal to the cave passage in Ioiô cave showing different levels of dissolution due to distinct carbonate rock textures. The location of the slice is shown in Fig. 7b. Key: FCZ: fracture corridor zone; HDZ: high-dissolution zone; SdB: Sedimentary breccia; MdSL: mudstone with siltstone level; Md: mudstone; St: stalactites.

2.2.4.2. Structural data

We divided this topic into quantitative and qualitative approaches. The qualitative approach included detailed structural mapping and LiDAR imaging analysis to identify the relationship between the fracture sets and principal fracture zones, as well as the characterization of the general cave features. A quantitative field fracture analysis was performed along the surveyed carbonate rock walls to distinguish the diffuse deformation from the fold-fault related deformation and determine their influence on the cave's nucleation and development.

2.2.4.2.1. General cave features

The qualitative structural analysis based on field observations, LiDAR imaging, and structural measurements was performed within the caves and along the external sub-vertical walls that surround the cave entrances. Commonly, bed-parallel stylolites are located at the bed interfaces within mm-thick, continuous, clay-rich marl layers. Less often, they are present within individual carbonate beds. Open-mode fractures may display hackles and ribs and thus were identified as joints. In some cases, a millimeter-to-centimeter offset of depositional surfaces was observed across them, and therefore we considered the above features to be sheared joints. Some of the cave passages exhibit an alignment of speleothems located in the central part of the cave roofs. These speleothems are mainly associated with several fracture zones parallel to the cave passages and running along the central part of the cave roofs (Fig. 4 a).

The cave passages are arranged in a linear or maze pattern, with rectilinear sub-horizontal passages developed parallel to fractures in an orthogonal pattern expressed on the roof (Figs. 4 b, Fig. 8 a). High dissolution zones occur in the middle portion of the cave passages (Fig. 4 c). In general, cave conduits could be divided into major chambers ~10-m high, and smaller conduits up to 2.5-m high that link the major chambers. The preferred direction of the cave passages coincides with the main persistent N–S- and E-W-striking fracture zones.

Fractures may be confined within individual carbonate beds as SB, or as NSB where they crosscut one or several beds, usually related to main dissolution zones. Both SB and NSB fractures are much more evident along the external portion of the caves, where the dissolution and mineralization processes do not entirely erase or overprint them (Fig. 5 a, b). The SB and NSB fractures are not necessarily parallel (Fig. 5 c).

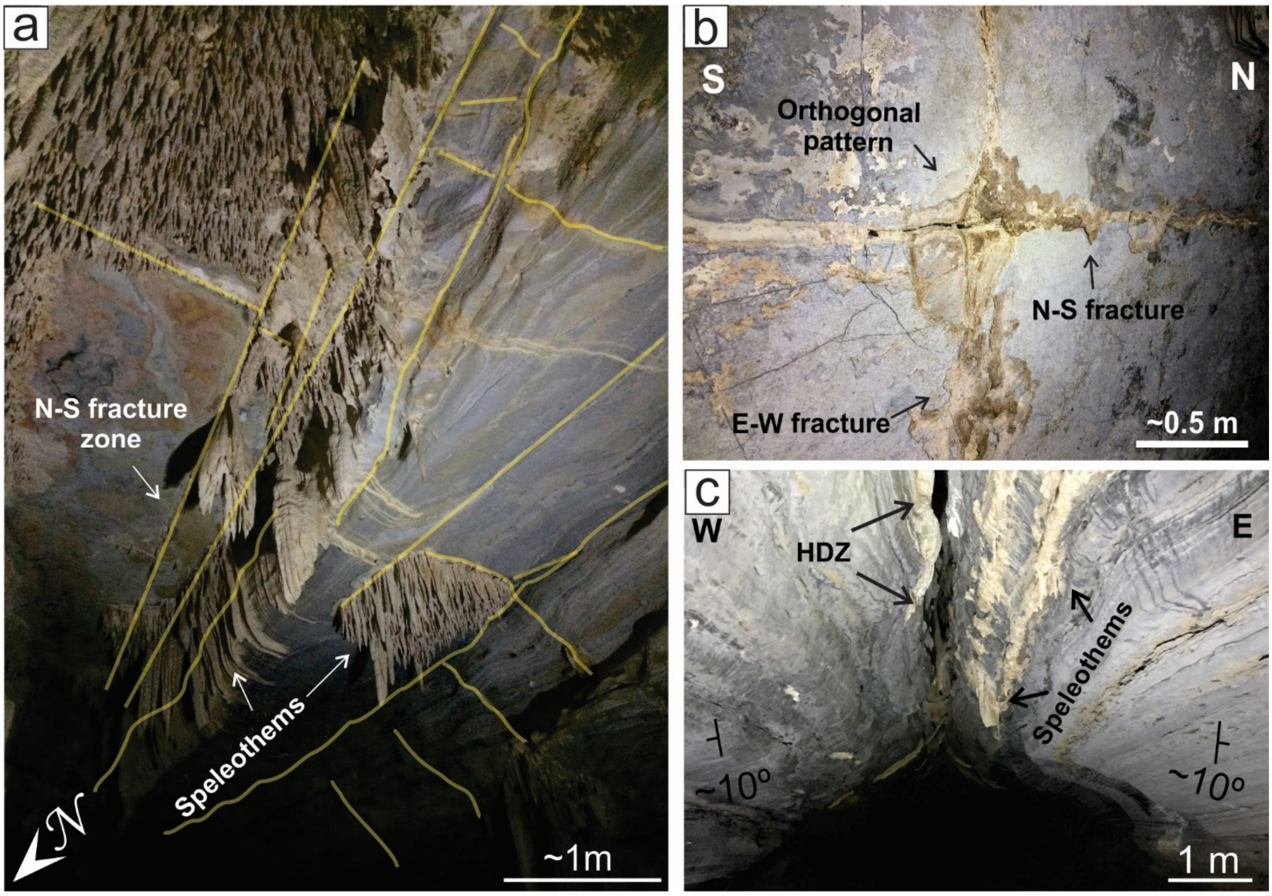

Figure 4. (a) View of the Ioiô cave ceiling displaying speleothems aligned along the main N–S- and E-W-striking fracture zones; (b) Orthogonal system of fractures on the cave ceiling; (c) gentle fold highlighting the high dissolution zone along the fold hinge. Note opposite bedding dips. Key: HDZ: high-dissolution zone.

Two main fracture sets were observed in the study sites, striking N–S and E-W; systematically, the E-W fractures terminate against the N–S ones, which indicates that the latter are older than the former (Fig. 6 a). Bed-parallel stylolites are common throughout the analyzed sites, at the surface, and inside the caves. We also documented bed-perpendicular folded veins (Fig. 6 b), N–S, and E-W bed-perpendicular veins with mutual abutting relation with bed-parallel stylolites (Fig. 6 c, d), and several high-angle normal faults characterized by extensional or oblique-slip kinematics (Fig. 6 e and f). Usually, these structures are composed of several discontinuous slip surfaces; the abutting/crosscutting relationships (Fig. 6 f) among the fracture sets are consistent with their hierarchical formation and the subsequent shearing of joint sets sub-parallel to the main slip surfaces (Davatzes and Aydin, 2003; Myers and Aydin, 2004).

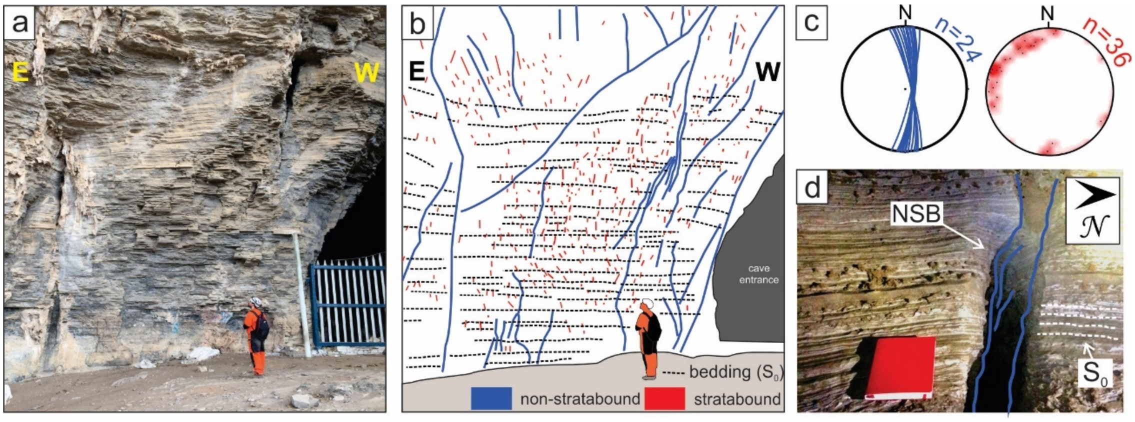

Figure 5. (a) Outcrop view of an external wall near Lapinha cave entrance; (b) linedrawing of (a); (c) lower hemisphere equal-area projections of the poles related to the NSB and SB; (d) close up view of a karst dissolution zone parallel to a persistent non-stratabound fracture zone inside the cave. Key: NSB = Non-Stratabound fracture; S_0 = bedding.

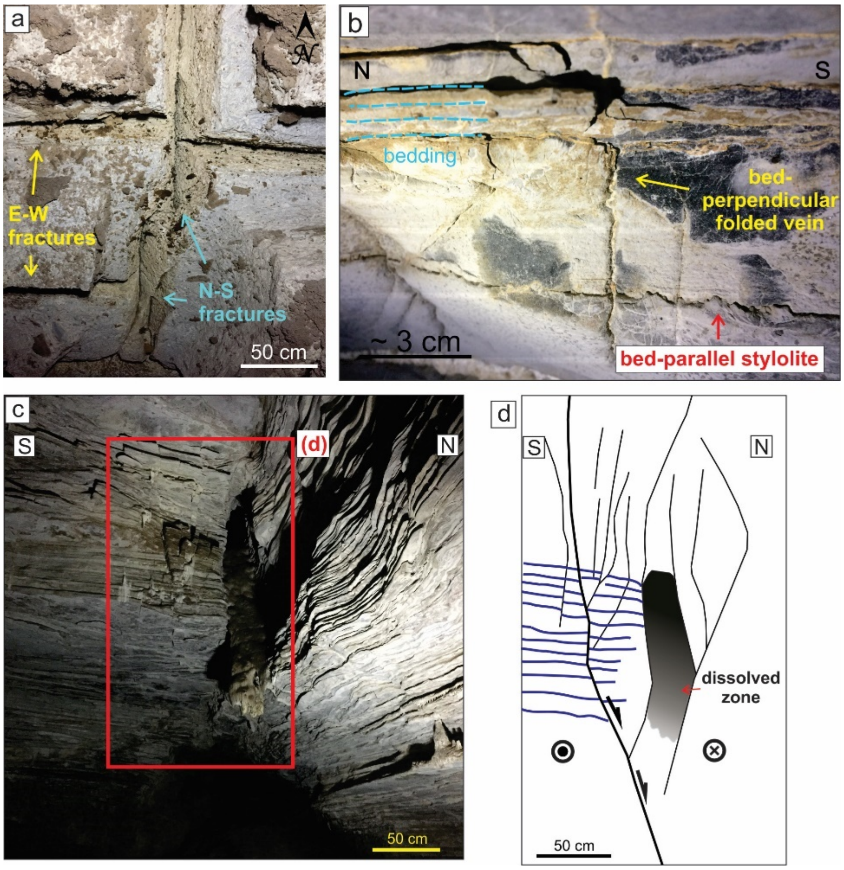

Figure 6. Close up view of fracture sets in the ceiling of caves: (a) abutting relation between E-W-striking fracture set and N–S-striking fracture set in the Torrinha cave; (b) bed-parallel stylolite and bedperpendicular folded vein in the Ioiô cave; (c) mutual abutting relation between bed-perpendicular vein and bed-parallel stylolite; (d) line drawing of (c); (e) normal fault with left-lateral strike-slip kinematics in the Lapinha cave; (f) line drawing of (e).

2.2.4.2.2. Identification of fold hinges and fracture sets

Two major gentle folds occur in the Ioiô cave (Fig. 7 a, b, c, d). These antiforms display a N–S fold axis, which is parallel to the main cave passage and the main fracture/dissolution zones (Fig. 7 e, f). Along the cave passages, the bed surfaces display a dip of approximately 10° toward the west (along the western cave wall) and 10° toward the east (along the eastern wall, Fig. 7 c, d, g).

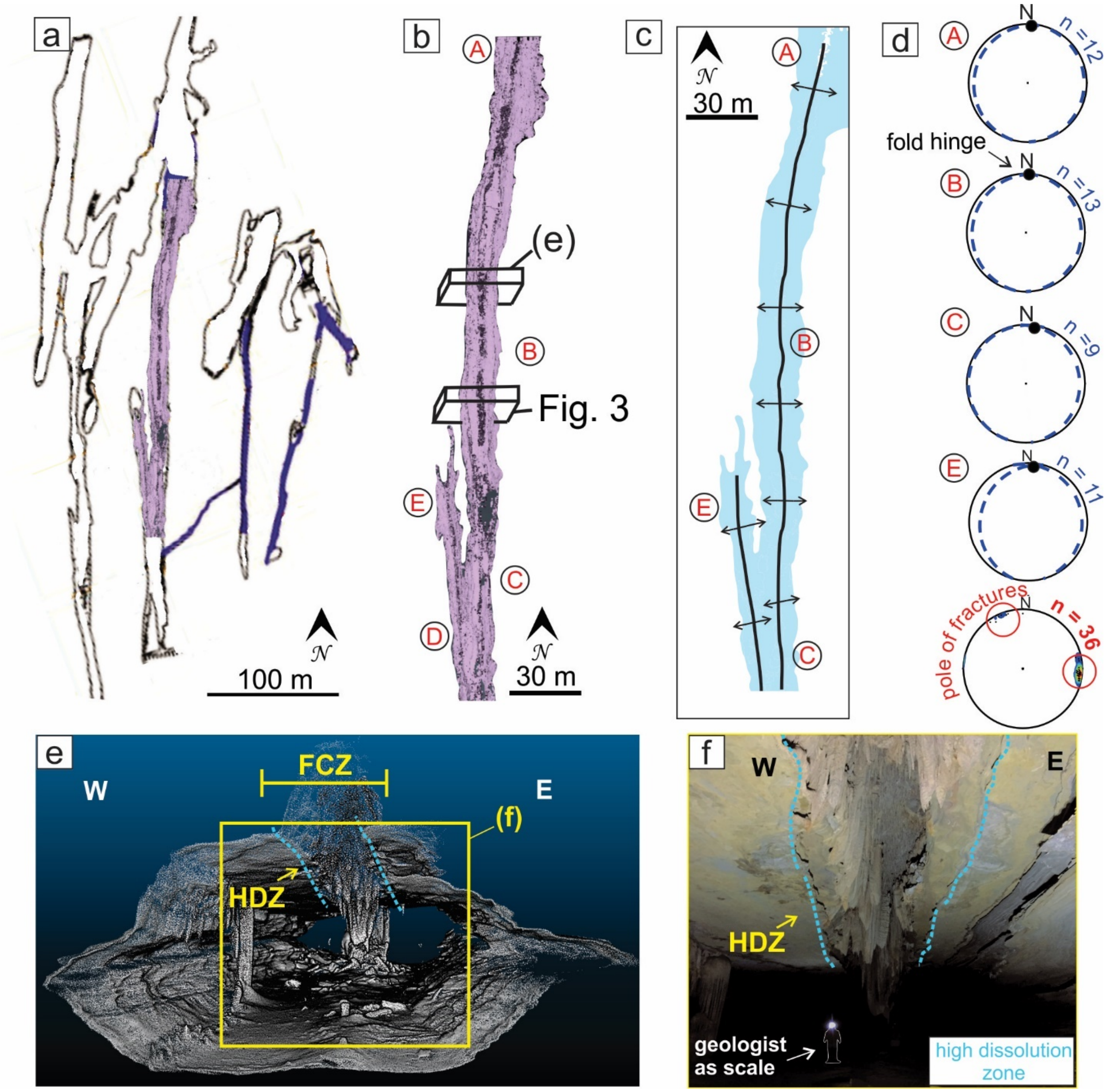

Figure 7. Structural and karst features of the Ioiô cave: (a) cave map with area surveyed with LiDAR; (b) 3D LiDAR model of the cave with the location of investigated sites; (c) main fold hinges of the cave; (d) lower hemisphere equal-area projection of the poles and relative density contour plots of bedding planes and fractures; (e) digital image of the slice on site B showing a high dissolution zone along a fracture corridor following the fold hinge in the central part of the cave passage; (f) detail of HDZ highlighted in (e) (yellow square). Key: FCZ: fracture corridor zone; HDZ: high-dissolution zone.

In the Lapinha cave (Fig. 8 a) the LiDAR survey was integrated with detailed structural analysis at 13 sites (Fig. 8 b). This cave is marked by the presence of two orthogonal, bed-perpendicular fracture sets that strike ~ N–S and E-W (Fig. 8 c). Along the ~ N–S passages, the bed surfaces show dip ranging from 3° to 15° toward the east and west. E-W cave passages show a bedding dip from 5° to 10° toward the north and south (Fig. 8 d and e). The main fracture/dissolution zones are parallel to the documented fold hinges and concentrated along the central portion of the cave ceilings (Fig. 8 c, d). Furthermore, the LiDAR data analysis allowed us to highlight and measure the fold wavelengths in the Lapinha cave. E-W and N–S folds display an almost equidistant wavelength of ca. 30 m (Fig. 8 e).

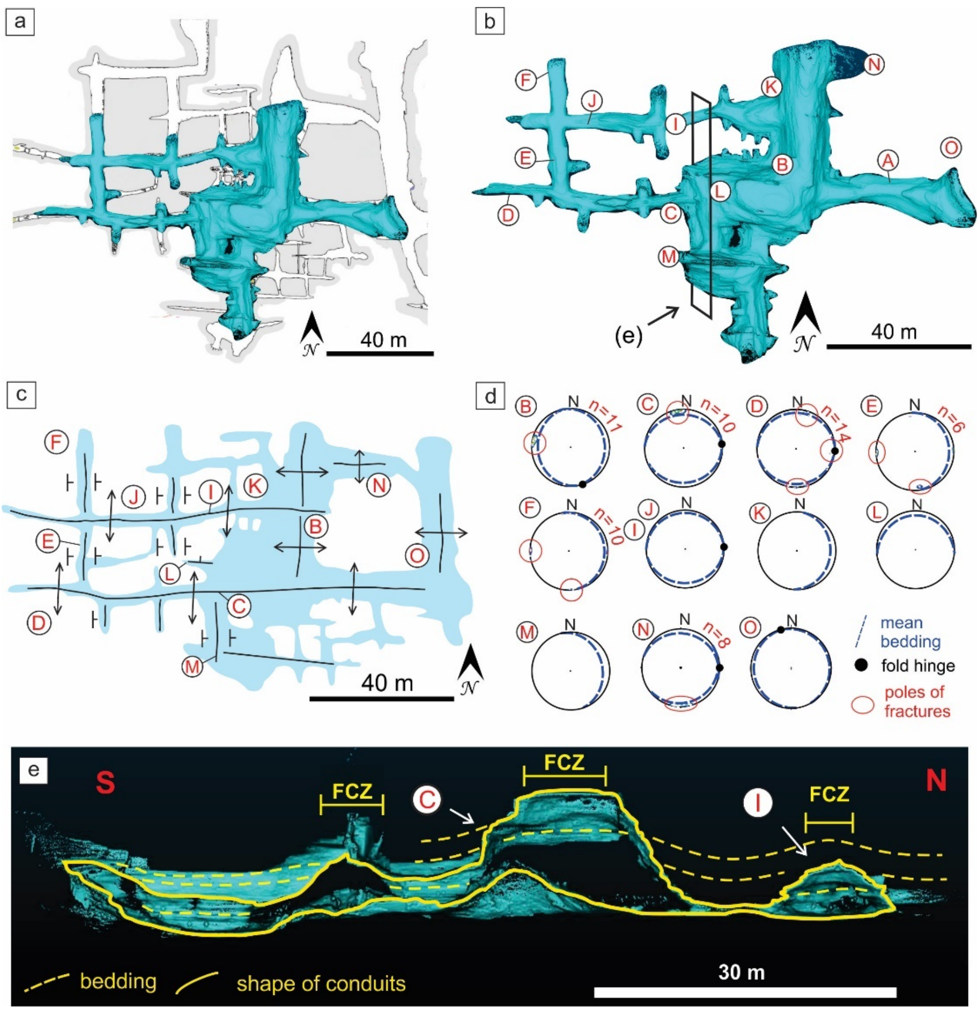

Figure 8. Structural and karst features of the Lapinha cave: (a) cave map with area surveyed with LiDAR; (b) 3D model of the cave with the location of investigated sites; (c) structural map of the central part of the cave showing two main directions of anticline folds (d) lower hemisphere equal area projection of the poles of NSB and SB fractures, mean bedding planes, and mean fold hinge (black dot); (e) digital slice between the (C) and (I) sites highlighting the wavelength of N–S folds. Key: FCZ: fracture corridor zone.

The high-resolution imaging provided by the MLS survey in a maze portion of the Torrinha cave provides a consistent representative model of the geometry of the cave passage (Fig. 9 a, b) and allowed for us to determine that the karstification processes followed the direction of fold hinges. The main geometric pattern observed for the cave passages could be associated with an ellipsoid with a major axis in a horizontal or vertical position (Fig. 9 b, c, d).

The dissolution processes are more developed near or at the fracture/fault intersection, as highlighted in the 3D model of the Paixão cave (Fig. 9 e and Fig. 4 b).

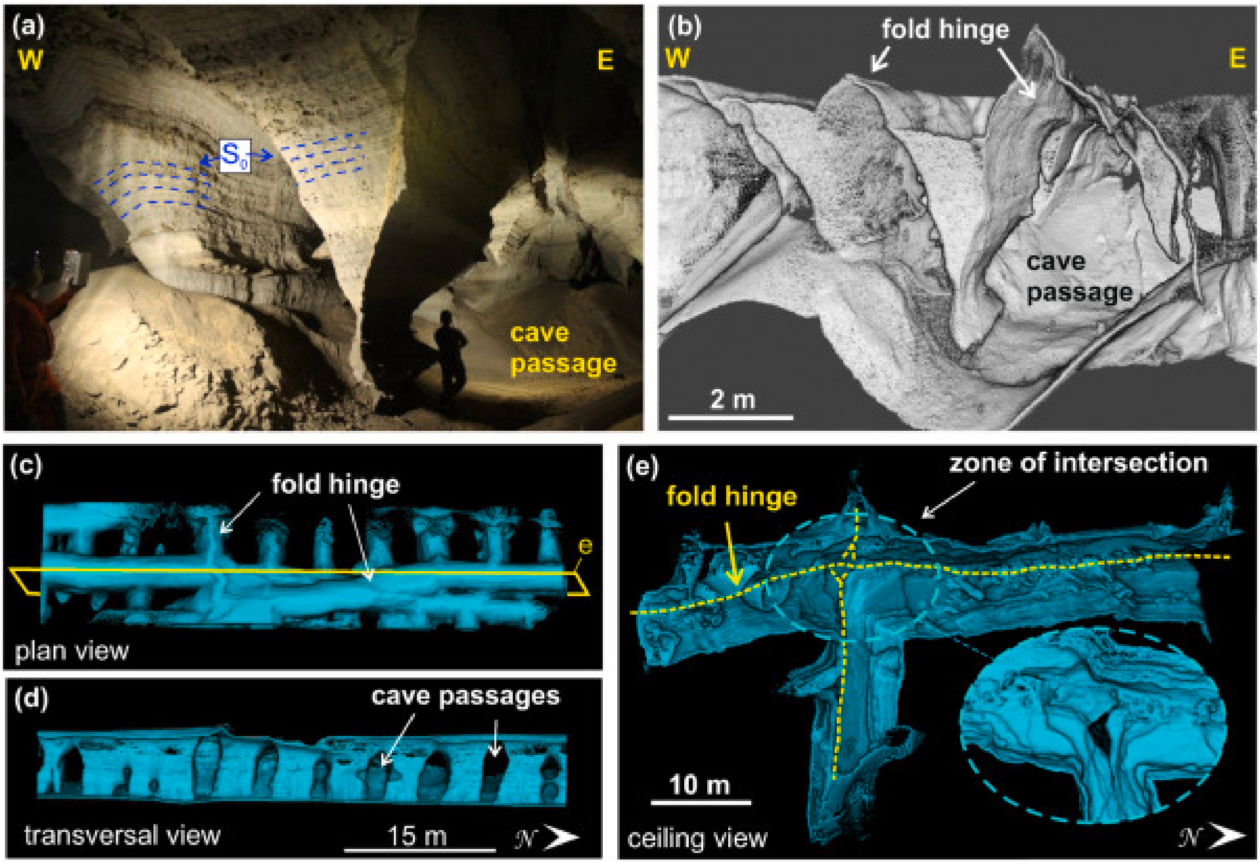

Figure 9. Geometric features of the Torrinha (a–d) and Paixão (e) caves: (a) internal view of the cave geometry showing widening of the passage along the fold hinge; (b) 3D LiDAR model of (a); (c) plan view of the site (e) (location in Fig. 9b) showing both major N–S- and subsidiary E-Woriented cave passages; (d) transversal view of (d) showing the vertical elliptical shape of the cave passages; (e) 3D LiDAR model of Paixão cave ceiling with a close up view of two N–S- and E-W-string fracture sets.

The studied mazes in Torrinha cave display a similar structure to the Lapinha cave, characterized by an orthogonal pattern of the cave passages. The LiDAR survey carried out in the southeastern part of the cave highlights this geometry (Fig. 10 a). Along this portion, the cave is affected by folds showing both N–S and E-W hinge directions (Fig. 10 b, c). The bedding dip ranges from 8° to 15°, usually in opposite directions, forming gentle folds (Fig. 10 c, d). The E-W passages usually terminate against the N–S structures, which are more persistent. A NW-SE strike-slip fault with a dextral kinematic (Fig. 10 c) causing a displacement of N–S fold hinges was observed. The detachment of carbonate layers indicates a compressive component (Fig. 10 e).

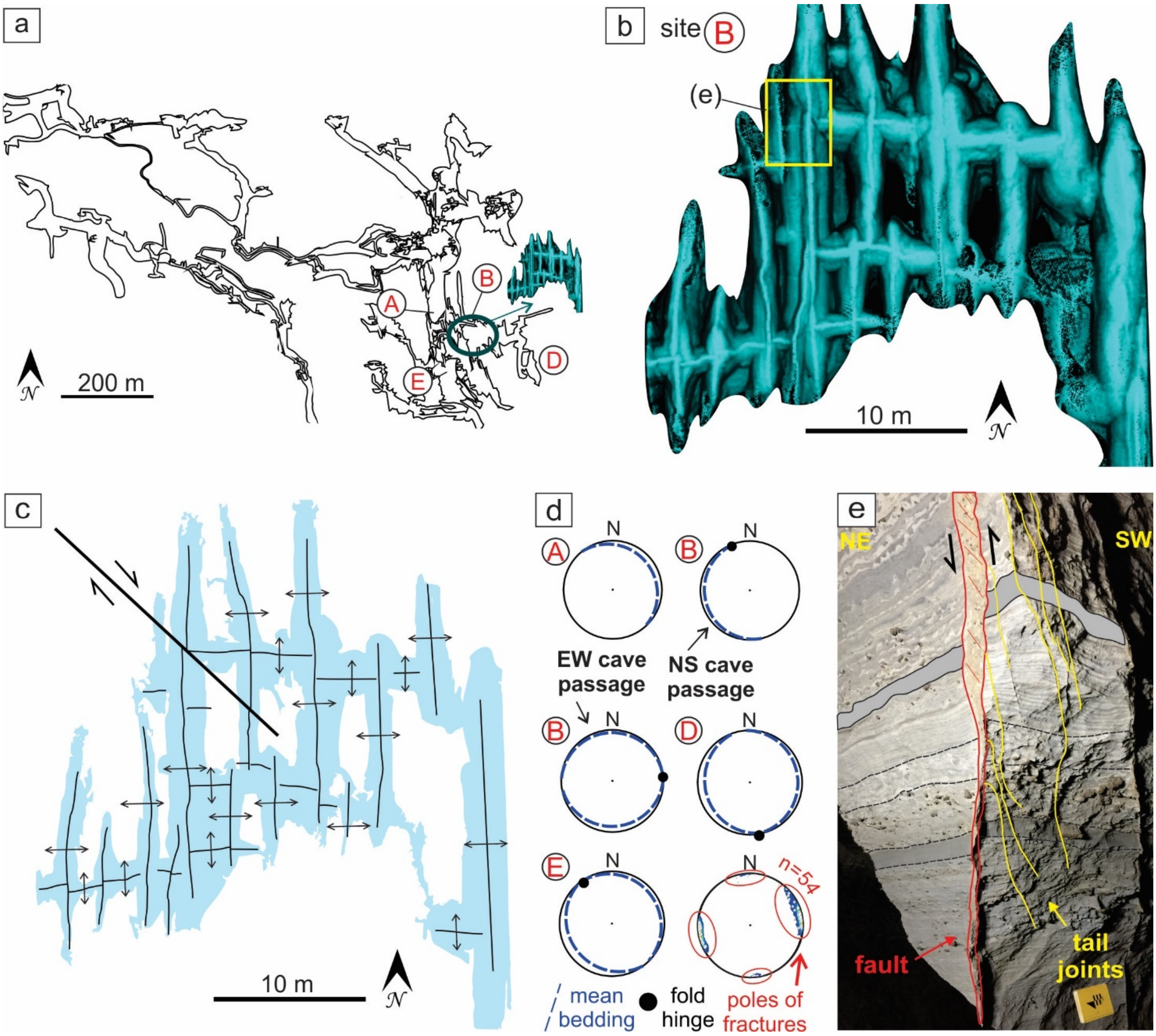

Figure 10. Structural and dissolutional features of Torrinha cave: (a) map highlighting the LiDAR surveyed area in the southern portion of the cave; (b) 3D model of the scanned areas with the location of investigated sites; (c) structural map of site B in the cave; (d) lower hemisphere equal-area projection of the poles of NSB and SB fractures, mean bedding planes, and mean fold hinge (black dot). (e) NW-SE strike-slip fault at site B of Torrinha cave.

The Paixão cave is characterized by orthogonal cave passages and related anticlines (Fig. 11 a), where these passages display an *en echelon* pattern associated with *en echelon* fold hinges (Fig. 11 b, c). The bedding dip ranges from 4° to 18° along the cave walls (Fig. 11d). One of the main cave passages is associated with a single fault zone (Fig. 11 e), showing high displacement (HD) in the central part, observed in the LiDAR digital model (Fig. 11 g). Along this fault zone, we also identified and characterized several dip-slip faults (Fig. 11 g, h).

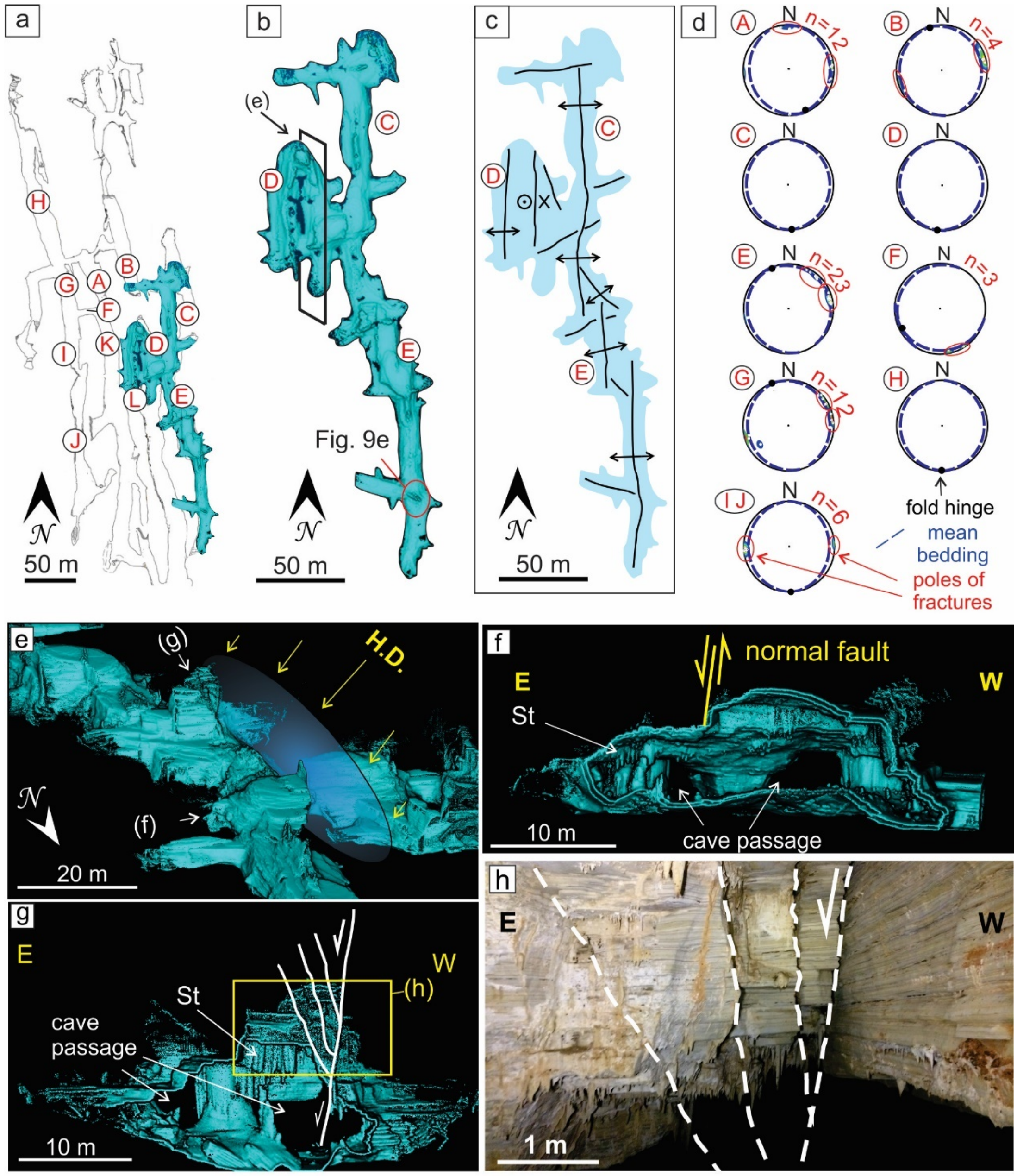

Figure 11. Structural and dissolutional features of the Paixão cave: (a) map highlighting the area surveyed with LiDAR and location of the investigated sites; (b) 3D LiDAR model of the studied part of the cave; (c) structural map of the eastern part of the Paixão cave highlighting the en echelon pattern

of fold hinges; (d) lower hemisphere equal-area projection of the poles of NSB and SB fractures, mean bedding planes, and mean fold hinge (black dot); (e) zoom on the central portion of the model highlighting the location of a fault zone (blue ellipsoid); (f) digital slice of the cave's central portion affected by a dip-slip fault zone; (g) orthogonal-to-dip view of a normal fault located in the central portion of the cave; (h) cave central portion highlighting the fault displayed in (e). Key: HD = High displacement; St = stalactite.

2.2.4.2.3. Background and clustered fractures

The quantitative structural analysis based on the scanline methodology was performed along the external vertical walls. The values of the exponential distribution, power law distribution, and Cv are summarized in Table 1.

The N–S-striking set shows Cv values higher than 1 for the Ioiô (Fig. 12 a), Lapinha (Fig. 13 a), and Torrinha sites (Fig. 14 a), and values lower than 1 for the Paixão site (Table 1). The same results were observed for the NNW-SSE-striking set. The Cv values of the NW-SE-striking set are close to 2 in the Ioiô site; they range from 0.8 to 1.7 in the Torrinha site, and from 0.3 to 0.9 in the Paixão site. In the Ioio site, the E-W- and NE-SW-striking sets show Cv values lower than 1. However, in the Torrinha and Lapinha sites, which exhibit caves with maze pattern, the E-W- and NE-SW-striking sets exhibit Cv values higher than 1, reaching 2.3 at scanline 1 of the set NE-SW (Table 1). Only in the Paixão site, all striking-sets (Fig. 15 a) present Cv values lower than 1 for all scanlines.

The multiscale spacing distribution computed for the SB and NSB fracture sets (Fig. 12 b, 13 b, 14 b, 15 a) is presented in Fig. 12 c, 13 c, 14 c, and 15 b, in which the fracture spacing is plotted in a log-log space versus as a cumulative number. In the Ioiô site, the N–S-striking set (Figs. 12 b, 13 b, 14 b, 15 a) shows a power-law distribution (Fig. 12 c); the same occurs at scanline 3 in the Torrinha site (Fig. 14 c). All other N–S striking-set scanlines show an exponential distribution in the Lapinha and Paixão sites (Fig. 13 c, 15 b). The NNW-SSE- and NW-SE-striking sets present the same behavior as the N–S-striking set. In the Ioiô and Torrinha sites, the E-W-striking set shows an exponential distribution. In the Lapinha site, the E-W-striking set presents both an exponential and power-law distribution (Fig. 13 c). In the Paixão cave, all measured striking-sets (N–S, NW-SE, and NNW-SSE) exhibit an exponential distribution (Fig. 15 b). The NE-SW-striking set in the Ioiô and Lapinha sites show a power-law distribution (Table 1). In all cave sites, the clustered fracture sets (fracture corridors) exhibit the same trend as in the main cave passage.

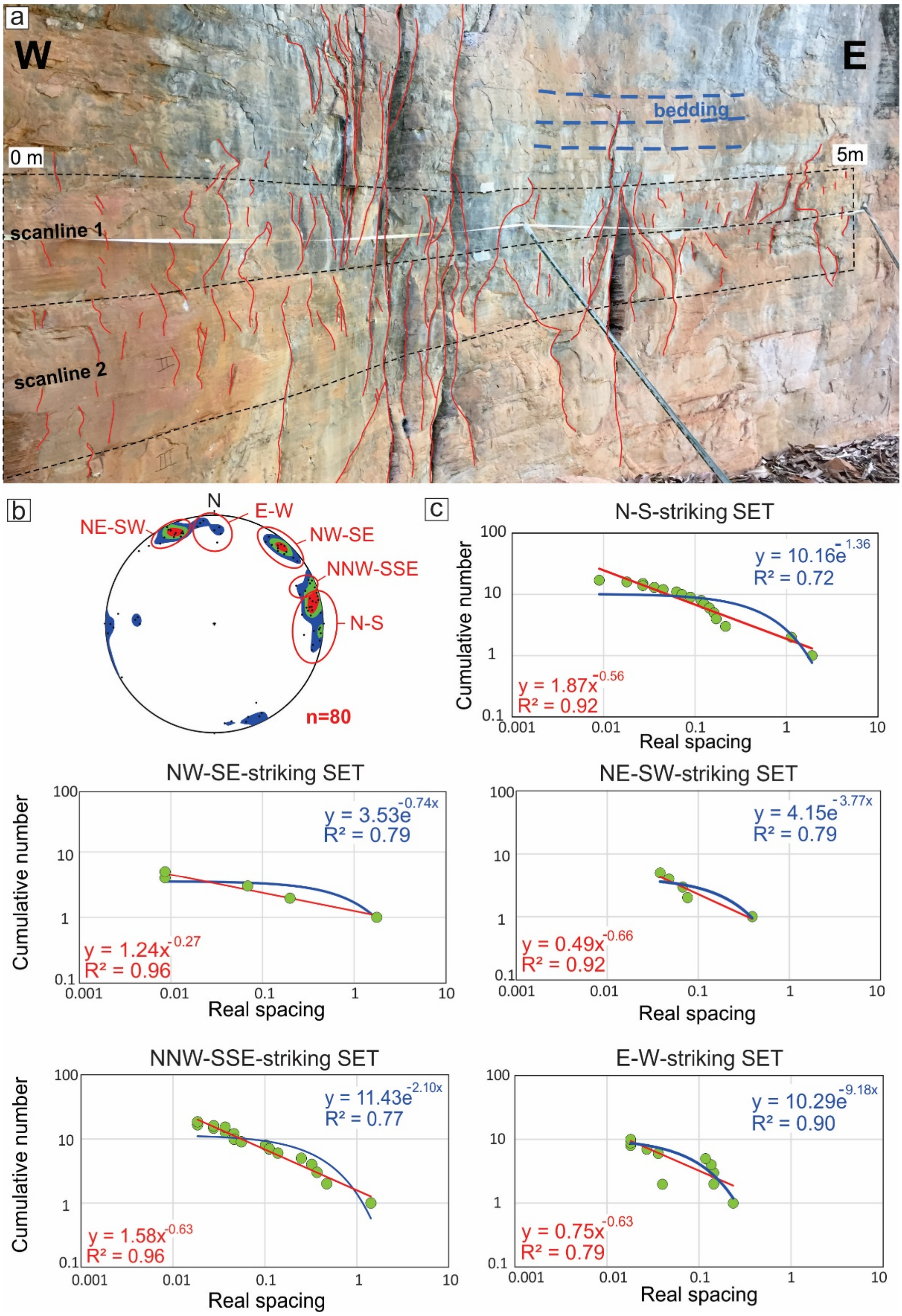

Figure 12. Quantitative data of the Ioiô site: (a) Outcrop oblique view of the site and the investigated beds; red lines used for the linedrawings are related to both SB and NSB fractures; (b) Lower hemisphere equal-area projection of the poles and relative density contour plots representing the fractures measured in the site; (c) Log-log diagrams of the cumulative frequency distribution for fracture spacing; blue lines correspond to exponential-law distribution, red lines correspond to power-law distribution calculated for the single fracture sets in the site.

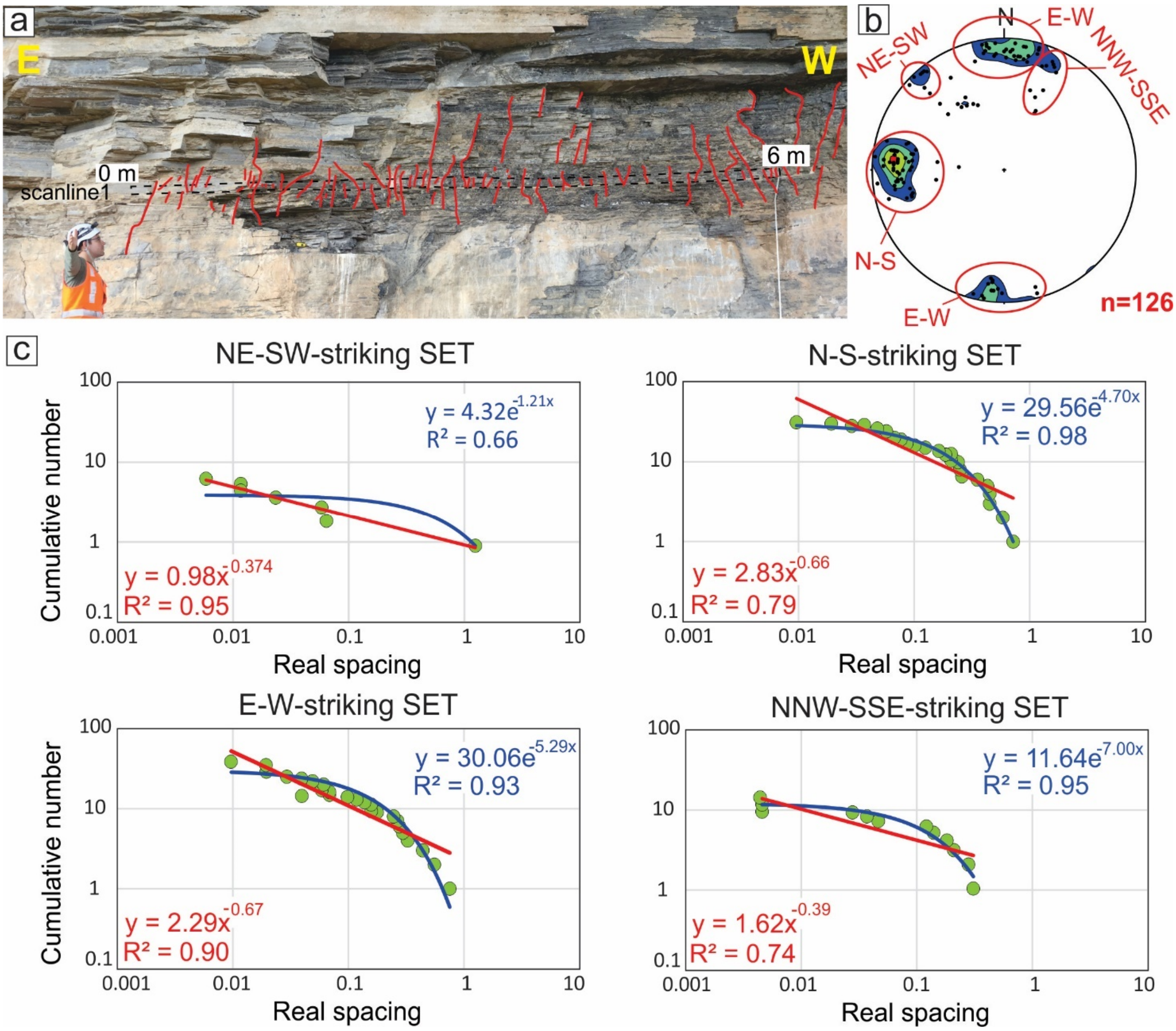

Figure 13. Quantitative data in the Lapinha site: (a) Outcrop view of beds; red lines used for the linedrawing are related to both SB and NSB fracture sets; (b) Lower hemisphere equal-area projection of poles and relative density contour plots representing fractures; (c) Log-log diagram of the cumulative frequency distribution for fracture spacing; blue lines correspond to exponential law distribution, red lines correspond to power-law distribution calculated for the single fracture sets.

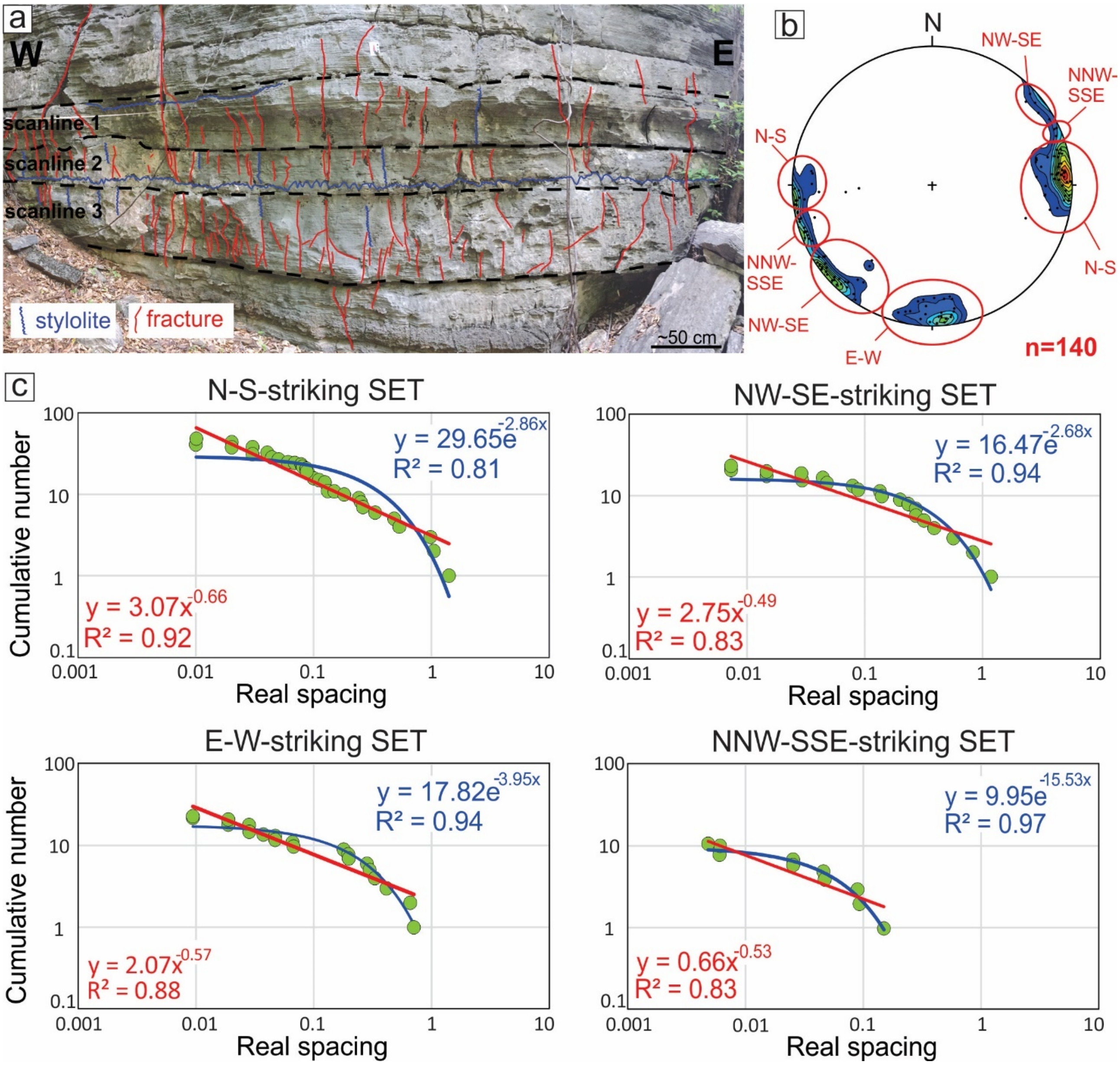

Figure 14. Quantitative structural data of the Torrinha site: (a) Outcrop view of the investigated beds outside the cave; red lines used for the linedrawing are related to both SB and NSB fractures; (b) lower hemisphere equal-area projection of the poles and relative density contour plots representing the fractures; (c) log-log diagrams of the cumulative frequency distribution for fracture spacing; blue lines correspond to exponential law distribution and red lines correspond to power-law distribution calculated for the single fracture sets in the site.

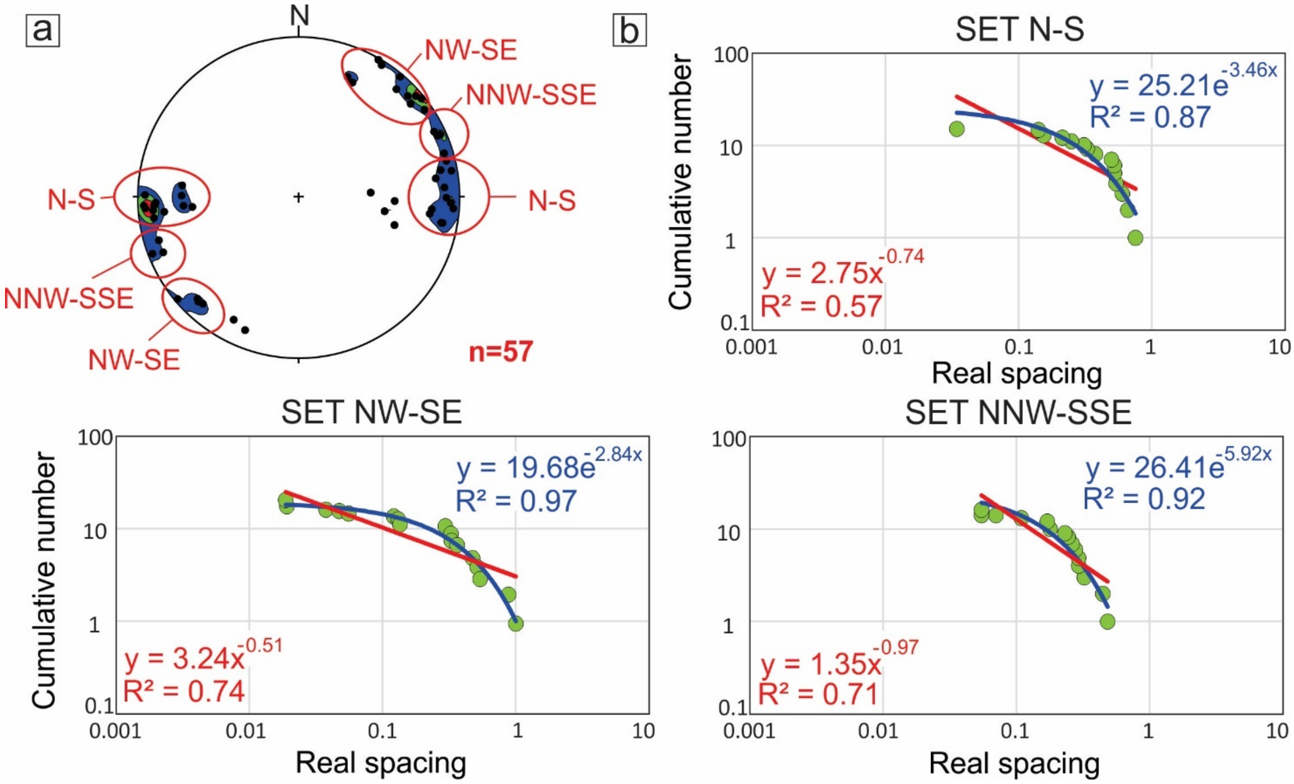

Figure 15. Quantitative data for the Paixão site: (a) lower hemisphere equal-area projection of the poles and relative density contour plots representing the fractures; (b) log-log diagram of the cumulative frequency distribution for fracture spacing; blue lines correspond to exponential-law distribution; red lines correspond to power-law distribution calculated for the single fracture sets in the site.

Table 1. The values of exponential distribution, power-law distribution, and Coefficient of variation (Cv) in different striking sets analyzed by scanline.

		Scanline direction (Az/dip)	**N-S striking set**			**NW-SE striking set**			**NNW-SSE striking set**			**E-W striking set**			**NE-SW striking set**			**Nº of fractures**
			Exponential dist. (R^2)	Power-law dist. (R^2)	Cv	Exponential dist. (R^2)	Power-law dist. (R^2)	Cv	Exponential dist. (R^2)	Power-law dist. (R^2)	Cv	Exponential dist. (R^2)	Power-law dist. (R^2)	Cv	Exponential dist. (R^2)	Power-law dist. (R^2)	Cv	
Ioiô cave	scanline 1	245/05	0.722	0.926	1.9	0.793	0.968	1.8	-	-	-	-	-	-	-	-	-	38
	scanline 2	245/05	-	-	-	0.763	0.954	1.9	0.772	0.968	1.7	-	-	-	-	-	-	33
	scanline 3	336/06	-	-	-	-	-	-	-	-	-	0.909	0.797	0.8	0.794	0.920	1.2	19
	scanline 4	336/06	-	-	-	-	-	-	-	-	-	-	-	-	0.945	0.948	0.7	15
Lapinha cave	scanline 1	084/02	0.984	0.798	1.0	-	-	-	0.956	0.747	1.0	-	-	-	0.661	0.952	2.3	65
	scanline 2	352/02	-	-	-	-	-	-	-	-	-	0.936	0.907	1.4	-	-	-	60
	scanline 3	078/03	0.962	0.743	1.0	-	-	-	-	-	-	-	-	-	0.658	0.797	2.1	43
Torrinha cave	scanline 1	082/01	0.961	0.856	1.1	-	-	-	0.970	0.840	1.0	-	-	-	-	-	-	36
	scanline 2	082/01	-	-	-	0.988	0.848	0.8	0.904	0.732	1.2	-	-	-	-	-	-	59
	scanline 3	082/01	0.782	0.896	1.5	0.939	0.830	0.9	-	-	-	-	-	-	-	-	-	80
	scanline 4	005/10	-	-	-	0.788	0.930	1.7	-	-	-	0.948	0.881	1.3	-	-	-	52
Paixão cave	scanline 1	064/05	0.856	0.743	0.3	-	-	-	-	-	-	-	-	-	-	-	-	28
	scanline 2	072/04	-	-	-	0.887	0.677	0.3	0.929	0.717	0.6	-	-	-	-	-	-	42
	scanline 3	072/04	0.966	0.707	0.6	0.970	0.767	0.9	-	-	-	-	-	-	-	-	-	43

2.2.5. Discussion

2.2.5.1. The origin of fracture corridors in multiple-direction fold hinges

The understanding of fracture corridors that connect different parts of reservoirs may provide useful information to predict fluid flow at a subseismic scale, optimizing oil field development planning. The studied cave systems suggest that subseismic flow pathways and related karst conduits developed along multiple-direction fold hinges following three stages of deformation: (i) burial-related background deformation that occurred during the overburden of the Salitre Formation, (ii) E-W compression, and (iii) N–S compression. Quantitative analysis performed in our study allowed for discriminating the fracture sets associated with burial (background deformation) from the fracture sets related to the fold-fault events (tectonic deformation) that played a key role in fluid migration.

Focusing on the fractures that have been analyzed, the first stage (background deformation) is characterized by cross-orthogonal bed perpendicular joints and veins in E-W and N–S striking sets (Fig. 4 a, b, 16 a). Such fracture sets and bed-parallel stylolites (Fig. 6 c, d), occurring both in bed-to-bed interfaces and within the beds could be associated with the overburden of the Salitre Formation (Ennes Silva et al., 2016).

Bed-parallel stylolites and bed-perpendicular folded veins indicate the variation in the stress fields that affected these carbonate rocks (Fig. 6 b). The crosscutting relationships indicate that the bed-parallel stylolites usually predate bed-perpendicular folded veins. However, mutual abutting relations occur between cross orthogonal bed-perpendicular joints and bed-parallel stylolites (Fig. 6 c, d). Permutation of the sub-horizontal σ_2 and σ_3 principal stress likely took place during burial diagenesis of the studied carbonate succession allowing for the formation of both N–S and E-W fracture sets (Figs. 4 b, 6 a) (Bai et al., 2002). The joint sets are mainly characterized by an exponential distribution, which is distinctive of a diffuse deformation (Ortega et al., 2006). Moreover, the range of Cv, between 0.34 and 0.85, is consistent with randomly distributed fractures (Gillespie et al., 1993).

The second stage of deformation is related to ENE-WSW shortening (Fig. 16 b) (D'Angelo et al., 2019). This tectonic compression is related to the Brasiliano orogeny (Ennes Silva et al., 2016), which developed gentle fold sets that display fold hinges mainly striking N–S (Fig. 7 d, e). During this second stage of deformation, nucleation and development of the NW-SE, NE-SW, NNE-SSW, and NNW-SSE-striking fracture sets occurred. These structural elements were associated with the reactivation of pre-existing N–S fractures and the development of incipient faults (and associated splays) observed by LiDAR images (Fig. 6 e, 6 f, 10 e, 11 e, 11 f, 11 g, 11 h). These fracture sets were described by a power-law distribution, typical of clustered deformation expressed along fold hinges. Cv values usually range from 1.0 to 2.2 (Table 1), and thus these fracture sets are ascribed to a folding event or a mature stage of faulting (de Joussineau and Aydin, 2007).

The third stage of deformation is associated with N–S shortening (Fig. 16 c), resulting in a basin-dome fold configuration (Ramsay, 1967). E-W-oriented fold hinges and NW-SE strike-slip faults (Fig. 10 c, e) are associated with this tectonic compression. The small right-lateral displacement of the N–S fold hinges (Fig. 10 a, b) reinforces the assumption that the N–S trends predate the NW-striking strike-slip fault development. The same contractional phases were also documented in other sites of the São Francisco craton (Cruz and Alkmim, 2006; Guimarães et al., 2011; Ennes-Silva et al., 2016; Klimchouk et al., 2016; D'Angelo et al., 2019).

In our study in the southern portion of the Salitre Formation, we suggest that the first contractional phase, evidenced by E-W shortening, originated N–S and NNE-SSW fold hinges and N–S-striking fractures that are more pervasive than the E-W fold hinges and E-W-striking fractures. The observed E-W-oriented fractures abutting against N–S-striking fractures (Figs. 4 a, 6 a), support this interpretation.

The proposed generation of superposed folds lead to the development of fracture corridors localized into fold hinges that predate the entry of fluid into the system. At the fractures intersections and fracture terminations, the karstification process is enhanced (Figs. 4 b, 9 d).

The development of karst conduits in the Salitre Formation carbonate units follows the structural and compositional controls mentioned above, but each cave has unique characteristics. We performed a statistical analysis to provide a useful model for comparing the fracture sets that influenced the development of karst conduits in each cave. For the Ioiô cave (Fig. 7), the N–S-, NW-SE-, and NE-SW-striking sets show a power-law distribution rather than an exponential distribution, and they could be associated with a localized deformation (fold-fault related, Ortega et al., 2006). The Cv of these fracture sets is higher than 1, whereas the N–S sets display Cv values greater than 1.9. Therefore, we affirm that the N–S-, NW-SE-, and NE-SW-striking sets are clustered and could be related to a folding process. The E-W-striking fracture set displays an exponential distribution and lower Cv of 0.8, which indicates a diffuse deformation. As the N–S-, NW-SE-, NNW-SSE-, and NE-SW-striking sets show a power-law distribution in the Ioiô site (Table 1), we conclude that the development of the Ioiô cave passages is related to fold-related fractures concentrated along fold hinges.

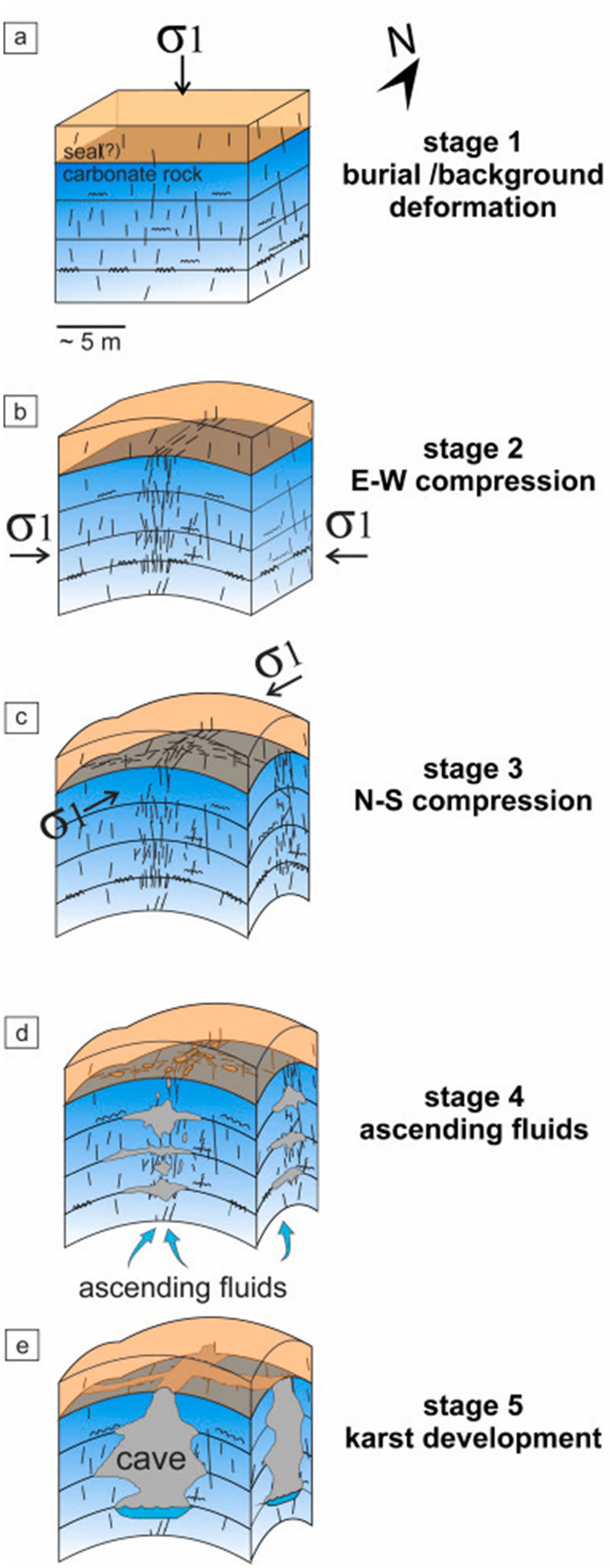

Figure 16. Evolutionary conceptual model proposed for development of the hypogenic conduits in carbonate units of the Salitre Formation, Brazil. (a) Background burial-related; (b) E-W; (c) N–S; (d) ascending fluids and; (e) karst development.

In the Lapinha cave (Fig. 8), all fracture sets (NE-SW, N–S, WNW-ESE, and E-W) show Cv values greater than 1, which indicates a clustered deformation (Gillespie et al., 1993; de Joussineau and Aydin, 2007). Only the NE-SW-striking set, with a Cv value of 2.3, shows a power-law distribution (Table 1). The range of Cv variations is consistent with both even-spaced and clustered fracture distributions in the carbonates (Gillespie et al., 1993). The Cv higher than 1 and variation in the power-law and exponential distributions implies that multiple-stage jointing occurred during the burial and subsequent evolution of the Salitre Formation.

The striking sets of the Torrinha cave (N–S, NNW-SSE, NW-SE and E-W, Fig. 10 b) show similar behavior, with Cv values higher than 1. Still, only the N–S striking set shows a more significant power-law distribution rather than exponential distribution, which is related to the aforementioned multiple-stage jointing. We suggest that mostly N–S-oriented joints were formed during the folding event, and the NNW-SSE-, NW-SE- and E-W-oriented striking sets may have formed during the burial and may have been reactivated during a tangential stress regime.

In the Paixão cave (Fig. 11 a), the N–S-, NW-SE- and NNW-SSE-striking sets (Fig. 15 a) are better explained by an exponential distribution rather than a power-law distribution. The Cv of these sets is lower than 1, from 0.3 to 0.9. Based on these values and the good fit with an exponential distribution, we suggest that these fractures did not originate during the folding process. These striking sets may have formed during the burial history of the Salitre Formation, and may have reactivated during the folding event.

2.2.5.2. Development of flow pathways along karst conduits

After the development of fracture sets and the extension localized along fold hinges causing the formation of fracture-corridors, rising fluid flow interacted with the surrounding rocks (Fig. 16 d). The dissolution process intensified, leading to the development of the conduits system (Fig. 16 e). Due to the very low primary porosity of the carbonate rocks, ranging from 0% to 7% (Cazarin et al., 2019), the fractures acted as initial preferential fluid pathways.

NSB fracture corridors localized along fold hinges increased permeability and connectivity (Fig. 3, Fig. 4 a, 4 b) (Bagni et al., 2020). The fluid-rock interaction may directly affect the fluid flow and storage (Evans and Fischer, 2012), creating high dissolution zones (super-K zones) (Fig. 4 c, 7 e, 7 f). The high dissolution/karstification along fracture corridors is evidenced by the cave pattern, forming a typical hypogene maze, lacking downward carving vadose infiltration passages typical of epigenic cave systems. The alignment of speleothems following these fractures highlights the presence of high permeability domains, which are still exploited by present epigenic infiltrating waters (Fig. 3, Fig. 4 a, Kim and Sanderson, 2010).

The vertical geometry and shape of the karst conduits is related to a lithologic/stratigraphic control. Even with the development of cave passages along fold hinges, differential degrees of karstification (Fig. 3) in the observed lithologies, based on the cross-section morphology of the cave, indicates that the development of the karst in carbonate rocks is also related to their composition. Field and laboratory analyses suggest that the composition of these rocks definitely influenced the karst development (de Melo et al., 2015; Baiyegunhi et al., 2017). Carbonate rocks with a finer grain size are more readily dissolved (Fig. 2 c). Moreover, the presence of pyrite (Palmer, 1990, Worthington and Ford, 1995) (Fig. 2 c) may have contributed to an increase in the karstification process by H_2S oxidation and production of aggressive H_2SO_4 (Auler and Smart, 2003; Tisato et al., 2012; D'Angeli et al., 2019). The primary porosity of these rocks is very low, so secondary porosity (i.e., fractures that are strongly related to the rock composition and layer properties, Balsamo et al., 2020) guides karstification (Cazarin et al., 2019). The layers characterized by lower dissolution correspond to grainstone with clasts and coarser grain size (Fig. 2 f, g) and mudstone interspersed with siltstone layers with high detritic mineral content (15–20%), mainly quartz grains (Fig. 2 d, e). The compositional variation in the wall rocks leads to the present-day visible karst geometry.

Also faults may form preferential flow paths and guide fluid migration (Ligtenberg, 2004; Wilson et al., 2011; Ogata et al., 2012, 2014; Balsamo et al., 2019). Karst development may also follow fracture corridors generated in fault damage zones (Fig. 10 e, Ogata et al., 2014; Pisani et al., 2021). The process of karstification in faults, as well as in folded zones, is observed worldwide, for example, in the Tarim Basin where these areas represent ideal targets for oil (Xu et al., 2017). In the Paixão Cave, it was observed that cave passages developed following an *en echelon* pattern (Fig. 10 b, c). In the central portion of the fault zone, which has the highest deformation and displacement (Ogata et al., 2014), a subvertical master fault was observed (Fig. 10 e, f) and a transtensive structure developed at the edge of the fault zone (Fig. 10 g, h). In our study area, faults and fault zones were observed in some of the analyzed caves (Figs. 10 e and Fig. 11 h). Some of these faults strongly condition the orientation and spatial distribution of the conduits, like in Paixão Cave (Fig. 11). In the central portion of the fault zone, which has the highest deformation and displacement rates (Ogata et al., 2014), a subvertical transtensive slip surface was observed (Fig. 10 e, f) and associated splay structures developed at the edge of the fault zone. The presence of splay fractures and damage zones with highly fractured rocks played a critical role for channeling fluid flow and dissolution zones. In other cases, such as the Torrinha Cave (Fig. 10), the NW-SE strike-slip fault seems not to be a controlling element for fluid flow. This evidence imply that fault zones architectures and the spatial-temporal evolution of their associated fractures may play a critical role for permeability and karstification.

2.2.5.3. Implications for fluid flow in carbonate units

Tectonic structures greatly impact the fluid flow in carbonate units (Goldscheider, 2005; Dewever et al., 2010; Pantou, 2014; Agosta et al., 2015; Cosgrove, 2015; Ennes-Silva et al., 2016; Wang et al., 2017; Boersma et al., 2019; Balsamo et al., 2020; Pisani et al., 2021). Structures such as fracture corridors often form preferential zones for fluid flow (Ogata et al., 2014; Souque et al., 2019), but the location of their occurrence is an enormous challenge for the oil industry because they are barely visible at a seismic resolution (Lamarche et al., 2018). Understanding the key factors in their formation, distribution and geometry may contribute to flow modeling for fractured carbonate rocks (Goldscheider, 2005) and to the assessment of their impacts on the development of karstified reservoirs.

Structural data allowed for correlating diffuse and localized fold-fault-related deformation with influence on the development of the hypogenic caves analyzed. This information provides new insights on storage and fluid flow properties. The qualitative analysis indicates that the development of the karst-conduits investigated is mainly related to highly persistent fractures, usually visible along the central portion of the ceiling of these caves and parallel to the fold hinges (Evans and Fischer, 2012), creating a high-dissolution zone (Fig. 4 c, 7 e, f). This evidence was also reported and documented in many other cases around the world, including the Middle East oil fields, pre-salt reservoirs offshore Brazil, and the Tarim Basin in China (Pollastro, 2003; Menezes et al., 2016; Li et al., 2018). Li et al. (2018) also highlighted that trending fractures in the extensional area of faulted folds are better developed than the fractures in the limb of folds, improving the migration of fluids and permeability in tight sandstone reservoirs. Based on our observations of high-dissolution zones located in the extensional area of folds (Fig. 3; 7 c, d), it is possible to verify the same behavior in carbonate rocks and carbonate reservoirs.

Fluid flow events in carbonates subdued by tectonic compression was described by Warren et al. (2014), who integrated isotope data with structural surveys. Morley et al. (2014) highlighted the relevance of fluid flow in fold-and-thrust belts in deep aquifers and onshore (offshore Brunei and the Central Basin of Iran, respectively), while Pisani et al. (2021) studied a similar outcropping setting with karstification focused in fault zones and fracture cluster zones in a thrust-related anticline characterized by accumulation of hydrocarbons. Both works emphasize the importance of fractures in the migration of fluids and in the fluid-rock interaction. Here, we highlight the importance of fracture corridors that, similar to fractures, act as fluid pathways in fold-and-thrust environments.

The LiDAR is a very useful tool for detailed cave mapping. Fabbri et al. (2017) used TLS to make detailed 3D models for morphometric measurements. De Waele et al. (2018) used TLS and 3D photogrammetry to identify different evolution stages of ceiling channels. Here, we applied both TLS and MLS to observe the karst geometry/shape (Fig. 3, Fig. 7 e, 11 f); the MLS showed more accurate results due to the ability to move the instrument through both narrow and large cave passages without interrupting during acquisition.

The karst conduit shape is a response to the interaction between flow, structural features, and the composition of the carbonate rocks. Structural features such as fractures and fracture corridors provide space for vertical rising flow, and horizontal enlargement occurs laterally along preferential carbonate layers (Klimchouk, 2009). This enlargement occurs mainly in presence of mudstones with a silt grain size and pyrite content that boost the carbonate dissolution by sulfide oxidation. Carbonate layers with a coarse grain size, a higher detrital mineral content, and an absence of pyrite may hinder the fluid flow and concentrate the dissolution in subjacent layers, confining the ascending fluid and intensifying a horizontal fluid circulation (Klimchouk et al., 2016), leading to the ellipsoidal cross-sectional shape of the karst corridors.

2.2.6. Conclusions

The hypogenic caves are mainly developed following fracture corridors along orthogonal fold hinges. These fracture sets were initially randomly distributed and reactivated during the folding event, with preferential N–S and E-W strikes, providing localized deformation in the fold hinges generated by the compressional stages that affected the carbonate rocks. These structural elements result from the shearing and linkage of pre-existing, bed-confined N–S- and E-W-striking fractures and the formation of NW-SE-, NE-SW-, NNE-SSW-, and NNW-SSE-striking tail joints, which clustered at the mode-II extensional quadrants and along the Mode-III terminations of the sheared N–S and E-W elements.

The positions of fold-hinges control the fold-related N–S- and E-W-striking fractures and the development of fracture corridors and karst conduits. Although fracture corridors are barely visible on the subseismic scale, these tectonic structures could be related to regional structures, such as fold hinges, that could be observed on maximum-curvature maps.

The structural data and the karstification processes that affect the carbonate rocks of the Salitre formation indicate that cave development following the main structural features of the area is strongly influenced by fold hinges and faults. The major results of this research contribute to the prediction of karst geometry and its occurrence are summarized below:

1. In plan view, the cave passages are orthogonal, with a maze pattern, following the structural control of the area, and are expressed as fracture corridors along fold hinges and faults. The development of subseismic flow pathways is directly related to the structural features that affect these rocks.
2. The vertical profile of the cave passages shows an ellipsoidal shape/geometry due to the textural variation that provides different karstification levels. Carbonate layers that have more pyrite and less detrital minerals in their composition are more karstified and can act as flow pathways. Carbonate layers with a coarser grain size and higher detrital minerals content hinder the karstification. These layers often act as seals to rising fluid flow.
3. Fracture corridors are formed along fold hinges, even in gentle folds with a bedding dip less than ~10°. These fracture corridors behave as high-permeability zones (super K-zones) that facilitate the vertical fluid percolation and the karstification process. These fracture corridors are strongly related to fluid migration.
4. Cave passages may develop during or after fracturing and faulting. The secondary porosity due to faulting is essential to fluid percolation. In addition, the karstification process is intensified at intersections between distinct fracture sets.
5. The subseismic flow pathways and karst conduits can be predicted by accurate structural analysis. Both diffuse and localized deformation, related to folds or faults, may increase the process of karstification. The development of subseismic flow pathways and karst conduits is intensified in a localized deformation due to the clustered fractures that provide pathways and enhance the fluid flow.

Acknowledgments

We thank an anonymous reviewer and the JSG editor for their comments, which improved our manuscript. This research was carried out in association with the ongoing R&D project registered as

ANP 20502–1, “Processos e Propriedades em Reservartórios Carbonáticos Fraturados e Carstificados – POROCARSTE 3D” (UFRN/UNB/UFRJ/UFC/Shell Brasil/ANP) – Porokarst – Processes and Properties in Fractured and Karstified Carbonate Reservoirs, sponsored by Shell Brasil under the ANP R&D levy as “Compromisso de Investimento com Pesquisa e Desenvolvimento”. Cave maps were kindly provided by Grupo Bambuí de Pesquisas Espeleológicas. Cave sampling was performed through SISBIO permit 63178/1. Many thanks to Alisson Jordão and Uilson Teixeira for the fieldwork and Umberto Del Vecchio of ViGeA Reggio Emilia (Italy) for the fieldwork and elaboration of the LiDAR surveys.

References

Agosta, F., Wilson, C., Aydin, A., 2015. The role of mechanical stratigraphy on normal fault growth across a Cretaceous carbonate multi-layer, central Texas (USA). Ital. J. Geosci. 134, 423–441.

Alkmim, F.F., Martins-Neto, M.A., 2012. Proterozoic first-order sedimentary sequences of the São Francisco craton, eastern Brazil. Mar. Pet. Geol. 33, 127–139.

Allmendinger, R.W., Cardozo, N., Fisher, D.M., 2011. Structural geology algorithms: Vectors and tensors, Structural Geology Algorithms: Vectors and Tensors.

Almeida, F.F.M. De, Brito Neves, B.B. De, Dal Ré Carneiro, C., 2000. The origin and evolution of the South American platform. Earth Sci. Rev. 50, 77–111.

Antonellini, M., Nannoni, A., Vigna, B., De Waele, J., 2019. Structural control on karst water circulation and speleogenesis in a lithological contact zone: The Bossea cave system (Western Alps, Italy). Geomorphology 345, 106832.

Araújo, R.E.B., La Bruna, V., Rustichelli, A., Bezerra, F.H.R., Xavier, M.M., Audra, P., Barbosa, J.A., Antonino, A.C.D., 2021. Structural and sedimentary discontinuities control the generation of karst dissolution cavities in a carbonate sequence, Potiguar Basin, Brazil. Marine and Petroleum Geology 123, 104753.

Audra, P., Palmer, A.N., 2011. Structure des réseaux karstiques : Les contrôles de la spéléogenèse épigène. Geomorphol. Reli. Process. Environ. 359–378.

Auler, A.S., 1999. Karst evolution and paleoclimate of eastern Brazil. University of Bristol.

Auler, A.S., Smart, P.L., 2003. The influence of bedrock-derived acidity in the development of surface and underground karst: Evidence from the Precambrian carbonates of semi-arid northeastern Brazil. Earth Surf. Process. Landforms 28, 157–168.

Auler, A.S., Klimchouk, A., Bezerra, F.H.R., Cazarin, C.L., Ennes-Silva, R., Balsamo, F., 2017. Origin and Evolution of Toca da Boa Vista and Toca da Barriguda Cave System in North-eastern Brazil, in: Hypogene Karst Regions and Caves of the World, Cave and Karst Systems of the World. 827–840.

Bagni, F.L., Bezerra, F.H., Balsamo, F., Maia, R.P., Dall'Aglio, M., 2020. Karst dissolution along fracture corridors in an anticline hinge, Jandaíra Formation, Brazil: Implications for reservoir quality. Mar. Pet. Geol. 115, 104249.

Bai, T., Maerten, L., Gross, M.R., Aydin, A., 2002. Orthogonal cross joints: Do they imply a regional stress rotation? J. Struct. Geol. 24, 77–88.

Baiyegunhi, C., Liu, K., Gwavava, O., 2017. Diagenesis and reservoir properties of the Permian Ecca Group sandstones and mudrocks in the Eastern Cape Province, South Africa. Minerals 7(6), 88.

Balsamo, F., Bezerra, F.H.R., Klimchouk, A.B., Cazarin, C.L., Auler, A.S., Nogueira, F.C., Pontes, C., 2020. Influence of fracture stratigraphy on hypogene cave development and fluid flow anisotropy in layered carbonates, NE Brazil. Mar. Pet. Geol. 114, 104207.

Balsamo, F., Clemenzi, L., Storti, F., Solum, J., Taberner, C., 2019. Tectonic control on vein attributes and deformation intensity in fault damage zones affecting Natih platform carbonates, Jabal Qusaybah, North Oman. Journal of Structural geology, v. 122, pp. 38-57.

Balsamo, F., Clemenzi, L., Storti, F., Mozafari, M., Solum, J., Swennen, R., Taberner, C., Tueckmantel, C., 2016. Anatomy and paleofluid evolution of laterally-restricted extensional fault zones in the Jabal Qusaybah anticline, Salakh Arc, Oman. Geological Society of America Bulletin 128, 957–972.

Bertotti, G., Audra, P., Auler, A., Bezerra, F.H., de Hoop, S., Pontes, C., Prabhakaran, R., Lima, R., 2020. The Morro Vermelho hypogenic karst system (Brazil): Stratigraphy, fractures, and flow in a carbonate strike-slip fault zone with implications for carbonate reservoirs. Am. Assoc. Pet. Geol. Bull. 104, 2029–2050.

Boersma, Q., Prabhakaran, R., Bezerra, F.H., Bertotti, G., 2019. Linking natural fractures to karst cave development: a case study combining drone imagery, a natural cave network and numerical modelling. Pet. Geosci. 25(4), 454-469.

Cazarin, C.L., Bezerra, F.H.R., Borghi, L., Santos, R. V., Favoreto, J., Brod, J.A., Auler, A.S., Srivastava, N.K., 2019. The conduit-seal system of hypogene karst in Neoproterozoic carbonates in northeastern Brazil. Mar. Pet. Geol. 101, 90–107.

Chen, Z., Auler, A.S., Bakalowicz, M., Drew, D., Griger, F., Hartmann, J., Jiang, G., Moosdorf, N., Richts, A., Stevanovic, Z., Veni, G., Goldscheider, N., 2017. The World Karst Aquifer Mapping project: concept, mapping procedure and map of Europe. Hydrogeology Journal 25, 771–785.

Condie, K.C., 2002. The supercontinent cycle: Are there two patterns of cyclicity? J. African Earth Sci. 35, 179–183.

Cosgrove, J.W., 2015. The association of folds and fractures and the link between folding, fracturing and fluid flow during the evolution of a fold-thrust belt: A brief review. Geol. Soc. Spec. Publ. 421, 41–68.

Cruz, S.C.P., Alkmim, F.F., 2006. The tectonic interaction between the Paramirim aulacogen and the Araçuaí belt, São Francisco craton region, Eastern Brazil. An. Acad. Bras. Cienc. 78, 151–173.

D'Angeli, I.M., Parise, M., Vattano, M., Madonia, G., Galdenzi, S., De Waele, J., 2019. Sulfuric acid caves of Italy: A review. Geomorphology 333, 105–122.

D'Angelo, T., Barbora, M. S. C., Danderfer Filho, A., 2019. Basement controls on cover deformation in eastern Chapada Diamantina, northern São Francisco Craton, Brazil: Insights from potential field data. Tectonophysics 772, 228-231.

Davatzes, N.C., Aydin, A., 2003. Overprinting faulting mechanisms in high porosity sandstones of SE Utah. J. Struct. Geol. 25, 1795–1813.

de Joussineau, G., Aydin, A., 2007. The evolution of the damage zone with fault growth in sandstone and its multiscale characteristics. J. Geophys. Res. Solid Earth 112, 1–19.

de Melo, M.S., Guimarães, G.B., Chinelatto, A.L., Giannini, P.C.F., Pontes, H.S., Chinelatto, A.S.A., Atencio, D., 2015. Kaolinite, illite and quartz dissolution in the karstification of Paleozoic sandstones of the Furnas Formation, Paraná Basin, Southern Brazil. J. South Am. Earth Sci. 63, 20–35.

De Waele, J., Fabbri, S., Santagata, T., Chiarini, V., Columbu, A., Pisani, L., 2018. Geomorphological and speleogenetical observations using terrestrial laser scanning and 3D photogrammetry in a gypsum cave (Emilia Romagna, N. Italy). Geomorphology 319, 47–61.

De Waele, J., Plan, L., Audra, P., 2009. Recent developments in surface and subsurface karst geomorphology: An introduction. Geomorphology 106, 1–8.

Dewever, B., Berwouts, I., Swennen, R., Breesch, L., Ellam, R.M., 2010. Fluid flow reconstruction in karstified Panormide platform limestones (north-central Sicily): Implications for hydrocarbon prospectivity in the Sicilian fold and thrust belt. Mar. Pet. Geol. 27, 939–958.

Dublyansky, Y., 2012. Hydrothermal caves, Second Edi. ed, Encyclopedia of Caves. Elsevier Inc.

Dunham, R.J., 1962. Classification of carbonate rocks according to depositional texture. In: Ham, W.E. (Ed.), Classification of Carbonates Rocks. AAPG Memoir I, 108–121.

Ennes-Silva, R.A., Bezerra, F.H.R., Nogueira, F.C.C., Balsamo, F., Klimchouk, A., Cazarin, C.L., Auler, A.S., 2016. Superposed folding and associated fracturing influence hypogene karst development in Neoproterozoic carbonates, São Francisco Craton, Brazil. Tectonophysics 666, 244–259.

Evans, M.A., Fischer, M.P., 2012. On the distribution of fluids in folds: A review of controlling factors and processes. J. Struct. Geol. 44, 2–24.

Fabbri, S., Sauro, F., Santagata, T., Rossi, G., Waele, D., 2017. High-resolution 3-D mapping using terrestrial laser scanning as a tool for geomorphological and speleogenetical studies in caves: an example from the Lessini mountains (North Italy). Geomorphology 280, 16-29.

Frumkin, A., 2013. New Developments of Karst Geomorphology Concepts. Treatise on Geomorphology 6, 1–13.

Gholpoiur, A.M., Cosgrove, J.W., Ala, M., 2016. New theoretical model for predicting and modelling fractures in folded fractured reservoirs. Pet. Geosci. 22, 257–280.

Gillespie, P.A., Howard, C.B., Walsh, J.J., Watterson, J., 1993. Measurement and characterisation of spatial distributions of fractures. Tectonophysics 226, 113–141.

Giuffrida, A., Agosta, F., Rustichelli, A., Panza, E., La Bruna, V., Eriksson, M., Torrieri, S. Giorgioni, M. (2020). Fracture stratigraphy and DFN modelling of tight carbonates, the case study of the Lower Cretaceous carbonates exposed at the Monte Alpi (Basilicata, Italy). Marine and Petroleum Geology, 112, 104045.

Giuffrida, A., La Bruna, V., Castelluccio, P., Panza, E., Rustichelli, A., Tondi, E., Giorgioni, M., Agosta, F., 2019. Fracture simulation parameters of fractured reservoirs: Analogy with outcropping carbonates of the Inner Apulian Platform, southern Italy. J. Struct. Geol. 123, 18–41.

Goldscheider, N., 2005. Fold structure and underground drainage pattern in the alpine karst system Hochifen-Gottesacker. Eclogae Geol. Helv. 98, 1–17.

Guerriero, V., Iannace, A., Mazzoli, S., Parente, M., Vitale, S., Giorgioni, M., 2010. Quantifying uncertainties in multi-scale studies of fractured reservoir analogues: Implemented statistical analysis of scan line data from carbonate rocks. J. Struct. Geol. 32, 1271–1278.

Guerriero, V., Vitale, S., Ciarcia, S., Mazzoli, S., 2011. Improved statistical multi-scale analysis of fractured reservoir analogues. Tectonophysics 504, 14–24.

Guimarães, J.T., Misi, A., Pedreira, A.J., Dominguez, J.M.L., 2011. The Bebedouro Formation, Una Group, Bahia (Brazil). Geol. Soc. Mem. 36, 503–508.

Jacquemyn, C., Swennen, R., Ronchi, P., 2012. Mechanical stratigraphy and (palaeo-) karstification of the Murge area (Apulia, southern Italy). Geol. Soc. London, Spec. Publ. 370, 169–186.

Kim, Y.S., Sanderson, D.J., 2010. Inferred fluid flow through fault damage zones based on the observation of stalactites in carbonate caves. J. Struct. Geol. 32, 1305–1316.

Klimchouk, A.B., Ford, D.C., 2000. Lithologic and structural controls of dissolutional cave development. Speleogenesis: Evolution of Karst Aquifers, 54–64.

Klimchouk, A., 2009. Morphogenesis of hypogenic caves. Geomorphology 106, 100–117.

Klimchouk, A., Auler, A.S., Bezerra, F.H.R., Cazarin, C.L., Balsamo, F., Dublyansky, Y., 2016. Hypogenic origin, geologic controls and functional organization of a giant cave system in Precambrian carbonates, Brazil. Geomorphology 253, 385–405.

Klimchouk, A., Palmer, A.N., De Waele, J., Auler, A.S., Audra, P., 2017. Hypogene Karst Regions and Caves of the World, Cave and Karst Systems of the World. Springer International Publishing, Cham.

La Bruna, V., Agosta, F., Prosser, G., 2017. New insights on the structural setting of the Monte Alpi area, Basilicata, Italy. Ital. J. Geosci. 136, 220–237.

La Bruna, V., Agosta, F., Lamarche, J., Viseur, S., Prosser, G., 2018. Fault growth mechanisms and scaling properties in foreland basin system: The case study of Monte Alpi, Southern Apennines, Italy. J. Struct. Geol. 116, 94–113.

La Bruna, V., Lamarche, J., Agosta, F., Rustichelli, A., Giuffrida, A., Salardon, R., Marié, L., 2020. Structural diagenesis of shallow platform carbonates: Role of early embrittlement on fracture setting and distribution, case study of Monte Alpi (Southern Apennines, Italy). J. Struct. Geol. 131, 103940.

Lamarche, J., Gauthier, B.D.M., Ondicolberry, G., Fleury, J.T., 2018. Fracture Corridors in Fold and Thrust Zone, Devonian Sandstones Icla Syncline (Bolivia). In Third EAGE Workshop on Naturally Fractured Reservoirs (Vol. 2018, No. 1, pp. 1-5). European Association of Geoscientists & Engineers.

Li, Y., Hou, G., Hari, K.R., Neng, Y., Lei, G., Tang, Y., Zhou, L., Sun, S., Zheng, C., 2018. The model of fracture development in the faulted folds: The role of folding and faulting. Mar. Pet. Geol. 89, 243–251.

Ligtenberg, H., 2004. Fault seal analysis by enhancing fluid flow paths and fault irregularities in seismic data. AAPG Int. Conf., October 24-27, 2004, Cancun, Mexico.

Lyu, X., Zhu, G., Liu, Z., 2020. Well-controlled dynamic hydrocarbon reserves calculation of fracture–cavity karst carbonate reservoirs based on production data analysis. J. Pet. Explor. Prod. Technol. 10, 2401–2410.

Marrett, R., Ortega, O.J., Kelsey, C.M., 1999. Extent of power-law scaling for natural fractures in rock. Geology 27, 799–802.

Matthäi, S.K., Belayneh, M., 2004. Fluid flow partitioning between fractures and a permeable rock matrix. Geophys. Res. Lett. 31, L07602.

Menezes, C., Martins Compan, A.L., Surmas, R., 2016. Permeability estimation using ultrasonic borehole image logs in dual-porosity carbonate reservoirs. Petrophysics 57, 620–637.

Miranda, T.S., Barbosa, J.A., Gale, J.F.W., Marrett, R., Gomes, I., Neumann, V.H.L.M., Matos, G.C., Correia, O.J., Alencar, M.L., 2014. Natural Fracture Characterization in Aptian Carbonates, Araripe Basin, NE Brazil, in: 76th EAGE Conference & Exhibition. Amsterdam, The Netherlands.

Misi, A., Veizer, J., 1998. Neoproterozoic carbonate sequences of the Una Group, Irecê Basin, Brazil: chemostratigraphy, age and correlations. Precambrian Res. 89, 87–100.

Montaron, B., 2008. Confronting Carbonates, in: Oil Review Middle East. Abu Dhabi.

Morley, C.K., Warren, J., Tingay, M., Boonyasaknanon, P., Julapour, A., 2014. Comparison of modern fluid distribution, pressure and flow in sediments associated with anticlines growing in deepwater (Brunei) and continental environments (Iran). Mar. Pet. Geol. 55, 230–249.

Myers, R., Aydin, A., 2004. The evolution of faults formed by shearing across joint zones in sandstone. J. Struct. Geol. 26, 947–966.

Mylroie, J.E., 2012. Coastal caves, Second Edi. ed, Encyclopedia of Caves. Elsevier Inc.

Narasimhan, T.N., 2005. Hydrogeology in North America: Past and future. Hydrogeol. J. 13, 7–24.

Odonne, F., Lézin, C., Massonnat, G., Escadeillas, G., 2007. The relationship between joint aperture, spacing distribution, vertical dimension and carbonate stratification: An example from the Kimmeridgian limestones of Pointe-du-Chay (France). J. Struct. Geol. 29, 746–758.

Ogata, K., Senger, K., Braathen, A., Tveranger, J., Olaussen, S., 2012. The importance of natural fractures in a tight reservoir for potential CO_2 storage: a case study of the upper Triassic–middle Jurassic Kapp Toscana Group (Spitsbergen, Arctic Norway). Geol. Soc. London, Spec. Publ. 374, 395–415.

Ogata, K., Senger, K., Braathen, A., Tveranger, J., 2014. Fracture corridors as seal-bypass systems in siliciclastic reservoir-cap rock successions: Field-based insights from the Jurassic Entrada Formation (SE Utah, USA). J. Struct. Geol. 66, 162–187.

Ortega, O.J., Marrett, R.A., Laubach, S.E., 2006. A scale-independent approach to fracture intensity and average spacing measurement. Am. Assoc. Pet. Geol. Bull. 90, 193–208.

Palmer, A., 2016. Groundwater processes in karst terrains.

Palmer, A.N., 2007. Cave geology. Cave Books, Dayton.

Pantou, I., 2014. Impact of stratigraphic heterogeneity on hydrocarbon recovery in carbonate reservoirs: Effect of karst. Imperial College London.

Pisani, L., Antonellini, M., Angeli, I.M.D., Waele, J. De, 2021. Structurally controlled development of a sulfuric hypogene karst system in a fold-and-thrust belt (Majella Massif , Italy). Journal of Structural Geology 145, 104305.

Pollard, D.D., Aydin, A., 1988. Progress in understanding jointing over the past century. Spec. Pap. Geol. Soc. Am. 253, 313–336.

Pollastro, R.M., 2003. Total Petroleum Systems of the Paleozoic and Jurassic, Greater Ghawar Uplift and Adjoining Provinces of Central Saudi Arabia and Northern Arabian-Persian Gulf U.S. Geological Survey Bulletin 2202-H Total Petroleum Systems of the Paleozoic and Jurassic, US Geological Survey 2202-H.

Pontes, C.C.C., Nogueira, F.C.C., Bezerra, F.H.R., Balsamo, F., Miranda, T.S., Nicchio, M.A., Souza, J.A.B., Carvalho, B.R.B.M., 2019. Petrophysical properties of deformation bands in high porous sandstones across fault zones in the Rio do Peixe Basin, Brazil. Int. J. Rock Mech. Min. Sci. 114, 153–163.

Popov, P., Qin, G., Bi, L., Efendiev, Y., Ewing, R., Kang, Z., Li, J., 2007. Multiscale methods for modeling fluid flow through naturally fractured carbonate karst reservoirs. Proc. - SPE Annu. Tech. Conf. Exhib. 6, 3714–3722.

Questiaux, J.-M., Couples, G., Ruby, N., 2010. Fractured reservoirs with fracture corridors. Geophys. Prospect. 58, 279–295.

Railsback, L.B., 1998. Evaluation of spacing of stylolites and its implications for self-organization of pressure dissolution. J. Sediment. Res. 68, 2–7.

Ramsay, J.G., 1967. Folding and Fracturing of Rocks. McGraw-Hill, New York, pp. 568.

Santos, R.F.V.C., Miranda, T.S., Barbosa, J.A., Gomes, I.F., Matos, G.C., Gale, J.F.W., Neumann, V.H.L.M., Guimarães, L.J.N., 2015. Characterization of natural fracture systems: Analysis of uncertainty effects in linear scanline results. Am. Assoc. Pet. Geol. Bull. 99, 2203–2219.

Smeraglia, L., Giuffrida, A., Grimaldi, S., Pullen, A., La Bruna, V., Billi, A., Agosta, F., 2021. Fault-controlled upwelling of low-T hydrothermal fluids tracked by travertines in a fold-and-thrust belt, Monte Alpi, southern apennines, Italy. Journal of Structural Geology 144, 104276.

Souque, C., Knipe, R.J., Davies, R.K., Jones, P., Welch, M.J., Lorenz, J., 2019. Fracture corridors and fault reactivation: Example from the Chalk, Isle of Thanet, Kent, England. J. Struct. Geol. 122, 11–26.

Terzaghi, R.D., 1965. Sources of Error in Joint Surveys. Géotechnique 15, 287–304.

Tian, F., Lu, X., Zheng, S., Zhang, H., Rong, Y., Yang, D., Liu, N., 2017. Structure and Filling Characteristics of Paleokarst Reservoirs in the Northern Tarim Basin, Revealed by Outcrop, Core and Borehole Images. Open Geosci. 9, 266–280.

Tian, F., Zhang, H., Zheng, S., Lei, Y., Rong, Y., Lu, X., Jin, Q., Zhang, L., Liu, N., 2015. Multi-layered ordovician paleokarst reservoir detection and spatial delineation: A case study in the Tahe Oilfield, Tarim Basin, Western China. Mar. Pet. Geol. 69, 53–73.

Tisato, N., Sauro, F., Bernasconi, S.M., Bruijn, R.H.C., De Waele, J., 2012. Geomorphology Hypogenic contribution to speleogenesis in a predominant epigenic karst system: A case study from the Venetian Alps, Italy. Geomorphology 151–152, 156–163.

Wang, X., Lei, Q., Lonergan, L., Jourde, H., Gosselin, O., Cosgrove, J., 2017. Heterogeneous fluid flow in fractured layered carbonates and its implication for generation of incipient karst. Adv. Water Resour. 107, 502–516.

Warren, J., Morley, C.K., Charoentitirat, T., Cartwright, I., Ampaiwan, P., Khositchaisri, P., Mirzaloo, M., Yingyuen, J., 2014. Structural and fluid evolution of Saraburi Group sedimentary carbonates, central Thailand: A tectonically driven fluid system. Mar. Pet. Geol. 55, 100–121.

Wilson, C.E., Aydin, A., Durlofsky, L.J., Sagy, A., Emily, E., Kreylos, O., Kellogg, L.H., 2011. From outcrop to flow simulation: Constructing discrete fracture models from a LIDAR survey. Am. Assoc. Pet. Geol. Bull. 95, 1883–1905.

Worthington, S.R.H., Ford, D.C., 1995. High sulfate concentrations in limestone springs: An important factor in conduit initiation? Environ. Geol. 25, 9–15.

Xu, X., Chen, Q., Chu, C., Li, G., 2017. Tectonic evolution and paleokarstification of carbonate rocks in the Paleozoic Tarim Basin. Carbonates and Evaporites 32, 487–496.

Zambrano, M., Tondi, E., Korneva, I., Panza, E., Agosta, F., Janiseck, J.M., Giorgioni, M., 2016. Fracture properties analysis and discrete fracture network modelling of faulted tight limestones, Murge Plateau, Italy. Ital. J. Geosci. 135, 55-67.

Zhao, K., Zhang, L., Zheng, D., Sun, C., Dang, Q., 2015. A reserve calculation method for fracture-cavity carbonate reservoirs in Tarim Basin, NW China. Pet. Explor. Dev. 42, 277–282.

3. Silicification and high-permeability zones produced by hydrothermal alteration in mixed carbonate-siliciclastic sequences

This section of the thesis is focused on the research carried out in a cave developed in a mixed carbonate-siliciclastic sequence in the São Francisco Craton (Brazil). This extensive cave represents an ideal analogue of a deep-seated conduit network associated with silicified carbonate layers, like those found in many karst reservoirs in sedimentary basins (e.g., Tarim Basin, China; Campos and Santos Basins, Brazil; Kwanza Basin, Angola; Parkland Gas Field, Canada). Karst features in these basins are poorly investigated; however, understanding their genesis and geometry represents a challenging task that may be tackled combining detailed stratigraphic, geomorphologic, and geochemical investigations in accessible cave analogues. This section is organized in two articles. The first has been published in Marine and Petroleum Geology during 2022. The second article has been published in Basin Research in 2023. Both papers involve me as first author and corresponding author.

3.1

Published in Marine and Petroleum Geology 139 (2022)
https://doi.org/10.1016/j.marpetgeo.2022.105611

Silicification, flow pathways, and deep-seated hypogene dissolution controlled by structural and stratigraphic variability in a carbonate-siliciclastic sequence (Brazil)

Luca PISANI[1*], Marco ANTONELLINI[1], Francisco H.R. BEZERRA[2], Cristina CARBONE[3], Augusto S. AULER[4], Philippe AUDRA[5], Vincenzo LA BRUNA[2], Giovanni BERTOTTI[6], Fabrizio BALSAMO[7], Cayo C.C. PONTES[2], Jo DE WAELE[1]

1 Bologna University, Department of Biological, Geological and Environmental Sciences, Via Zamboni 67, 40126, Bologna, Italy. lucapiso94@gmail.com; marco.antonellini@unibo.it; jo.dewaele@unibo.it

2 Programa de Pós-Graduação em Geodinâmica e Geofísica, Federal University of Rio Grande Do Norte, Natal, Brazil. hilario.bezerra@ufrn.br; vincenzolabruna@gmail.com; cayopontes@gmail.com

3 DISTAV, Dipartimento di Scienze della Terra, dell'Ambiente e della Vita, Università di Genova, Corso Europa 26, Genova, Italy. carbone@dipteris.unige.it

4 Instituto Do Carste, Carste Ciência e Meio Ambiente, Belo Horizonte, Brazil. aauler@gmail.com

5 Polytech'Lab UPR 7498, University Cote d'Azur, Nice, France. Philippe.AUDRA@univ-cotedazur.fr

6 Department geoscience engineering, Technical University of Delft, Netherlands. G.Bertotti@tudelft.nl

7 Department of Chemistry, Life Sciences and Environmental Sustainability, University of Parma, Italy. fabrizio.balsamo@unipr.it

* Corresponding author

Abstract

Fractured and karstified carbonate units are key exploration targets for the hydrocarbon industry as they represent important reservoirs. Furthermore, large water reserves and geothermal systems are hosted in carbonate aquifers. This paper documents the relationships between stratigraphy, structural patterns, silicification, and the spatial-morphological organization of a 3D multistorey cave system developed in a Neoproterozoic mixed carbonate-siliciclastic sequence. We found that the combination of lithology, silicification, fracture patterns (controlled by lithostratigraphic variability), and petrophysical properties control the formation of high or low permeability zones;

their distribution was fundamental for the spatial organization of dissolution and the compartmentalization of the resulting conduit system in different speleogenetic storeys. We propose a deep-seated hydrothermal origin for the fluids involved in the main phases of karst formation. Warm and alkaline hydrothermal fluids caused silica dissolution, followed by chalcedony and quartz reprecipitation in pore space and fractures. Rising fluids concentrated along through-going vertical fracture zones in the lower storey, whereas sub-horizontal bedding-parallel fluid flow was focused on sedimentary packages containing highly silicified dolostones (SiO_2>80 wt.%) characterized by high permeability. The Calixto Cave is an enlightening example for the complex speleogenetic history affecting a mixed carbonate-siliciclastic succession where the combined effect of silicification and hydrothermal karst dissolution can potentially generate high-quality reservoirs.

Key words

Deep hydrothermal karst; Hypogene caves; Fluid flow; Karst reservoirs; Speleogenesis

3.1.1. Introduction

Silicification and karst dissolution in carbonate reservoirs are crucial processes that modify textures, mineralogy, and petrophysical properties of the host rock (Hesse, 1989; Lima et al., 2020; Souza et al., 2021). Karst features may be the result of rising fluid flow (hypogene speleogenesis; *sensu* Klimchouk, 2007), whose recharge and solutional efficiency are not connected to meteoric water percolation (i.e., epigene or supergene speleogenesis). The aggressivity of this rising flow is usually acquired from deep-seated sources, possibly associated with thermal processes, and is independent of soil or meteoric acids (Palmer, 2000; Audra and Palmer, 2015).

Many productive oil and gas deposits hosted in carbonate reservoirs are characterized by silicification and/or processes that can be assigned to hypogene karstification, like the Parkland field in Western Canada (Packard et al., 2001), the Tarim basin in China (Wu et al., 2007; Zhou et al., 2014; Dong et al., 2018; You et al., 2018), pre-salt reservoirs in Santos and Kwanza basins (Girard and San Miguel, 2017; Poros et al., 2017), and Campos Basin offshore Brazil (De Luca et al., 2017; Lima et al., 2020). Networks of deep-seated conduits formed by dissolution are often intercepted during drilling in hydrocarbon exploration within soluble rocks (Maximov et al., 1984; Mazzullo et al., 1996; Mazzullo, 2004). The result is loss of fluid circulation or borehole collapse (Xu et al., 2017). Furthermore, carbonate aquifers constitute the most significant geothermal water resources worldwide (Goldscheider et al., 2010; Montanari et al., 2017) and important groundwater reserves (Ford and Williams, 2007).

Even if less common than conventional carbonate-hosted karst, hypogene speleogenesis has also been documented in silicified carbonates, quartz sandstones, and quartzite rocks (La Bruna et al., 2021; Sauro et al., 2014; Souza et al., 2021). Cavities enlarged by solution in quartzites were also described associated with hydrothermal Sb–Hg mineralization in Kirghizstan (Leven, 1961; Kornilov, 1978) and in Ukraine (Tsykin, 1989).

The presence of solutional voids and karst porosity in quartzites or highly silicified carbonates is thought to be common at depth where the solubility of silica is larger due to the high temperatures and alkalinity of circulating solutions (Lovering et al., 1978; Andreychouk et al., 2009; Sauro et al., 2014; Wray and Sauro, 2017; Klimchouk, 2019). However, in the existing literature, only few publications addressed the link between silicification and the stratigraphic-structural control on karst development, with its relative implications in the study of carbonate reservoirs (La Bruna et al., 2021; Souza et al., 2021). These studies focused on the main geological, diagenetic, and structural framework of the cave-hosting rocks, without exploring the speleogenetic mechanisms involved in the formation of solutional porosity.

In the past decades there has been a growing interest on the source of karst forming fluids, subsurface flow pathways, and geometry of the conduits' networks, with particular attention to deep hypogene speleogenesis (Klimchouk, 2007, 2009, 2019; Audra et al., 2009; De Waele et al., 2009, 2016; Audra and Palmer, 2015; Ennes-Silva et al., 2016; Klimchouk et al., 2016; Columbu et al., 2021; Spötl et al., 2021). Hypogene dissolution at depth has strong implications for carbonate reservoir properties and quality, given that the geometry of the conduits and their spatial distribution may focus fluid flow and generate strong heterogeneities in porosity and permeability (Klimchouk et al., 2016; Balsamo et al., 2020). The characterization of karst reservoir porosity is, therefore, a challenging task, also because most of the dissolution voids are below seismic resolution (Cazarin et al., 2019; Lyu et al., 2020; La Bruna et al., 2021). To fill this knowledge gap and optimize decision-making strategies in the conceptualization and characterization of karst reservoirs, detailed investigations on analog accessible caves are needed (Balsamo et al., 2020; Bertotti et al., 2020; La Bruna et al., 2021; Pisani et al., 2021; Pontes et al., 2021).

Karst porosity and permeability development can result from different processes. Several factors, such as lithology, hydrogeologic setting and source of aggressive fluids (epigene vs. hypogene), geological structures, stratigraphy, geochemistry, and climate contribute to the large variety of karst features, their morphologies, and the spatial organization of conduit networks (Klimchouk et al., 2000; Palmer, 2000; Ford and Williams, 2007). In carbonate sequences, fracture properties, pattern, and mechanical stratigraphy may affect hypogene karst development, given that fluid flow in low primary porosity rocks is mainly controlled by open discontinuities (i.e., joints) (Antonellini et al., 2014; Guha Roy and Singh, 2016; Lei et al., 2017; Lavrov, 2017; Giuffrida et al., 2019, 2020). The spatial arrangement of bedding interfaces, stratabound fractures, stylolites, fault zones, and through-going vertical fracture-zones generates a complex tridimensional network that controls fluid flow in hypogene conditions. In this context, mechanical stratigraphy and fracture distribution cause a strong anisotropy in the tridimensional organization of flow pathways, speleogenesis, and conduit geometry (Klimchouk et al., 2009, 2016; Klimchouk, 2019; Balsamo et al., 2020; La Bruna et al., 2021).

The objective of this work is to unravel the structural and stratigraphic controls on hypogene dissolution in a complex 3D cave network (Calixto Cave, Northeastern Brazil) characterized by silicification of carbonate layers. Following a multidisciplinary approach, quantitative structural analyses, stratigraphic, petrographic and petrophysical investigations on rock samples were used to characterize the sedimentary sequence in the cave. Furthermore, compositional analysis (XRD, XRF) and SEM-EDS investigations on cave mineral deposits and bedrock were performed to study silicification and solutional micro-textures. Combining this approach with a comprehensive geomorphological analysis of the conduit system, we assessed the role of structural-stratigraphic variability in controlling the karst-forming flow pathways and the resulting spatial-morphological organization of the conduit system. The results from this study may be of great interest for improving conceptual models of deep-seated hypogene dissolution in silicified carbonate units, allowing more reliable reservoir or aquifer reconstructions, and optimizing conceptual predictive models.

3.1.2. Study area

3.1.2.1. Geological setting

The Calixto Cave System (CCS) is a 1.4 km long and 55 m deep cave located in the Una-Utinga Basin in the São Francisco Craton (State of Bahia, Brazil) (Fig. 1).

The São Francisco Craton is the western portion of a large crustal block segmented during the Pangea breakup and the opening of the South Atlantic Ocean (Almeida et al., 2000; Misi et al., 2011). The Una-Utinga basin (Fig. 2A) hosts a sedimentary succession of Neoproterozoic age (Una Group), which overlies the Archean and Paleoproterozoic basement composed of metamorphic and igneous rocks (Fig. 2B). The Una-Utinga and the Irecê basins formed during rifting of the Rodinia supercontinent between 950 and 600 Ma (Condie, 2002). The Bebedouro Fm, composed of glacio-marine diamictites, marks the bottom of the Group (Misi and Veizer, 1998; Misi et al., 2011). The Salitre Fm overlies in stratigraphic unconformity the Bebedouro Fm and is characterized by a mostly carbonate succession with variable thickness (minimum 500 m), intercalated with siliciclastic or heterolithic beds (Misi, 1993; Misi et al., 2007, 2011; Santana et al., 2021).

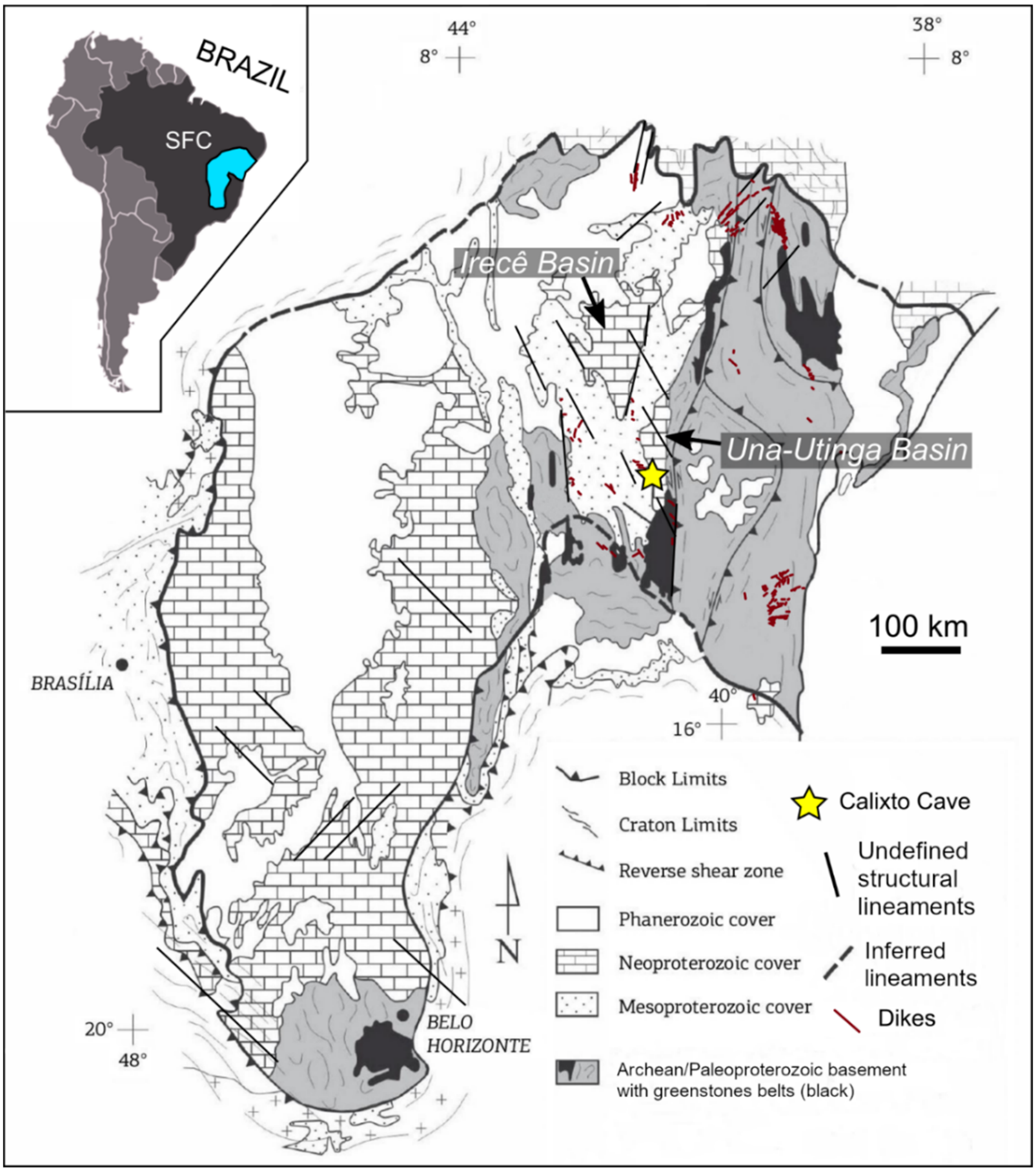

Figure 1. Simplified geological map showing the location of the Calixto Cave system (CCS) and the main structural lineaments of the São Francisco Craton (light blue color in the inset; modified after Almeida et al., 2000; Peucat et al., 2011, and Misi et al., 2011). Dike lineaments in the Bahia region were extracted from the 1:1,000,000 geological map of the State of Bahia (https://rigeo.cprm.gov.br/xmlui/handle/doc/8665).

Several geodynamic and tectonic events occurred in this area from ca. 740 to 560 Ma (Brito Neves et al., 2014). These events are broadly referred to as the Pan-African Cycle, or the *Brasiliano* Orogeny in South America (Teixeira et al., 2007). Strain in the Salitre Fm during the *Brasiliano* Orogeny resulted in a complex network of E-W- and NNE-SSW-trending deformed belts (Balsamo et al., 2020; Cazarin et al., 2021). These deformed belts include several fracture sets and a complex architecture of gentle folds characterized by fracture corridors localized in the hinge zone of the folds (Pontes et al., 2021). The most recent deformation events (540–510 Ma) were characterized by fissure magmatism and associated hydrothermal fluid flow along faults and fracture zones (Almeida et al., 2000; Guimarães et al., 2011; Klimchouk et al., 2016).

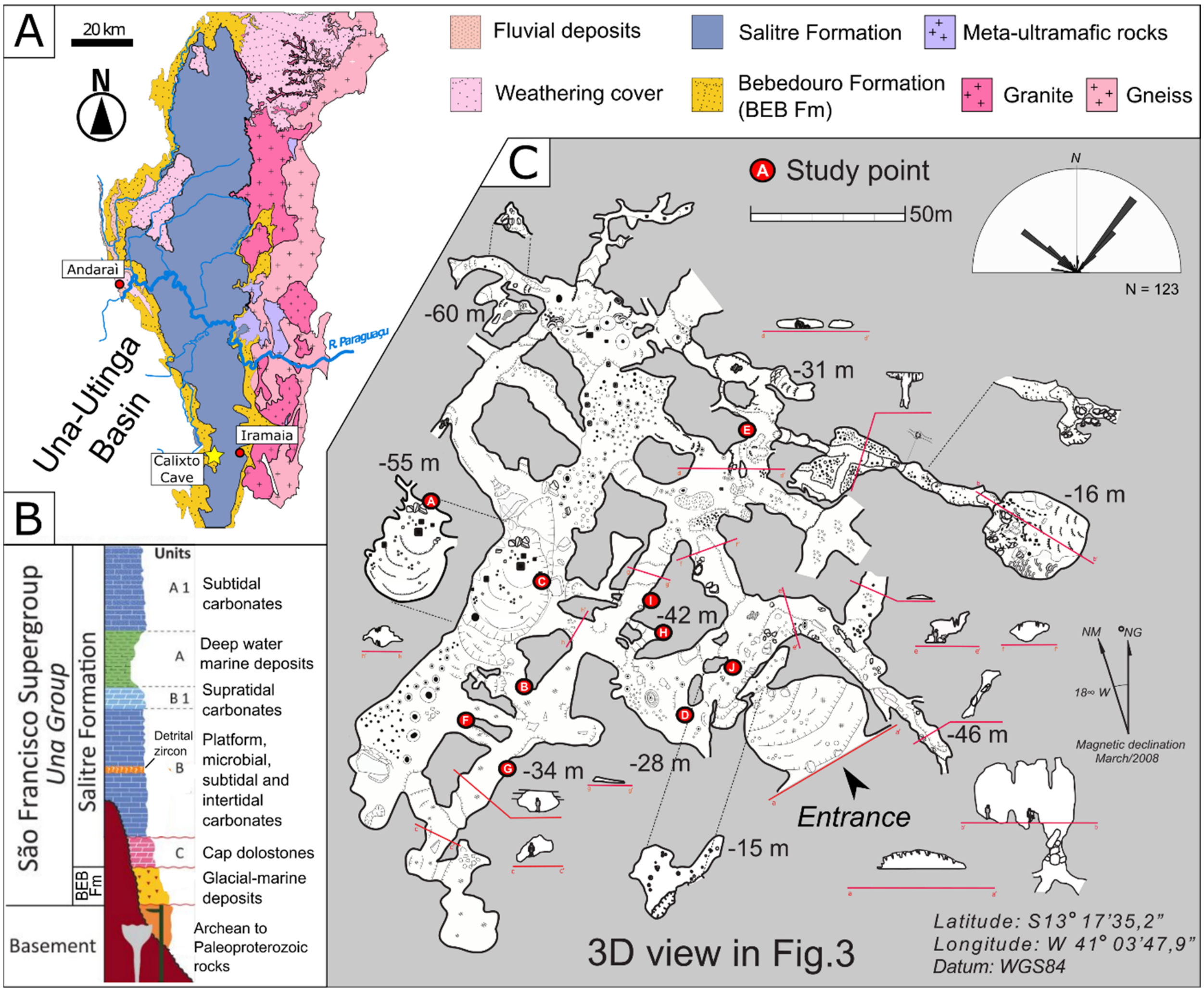

Figure 2. A) Simplified geological map of the Una-Utinga basin. B) Simplified stratigraphic log of the main formations outcropping in the Una Group (modified from Santana et al., 2021). C) Topographic plan map of the CCS. The rose diagram in the right corner shows the frequency distribution of conduits' orientation. Red circles indicate study points and depth values are reported for different locations. Cave map acquired by Grupo Pierre Marin de Espeleologia (GPME) in 2008. The coordinates shown in the lower-right corner refer to the cave entrance.

3.1.2.2. Hypogene caves and hydrothermal mineralization in the São Francisco Craton

The Una-Utinga and the Irecê basins host hundreds of karst systems, some of which are among the longest known in South America, with a combined cumulative length of over 140 km (Auler, 2017). Some of these karst systems developed in hypogene conditions by rising hydrothermal fluids that migrated upward through the fractured basement and that were horizontally confined by low-permeability (seal) layers (Klimchouk et al., 2016; Cazarin et al., 2019; Balsamo et al., 2020; Pontes et al., 2021). Following this, late-stage supergene sulfuric acid speleogenesis developed in shallow aquifers due to oxidation of bedrock sulfides (Auler and Smart, 2003).

Other works focused on silicified carbonate units and hypogene speleogenesis in the São Francisco Craton. Bertotti et al. (2020) highlighted the local development of caves associated with strike-slip fault zones and late silicification of dolostone layers (Morro Vermelho Cave, Irecê basin). North of the study area, in the Mesoproterozoic carbonates of Cabloco Fm, the Crystal Cave karst system shows dissolution features controlled by stratigraphy, deep tectonic structures, fracture corridors in fold hinges, and highly silicified layers (La Bruna et al., 2021; Souza et al., 2021). Furthermore, several cave systems in the Salitre Fm contain veins and deposits associated with hydrothermal mineral assemblages comprising quartz, chalcedony, barite, apatite, K-feldspar, hyalophane, iron oxides/hydroxides, iron-titanium oxides, and minor amounts of monticellite and diopside (Cazarin et al., 2019; Souza et al., 2021). Hydrothermal mineral assemblages and ore deposits have also been identified in the Una-Utinga and Irecê basins and their surrounding areas. These assemblages form Mississippi Valley-type (MVT) deposits containing quartz, sphalerite, barite, and galena (Kyle and Misi, 1997; Misi et al., 2012; Cazarin et al., 2021).

The Cambrian tectono-thermal event (~520 Ma) has been indicated as one of the probable drivers for hypogene speleogenesis in the Salitre Fm (Klimchouk et al., 2016). Late fracture reactivation and hydrothermal events during the Pangea breakup in the Jurassic-Cretaceous have also been proposed for the cave systems located in the northern part of the craton (Klimchouk et al., 2016; Cazarin et al., 2019). Other studies (Bertotti et al., 2020; Souza et al., 2021) proposed that the interplay between Si-rich fluids and karstification happened in mesodiagenetic deep-seated conditions during the late Proterozoic. If this is true, the solutional cavities in the silicified carbonates of the São Francisco Craton would be among the oldest known on Earth.

3.1.3. Material and methods

3.1.3.1. Cave morphological and topographic analysis

Karst features are the result of mineral dissolution by fluid flow and fluid-rock interactions (Klimchouk et al., 2016). Morphologies and patterns of karst conduits, together with their infillings, are the fundamental attributes that reflect their origin and evolution. The spatial and morphological organization of the CCS conduits were analyzed by direct field investigation, detailed morphological observations, and the processing of a speleological topographic survey (Fig. 2C) made in 2008 by the *Grupo Pierre Martin de Espeleologia* (GPME).

The CCS morphology and geological features were studied and mapped in 10 representative sites (Fig. 2C) and systematically documented throughout the whole karst system. The morphological analysis of the CCS included the study of cave macro-morphology in plan, profile, and 3D view as well as the examination of spatial-temporal relationships between the identified morphological features and the local stratigraphy, structures, and former fluid flow pathways.

The cave survey was processed using the *cSurvey* software (https://www.csurvey.it/) to obtain a tridimensional, geographically referenced model corrected for the 2008 magnetic declination. The *cSurvey* software allows reconstructing the volumes of the cave by interpolation of azimuth, distance, and inclination measurements collected with a handheld modified Leica DISTOX laser-meter (Heeb, 2009). The *cSurvey* data were merged with the manually edited sketch maps drafted by the surveyor (Heeb, 2009; Lønøy et al., 2020; Pisani et al., 2021). With this approach, a raw 3D georeferenced model of the whole 1.4 km-long system was assembled. Following this step, the planimetry of the cave was processed in *ArcGis* software to manually measure the preferential direction of the conduits, normalized by the length of each cave segment (same method described in Pisani et al., 2019).

3.1.3.2. Stratigraphic and structural analyses

We performed a detailed lithological and sedimentary facies description at several representative sites in the CCS (Fig. 2C) using outcrop observations and thin section petrographic analysis. Rock samples were collected using a geological hammer or a handheld electric driller to extract mini drill-cores from the cave walls (3.8 or 2.5 cm in diameter). 23 standard-thickness polished thin sections stained with blue epoxy were prepared and analyzed with an optical petrographic microscope both under transmitted and reflected light. Following the field and petrographic observations, the sedimentary sequence hosting the cave was subdivided in units, grouped according to their compositional and textural features. Carbonate rocks were classified based on their texture according to Dunham (1962) and Embry and Klovan (1971).

Structural measurements were collected in the survey points to unravel the nature, attitude, and kinematics of the observed fracture sets. Structural elements in the CCS were measured with classic geo-surveying tools (compass and clinometer) and classified according to their type: open-mode fractures (joints and veins), pressure solution seams (stylolites), faults, and fracture zones (FZ; defined as zones of through-going clustered fractures with an intensity larger than the background of the host rock). Joints, veins, and FZ include stratabound (bedding confined) and non-stratabound (through-going) structures. Statistical analysis of fracture sets was performed with the *DAISY3* software plotting lower-hemisphere equal-area stereograms, rose diagrams, and frequency histograms (Salvini, 2004). Grouping of the different fracture sets was performed by calculating the best-fit Gaussian-curves for each cluster of orientations (Salvini, 2004; Del Sole et al., 2020).

Furthermore, fracture attributes were measured along 12 linear scanlines in 5 representative transects (Marrett et al., 1999; Ortega et al., 2006) to estimate fracture permeability from field data (Giuffrida et al., 2019, 2020). The following parameters were measured for each discontinuity along the transect: attitude, distance from the origin of the scanline, type, mechanic aperture, height (when measurable), roughness, and infilling (if present). Along the transects, we also calculated fracture linear intensity P_{10} (Ortega et al., 2006) and the coefficient of variation (Cv), defined as the ratio between the $\pm 1\sigma$ standard deviation and the mean value of fracture spacing of individual fracture sets (Odling et al., 1999; Zambrano et al., 2016; Pontes et al., 2021).

The mechanic aperture (B) and roughness coefficient (JRC) of the fractures were measured using analogical profile comparators developed by Barton and Choubey (1977), and Ortega et al. (2006). Estimates for permeabilities of individual fractures were obtained using the parallel-plate model approximation (Taylor et al., 1999; Philipp et al., 2013; Giuffrida et al., 2020). Hydraulic aperture (*b*) was computed by considering the JRC and by applying the following equation (Barton and Choubey, 1977; Olsson and Barton, 2001; Giuffrida et al., 2020):

$$b = B^2 / \, JRC^{2.5}$$

Additionally, the real fracture spacing between individual features was calculated applying the Terzaghi method (1965).

The bulk permeability for each unit was then modeled as an Equivalent Porous Media (EPM; Taylor et al., 1999) combining the values of bedding-normal and bedding-parallel rock plugs permeability (considered equivalent to matrix permeability), fracture spacing, and estimated fracture permeability of individual sets. Bedding-parallel average permeability normal to the main fracture sets (K_N) and bedding-normal average permeability parallel to the main fracture sets (K_P) were calculated based on an elementary cubic volume of 1 m side using the equations described in Freeze and Cherry (1979) and reported in the Appendix B.

Given that natural fractures are neither smooth nor parallel, the reliability of applying the parallel-plate model to compute fracture permeability must be carefully considered (Zhang, 2019). Since our purpose was limited to evaluate the relative variability in fracture patterns and properties within the different sedimentary units, we did not perform any further analysis. Stochastic fracture aperture distribution and numerical modelling to upscale or calculate equivalent fracture permeability at confining pressure (Cacas et al., 1990; Flodin et al., 2004; Antonellini et al., 2014; Bisdom et al., 2016; Zheng et al., 2020; Smeraglia et al., 2021) are beyond the scope of this work.

3.1.3.3. X-ray analyses

Eighteen rock samples from the sedimentary sequence exposed in the cave were collected and analyzed to measure the major (>1 g/100 g) and minor (0.1–1.0 g/100 g) compounds with X-ray fluorescence (XRF). The powdered samples were analyzed with a sequential wavelength dispersive XRF spectrometer equipped on a Malvern Panalytical - model Zetium. The analyses were performed after STD-1 calibration and the values were normalized to 100 wt.%. Finally, loss of ignition (LOI) was calculated heating the samples at 1020 °C for 2 h. The main mineral phases were also investigated with an Empyrean-Panalytical X-ray diffractometer mounting a Cu-anode (λ=1.542 Å; 2.2 kW, range 2θ=2.5–70°, step size =0.02° 2θ) at the *Laboratório de Caracterização Tecnológica* from the University of *São Paulo* (Brazil). The identification of crystalline phases was performed using the standard dataset of the PDF2 database from the ICDD (International Centre for Diffraction Data) and ICSD (Inorganic Crystal Structure Database). XRD analyses were also performed on selected samples of cave sediments at the *Laboratório do Centro de Tecnologias do Gás e Energias Renováveis-LTG-ER, Laboratório de Ensaios de Materiais* (Lagoa Nova, Brazil) with a Shimadzu XRD-6000 X-ray diffractometer mounting a Cu-anode (current: 20 mA, voltage =40 kV, range 2θ=5–80°, step size =0.02° 2θ).

3.1.3.4. SEM-EDS analyses

SEM-EDS analyses were carried out on five selected polished thin-sections from highly silicified rocks with a Tescan Vega 3 LMU equipped with an Energy Dispersive Spectroscopy (EDS) EDAX Apollo-X SDD detector, at 20 kV accelerating voltage, 1.2 nA beam current, and 5–10 µm beam diameter, operating at the DISTAV Department of the University of Genova. Additionally, *in situ* SEM analyses on eight silicified bulk rock fragments were performed at the BIGEA Department of the University of Bologna with a JEOL JSM-5400 equipped with an IXRF system for X-ray EDS spectroscopy to evaluate the microtexture and morphologies of quartz grains. All samples were prepared with gold coating and imaged both as backscattered electron (BSE) images or secondary electron (SE) images.

3.1.3.5. Petrophysical properties

Petrophysical analyses were performed to measure porosity, permeability, density, and pore volume on 50 rock plugs covering the whole stratigraphic sequence exposed in the cave. The analyses were performed using a *Coreval 700* unsteady-state gas permeameter and porosimeter at the *LABRES-Departamento de Engenharia de Petróleo* of the *Universidad Federal do Rio Grande do Norte.* Petrophysical properties were measured on 2.5 cm-diameter and 3 cm-high rock plugs cut from mini-drill cores extracted from the cave walls. For each unit, parallel and normal (or oblique) to bedding samples were collected to quantify the permeability tensor. The pore volume calculations were made in a N_2 gas injection porosimeter at a confining pressure of 600 psi. Additionally, the Klinkenberg correction was applied to calculate the permeability in mD (Klinkenberg, 1941; Araújo et al., 2021).

3.1.4. Results

The results of our multidisciplinary study in the CCS are reported in the following sections. The sedimentary and speleogenetic units in the cave are presented moving from bottom to top of the sequence, describing their main sedimentary, petrographic, compositional, and geomorphological characteristics. Microtextural, and mineralogical data associated with the silicified units are illustrated. Finally, the structural and petrophysical properties of the different sedimentary and speleogenetic units are shown.

3.1.4.1. Sedimentary and speleogenetic units in the CCS

The sedimentary sequence exposed in the CCS includes the following sedimentary units (Fig. 3A): (A) dolostones with tabular cross-stratification, (B1) highly silicified dolostones, (B2) heteroliths, (B3) siliciclastic tempestites, and (C) cherty dolostones. The bulk chemical and mineralogical compositions of 18 samples from the entire sedimentary succession and of four cave sediment samples are reported as Supplementary Materials in the online version of this article. XRF results are also reported in the diagrams of Fig. 4.

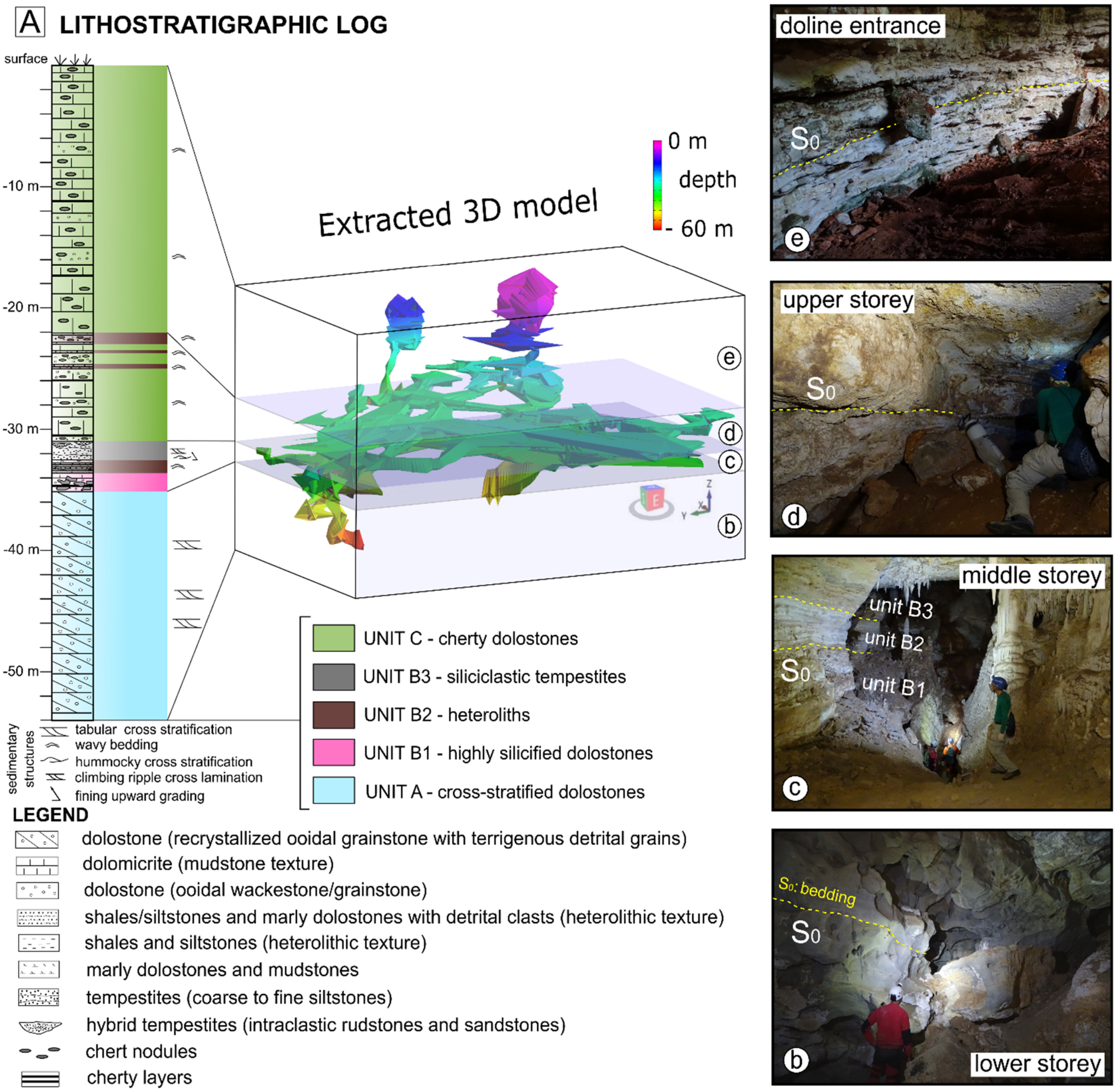

Figure 3. A) Lithostratigraphic log of the sedimentary sequence exposed in the CCS, subdivided according to the units described in the main text. The 3D model extracted from the topographic survey of the cave is also shown. B) Lower storey typical morphologies, with phreatic spongework

patterns, blind-ending passages, and rising conduits. White crusts covering the walls are calcite coralloids. C) Middle storey morphology with sub-elliptical or sub-rounded stratigraphically confined conduits. The longest and most developed sector of the CCS (expressed with green colors in the 3D model) belongs to this unit. D) Typical shapes and dimensions of the upper storey with small secondary passages. Condensation-corrosion features are commonly observed next to the entrance. E) Collapsed doline entrance. Red soil and debris are transported in the upper sector of the CCS by recent but ephemeral mudflows and streams. Bedding (S_0) is shown with dashed yellow lines.

Based on its topography and tridimensional organization (Fig. 3), the CCS can be classified as a 3D multistorey cave system (Audra et al., 2009; Audra and Palmer, 2015). The spatial organization of the conduit system and its morphology are strongly heterogeneous and reflect the vertical stratigraphic variations in the sedimentary column. Four speleogenetic units, grouped based on their morphological, geometric, and genetic characteristics, are defined from bottom to top as: lower storey (Fig. 3B), middle storey (Fig. 3C), upper storey (Fig. 3D), and doline entrance (Fig. 3E).

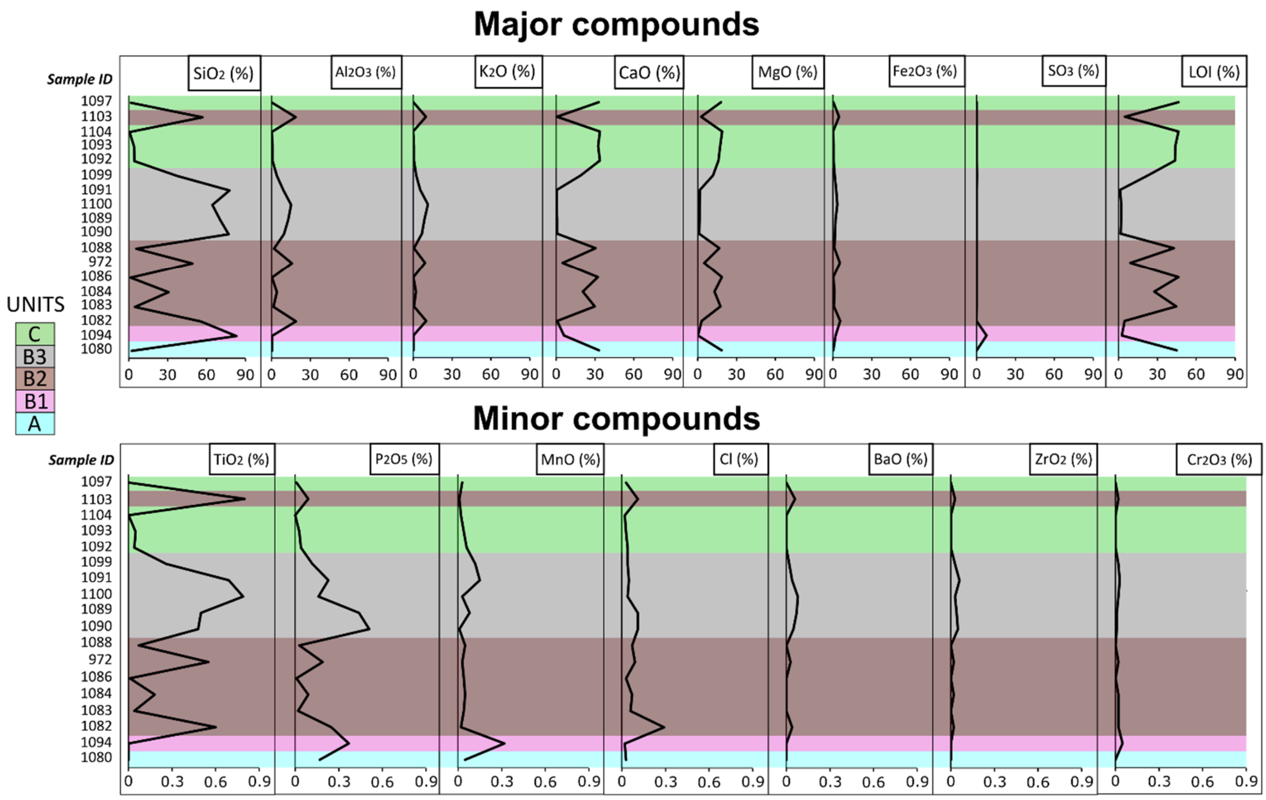

Figure 4. XRF bulk rock chemical composition of 18 representative hand samples collected in the cave and grouped according to their sedimentary unit. For the detailed description of the samples, the reader is referred to the Supplementary Materials in the online version of the article.

The network of conduits shows four clustered orientation trends in map view (Fig. 2C): the NE-SW (N35E-N45E) and NW-SE (N125E-N135E) trends are the most frequent whereas the N–S (N0E-N10E) and E-W (N90E-N100E) are secondary trends. The cave does not show the typical geomorphic features deriving from epigenic speleogenesis (i.e., lack of surface-derived sedimentation, vadose speleogens, scallops or notches, etc.) and any link to surface geomorphology and drainage, except for the collapsed doline entrance. The typical cave sediments in the CCS are authigenic, deriving from block collapse or degradation by condensation-corrosion of the host rock. Secondary minerals resulting from guano-related processes (gypsum crystals and powders, phosphate crusts) are also present.

3.1.4.1.1. Lower storey – unit A

The lower storey spans from the cave bottom to 35 m depth relative to the surface. The rocks exposed are medium to thick beds of dolostones with tabular cross-stratification (Fig. 5A). Bedding-parallel stylolites are commonly observed, and they define the mechanical layering (spacing from a few cm up to 60–80 cm). This storey is characterized by vertical chambers with spongework morphologies (Fig. 3B), rising conduits, cupolas, blind ending passages, and rift-like discharge feeders localized along the intersection of multiple fracture sets, faults, or FZ (Fig. 5C). Such geomorphic features are typical (but not exclusive) of hypogene caves (Klimchouk, 2007, 2019; Audra et al., 2009; De Waele et al., 2009, 2016; Audra and Palmer, 2015). Fractures controlling the localization of feeders and rising conduits often present cm-wide reactive fronts (Fig. 5B) and bleaching halos (whitening fabric due to fluid-rock interactions indicating mobilization of metal ions; Ming et al., 2016).

Dolostones have a crystalline texture (Fig. 5D) deriving from the dolomitization of pristine ooidal grainstones (or less common wackestones) with terrigenous detrital clasts (mainly sub-rounded quartz grains, Fig. 5E) and fine pyrite crystals, often replaced by pseudomorphs of iron-oxides and hydroxides. The original ooidal texture is occasionally visible in thin sections (Fig. 5E). Porosity is mainly represented by vuggy, moldic or intercrystalline pores, often filled by euhedral mega-quartz, K-feldspar (microcline) or apatite crystals (Fig. 5D and F). White crusts of coralloid calcite growing on the dolostone rock characterize the cave walls at the bottom of the lower storey (Fig. 3B).

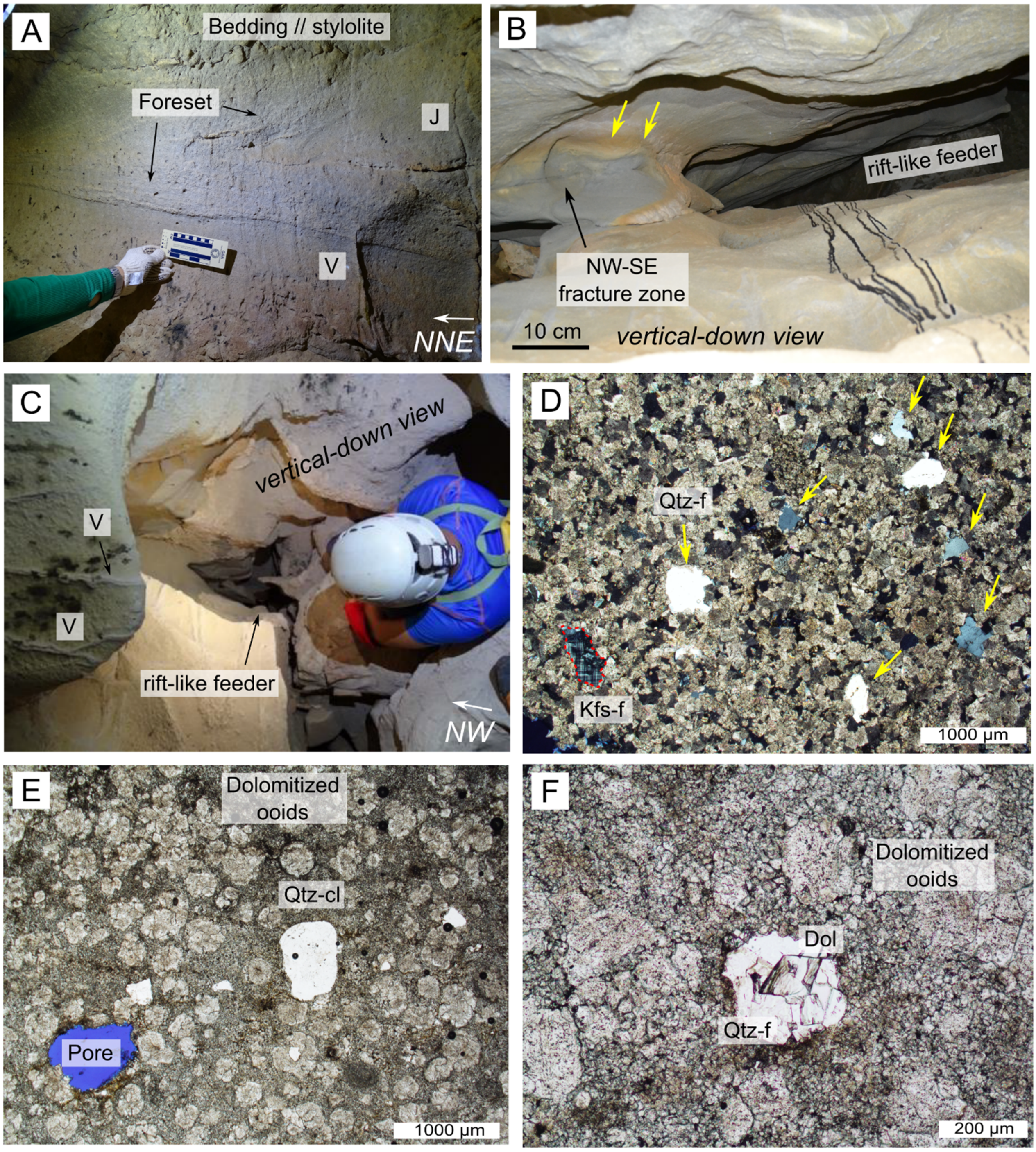

Figure. 5. Mesoscale (outcrop) and microscale (thin section) observations in the lower storey developed in unit A. A) Tabular cross-stratification with foresets occasionally preserved from the dolomitization process. B) Vertical-down view of a typical rift-like feeder localized on a NW-SE striking fracture zone composed of sub-parallel joints with bleaching reactive halos (pointed by the yellow arrows). C) Vertical-down view of a rift-like feeder localized at the intersection between NW-SE and N–S striking fracture zones. Nearby fractures are boxwork veins filled with quartz. D) Dolostone with crystalline texture and vuggy porosity filled with mega-quartz crystals (indicated by yellow arrows) and K-feldspar (microcline with typical cross-hatched twinning). Image under cross-

polarized light. E) The original ooidal grainstone texture is occasionally preserved in the dolostone. Sub-rounded terrigenous detrital quartz is common in unit A. Image under parallel-polarized light. F) Detail of the dolomite grains and cement, with moldic porosity filled by quartz. Relict euhedral dolomite grains are included in the quartz cement. Image under parallel-polarized light. Label abbreviations: J (joint), V (veins), FZ (fracture zone), Qtz-f (mega-quartz fillings), Kfs-f (K-feldspar fillings), Qtz-cl (quartz detrital clast), Dol (dolomite).

3.1.4.1.2. Middle storey – units B1, B2 and B3

The middle storey includes the most interesting and longest portion of the CCS, characterized by a maze network of sub-horizontal galleries developed between 35 and 31 m of depth from the surface. This section contains a mixed carbonate-siliciclastic interval (∼4 m-thick, Fig. 6A) hosting ∼80% of the entire cave passages.

The lower part of the middle storey is developed in unit B1, a 1.8 m-thick dolostone pack, with ooidal wackestone or mudstone (dolomicrite) textures, characterized by intense silicification (SiO_2>80 wt.%, Fig. 4). Layering and ooidal structures are rarely preserved. Micro-crystalline quartz (defined as Qtz-A, forming chert) is concentrated in nodules or irregular layers replacing the dolomite grains (Fig. 6B and C) and as cement between residual dolomite often associated with iron oxides and less frequently with pyrite. Residual dolostone and Qtz-A (chert) show abundant vuggy and fracture porosity. Open fractures and vuggy pores are partially filled with euhedral blocky mega-quartz (Qtz-B) and chalcedony quartz (Qtz-C), both having mineral inclusions that will be further described in the following sections.

The highly silicified package is sealed by unit B2, a 0.9 m-thick interval characterized by the alternation of thin heterolith layers (defined as a sedimentary structure made up of interbedded deposits of sand/silt and mud formed in a tidal environment; Reineck and Wunderlich, 1968), marly dolostones with detrital clasts, and dolomicrites with chert nodules (Fig. 6D and E). Heteroliths are composed of mm-thick intercalations of mud and silt with wavy bedding (Fig. 6D) or dolostones with ooidal grainstone texture with terrigenous detrital clasts and coarse silt grain size. Pyrite crystals and their iron oxides/hydroxides associated pseudomorphs are common in unit B2.

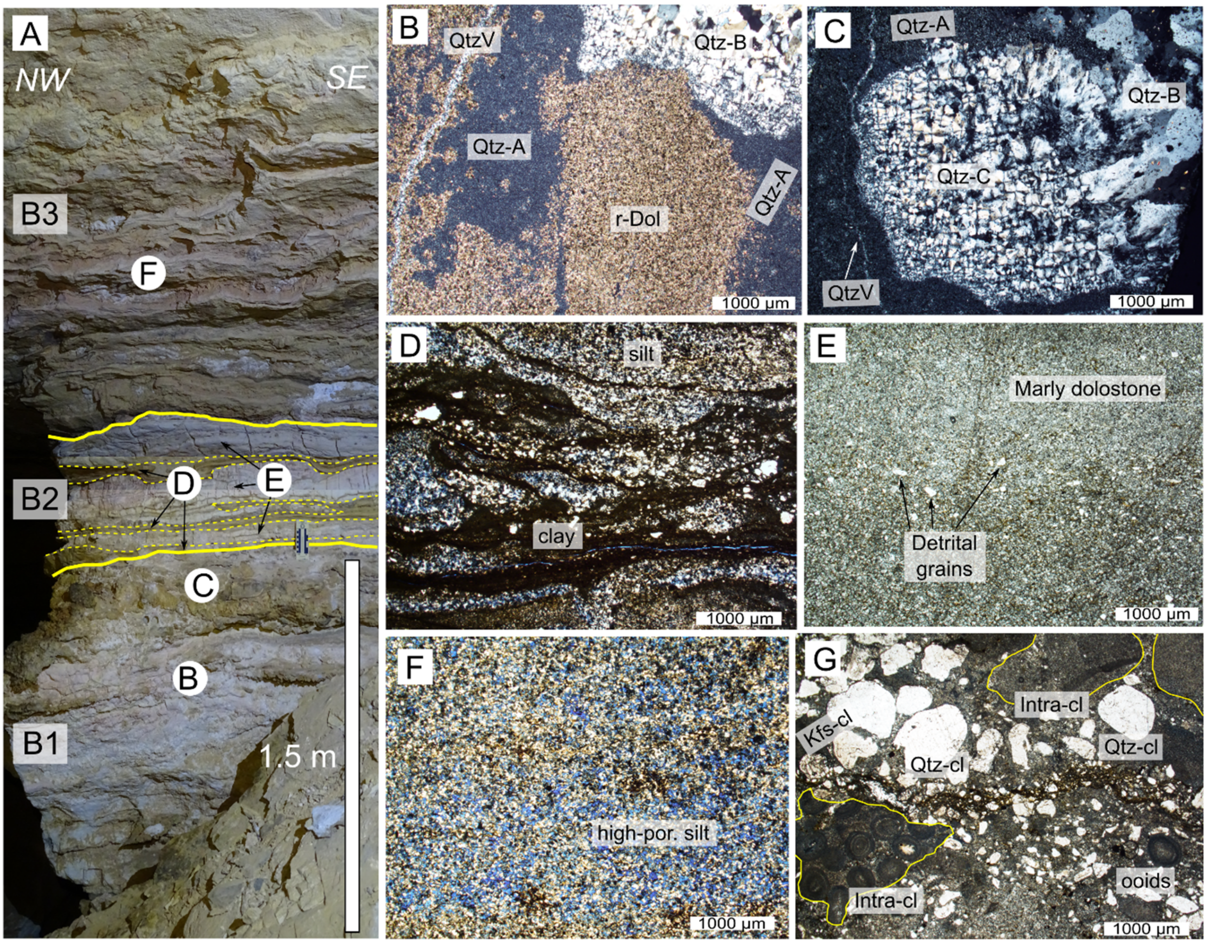

Figure 6. Mesoscale (outcrop) and microscale (thin section microphotographs) observations in the middle storey developed in units B1, B2, and B3. A) Outcrop view of the sedimentary interval between unit B1 and unit B3. Letters in the circles point to the locations of the microphotographs displayed in this figure. B–C) Micro-crystalline quartz (Qtz-A) replacing dolomite grains and cement in unit B1. Solutional pores and enlarged fractures are filled with euhedral blocky mega-quartz (Qtz-B) or chalcedony-spherulitic quartz (Qtz-C). Qtz-C is lining the solutional voids. Images under cross-polarized light. D) Heterolithic texture in unit B2, with sub-mm to mm-thick intercalations of clay and silt characterized by wavy-bedding. Image under parallel-polarized light. E) Marly dolostone with dolomicrite matrix and high content of terrigenous detrital grains composed of quartz and K-feldspar. Image under parallel-polarized light. F) Siltstone in the tempestite facies of unit B3. Siltstones have a high porosity at thin section scale and present disseminated iron oxides-hydroxides. Image under parallel-polarized light. G) Rudstone texture in unit B3 made of Intraclasts (highlighted in yellow) and detrital grains composed of quartz and K-feldspar. Image under parallel-polarized light. Label abbreviations: r-dol (relict dolomite), Qtz-V (quartz veins), Qtz-A (micro-crystalline chert), Qtz-B (euhedral blocky mega-quartz), Qtz-C (chalcedony), Kfs-cl (detrital K-feldspar clast), Qtz-cl (detrital quartz clast), Intra-cl (carbonate intraclasts).

This heterolithic facies is capped by a 1.1 m-thick interval (unit B3) of graded coarse-to-fine siltstones (Fig. 6F) organized in a rhythmic sequence with (from bottom to top) parallel lamination, hummocky-cross-stratification, and cross-lamination with climbing ripples, identified as a tempestite facies (Myrow and Southard, 1996). In the upper part of the unit, some hybrid carbonate-siliciclastic tempestites show massive, graded beds of intraclastic rudstones and coarse sandstones with carbonate intraclasts and dolomitized ooids (Fig. 6G). Iron oxide and hydroxide stains are commonly found in the tempestite facies (Fig. 6F).

The middle storey is a vast network of sub-horizontal passages with a maze pattern, connected to the lower storey by rising narrow feeders or conduits (Fig. 7A). The main horizontal galleries are confined in the highly silicified unit B1, below the heterolithic/siliciclastic interval of units B2 and B3 (Fig. 7B).

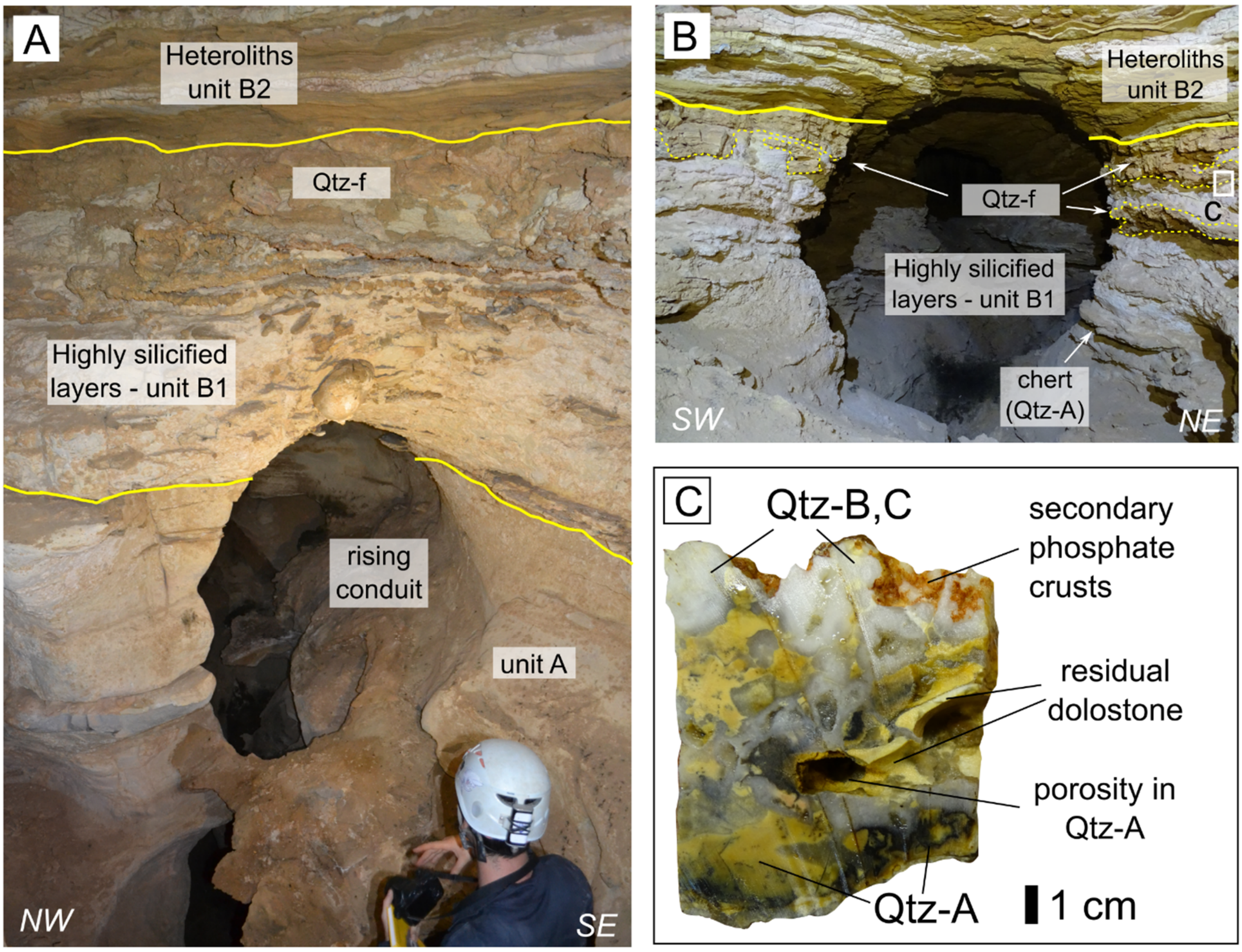

Figure 7. A) Rising conduit localized in the dolomitized grainstones of unit A, at the top contact with units B1 and B2 where the middle storey (picture in box B) develops. Note the high concentration of quartz-rich mineral deposits in the upper part of unit B1. B) Sub-horizontal and rounded galleries in the middle storey. Galleries are organized in a maze network confined by units B2 and B3. Frequent

collapses and evidence of dissolution by condensation-corrosion in the dolostone layers of units B2 and B3 contributed to the enlargement of the passages. C) Hand sample taken in the silicified unit B1 (location pointed in the picture in box B). Secondary guano-related phosphatic overgrowths (identified by SEM-EDS, Tab.1) form brown crusts on the mega-quartz crystals. Vuggy porosity (barren or filled) is concentrated in Qtz-A. Labels abbreviations: Qtz-f (undifferentiated quartz filling), Qtz-A (micro-crystalline chert), Qtz-B (euhedral blocky mega-quartz), Qtz-C (chalcedony).

Just below unit B2, there are extensive mega-quartz (Qtz-B) or chalcedony (Qtz-C) mineral deposits filling vuggy pores and veins (Fig. 7A). Most of these quartz-rich mineral deposits are associated with pore space developed in the micro-crystalline quartz facies (chert, Qtz-A) or, secondarily, in the residual dolostone facies (Fig. 7C).

The sub-horizontal galleries have a sub-elliptical or circular shape (Fig. 3, Fig. 7B) with a stepping roof profile, which reflects the collapse of layers in the ceiling above the silicified unit B1. Dolostones and marls in unit B2 have a cm-thick crushed texture at the contact with the cave walls. The pavements are made up of collapsed layers from the overlying units and soft white powders composed of gypsum and minor amounts of iron oxides/hydroxides or guano-derived phosphates. Secondary phosphates and iron-manganese oxides/hydroxides have also been found as overgrowths on the host rock. Calcite speleothems from percolation/evaporation of meteoric water decorate the walls and pavements in different sites of the middle storey.

3.1.4.1.3. Upper storey and doline entrance – unit C

The upper part of the CCS, from the entrance at the surface down to a depth of approximately 31 m, is characterized by isolated and small sub-horizontal galleries (Fig. 3D) connected with the middle storey by inclined or vertical conduits developed along through-going fracture zones. These small and short galleries are hosted in cherty dolostone layers (Fig. 8A, B, 8C) made up of thin-to medium-thick intercalations of dolomicrites and highly silicified ooidal grainstones/wackestones (unit C) and heteroliths (unit B2) (Fig. 8C and D).

Unit C is composed of medium-to thick-layers of dolostones with mudstone texture (Fig. 8E) or ooidal wackestone/grainstone texture with low content of detrital grains. Micro-crystalline quartz replacements of dolomite grains and cement are common (Qtz-A) and frequently associated with the ooid-rich facies (Fig. 8F). Chalcedony (Qtz-C) or euhedral blocky mega-quartz (Qtz-B) filling vuggy pores and veins are also observed in this unit (Fig. 8D). Vuggy pores and veins in the upper part of unit C may also be filled with calcite crystals (Fig. 8E). Pressure solution by bedding parallel stylolites postdates the Qtz-A silicification episode both in thin-section and outcrop scale, causing apparent offsets and plastic deformation of chert nodules (Fig. 8B).

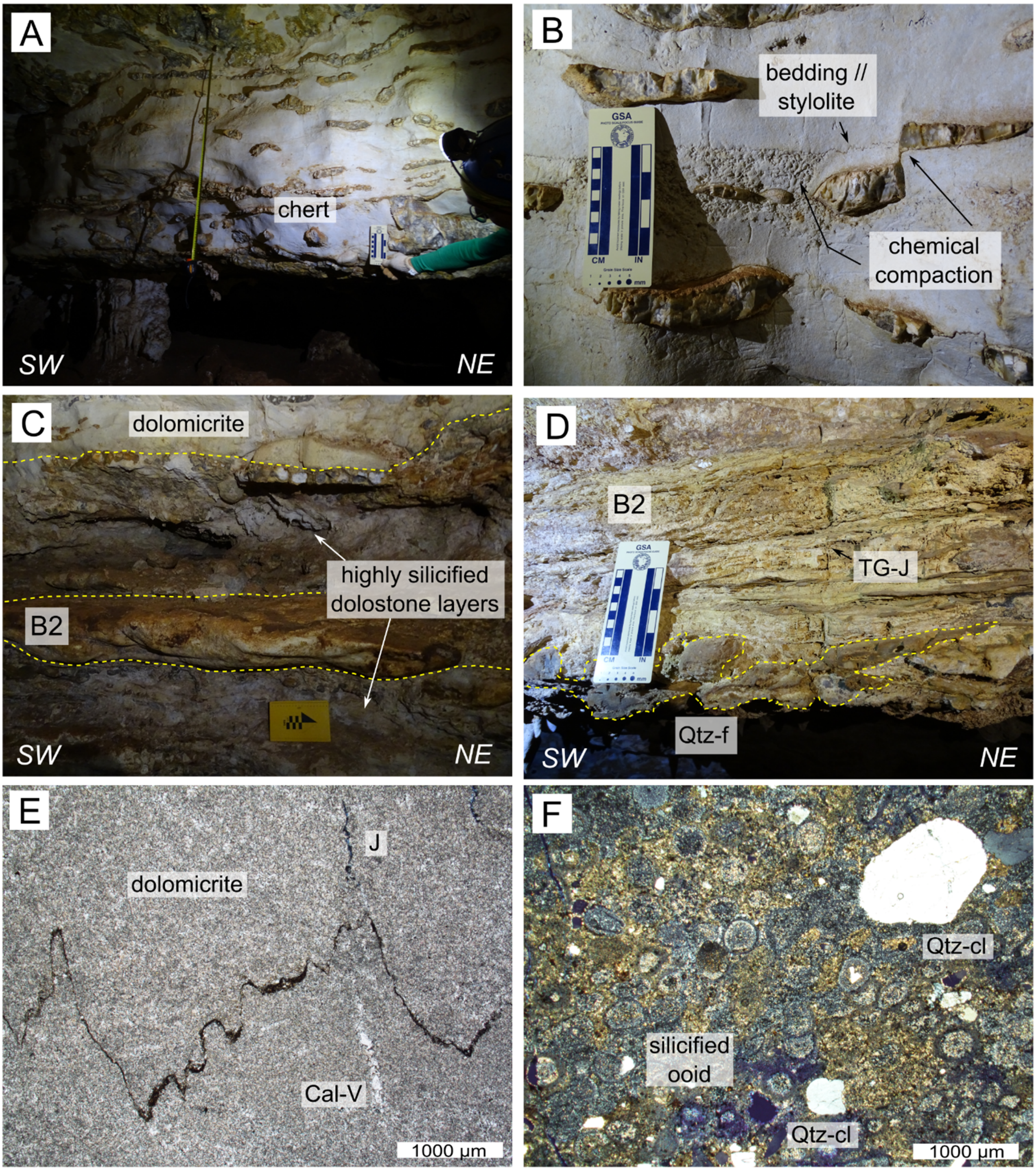

Figure 8. Mesoscale (outcrop) and microscale (thin-section microphotographs) observations in unit C. A) Thick dolostone layer composed of dolomicrite (microphotograph in box E) with chert nodules. B) Close-up view of chert nodules deformed by bedding-parallel pressure solution (stylolites). Differential dissolution produced an apparent offset in the chert nodules, indicating that it postdates

the formation of the chert nodules in the dolostone. C) Typical cave passage in the upper storey with the greatest widening localized in the cherty dolostone layers. D) Heterolith layers with wavy bedding and quartz-rich mineral deposits in unit B2. E) Dolomicrite with bedding-parallel stylolite in unit C. Image under parallel-polarized light. F) Silicified dolostone layer in the upper storey (see picture in box C) with ooidal grainstone texture and abundant detrital quartz grains. Silicification is represented by Qtz-A replacing dolomite grains and cement. Image under cross-polarized light. Label abbreviations: TG-J (through-going joint), J (joint), Qtz-f (mega-quartz filling porosity), Cal-V (calcite vein), Qtz-cl (quartz clast).

Above the heterolith intercalations, the cave morphology consists of collapse halls and small chambers connected with the surface by a collapse. The entrance has a gentle slope covered with debris, boulders, and red soil coming from the surface (Fig. 3E). The passages near the entrance present condensation-corrosion features.

3.1.4.2. Silicification textures

Quartz and silicified textures occur in all sedimentary units outcropping in the CCS. However, the highest concentration of silica and quartz-rich facies is observed in unit B1, associated with the sub-horizontal maze network of the middle storey (Fig. 7). Silicification occurs mainly as diagenetic replacement of dolomite grains and cement by micro-crystalline quartz (Qtz-A; Fig. 6, Fig. 9). Qtz-A forms nodules and irregular layers, mainly localized in the dolomitized ooidal wackestone or mudstone textures and associated with small size (< 20 µm) iron- and iron-titanium oxides or, less commonly, pyrite.

The replacement process is shown by micron-sized ghosts of the precursor carbonates (Maliva and Siever, 1989). Ghosts resemble the typical rhombohedral dolomite grains and are mostly composed of fluid inclusions or microcavities that were not completely replaced by micro-crystalline quartz (Fig. 9, Fig. 10B). At the meso-scale, different tones of chert (from light yellow to dark grey, Fig. 7C) reflect the amount of associated iron oxides, rhombohedral-shaped inclusions, grain size, and porosity.

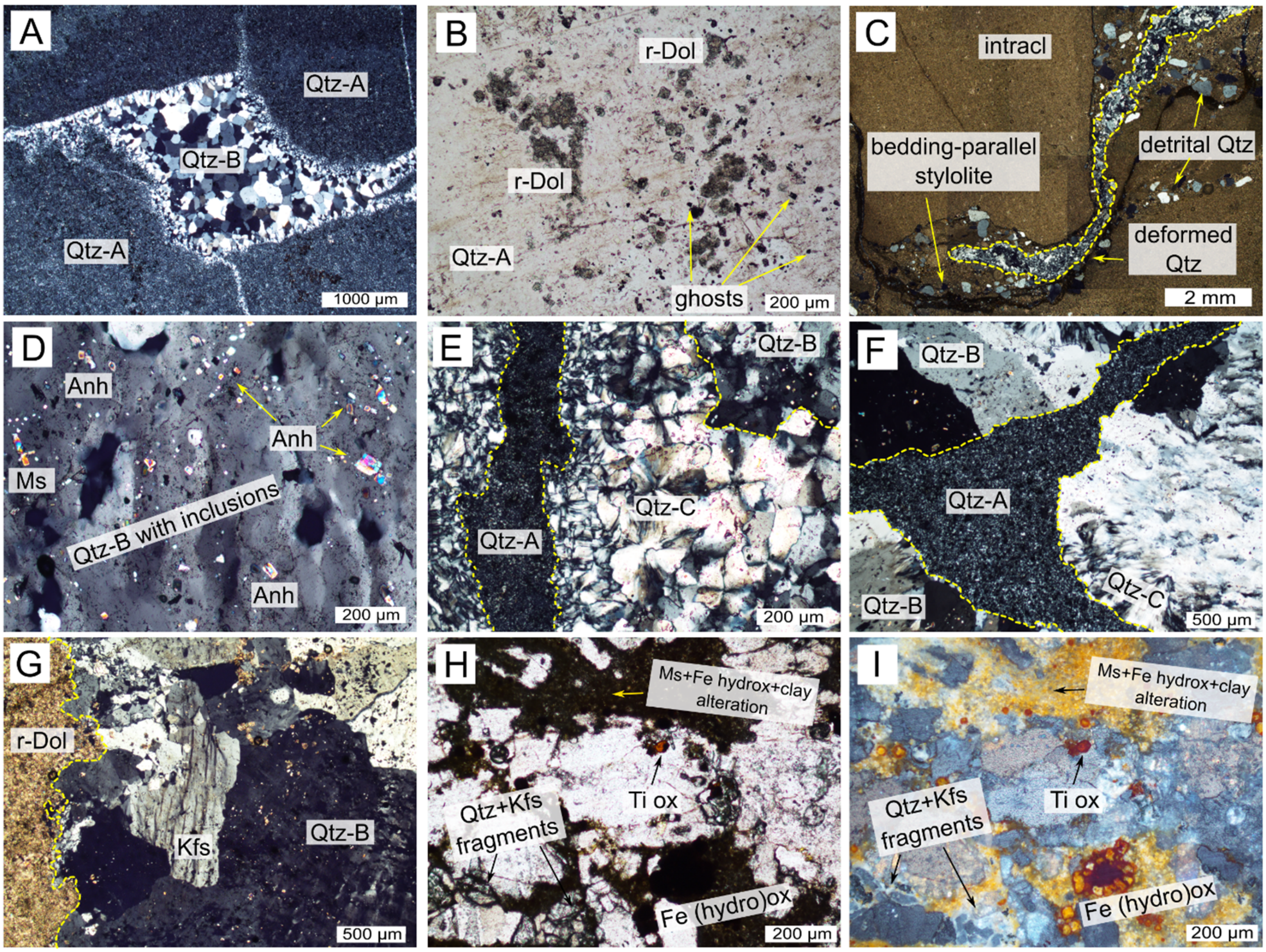

Figure 9. Silicification microtextural observations at optical microscopy. A) Microcavity and veins in Qtz-A (chert) filled by euhedral blocky mega-quartz (Qtz-B). Image under cross-polarized light. B) Qtz-A replacing dolomite crystals. Ghosts of relict rhombohedral dolomite crystals are still visible. Image under parallel-polarized light. C) Mosaic of multiple microphotographs showing silicification features plastically deformed by bedding-parallel pressure solution in an intraclastic rudstone of unit B3. Images under cross-polarized light. D) Secondary mineral inclusions in a mega-quartz crystal (Qtz-B). Minerals with high interference colors are anhydrite, barite, or muscovite crystals. Image under cross-polarized light. E) Detail of spherulitic-chalcedony quartz (Qtz-C) and micro-crystalline quartz (Qtz-A). In the upper right corner, there are euhedral blocky quartz crystals (Qtz-B) with mineral inclusions. Image under cross-polarized light. F) Qtz-A with sharp rims and Qtz-B and Qtz-C crystallizations. Image under cross-polarized light. G) Association of Qtz-B with undulose extinction and K-feldspar with perthitic texture. On the left side, there are residual non-silicified dolomite crystals. Image under cross-polarized light. H) Micro-scale hydraulic breccia textures with quartz and K-feldspar fragments supported by a matrix composed of muscovite, iron-oxides/hydroxides, and altered clay or feldspar minerals. Images under parallel-polarized light. Quartz crystals have iron-titanium oxides inclusions. I) Same picture of box H under reflected light microscope with crossed

nicols. Label abbreviations: Qtz-A (micro-crystalline quartz), Qtz-B (euhedral blocky mega-quartz), Qtz-C (chalcedony/spherulitic quartz), Qtz (quartz), Ms (muscovite), Anh (anhydrite; high interference colors), Kfs (K-feldspar), intracl (intraclasts), Fe (hydro)ox (iron-oxides and iron-hydroxides), Ti ox (titanium oxide, rutile), r-Dol (relict dolomite).

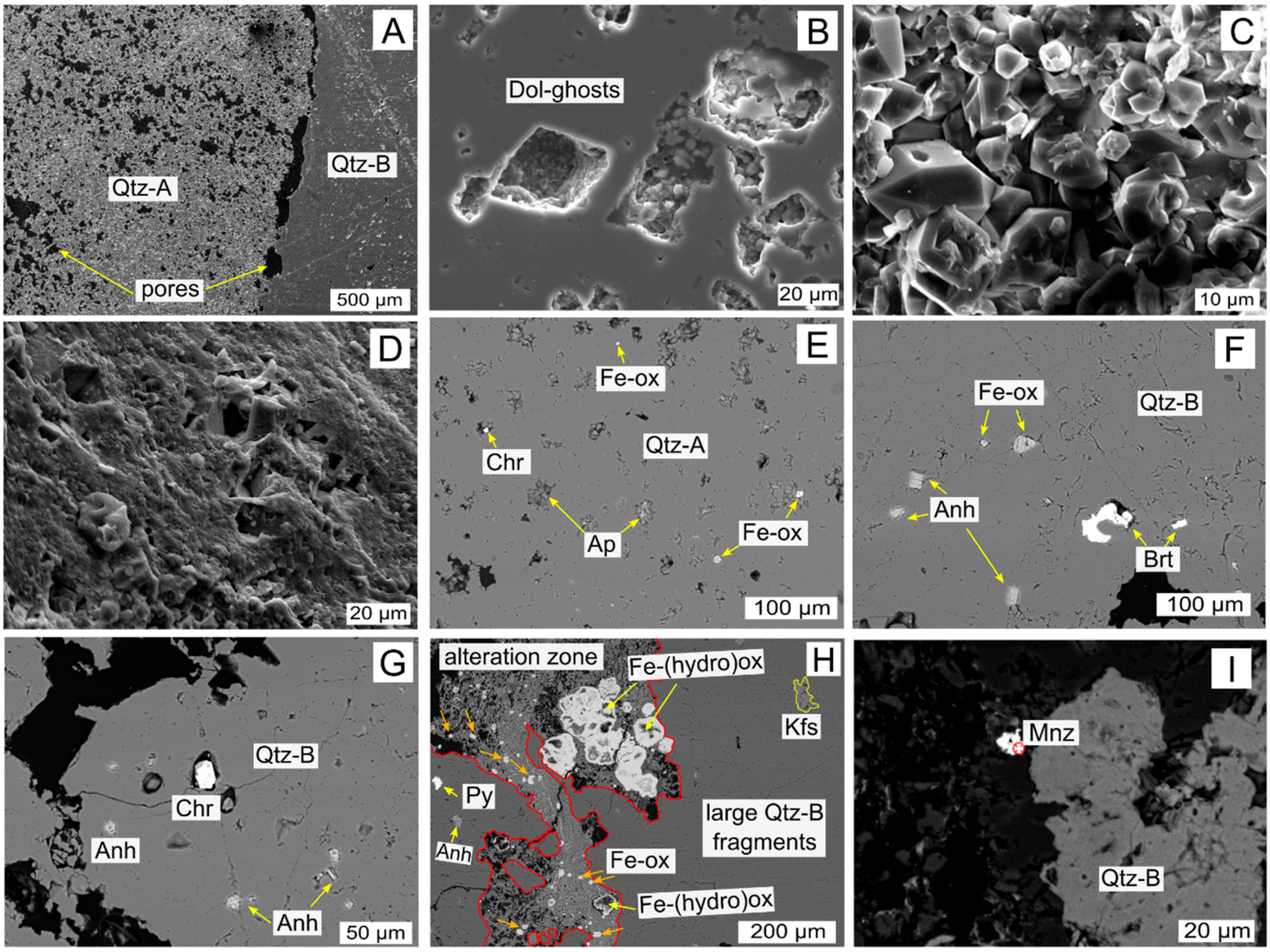

Figure 10. Silicification micro-textures observed at SEM. A) Contact between Qtz-A and Qtz-B. Note the vuggy and intercrystalline porosity (~15–20%) in the Qtz-A texture. B) Rhombohedral-shaped dolomite ghost inclusions in Qtz-A. C-D) Micro-textures typical of slow dissolution kinetics (Mecchia et al., 2019) in Qtz-A, like: "V"-shaped notches, corrosion holes and etch pits. E) Qtz-A associated with iron-oxide crystals and intercrystalline voids filled with Fe–Cr spinel and apatite crystals. F) Qtz-B with inclusions of anhydrite, iron oxides, and barite crystals. G) Qtz-B with inclusions of Fe–Cr spinel and sulfates (mostly anhydrite). H) Hydraulic breccia micro-texture with associated alteration zone in a heterolith layer of unit B2. The orange arrows point to iron oxide-hydroxide aggregates disseminated in the alteration zone. I) REE (Ce, La, Nd, Th)-phosphate (monazite) in the hydraulic breccia alteration zone. From A to D: SE images; from E to L: BSE images. Label abbreviations: Qtz-A (micro-crystalline quartz), Qtz-B (euhedral blocky mega-quartz), Qtz (quartz), Kfs (K-feldspar), Anh

(anhydrite), Brt (barite), Py (pyrite), Chr (Fe–Cr spinel group), Fe-ox (iron oxides), Fe-(hydro)ox (iron-oxides and iron-hydroxides), Ap (apatite), Mnz (REE-phosphate, monazite).

Chert nodules are often characterized by high porosity textures (up to 10–15%), occasionally filled with euhedral mega-quartz (Qtz-B; Fig. 6, Fig. 9G), chalcedony/spherulitic quartz (Qtz-C; Fig. 6, Fig. 9F) or apatite (Fig. 10E). The contact between Qtz-A and Qtz-B/Qtz-C fillings is usually sharp with irregular rims (Fig. 9E and F). These mega-quartz and chalcedony deposits are characterized by several mineral inclusions illustrated in the SEM images of Fig. 10. Mineral inclusions in Qtz-B/Qtz-C are composed of Ca-sulfates (anhydrite and gypsum), barite, K-feldspar, Fe–Ti oxides and hydroxides, muscovite, apatite, and accessory Fe–Cr spinels (chromite group), sphalerite (very small crystals found in association with Ca-sulfates), and pyrite. Furthermore, Qtz-B occasionally displays colloform-plumose textures and undulose extinction.

Silicification expressed by Qtz-B and Qtz-C is mainly concentrated in the middle and lower storeys, below the heterolithic and tempestite facies of units B2 and B3. Quartz-filled veins are observed also in the upper storey, near faults and through-going FZ (Fig. 8D). Furthermore, mm-to cm-thick lenses of hydraulic breccias have been observed in thin sections from the middle storey (Fig. 9, Fig. 10H). These hydraulic breccias are composed of sub-euhedral grains and fragments of quartz, K-feldspar, and phosphates (apatite, monazite; Fig. 10I) supported by a matrix of weathered host rock (mostly clay minerals and feldspars altered in muscovite, and pseudomorphs of hematite-goethite). Due to their small size and irregular textures, it was not possible to clearly establish if the REE-phosphates found in the alteration zones are relict detrital grains or authigenic.

The mineral list identified with SEM-EDS combined with petrographic analyses in the highly silicified unit B1 are summarized in Table 1.

Table 1. List of the mineral phases associated with silicification identified by combined SEM-EDS and petrographic microscopy.

Name	**Simplified formula**	**Description**
Quartz	SiO_2	microcrystalline chert (Qtz-A) replacing dolomite; blocky mega-quartz (Qtz-B) or chalcedony (Qtz-C) filling porosity and fractures; fragments in hydraulic breccias
Hematite	Fe_2O_3	pseudomorphs of pyrite; associated with silicification and hydraulic breccias; inclusions in hydrothermal quartz; overgrowths and coatings
Pyrite	FeS_2	disseminated in dolomitized carbonate, mainly replaced by hematite-goethite; inclusions in hydrothermal quartz
Sphalerite	ZnS	rare inclusions in hydrothermal quartz
Goethite	FeO(OH)	alteration of hematite crystals; coatings
Pyrolusite	MnO_2	alteration of bedrock
Gypsum	$CaSO_4 \cdot 2H_2O$	lamellar gypsum filling porosity and as overgrowths; soft powders on cave floors; inclusions in hydrothermal quartz
Anhydrite	$CaSO_4$	inclusions in hydrothermal quartz
Barite	$BaSO_4$	inclusions in hydrothermal quartz
K-feldspar	$K(AlSi_3O_8)$	inclusions in hydrothermal quartz and filling pores; fragments in hydraulic breccias
Muscovite	$KAl_2(AlSi_3O_{10})(OH)_2$	inclusions in hydrothermal quartz; alteration zones associated with hydraulic breccias
Calcite	$CaCO_3$	vein fillings
Dolomite	$CaMg(CO_3)_2$	primary dolomitization of calcite grains and cement
Montmorillonite	$(Na,Ca)_{0.33}(Al,Mg)_2(Si_4O_{10})(OH)_2 \cdot nH_2O$	residual clay minerals in bedrock
Taranakite	$K_3Al_5(PO_3OH)_6(PO_4)_2 \cdot 18H_2O$	crusts on cave walls and overgrowths on quartz deposits, guano-related phosphates

Robertsite-Mitridatite series	$Ca_2(Mn^{3+}, Fe^{3+})_3O_2(PO_4)_3 \cdot 3H_2O$	crusts on cave walls and overgrowths on quartz deposits, guano-related phosphates
Brushite	$Ca(PO_3OH)\cdot 2H_2O$	crusts and acicular overgrowths on quartz deposits, guano-related phosphates
Apatite	Ca5(PO4)3(OH)	inclusions in hydrothermal quartz deposits and filling pores, or guano-related overgrowths on quartz deposits
Berlinite-Variscite group (?)	$Al(PO_4)$ - $Al(PO_4)\cdot 2H_2O$	guano-related phosphates
Hematite-Ilmenite series	Fe_2O_3 - $FeTiO_3$	inclusions in hydrothermal quartz
Rutile	TiO_2	inclusions in hydrothermal quartz
Chromite group	$FeCr_2O_4$	inclusions in hydrothermal quartz
REE-phosphates (Monazite Group)	REE (PO_4)	small grains in the alteration zones of hydraulic breccias or detrital (?)
Ni-phosphate (?)	?	small grains in the alteration zones of hydraulic breccias or detrital (?)

3.1.4.3. Deformation and fracture patterns

The structural elements observed in the CCS were classified as: stylolites, open-mode fractures (joints/veins), through-going fracture zones (FZ), and faults (Fig. 11A).

Bedding in the CCS is sub-horizontal to gently dipping to the NW (<5–15°) (Fig. 11B). Bedding-parallel stylolites due to burial were observed in all carbonate units and, especially, in units A and B1.

Open-mode fractures are joints and veins (Fig. 11B and C). Infilling of veins is made up of carbonates (mostly dolomite and calcite) or quartz. Boxwork quartz veins (Fig. 6B and C) are common in the lower and middle storey and are composed of Qtz-B or Qtz-C assemblages (Fig. 5C). Open-mode fractures are commonly bed-perpendicular or high angle to bedding, and either stratabound (confined to bedding interfaces) or shorter than single bed thickness. Based on the statistical analysis of fracture orientations, four sets of open-mode fractures were identified: NW-SE, N–S to NNE-SSW, NE-SW, and E-W (Fig. 11F). Non-stratabound (through-going) fracture zones (FZ), on the contrary, are formed by cm-spaced joints, veins, or sheared joints organized in connected arrays, which cut across bedding (Fig. 11D). Through-going FZ include NW-SE and N–S to NNE-SSW sets (Fig. 11G). These structures are mostly developed in the lower storey (unit A).

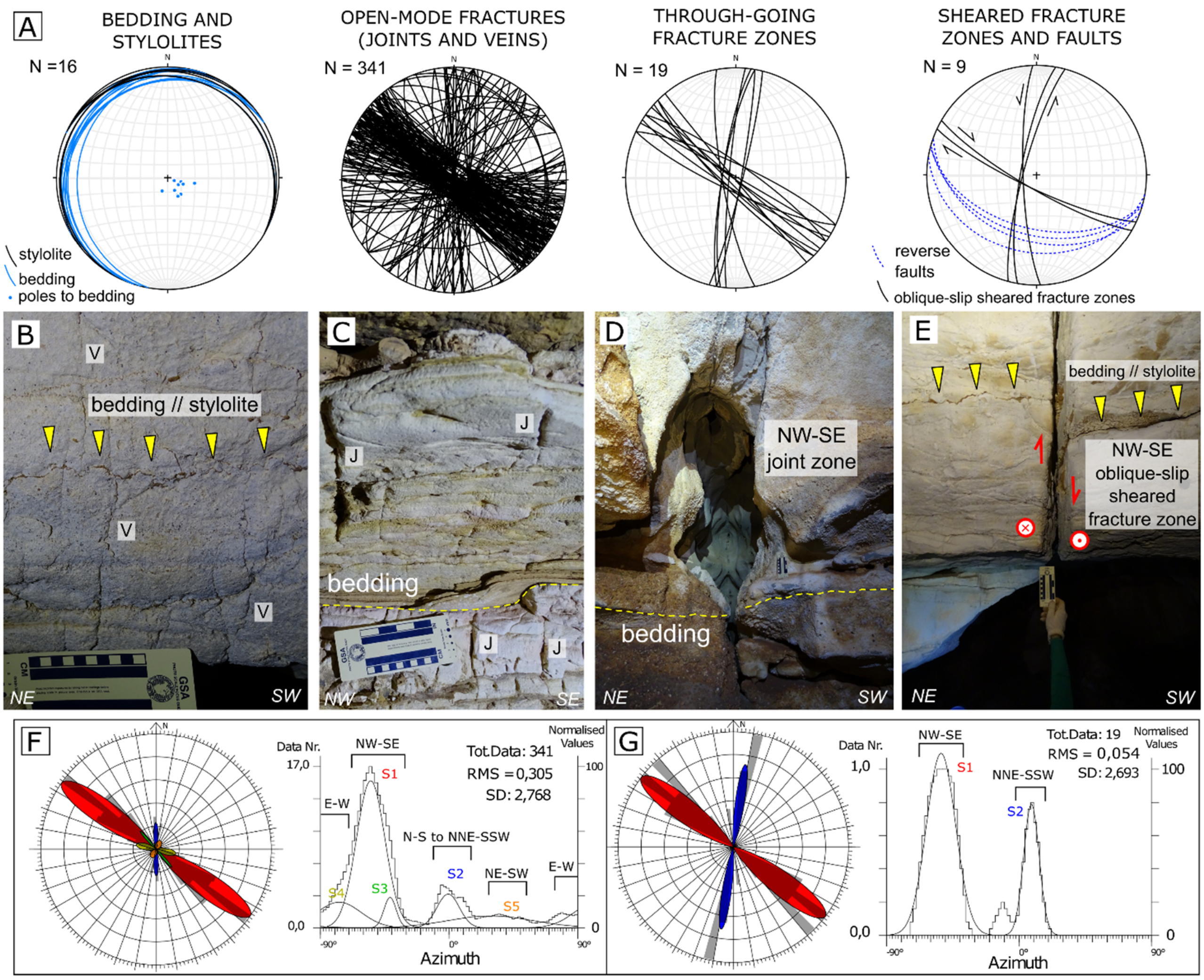

Figure 11. A) Structural features measured in the CCS displayed with lower-hemisphere equal-area stereographic projections and classified by type. B) Example of bedding-parallel stylolites and stratabound veins in the dolostones of unit A. C) Example of open-mode stratabound fractures (joints) in the dolomicrites and marly dolostones of unit B2. D) Karst dissolution along a through-going FZ composed of clustered open-mode fractures (joints) in unit A. E) Example of a small-scale fault along a NW-SE through-going fracture zone reactivated in shear (oblique-slip). F-G) Statistical analysis by Gaussian-best fit calculated from the normalized frequency distribution histograms for both the open-mode fracture dataset (F) and the through-going FZ dataset (G). Azimuth data are given in ±90°. RMS: root mean square error; SD: standard deviation.

The dolomitized grainstones in unit A are also affected by rare small-scale faults (Fig. 11E) interpreted as sheared through-going fracture zones (Myers and Aydin, 2004), which display similar characteristics and orientation to the previously mentioned FZ sets. In these faults, kinematic indicators are rarely observed, so that slip sense is generally evinced from the vertical throw of bedding interfaces or bedding-parallel stylolites. These small-offset (<1 m) faults have oblique-slip kinematics: right-lateral on the NW-SE trend and left-lateral on the NNE-SSW trend (Fig. 11A and E). Furthermore, secondary E-W-striking low angle reverse faults are observed; they cause small-scale detachments (throws up to 1–5 cm) of heterolith layers in the middle storey.

Fracture properties of open mode stratabound fractures measured along linear scanline are shown in Table 2.

Table 2. Scanline properties and quantitative fracture attributes measured for the open-mode fracture sets identified in the CCS.

	Scanlines properties						
Sedimentary unit	**Study site**	**Lithology**	**Scanline trend**	**Scanline length (m)**	**Layer thickness**	**n**	**Linear intensity P_{10} (m^{-1})**
A	point H	Crystalline dolostone	N12E	0.8	36 cm	15	18.75
	point A	Crystalline dolostone	N120E	0.75	41 cm	14	18.67
B1	point G	Highly silicified dolostone	N50E	0.35	8 cm	13	37.14
	point F	Highly silicified dolostone	N107E	0.9	6 cm	27	30.00
B2	point F	Marly dolostone	N107E	1.8	8 cm	19	10.55
	point G	Dolomicrite	N50E	0.8	10 cm	15	18.75
	point G	Marly dolostone	N50E	1.4	18 cm	9	6.43
B3	point F	Coarse laminated siltstone	N90E	3	20 cm	11	3.67
	point G	Mixed carbonate-siliciclastic coarse sandstone	N40E	3	36 cm	14	4.67
C	point J	Dolomicrite	N120E	0.6	28 cm	8	13.33
	point J	Dolomicrite	N35E	1.8	100 cm	18	10.00
C (chert)	point J	Silicified cherty dolostone	N35E	0.5	9 cm	23	46.00

Structural analysis

Sedimentary unit	Fracture Set, Strike	Type of fractures	Mean normal spacing (mm)	Cv	Mean mechanic aperture (mm)	Mean hydraulic aperture (mm)
A	NW-SE, N122E	Stratabound joints/veins	65.67 ± 0.51	1.07	1.06 ± 0.74	0.053 ± 0.072
	N–S, N177E	Stratabound joints/veins	29.71 ± 0.31	0.73	0.48 ± 0.27	0.010 ± 0.011
	NE-SW, N33E	Stratabound joints/veins	56.92 ± 0.22	0.56	0.92 ± 0.60	0.037 ± 0.054
	N–S, N2E	Fracture zones (n = 2)	–	–	–	–
	NW-SE, N128E	Fracture zones (n = 9)	–	–	–	–
B1	NW-SE, N118E	Stratabound joints	12.92 ± 0.41	1.29	0.31 ± 0.12	0.042 ± 0.038
	N–S, N12E	Stratabound joints	53.19 ± 0.35	0.68	0.46 ± 0.15	0.043 ± 0.039
B2	NW-SE, N130E	Stratabound joints/veins	92.38 ± 0.26	0.71	0.56 ± 0.29	0.016 ± 0.019
	NE-SW, N55E	Stratabound joints/veins	129.86 ± 0.20	0.42	0.71 ± 0.35	0.005 ± 0.004
	E-W, N94E	Stratabound joints/veins	22.94 ± 0.41	0.70	0.73 ± 0.35	0.004 ± 0.002
B3	NW-SE, N131E	Stratabound joints	210.8 ± 0.24	0.47	1.16 ± 0.56	0.029 ± 0.030
	NE-SW, N21E	Stratabound joints	196.05 ± 0.21	0.52	0.9 ± 0.30	0.028 ± 0.017
C	NW-SE, N134E	Stratabound joints/veins	95.28 ± 0.54	1.43	0.15 ± 0.11	0.001 ± 0.001
	N–S, N4E	Stratabound joints/veins	51.35 ± 0.31	0.79	0.17 ± 0.08	0.001 ± 0.001
C (chert)	NW-SE, N128E	Stratabound joints	53.92 ± 0.45	1.01	0.08 ± 0.03	0.003 ± 0.001
	N–S, N178E	Stratabound joints	16.76 ± 0.38	0.97	0.09 ± 0.03	0.003 ± 0.002

NW-SE, N–S, and NE-SW sets were measured in unit A. The NW-SE set shows a mean fracture spacing of 65–66 mm and a Cv value of 1.07. The N–S set has a mean spacing of 29–30 mm and a Cv value of 0.73. Finally, the NE-SW set shows a mean spacing of 56–57 mm and a Cv value of 0.56. In unit A, NW-SE and N–S through-going FZ were encountered along the linear scanlines; their real properties, however, were not measured due to the intense karst weathering.

The highly silicified layers in unit B1 (middle storey) show a high intensity of stratabound fractures (P_{10} ranging from 30 to 37 m^{-1}) with respect to the surrounding carbonate layers. Two main joint sets were recognized: NW-SE, with a mean spacing of 12–13 mm, and N–S, with a mean spacing of 52–53 mm. The Cv values are respectively 1.29 and 0.68. These two closely spaced fracture sets are organized in well-connected clusters.

In the scanlines through the marly dolostones and mudstones of unit B2, three main sets of stratabound open-mode fractures were identified: NW-SE, NE-SW and E-W. The NW-SE set shows a mean fracture spacing of 92–93 mm and a Cv value of 0.71. The NE-SW set has a mean spacing of 129–130 mm, and a Cv value of 0.42. Finally, the E-W set shows a mean spacing of 22–23 mm, and a Cv value of 0.7.

In the tempestite facies of unit B3, a minor intensity of brittle deformation (P_{10} ranging from 3.7 to 4.7 m^{-1}) is observed with two main joint sets striking NW-SE and NE-SW. Both sets show mean spacing around 20–21 cm and Cv values of 0.47 and 0.52, respectively.

In unit C, scanlines were measured both on chert nodules and carbonate layers (dolomicrite). The main sets measured are NW-SE and N–S. In the dolomicrite layer, the NW-SE set shows a mean spacing of 95–96 mm and a Cv value of 1.43, whereas the N–S set shows a mean spacing of 51–52 mm and a Cv value of 0.79. The NW-SE and N–S joint sets in the chert nodules result respectively in mean fracture spacing of 53–54 mm and 16–17 mm, and Cv values of 1.01 and 0.97, respectively. The silicified and cherty dolostone facies show the closest-spaced fracture sets, as well as the highest degree of fracture connectivity noticed by field observations both in map (Fig. 12A) and section view (Fig. 12B). On the contrary, in the carbonate-dominant and siliciclastic facies (Fig. 12C and D) fractures are mainly constituted of stratabound veins with variable apertures and wide spacing. In the lower storey, localization of through-going FZ and faults can produce volumes of channelized fracture permeability testified by their association with feeders (Fig. 5B and C), rising conduits (Fig. 7A), and karst development (Fig. 11D). The fracture intensity (P_{10}) was calculated for each scanline and is reported in Fig. 12E and Table 2.

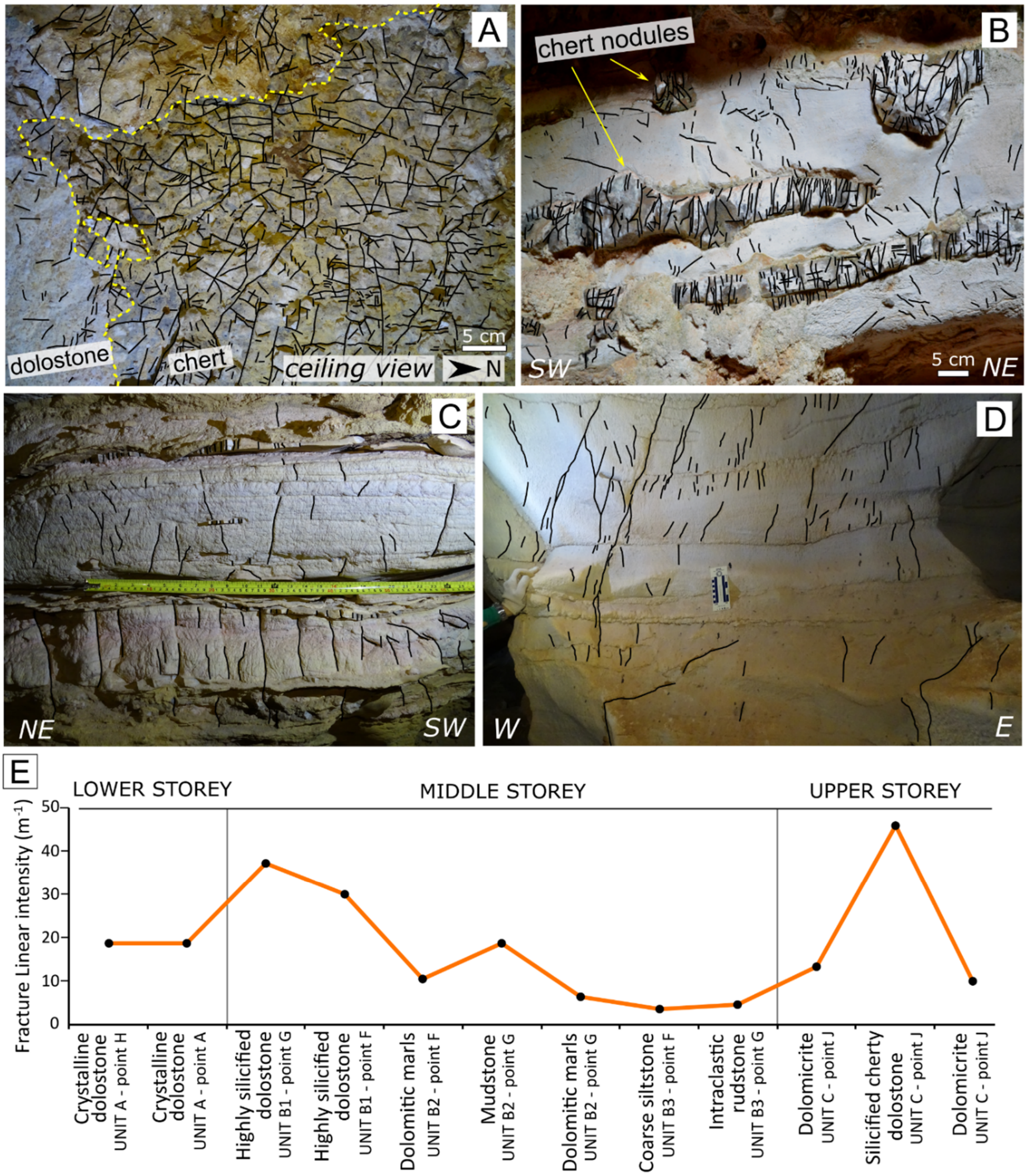

Figure 12. Fracture patterns highlighted by line drawing in the different sedimentary units of the CCS. A) Example of fracture development in dolostone (low connectivity, low fracture density) and chert (high connectivity, high fracture density) in the highly silicified layers of the middle storey. Note that the picture represents a planimetric view of the ceiling. B) Different fracture patterns in the cherty dolomicrites of unit C (upper storey). Chert nodules localize brittle deformation and fracturing. C) Example of widely spaced and stratabound fractures in unit B2 (middle storey). Occasional through-going but poorly connected fractures are observed. D) Stratabound and clustered through-going fractures in unit A (lower storey). E) Fracture linear intensity (P_{10}) calculated for each scanline. Chert nodules in the highly silicified layers localize the highest values of P_{10} (30-40 m^{-1}).

3.1.4.4. Petrophysical properties

The fracture properties collected from different scanlines in the cave allowed to characterize the variations in fracture normal spacing and to estimate individual fracture permeability for the whole sedimentary sequence outcropping in the CCS (Philipp et al., 2013; Giuffrida et al., 2020). The results are displayed in $\log_{10}$ scale as box-plot diagrams (Fig. 13), subdivided by fracture sets and grouped according to the different sedimentary units described in the previous sections. The crosses in the boxplots refer to mean values, whereas the left and right box sides are the 1st and 3rd quartiles, respectively. The box whiskers define the minimum and maximum values in the data range excluding outliers. Estimated individual fracture permeability in unit A ranges from 10^3 to 10^5 mD, with a mean value around 10^4 mD. In unit B1, stratabound fractures are closely spaced (mean values around 10^1 mm), and they have a fracture permeability with mean values between 10^4 and 10^5 mD for each individual set. Unit B2 has variable permeability values, with means around 10^3 mD. In the siltstones of unit B3, fracture spacing is wide (up to 10^2–10^3 mm) and the mean fracture permeability is around 10^4–10^5 mD. Finally, in unit C fracture permeability is higher in the silicified zones with chert nodules (means between 10^2 and 10^3 mD) than in the dolomicrite facies (means between 10° and 10^1 mD).

On the right side of Fig. 13, the rock plug measurements of porosity (expressed in %) and permeability (expressed in mD) are displayed in a $\log_{10}$ scale. Rock plug permeability values are subdivided into horizontal and vertical permeability. The colored dots represent the mean values, whereas the whiskers refer to the 1st and 3rd quartiles of the datasets. The results from the analyses are displayed in a $\log_{10}$-$\log_{10}$ diagram in Fig. 14, where trendlines represent the best fit power-law distribution of the datasets subdivided by sedimentary units. All R^2 values are >0.7 except in the silicified unit B1, where alteration and karst dissolution are intense and permeability values are scattered (R^2 value is 0.48). The mean R^2 value (R^2=0.72) of the trendlines confirms a good fit of the power-law distribution for the datasets.

Fig. 13 graphically describes the variations of petrophysical properties relative to the CCS lithostratigraphic profile and the spatial organization (pattern) of the hypogene conduit system. Rocks in unit A have low-medium porosity (ranging from 2% to 15%, mean value of 6%) and permeability values range from 10^{-3} to 10^2 mD (maximum 129.1 mD). The silicified unit B1 presents medium porosity (from 5% to 16%, with a mean of 11%) and variable permeability with values ranging from 10^{-2} to 10^3 mD (maximum 231.7 mD in bedding-parallel plugs). The heterolithic and tempestite facies of units B2 and B3 have the highest porosity values, ranging from 6% to 29%, with mean values respectively of 11% and 20%. On the other hand, the permeability of rock plugs is low, with values ranging from 10^{-3} to 10^{1} mD. In unit C, values of porosity are significantly different between the rocks in the upper speleogenetic storey (mean value of 6%) and those from the passages comprised between the entrance and the intercalations of unit B2. The latter have the lowest porosity of the entire dataset (1–2%). In a similar way, the permeability of rock plugs has low values around 10^{-3} mD in the upper interval of unit C, and variable values ranging from 10^{-3} to 10^{1} mD in the karstified upper storey.

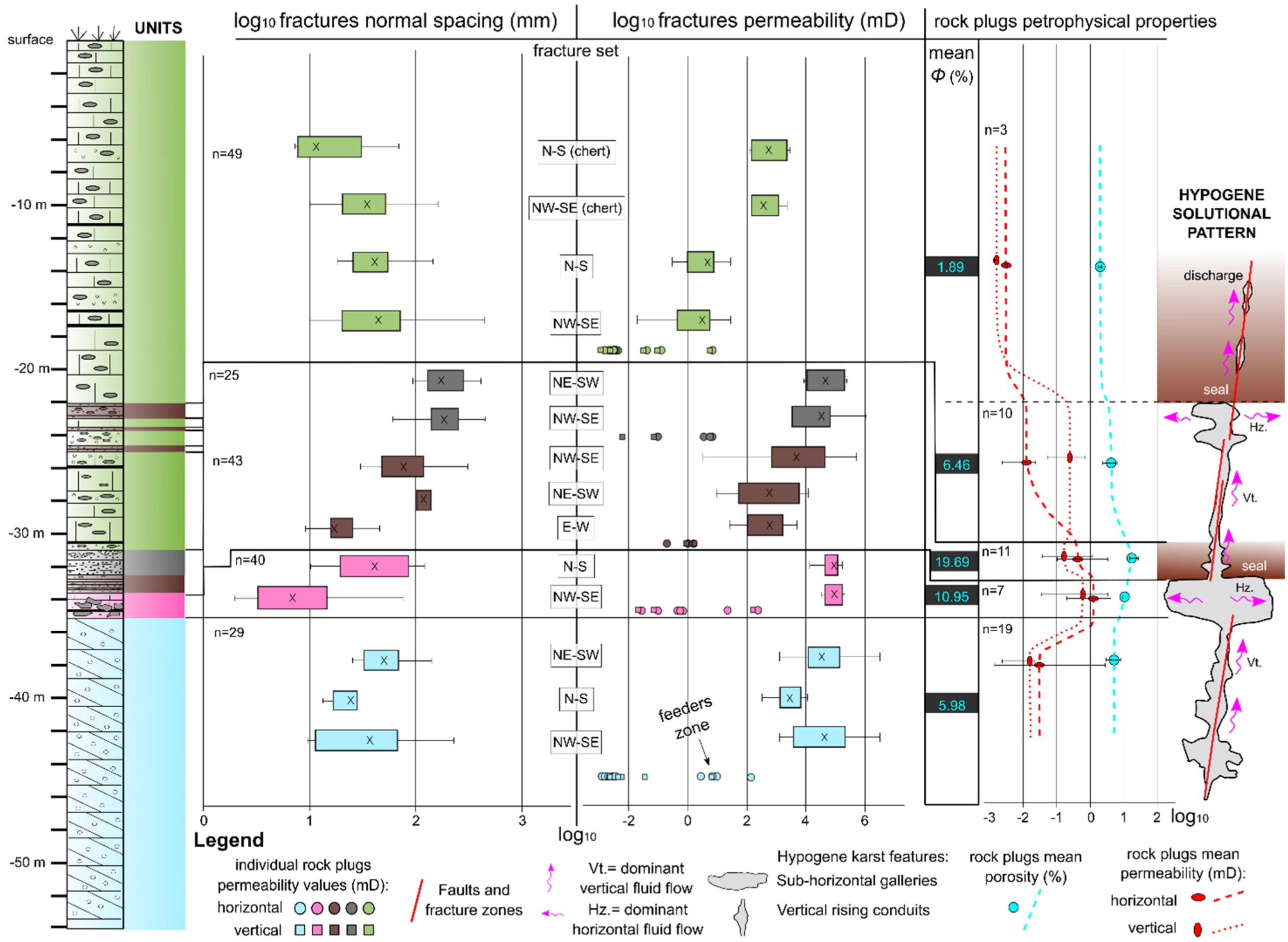

Figure 13. Boxplots show the variation of petrophysical properties, fracture normal spacing, and fracture permeability of individual sets along the lithostratigraphic profile in the CCS gallery-conduit system. For the legend of the lithostratigraphic log, the reader is referred to Fig. 3.

EPM permeabilities for each speleogenetic unit in the CCS, calculated for discharge parallel to the main fracture sets (K_P) or normal to the main fracture sets (K_N), are summarized in Table 3. These values reflect the anisotropy in permeability for the different speleogenetic units in the CCS.

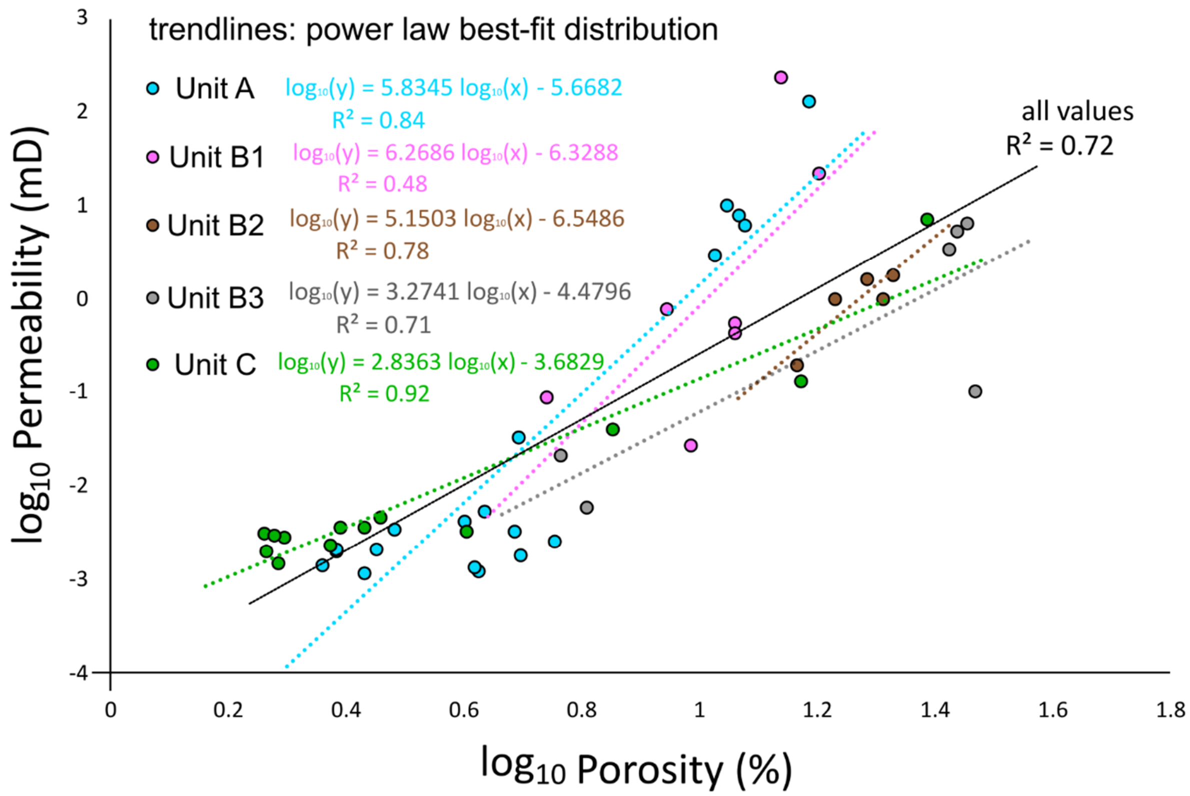

Figure 14. Log-log diagrams showing the relationship between rock plug porosity and permeability grouped according to sedimentary units. The trendlines correspond to the best fit, power-law distribution for each dataset and for the whole population (black trendline, R^2 value of 0.72).

Table 3. Equivalent Porous Media (EPM) permeability calculated for the different CCS speleogenetic units considering an elementary cubic cell of 1 m width.

Speleogenetic units	**Sedimentary units**	**K_P (mD)**	**K_N (mD)**
Doline entrance	C	0.019	0.003
Upper storey	C–B2	1.30	0.74
Middle storey (siliciclastic seal)	B3	34.22	3.09
Middle storey (heterolithic seal)	B2	10.93	0.96
Middle storey (high-K silicified dolostones)	B1	1176.38	36.67
Lower storey	A	737.60	11.55

3.1.5. Discussion

This study provides evidence for hypogene flow and karst dissolution in a silicified carbonate-siliciclastic sequence. Our observations allow us to propose a conceptual evolutionary model for the CCS, identifying different fluid flow pathways and hypogene speleogenetic mechanisms that drastically modified the original porosity-permeability of the layered sedimentary sequence. Furthermore, the CCS represents a conceptual analog of many deep carbonate reservoirs where silicification and hydrothermal alteration are common processes making the characterization of the reservoir properties a challenging task (De Luca et al., 2017; Montanari et al., 2017; Lima et al., 2020). In particular, the pre-salt carbonate reservoirs of Campos-Santos Basin (Lima et al., 2020) and Kwanza Basin (Poros et al., 2017) show silicification and dissolution features similar to those documented in the CCS.

In the next sections, we discuss the role of structural-stratigraphic variability in the definition of high vs. low permeability zones, hypogene fluid migration, and dissolution. Our observations are integrated into conceptual models illustrating the spatial-temporal evolution of the sequence and its implications for karst reservoirs.

3.1.5.1. High permeability vs. seal (buffering) units, fluid flow pathways, and hypogene dissolution

Permeability pathways and karst formation in fractured and layered carbonates mostly depend on the interaction between stratigraphy, fracture patterns, diagenetic features, and the hydrogeological-speleogenetic setting (Audra and Palmer, 2015; Klimchouk, 2019; Balsamo et al., 2020). The recognition of the main hydrological behavior of the sedimentary units composing a layered sequence is therefore fundamental to correctly interpret its speleogenetic evolution in space and time (Klimchouk, 2007; Klimchouk et al., 2009).

The analyses of fracture patterns, petrophysical properties, and speleogenetic features in the different sedimentary units of the CCS allowed to recognize high permeability and “seal” (buffering) units (Table 3; Fig. 13). These hydrogeological-speleogenetic units strongly influenced fluid flow directions and resultant karst geometries. Due to the limited scale of observation and the lack of regional data, we define these “seal” units as low permeability buffer zones. Such zones vary in lateral thickness and might be breached by non-stratabound fractures (Fig. 11). These vertically extended fractures act as conduits in specific discharge areas of the regional groundwater system (Klimchouk et al., 2016).

Based on the field analyses, microtextural observations and analytical results presented in the previous sections, we propose a timeline for the main diagenetic, structural and speleogenetic phases that affected the CCS sequence. The spatial-temporal evolution is illustrated in the conceptual model of Fig. 15. In the following sections, we refer to three main diagenetic evolution stages as defined by Choquette and Pray (1970) and Morad et al. (2000): eodiagenesis, corresponding to the early processes taking place at shallow depth near the surface (commonly up to a few hundred meters below the surface); mesodiagenesis, corresponding to the burial interval below the influence of near-surface processes until the onset of low-grade metamorphism; and telodiagenesis, corresponding to the processes that take place during uplift and exhumation of previously buried rocks.

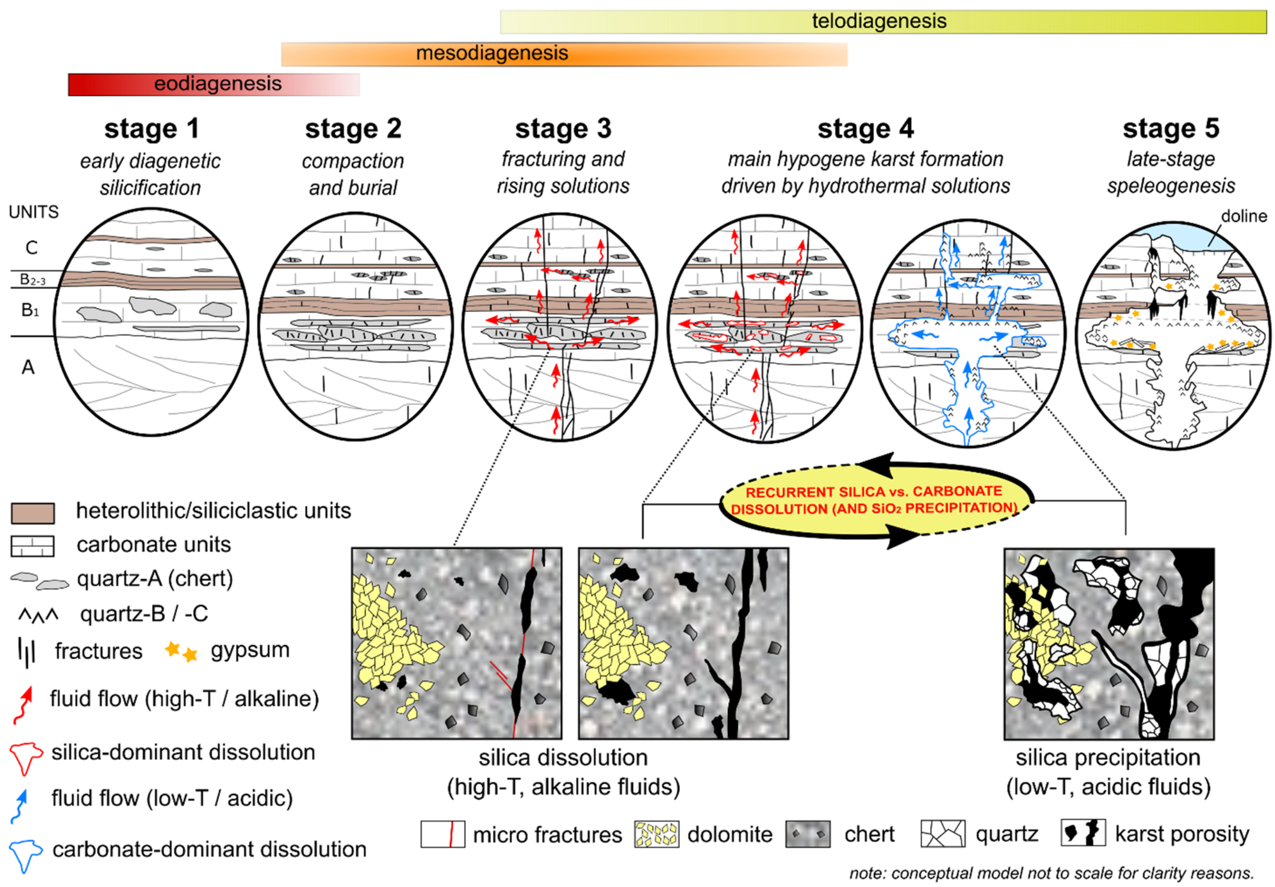

Figure 15. Conceptual spatial-temporal development model for the Calixto Cave system at the micro-scale (vuggy karst porosity formation; lower part of the panel) and macro-scale (solutional human-sized cave passages; upper part of the panel). See the Discussion section 3.1.5.1. in the main text for further explanations.

3.1.5.1.1. Stages 1 and 2 – early diagenetic silicification and burial

Silicification in the CCS affected selected carbonate layers; in some of these layers (unit B1) SiO_2 content can reach up to 80-85 wt.% (Fig. 4). The main episode of diffuse silicification is represented by the formation of chert nodules. Micro-crystalline quartz (Qtz-A) replaces the carbonate grains and cement and forms nodular aggregates (Fig. 6, Fig. 9, Fig. 10).

The precursor carbonate units in the CCS are entirely composed of dolostones. Almost no calcite has been found, although several fabric characteristics and microtextures (like ooids) are still preserved in thin sections indicating original calcite deposition. Since it is not the focus of this work, we will not discuss the dolomitization process. However, we hypothesize that the dolomitization should have occurred during eodiagenesis before the formation of chert nodules and after the diagenetic cementation of the original carbonate sediments.

From meso-to microscopic observations, the chert nodules in the carbonates predate pressure solution caused by burial (Fig. 8, Fig. 9C), which developed at a depth generally < 800–900 m (Van Golf-Racht, 1982; Rolland et al., 2014; Araújo et al., 2021). Furthermore, burial-related stylolites are common features consistent with eodiagenetic to early-mesodiagenetic settings (Caracciolo et al., 2014; Souza et al., 2021). We suggest, therefore, that the diffuse dolomite replacement and the formation of the chert nodules was likely restricted to shallow burial conditions and early diagenetic settings (< 1 km: Fig. 15). The sources of Si-rich fluids which could have triggered this diffuse silicification, common also in other carbonates of the Salitre Fm, are still unknown. The hypothesis of hydrothermal solutions rising through the underlying Chapada Diamantina quartzites along basement-rooted structures has been suggested by some authors (Bertotti et al., 2020; Cazarin et al., 2021).

Mechanical compaction during progressive burial until the transition to early-mesodiagenesis caused open-mode regularly spaced fractures represented by the NE-SW and NW-SE striking sets (Fig. 11A; Table 2). Fracture localization in layers with high concentration of stiff chert nodules (unit B1) forms highly-connected joint networks (Fig. 12A and B).

3.1.5.1.2. Stage 3 – rising flow and deep-seated silica dissolution

Chert nodules in the CCS show a porous texture (Fig. 7, Fig. 10A) and single quartz grains characterized by solutional pits, "V"-shaped notches, and dissolution related vugs (Fig. 10C and D; Higgs, 1979; Burley and Kantorowicz, 1986; Shanmugan and Higgins, 1988; Sauro et al., 2014; Itamiya et al., 2019). Dissolution features at different scales (Fig. 7, Fig. 10), blocky mega-quartz and chalcedony filling solutional pores and fractures, and quartz-rich brecciated micro-textures suggest a complex history of fluid-rock interaction and mineralization during mesodiagenesis.

The widespread evidence of silica dissolution observed at the micro-scale in the CCS is particularly relevant for its implications regarding deep carbonate reservoirs. It is commonly known that quartz solubility exponentially increases with temperature (Siever, 1962; Rimstidt, 1997; Dove, 1999; Gunnarsson and Arnórsson, 2000; Marin-Carbonne et al., 2014; Sauro et al., 2014; Cui et al., 2017). Furthermore, silica solubility is nearly constant at pH<8, and significantly increases at greater values (Mitsiuk, 1974; Andreychouk et al., 2009; Mecchia et al., 2019). Also, Ba^{2+} transported in solution (suggested by the presence of barite mineralization in the CCS) could have determined a significant positive effect on quartz solubility, as reported by previous works (Dove and Nix, 1997; Sauro et al., 2014; Mecchia et al., 2019).

We propose that an early phase of hypogene dissolution occurred in deep-seated conditions, where silica-dominant dissolution was driven by warm (likely >100–150 °C) and alkaline fluids able to reach the silicified layers. The result was the formation of micro-scale karst (vuggy) porosity and solutionally-enlarged fractures in the cherts (Fig. 15). Mineral phases such as Fe–Cr spinels, Fe–Ti oxides, barite, anhydrite, sulfides, rutile, and phosphates (mainly apatite) found as solid inclusions associated with quartz mineralizations (Fig. 9, Fig. 10; Table 1) strongly support a hydrothermal origin for this deep-seated hypogene phase.

Mechanical compaction during progressive burial and multiple tectonic events at the time of the *Brasiliano* Orogeny caused the formation of many different permeable structures (Fig. 11). Driven by pressure gradient and/or fluid buoyancy, the permeable structures focused upward flow, as suggested by the presence of the solutionally-enlarged feeders in the lower storey of the cave.

Our structural data indicate two main contractional events that postdate burial. The E-W striking open-mode fracture set is consistent with the first contractional phase (~E-W direction of maximum shortening) recorded also in other areas of the Una-Utinga basin (D'Angelo et al., 2019; Pontes et al., 2021). The second contractional event is related to the formation of the N–S to NNE-SSW open-mode fracture sets formed parallel to a roughly NNE-SSW direction of maximum shortening. Progressive deformation during this contractional phase produced the clustering of NNE-SSW joints/veins with the formation of through-going FZ in unit A. Based on our structural analysis, we propose that the same NNE-SSW contractional phase also controlled the reactivation of the pre-existent NW-SE joints/veins sets, causing the formation of clustered FZ eventually reactivated in shear (Myers and Aydin, 2004) with oblique-slip kinematics (Fig. 11E). These vertical structures acted as the main permeability pathways for rising fluid flow (Fig. 5B). Bedding-parallel NNE-SSW-oriented shortening also caused the formation of ESE-WNW small-scale reverse faults observed in the middle storey (Fig. 11A).

Similar deformation patterns were documented in the region by D'Angelo et al. (2019). These latter authors interpreted left-lateral N–S and right-lateral NW-SE strike-slip faults as reactivated deep-rooted structures related to a N–S- to NNE-SSW-oriented contractional phase. Main migration routes of rising hydrothermal fluids may be related to these buried strike-slip fault zones cross-cutting the basement (D'Angelo et al., 2019; Bertotti et al., 2020). Similar fault orientations occur in the CCS (Fig. 11A and E).

3.1.5.1.3. Stage 4 – main hypogene karst formation and silica reprecipitation

During stage 4 (Fig. 15) the rising hydrothermal fluids driven by pressure gradients and/or fluid buoyancy shaped the main hypogene karst in the CCS. The timing of the proposed hypogene large-scale karst porosity formation is still unknown. The occurrence of other hydrothermal events in the São Francisco Craton with similar mineral paragenesis (Kyle and Misi, 1997; Misi et al., 2005, 2012) and hypogene caves (Klimchouk et al., 2016) suggest a possible late Cambrian age. However, multiple phases of burial and denudation after the Early Cretaceous Pangea break-up occurred in the São Francisco Craton. The cumulative overburden above the present-day surface in the Chapada Diamantina quartzites (west of the study area) was estimated around 2–3 km (Japsen et al., 2012). This evidence suggests a complex and long burial-exhumation history for the carbonates of the Salitre Fm, during which hydrothermal fluids could have been able to drive dissolution generating large-scale karst porosity in hypogene settings.

The variability in petrophysical properties among the sedimentary units in the CCS (Fig. 13) determined the formation of the different speleogenetic storeys (and their associated morphologies). The lower storey hosted channelized vertical permeability pathways that acted as feeders for vertical fluid flow. In this storey, permeability pathways are mainly expressed by through-going fracture zones with high hydraulic apertures and good connectivity, which provided high vertical permeability ($K_P=10^2$ mD, Table 3). On the contrary, the middle storey is characterized by a sub-horizontal network of galleries developed mainly in the silicified unit (B1). The contrasting mechanical behavior of stiff chert nodules in the silicified layers with respect to surrounding dolostones, heteroliths, and marls, concentrated stress and caused fracture localization (Alvarez et al., 1976; Antonellini et al., 2020), producing networks of high permeability clustered joints (Fig. 12).

As a result of high fracture permeability and early dissolution of silica during stage 3, K_P in unit B1 is the highest observed in the whole CCS ($K_P=10^3$ mD, Table 3), with values 2 to 3 orders of magnitude higher than those from units B2, B3, and C, and around 10 times the values observed in unit A. Unit B1 acted, therefore, as an inception horizon, defined as a lithostratigraphically-controlled element that favored hydraulic conductivity and the onset of dissolution (Lowe and Gunn, 1997).

At the same time, the heterolithic and siliciclastic rocks of units B2 and B3, despite having high porosity (∼10–20%), have a low EPM permeability ($K_P=10^1$ mD, $K_N=10^0$ mD; Fig. 13, Table 3). This evidence, combined with the morphological observations on conduit geometries and distribution, indicates that they acted as low permeability buffering units promoting sub-horizontal flow in the underlying layers (Klimchouk et al., 2016; Balsamo et al., 2020). Additionally, these units are mostly composed of heterogeneous siliciclastic grains (i.e., K-feldspar, muscovite, quartz, kaolinite, chlorite, clay minerals), which are less soluble. Karst formation eventually occurred in focused discharge areas along through-going FZ connecting the middle and upper storey (Fig. 13, Fig. 15). Like unit B1, the occurrence of sub-horizontal solutional galleries in the upper storey is focused on the silicified ooidal grainstone and wackestone layers (Fig. 8, Fig. 13) sealed at the top by intercalations of low permeability heterolith layers.

The very low porosity (∼1–2%) and permeability of the dolomicrites in the upper sector of unit C ($K_P=10^{-2}$ mD, $K_N=10^{-3}$ mD; Table 3) is 5–6 orders of magnitude lower than the middle and lower storey permeability. This suggests that unit C acted as an efficient buffer for vertical fluid migration and karst formation, although a certain degree of discharge is expected to guarantee rising flow at the regional scale (Klimchouk et al., 2016).

The dissolution of carbonate and silicified layers to form the main conduit network required specific (and almost opposite) conditions, with the dolostone dissolution promoted by acidic and low temperature conditions, and the silica dissolution promoted by alkaline and high temperature conditions (Andreychouk et al., 2009; Cui et al., 2017). These two “end-members” of the hydrothermal fluids (at different temperature and/or geochemistry) do not necessarily imply distinct temporal intervals. On the contrary, we propose that a recurrent system of multiple silica- vs. carbonate-dominant dissolution (and silica reprecipitation) phases happened during stage 4 (Fig. 15). Hot and alkaline conditions promoted the silica-dominant dissolution of the silicified layers, enlarging and connecting the vuggy pores in chert nodules (mostly concentrated in unit B1). Water cooling and/or gradual pH changes in the hydrothermal flow system led towards more acidic conditions and caused the switch from silica-dominant dissolution to carbonate-dominant dissolution. Conduit morphology in the lower storey (spongework pattern, vertically extended rising conduits and rift-like feeders with reactive fronts) and widespread vuggy porosity in the dolostones indicate the weathering and corrosion effects of the hydrothermal fluids on these carbonate units. The precipitation of Qtz-B/Qtz-C and the associated hydrothermal mineral suite of Ca-sulfates, barite, muscovite, K-feldspar, Fe–Ti oxides, Fe–Cr spinels, sulfides, and phosphates (Table 1) occurred mainly in the lower sector of the cave below the heterolithic/siliciclastic units. The precipitation of these minerals caused partial occlusion of pore space in the vuggy and fracture porosity (Fig. 7, Fig. 9, Fig. 15). Similar hydrothermal mineral assemblages are common also in the Brazilian pre-salt reservoirs (Lima and De Ros, 2019; Lima et al., 2020) and associated with MVT-type ore deposits found in the São Francisco Craton (Kyle and Misi, 1997; Cazarin et al., 2019, 2021).

3.1.5.1.4. Stage 5 – late-stage speleogenesis

The final stage of karst development (stage 5, Fig. 15) involved sulfuric acid formation in supergene conditions derived from pyrite oxidation within a shallow oxygenated (aerated) environment (Auler and Smart, 2003). This is indicated by the occurrence of iron oxide and hydroxide pseudomorphs replacing pyrite disseminated in the host rock, and secondary gypsum overgrowths and powders widely distributed in the cave system. The latter could be also the product of bat guano reactions. Condensation-corrosion processes likely enhanced the carbonate weathering in the cave system, as also suggested by the presence of condensation-corrosion features and dolostone weathering. Finally, collapse processes favored the widening of karst voids in the upper sector of the cave, ultimately causing the connection to the surface and the related transport of clastic sediments into the upper part of the CCS. All these late-stage processes overprinted the original dissolution morphologies of the karst system and amplified the dimensions of the passages observed today.

3.1.5.2. Cave spatial-morphological organization and implications for karst reservoirs

The 3D multistorey organization of the CCS is conceptually summarized in the sketch diagram of Fig. 16. The strong heterogeneity observed in the cave pattern and morphology is related to the lithological differences (Fig. 3, Fig. 4) and the vertical distribution of fractures (Fig. 12, Fig. 13). At the same time, petrophysical properties at the scale of the rock plugs indicate significant differences among the sedimentary units, especially those affected by silicification (Fig. 13). The variability in fracture spacing, individual fracture permeability, and petrophysical properties at the meso-scale (rock plugs) may be useful to recognize different hydrological units, fluid flow pathways and, therefore, speleogenetic storeys (Fig. 13, Fig. 16; Table 3).

Estimated fracture permeability is calculated from present-day hydraulic apertures of the discontinuities but, at the time of speleogenesis, these apertures could have been significantly lower due to stress-dependency laws and fracture closing induced by loading (Holt, 1990; Min et al., 2004). Such calculations are beyond the scope of this work. However, based on our geomorphological observations of the cave pattern, morphology, and former flow pathways, we propose that the spatial organization of the karst system is expression of the structural-stratigraphic variability in the sequence.

In layered carbonate sequences of low primary porosity, through-going fractures (faults and fracture zones) are crucial for cross-formational fluid flow as they may determine the vertical connectivity of different sedimentary units. At the same time, the interplay between low-permeability buffering units and high-permeability units ($K>10^3$ mD) provided by high-aperture and closed-spaced (clustered) stratabound fractures may control horizontal permeability development and the formation of stratigraphically controlled voids. The combination of sub-seismic, meter-thick intercalations of low- ($K<1$ mD) and high-permeability ($K>10^3$ mD) units enhanced sub-horizontal karst formation in the CCS middle storey generating more than 1 km of large-scale, human-sized galleries (Fig. 16). Additionally, through-going fracture zones form vertical permeability pathways that crosscut the seal/buffer units, allowing fluids to rise into the upper sectors of the sequence, and promoting the formation of multiple levels of sub-horizontal cave passages at different stratigraphic positions (Fig. 16). The occurrence of similar multistorey karst patterns is not uncommon, especially in the Salitre Fm (Klimchouk, 2007; Klimchouk et al., 2016; Cazarin et al., 2019).

Our results provide new insights for the understanding of deep-seated karst formation and dissolution/precipitation involving silicified carbonate units. The spatial and morphological organization of dissolution features documented in the CCS (both at macroscopic and microscopic scale; Fig. 15, Fig. 16) may be used as a conceptual analog or a proxy for many carbonate reservoirs where silicification and karst development are associated with specific sedimentary packages, like in the offshore pre-salt reservoirs of Brazil and Africa (Poros et al., 2017; Lima et al., 2020) or in the silicified reservoirs of the Tarim Basin (You et al., 2018). Karst cavities more than 2 m in diameter were observed at depths of 0.5–1.5 km in the Devonian and Carboniferous carbonate rocks of the Kizelovski basin and in the North Ural oil and gas basins (Andreychouk et al., 2009). Abundant cavities and macro-scale karst zones were intercepted by drillings at a depth down to 3–6 km in limestones, dolostones, and silicified carbonates of many basins worldwide (Zhao et al., 2018). Small-scale voids (vugs and fractures enlarged by dissolution) were also detected at depths larger than 5–10 km (Maximov et al., 1984; Andreychouk et al., 2009).

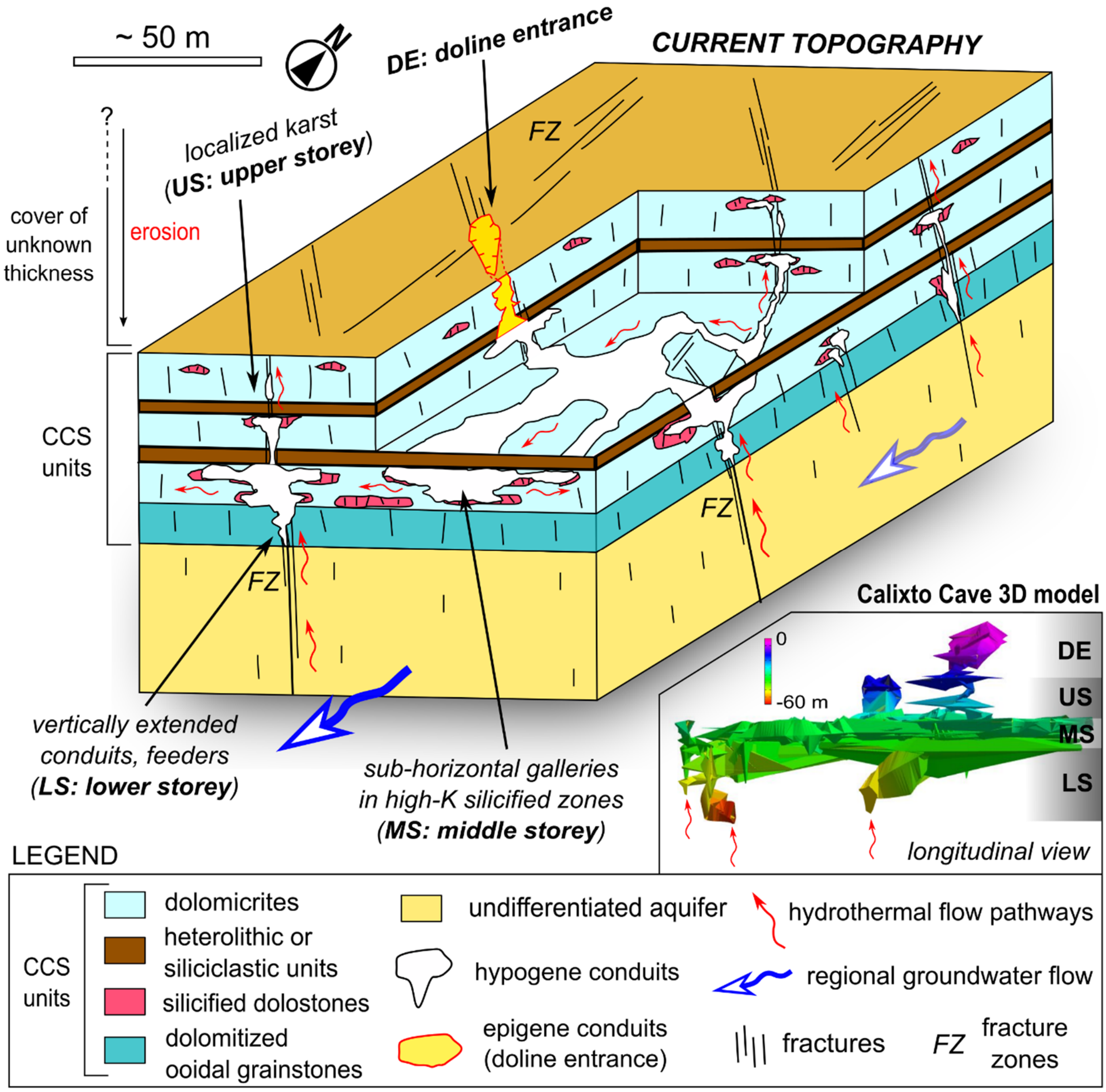

Figure 16. Schematic block diagram illustrating the spatial-morphological organization of the CCS and the main fluid flow pathways. In the lower right corner, the 3D model of the cave (see also Fig. 3) is shown in a longitudinal section to visualize the vertical pattern of the multistorey system. Labels abbreviations: LS (lower storey), MS (middle storey), US (upper storey), DE (doline entrance).

The observations presented in this paper may help to better understand the relations between silicification and hypogene dissolution in deep-seated settings, contributing to the prediction of karst patterns at different scales. Furthermore, the CCS provided an enlightening example of the complex speleogenetic history that could affect ancient basins, where deep-seated dissolution (and precipitation) may drastically modify porosity in quartz-rich rocks such as highly silicified carbonates, commonly considered less prone to karst formation.

3.1.6. Conclusions

Our analytical and field studies support a conceptual model on the relation among stratigraphy, silicification, fracture patterns, petrophysical properties, and hypogene karst formation in the CCS. The main outcomes are summarized in the following points:

1. The mineralogy of the deposits and the geomorphological features of the cave suggest a deep-seated hypogene (hydrothermal) origin for the early karst phase. Early diagenetic silicification caused the replacement of dolomite grains and cement with microcrystalline quartz (up to 80-85 wt.% of the bulk rock content). Below low permeability units, extensive mineral deposits are associated with blocky mega-quartz, chalcedony and a paragenesis of solid inclusions supporting the hydrothermal hypothesis.
2. The structural and stratigraphic variability in the CCS determined a strong anisotropy in fracture patterns, petrophysical properties, and fluid flow pathways. Fracturing concentrated in chert nodules causes a high intensity of open-mode fractures contributing to high permeability and dissolution localization. At the same time, through-going fracture zones and faults in the lower sector of the cave (characterized by low primary porosity and permeability) focused rising fluid flow along vertical permeability pathways (feeders and rising conduits).
3. Sedimentary units composed of heteroliths, marly dolostones, and fine-grained siliciclastic rocks represent a low-permeability seal/buffer unit that stopped/buffered vertical fluid flow. Through-going fracture zones breached these units, allowing vertical discharge and providing interconnectivity among the different sedimentary units.
4. The structural and stratigraphic variability in the CCS determined the formation of a complex 3D multistorey karst system. Silica-dominant dissolution (likely at $T \geq 100$–150 °C and $pH \geq 8$-9) promoted the formation of a stratigraphically-controlled inception horizon in the silicified and high-permeability dolostones of the middle storey. Multiple silica-vs. carbonate-

dominant dissolution phases driven by hydrothermal solutions produced large-scale karst porosity, as well as the precipitation of the quartz-rich mineral deposits filling pore space and fractures. During telodiagenesis, collapses, condensation-corrosion, and karstification in supergene and epigene settings further amplified the conduit dimensions until today.

5. The results presented in this study contribute to expand our understanding of hypogene karst development in layered carbonate-siliciclastic units affected by silicification. The CCS example may be used to improve the conceptualization of predictive models on the spatial and morphological organization of buried hypogene conduit networks.

Acknowledgments

This research was carried out in association with the ongoing R&D project registered as ANP 20502-1, "*Processos e Propriedades em Reservartórios Carbonáticos Fraturados e Carstificados – POROCARSTE 3D" (UFRN/UNB/UFRJ/UFC/Shell Brasil/ANP*) – Porokarst – Processes and Properties in Fractured and Karstified Carbonate Reservoirs, sponsored by Shell Brasil under the ANP R&D levy as "*Compromisso de Investimento com Pesquisa e Desenvolvimento*". Cave map data were kindly provided by *Grupo Pierre Marin de Espeleologia* (GPME). Cave sampling was performed through SISBIO permit 63178/1. Many thanks to Alisson Jordão, Uilson Teixeira and Vicente Antonio Do Nascimento for the help during fieldwork.

We sincerely thank the Iramaia municipality (State of Bahia) and the Brazilian Federal Environmental Agency, *Instituto Chico Mendes*, for providing the access to the cave and the special permission for collecting rock samples. We also thank Giulio Viola and Paolo Garofalo for the access to the optical microscopy laboratory (University of Bologna), Fabio Gamberini for thin sections preparation, Giorgio Gasparotto for the access to the SEM laboratory in Bologna, and Gabriella Koltai, Yuri Dublyansky, and Christoph Spötl for the fruitful discussions. Finally, we thank Alexander Klimchouk and three anonymous reviewers for the detailed and constructive review that significantly improved our work.

References

Almeida, F.F.M., Brito Neves, B.B., Dal Rè Carneiro, C., 2000. The origin and evolution of the South American Platform. Earth Sci. Rev. 50, 77–111.

Alvarez, W., Engelder, T., Lowrie, W., 1976. Formation of spaced cleavage and folds in brittle limestone by dissolution. Geology, 4, 698–701.

Andreychouk, V., Dublyansky, Y., Ezhov, Y., Lisenin, G., 2009. Karst in the Earth's Crust: Its Distribution and Principal Types. University of Silezia — Ukrainian Institute of Speleology and Karstology, Sosnovec–Simferopol, 72 pp.

Antonellini, M., Cilona, A., Tondi, E., Zambrano, M., Agosta, F., 2014. Fluid flow numerical experiments of faulted porous carbonates, Northwest Sicily (Italy). Mar. Pet. Geol. 55, 186–201.

Antonellini, M., Del Sole, L., Mollema, P.N., 2020. Chert nodules in pelagic limestones as paleo-stress indicators: A 3D geomechanical analysis. J. Struct. Geol. 132, 103979.

Araújo, R.E.B., La Bruna, V., Rustichelli, A., Bezerra, F.H.R., Xavier, M.M., Audra, P., Barbosa, J.A., Antonino, A.C.D., 2021. Structural and sedimentary discontinuities control the generation of karst dissolution cavities in a carbonate sequence, Potiguar Basin, Brazil. Mar. Pet. Geol. 123, 104753.

Audra, P., Palmer, A.N., 2015. Research frontiers in speleogenesis. Dominant processes, hydrogeological conditions and resulting cave patterns. Acta Carsologica 44 (3), 315–348.

Audra, P., L. Mocochain, J.-Y. Bigot, and J.-C. Nobecourt, 2009, Morphological indicators of speleogenesis: Hypogenic speleogens, in A. B. Klimchouk and D. C. Ford, eds., Hypogenic speleogenesis and karst hydrogeology of artesian basins: Simferopol, Ukraine, Ukrainian Institute of Speleology and Karstology, p. 13–17.

Auler, A.S., 2017. Hypogene caves and karst of South America. In: Klimchouk, A., Palmer, A.N., De Waele, J., Auler, A.S., Audra, P. (Eds.), Hypogene Karst Regions and Caves of the World, Cave and Karst Systems of the World, vol. 2017 Springer International Publishing, Cham, 817-826.

Auler, A.S., Smart, P.L., 2003. The influence of bedrock-derived acidity in the development of surface and underground karst: evidence from the Precambrian carbonates of semi-arid northeastern Brazil. Earth Surf. Proc. Landf. 28, 157–168.

Balsamo, F., Bezerra, F.H.R., Klimchouk, A.B., Cazarin, C.L., Auler, A.S., Nogueira, F.C., Pontes, C., 2020. Influence of fracture stratigraphy on hypogene cave development and fluid flow anisotropy in layered carbonates, NE Brazil. Mar. Pet. Geol. 114, 104207.

Barton, N., Choubey, V., 1977. The shear strength of rock joints in theory and practice. Rock Mech. Rock Engin. 10(1), 1-54.

Bertotti, G., Audra, P., Auler, A., Bezerra, F.H., de Hoop, S., Pontes, C., Prabhakaran, R., Lima, R., 2020. The Morro Vermelho hypogenic karst system (Brazil): Stratigraphy, fractures, and flow in a carbonate strike-slip fault zone with implications for carbonate reservoirs. AAPG Bull. 104, 2029–2050.

Bisdom, K., Bertotti, G., Nick, H.M., 2016. The impact of in-situ stress and outcrop-based fracture geometry on hydraulic aperture and upscaled permeability in fractured reservoirs. Tectonophysics, 690, 63–75.

Brito Neves, B.B., Fuck, R.A., Martins, M., 2014. The Brasiliano collage in South America: a review. Braz. J. Geol. 44, 493–518.

Burley, S. D., Kantorowicz, J. D., 1986. Thin section and SEM textural criteria for the recognition of cement-dissolution porosity in sandstones. Sedimentology 33(4), 587-604.

Cacas, M. C., Ledoux, E., de Marsily, G., Tillie, B., Barbreau, A., Durand, E., Feuga, B., Peaudecerf, P., 1990. Modeling fracture flow with a stochastic discrete fracture network: calibration and validation: 1. The flow model. Water Res. Res. 26(3), 479-489.

Caracciolo, L., Arribas, J., Ingersoll, R.V., Critelli, S., 2014. The diagenetic destruction of porosity in plutoniclastic petrofacies: the Miocene Diligencia and Eocene Maniobra formations, Orocopia Mountains, southern California, USA. In: Scott, R., Morton, A. (Eds.), Provenance Analyses in Hydrocarbon Exploration, Geol. Soc. London Sp. Pub. 386(1), 49-62.

Cazarin, C.L., Bezerra, F.H.R., Borghi, L., Santos, R.V., Favoreto, J., Brod, J.A., Auler, A.S., Srivastava, N.K., 2019. The conduit-seal system of hypogene karst in Neoproterozoic carbonates in northeastern Brazil. Mar. Pet. Geol. 101, 90–107.

Cazarin, C.L., van der Velde, R., Santos, R.V., Reijmer, J.J.G., Bezerra, F.H.R., Bertotti, G., La Bruna, V., Silva, D.C.C., de Castro, D.L., Srivastava, N.K., Barbosa, P.F., 2021. Hydrothermal activity along a strike-slip fault zone and host units in the São Francisco Craton, Brazil – Implications for fluid flow in sedimentary basins. Precambrian Res. 106365.

Choquette, P.W., Pray, L.C., 1970. Geologic nomenclature and classification of porosity in sedimentary carbonates. AAPG Bull. 54, 207–244.

Columbu, A., Audra, P., Gázquez, F., D'Angeli, I.M., Bigot, J.Y., Koltai, G., Chiesa, R., Yu, T.L., Hu, H.M., Shen, C.C., Carbone, C., Heresanu, V., Nobécourt, J.C., De Waele, J., 2021. Hypogenic speleogenesis, late stage epigenic overprinting and condensation-corrosion in a complex cave system in relation to landscape evolution (Toirano, Liguria, Italy). Geomorphology 376, 107561.

Condie, K.C., 2002. The supercontinent cycle: are there two patterns of cyclicity? J. Afr. Earth Sci. 35, 179–183.

Cui, H., Kaufman, A.J., Xiao, S., Zhou, C., Liu, X.M., 2017. Was the Ediacaran Shuram Excursion a globally synchronized early diagenetic event? Insights from methane-derived authigenic carbonates in the uppermost Doushantuo Formation, South China. Chem. Geol. 450, 59–80.

D'Angelo, T., Barbosa, M.S.C., Danderfer Filho, A., 2019. Basement controls on cover deformation in eastern Chapada Diamantina, northern São Francisco Craton, Brazil: Insights from potential field data. Tectonophysics 772, 228231.

De Luca, P.H.V., Matias, H., Carballo, J., Sineva, D., Pimentel, G.A., Tritlla, J., Esteban, M., Loma, R., Alonso, J.L.A., Jiménez, R.P., Pontet, M., Martinez, P.B., Vega, V., 2017. Breaking barriers and paradigms in presalt exploration: The Pão de Açúcar discovery (Offshore Brazil). AAPG Memoir 113, 177–193.

De Waele, J., Plan, L., Audra, P., 2009. Recent developments in surface and subsurface karst geomorphology: an introduction. Geomorphology 106, 1–8.

De Waele, J., Audra, P., Madonia, G., Vattano, M., Plan, L., D'Angeli, I. M., Bigot, J.Y., Nobécourt, J. C., 2016. Sulfuric acid speleogenesis (SAS) close to the water table: examples from southern France, Austria, and Sicily. Geomorphology 253, 452-467.

Del Sole, L., Antonellini, M., Soliva, R., Ballas, G., Balsamo, F., Viola, G., 2020. Structural control on fluid flow and shallow diagenesis: Insights from calcite cementation along deformation bands in porous sandstones. Solid Earth 11, 2169–2195.

Dong, S., You, D., Guo, Z., Guo, C., Chen, D., 2018. Intense silicification of Ordovician carbonates in the Tarim Basin: constraints from fluid inclusion Rb–Sr isotope dating and geochemistry of quartz. Terra Nova 30, 406–413.

Dove, P.M., 1999. The dissolution kinetics of quartz in aqueous mixed cation solutions. Geochim. Cosmochim. Acta 63(22), 3715–3727.

Dove, P.M., Nix, C.J., 1997. The influence of the alkaline earth cations, magnesium, calcium, and barium on the dissolution kinetics of quartz. Geochim. Cosmochim. Acta. 61 (16), 3329–3340.

Dublyansky, Y.V., 1990. Zakonomernosti formirovaniya i modelirovaniye gidrotermokarsta (Particularities of the development and modeling of hydrothermal karst). Nauka. Novosibirsk. 151 pp. (In Russian)

Dunham, R.J., 1962. Classification of carbonate rocks according to depositional texture. In: Ham, W.E. (Ed.), Classification of Carbonates Rocks. AAPG Memoir I, 108–121.

Embry, A.F., Klovan, J.E., 1971. A late Devonian reef tract on northeastern Banks Island, NWT. Bull. Can. Petrol. Geol. 19, 730–781.

Ennes-Silva, R.A., Bezerra, F.H.R., Nogueira, F.C.C., Balsamo, F., Klimchouk, A., Cazarin, C.L., Auler, A.S., 2016. Superposed folding and associated fracturing influence hypogene karst development in Neoproterozoic carbonates, São Francisco Craton, Brazil. Tectonophysics 666, 244–259.

Ford D.C., Williams P.W., 2007. Karst hydrogeology and geomorphology. John Wiley & Sons: 562 pp.

Girard, J.-P., San Miguel, G., 2017. Evidence of high temperature hydrothermal regimes in the pre-salt series, Kwanza Basin, offshore Angola. In: American Association of Petroleum Geologists Annual Convention and Exhibition (Houston, Texas, USA, Abstracts).

Giuffrida, A., La Bruna, V., Castelluccio, P., Panza, E., Rustichelli, A., Tondi, E., Giorgioni, M. Agosta, F. (2019). Fracture simulation parameters of fractured reservoirs: Analogy with outcropping carbonates of the Inner Apulian Platform, southern Italy. J. Struct. Geol. 123, 18-41.

Giuffrida, A., Agosta, F., Rustichelli, A., Panza, E., La Bruna, V., Eriksson, M., Torrieri, S., Giorgioni, M., 2020. Fracture stratigraphy and DFN modelling of tight carbonates, the case study of the Lower Cretaceous carbonates exposed at the Monte Alpi (Basilicata, Italy). Mar. Pet. Geol. 112, 104045.

Goldscheider, N., Mádl-Szőnyi, J., Erőss, A., Schill, E., 2010. Thermal water resources in carbonate rock aquifers. Hydrogeol. J. 18, 1303–1318.

Guha Roy, D, Singh, T.N., 2016. Fluid flow through rough rock fractures: Parametric study. Int. J. Geomech. 16(3), 04015067.

Guimarães, J.T., Misi, A., Pedreira, A.J., Dominguez, J.M.L., 2011. The Bebedouro formation, Una Group, Bahia (Brazil). Geol. Soc. Mem. 36, 503–508.

Gunnarsson, I., Arnórsson, S., 2000. Amorphous silica solubility and the thermodynamic properties of H4SiO4 in the range of 0° to 350°C at P(sat). Geochim. Cosmochim. Acta 64, 2295–2307.

Heeb, B., 2009. An all-in-one electronic cave surveying device. CREG J. 72, 8–10.

Hesse, R., 1989. Silica diagenesis: origin of inorganic and replacement cherts. Earth-Sci. Rev. 26, 253–284.

Higgs, R., 1979. Quartz-grain surface features of Mesozoic-Cenozoic sands from the Labrador and western Greenland continental margins. J. Sed. Res. 49, 599–610.

Holt, R.M., 1990. Permeability reduction induced by a nonhydrostatic stress field. SPE Form. Eval. 5, 444–448.

Itamiya, H., Sugita, R., Sugai, T., 2019. Analysis of the surface microtextures and morphologies of beach quartz grains in Japan and implications for provenance research. Prog. Earth Planet. Sci. 6, 1–14.

Japsen, P., Bonow, J.M., Green, P.F., Cobbold, P.R., Chiossi, D., Lilletveit, R., Magnavita, L.P., Pedreira, A.J., 2012. Episodic burial and exhumation history of NE Brazil after opening of the south Atlantic. GSA Bull. 124, 800–816.

Klimchouk A., 2007. Hypogene speleogenesis: hydrogeological and morphometric perspective. Carlsbad, National Cave and Karst Research Institute: 106 pp.

Klimchouk, A., 2009. Morphogenesis of hypogenic caves. Geomorphology 106, 100–117.

Klimchouk, A., 2019. Speleogenesis, hypogene. In: White, W.B., Culver, D.C., Pipan, T. (Eds.), Encyclopedia of Caves, 3rd edition. Academic Press, New York, 974–988.

Klimchouk, A., Ford, D.C., Palmer, A.N., Dreybrodt, W., 2000. Speleogenesis: Evolution of Karst Aquifers. National Speleological Society, Huntsville, Al.

Klimchouk, A.B., Andreychouk, V.N., Turchinov, I.I., 2009. The structural prerequisites of speleogenesis in gypsum in the Western Ukraine, 2nd edition. University of Silesia - Ukrainian Institute of Speleology and Karstology, Sosnowiec-Simferopol, 96 pp.

Klimchouk, A., Auler, A.S., Bezerra, F.H.R., Cazarin, C.L., Balsamo, F., Dublyansky, Y., 2016. Hypogenic origin, geologic controls, and functional organization of a giant cave system in Precambrian carbonates, Brazil. Geomorphology 253, 385–405.

Klinkenberg, L.J., 1941. The permeability of porous media to liquids and gases. In: Drilling and Production Practice. American Petroleum Institute, 200-213.

Kornilov, V.F., 1978. The temperature regime of formation of the mercury–antimony mineralization (Southern Kirghizia). In: Ermakov, N.P. (Ed.), Thermobarogeochemistry of the Earth's Crust. Nauka, Moscow, pp. 155–161.

Kyle, J.R., Misi, A., 1997. Origin of Zn-Pb-Ag sulfide mineralization within upper proterozoic phosphate-rich carbonate strata, Irêce Basin, Bahia, Brazil. Int. Geol. Rev. 39, 383–399.

La Bruna, V., Bezerra, F.H.R., Souza, V.H.P., Maia, R.P., Auler, A.S., Araújo, R.E.B., Cazarin, C.L., Rodrigues, M.A.F., Vieira, L.C., Sousa, M.O.L., 2021. High-permeability zones in folded and faulted silicified carbonate rocks – Implications for karstified carbonate reservoirs. Mar. Pet. Geol. 128, 105046.

Lavrov, A., 2017. Fracture permeability under normal stress: a fully computational approach. J. Pet. Explor. Prod. Technol. 7, 181–194.

Lei, Q., Latham, J.P., Tsang, C.F., 2017. The use of discrete fracture networks for modelling coupled geomechanical and hydrological behaviour of fractured rocks. Comput. Geotech. 85, 151–176.

Leven, J.A., 1961. Problems of origin of optical-quality fluorite from deposits of the Zeravshan–Gissar Mountains. Trans. Samarkand Univ. 16, 35–51.

Lima, B.E.M., De Ros, L.F., 2019. Deposition, diagenetic and hydrothermal processes in the Aptian Pre-Salt lacustrine carbonate reservoirs of the northern Campos Basin, offshore Brazil. Sediment. Geol. 383, 55–81.

Lima, B.E.M., Tedeschi, L.R., Pestilho, A.L.S., Santos, R.V., Vazquez, J.C., Guzzo, J.V.P., De Ros, L.F., 2020. Deep-burial hydrothermal alteration of the Pre-Salt carbonate reservoirs from northern Campos Basin, offshore Brazil: evidence from petrography, fluid inclusions, Sr, C and O isotopes. Mar. Pet. Geol. 113, 104143.

Lønøy, B., Tveranger, J., Pennos, C., Whitaker, F., Lauritzen, S.E., 2020. Geocellular rendering of cave surveys in paleokarst reservoir models. Mar. Pet. Geol. 122, 104652.

Lyu, X., Zhu, G., Liu, Z., 2020. Well-controlled dynamic hydrocarbon reserves calculation of fracture–cavity karst carbonate reservoirs based on production data analysis. J. Pet. Explor. Prod. Technol. 10, 2401–2410.

Lovering, T.S., Tweto, O., Loweing, T.G., 1978. Ore deposits of the Gilman District, Eagle Country, Colorado. U.S. Geological Survey Professional Paper 1017. 90 pp.

Lowe, D.J., Gunn, J., 1997. Carbonate speleogenesis: an inception horizon hypothesis. Acta Carsologica 26(2), 457-488.

Maliva, R.G., Siever, R., 1989. Nodular Chert Formation in Carbonate Rocks. J. Geol. 97, 421–433.

Marin-Carbonne, J., Robert, F., Chaussidon, M., 2014. The silicon and oxygen isotope compositions of Precambrian cherts: A record of oceanic paleo-temperatures? Precambrian Res. 247, 223–234.

Marrett, R., Ortega, O., Kelsey, C. 1999. Extent of power-law scaling for natural fractures in rock: Geology 27(9), 799–802.

Maximov, S.P., Zolotov, A.N., Lodzhevskaya, M.I., 1984. Tectonic conditions for oil and gas generation and distribution on ancient platforms. J. Pet. Geol. 7(3), 329-340.

Mazzullo, S.J., 2004. Overview of porosity evolution in carbonate reservoirs. Kansas Geol. Soc. Bull. 79 (1, 2), 1-19.

Mazzullo, S.J., Rieke, H.H., Chilingarian, G., 1996. Carbonate Reservoir Characterization: A Geological-engineering Analysis, Part II. Development in Petroleum Science, 44, 994 p. Elsevier.

Mecchia, M., Sauro, F., Piccini, L., Columbu, A., De Waele, J., 2019. A hybrid model to evaluate subsurface chemical weathering and fracture karstification in quartz sandstone. J. Hydrol. 572, 745-760.

Min, K.B., Rutqvist, J., Tsang, C.F., Jing, L., 2004. Stress-dependent permeability of fractured rock masses: A numerical study. Int. J. Rock Mech. Min. Sci. 41, 1191–1210.

Ming, X.R., Liu, L., Yu, M., Bai, H.G., Yu, L., Peng, X.L., Yang, T.H., 2016. Bleached mudstone, iron concretions, and calcite veins: a natural analogue for the effects of reducing CO2-bearing fluids on migration and mineralization of iron, sealing properties, and composition of mudstone cap rocks. Geofluids 16, 1017–1042.

Misi, A., 1993. A Sedimentação Carbonática do Proterozóico Superior no Cráton do São Francisco: Evolução Diagenética e Estratigrafia Isotópica. II Symposium on the São Francisco Craton. Extended abstracts, Salvador, Brazil, pp. 192–193.

Misi, A., Veizer, J., 1998. Neoproterozoic carbonate sequences of the Una Group, Irêce Basin, Brazil: chemostratigraphy, age and correlations. Precambrian Res. 89, 87–100.

Misi, A., Iyer, S.S.S., Coelho, C.E.S., Tassinari, C.C.G., Franca-Rocha, W.J.S., Cunha, I.D.A., Gomes, A.S.R., de Oliveira, T.F., Teixeira, J.B.G., Filho, V.M.C., 2005. Sediment hosted lead–zinc deposits of the Neoproterozoic Bambuí Group and correlative sequences, São Francisco craton, Brazil: a review and a possible metallogenic evolution model. Ore Geol. Rev. 26, 263–304.

Misi, A., Kaufman, A.J., Veizer, J., Powis, K., Azmy, K., Boggiani, P.C., Gaucher, C., Teixeira, J.B.G., Sanches, A.L., Iyer, S.S., 2007. Chemostratigraphic correlation of Neoproterozoic successions in South America. Chem. Geol. 237, 22–45.

Misi, A., Kaufman, A.J., Azmy, K., Dardenne, M.A., 2011. Neoproterozoic successions of the São Francisco craton, Brazil: The Bambuí, Una, Vazante and Vaza Barris/Miaba groups and their glaciogenic deposits. Geol. Rec. Neoproterozoic Glaciat. 36, 509–522.

Misi, A., Batista, J., Teixeira, G., 2012. Mapa Metalogenético Digital do Estado da Bahia e Principais Províncias Minerais. Série Publicações Especiais 11.

Mitsiuk, B.N., 1974. Vzaimodeistvie kremnezema s vodoy v hydrotermalnych usloviach (Interaction between silica and water in hydrothermal conditions). Naukova Dumka. Kiev, 86 pp. (In Russian)

Montanari, D., Minissale, A., Doveri, M., Gola, G., Trumpy, E., Santilano, A., Manzella, A., 2017. Geothermal resources within carbonate reservoirs in western Sicily (Italy): A review. Earth-Science Rev. 169, 180–201.

Morad, S., Ketzer, J.M., Ros, L.F. De, 2000. Spatial and temporal distribution of diagenetic alterations in siliciclastic rocks: implications for mass transfer in sedimentary basins. Sedimentology 47, 95–120.

Myers, R., Aydin, A., 2004. The evolution of faults formed by shearing across joint zones in sandstone, J. Struct. Geol. 26(5), 947-966.

Myrow, P.M., Southard, J.B., 1996. Tempestite deposition. J. Sediment. Res., 66, 875 –887.

Odling, N.E., Gillespie, P., Bourgine, B., Castaing, C., Chilés, J.P., Christensen, N.P., Fillion, E., Genter, A., Olsen, C., Thrane, L., Trice, R., Aarseth, E., Walsh, J.J., Watterson, J., 1999. Variations in fracture system geometry and their implications for fluid flow in fractured hydrocarbon reservoirs. Pet. Geosci. 5, 373–384.

Olsson, R., Barton, N., 2001. An improved model for hydromechanical coupling during shearing of rock joints. Int. J. Rock Mech. Min. Sci. 38, 317-329.

Ortega, O.J., Marrett, R.A., Laubach, S.E., 2006. A scale-independent approach to fracture intensity and average spacing measurement. AAPG Bull. 90, 193–208.

Packard, J.J., Al-Aasm, I., Samson, I., 2001. A Devonian hydrothermal chert reservoir: The 225 bcf Parkland field, British Columbia, Canada. AAPG Bulletin 85(1), 51–84.

Palmer, A.N., 2000. Hydrogeologic control of cave patterns. 2000 In: In: Klimchouk, A., Ford, D.C., Palmer, A.N., Dreybrodt, W. (Eds.), Speleogenesis: Evolution of Karst Aquifers, vol. 240. pp. 145–146.

Peucat, J.J., Figueiredo Barbosa, J.S., Conceição de Araújo Pinho, I., Paquette, J.L., Martin, H., Fanning, C.M., Beatriz de Menezes Leal, A., Cruz, S., 2011. Geochronology of granulites from the south Itabuna-Salvador-Curaçá Block, São Francisco Craton (Brazil): Nd isotopes and U-Pb zircon ages. J. South Am. Earth Sci. 31, 397–413.

Philipp, S.L., Afşar, F., Gudmundsson, A., 2013. Effects of mechanical layering on hydrofracture emplacement and fluid transport in reservoirs. Front. Earth Sci. 1, 4.

Pisani, L., Antonellini, M., De Waele, J., 2019. Structural control on epigenic gypsum caves: evidences from Messinian evaporites (Northern Apennines, Italy). Geomorphology 332, 170–186.

Pisani, L., Antonellini, M., D'Angeli, I.M., De Waele, J., 2021. Structurally controlled development of a sulfuric hypogene karst system in a fold-and-thrust belt (Majella Massif, Italy). J. Struct. Geol. 145, 104305.

Pontes, C.C.C., Bezerra, F.H.R., Bertotti, G., La Bruna, V., Audra, P., De Waele, J., Auler, A.S., Balsamo, F., De Hoop, S., Pisani, L., 2021. Flow pathways in multiple-direction fold hinges: implications for fractured and karstified carbonate reservoirs. J. Struct. Geol. 146, 104324.

Poros, Z., Jagniecki, E., Luczaj, J., Kenter, J., Gal, B., Correa, T.S., Ferreira, E., McFadden, K.A., Elifritz, A., Heumann, M., Johnston, M., Matt, V., 2017. Origin of silica in pre-salt carbonates, Kwanza Basin, Angola. In: American Association of Petroleum Geologists Annual Convention and Exhibition (Houston, Texas, USA).

Rimstidt, J.D., 1997. Quartz solubility at low temperatures. Geochim. Cosmochim. Acta. 61, 2553–2558.

Reineck, H., Wunderlich, F., 1968. Classification and Origin of Flaser and Lenticular Bedding, Sedimentology 11, 99-104.

Rolland, A., Toussaint, R., Baud, P., Conil, N., Landrein, P., 2014. Morphological analysis of stylolites for paleostress estimation in limestones. Int. J. Rock Mech. Min. Sci. 67, 212–225.

Salvini, F., 2004. Daisy 3: The Structural Data Integrated System Analyzer Software, University of Roma Tre, Rome, available at: http: //host.uniroma3.it/progetti/fralab/Downloads/Programs/.

Santana, A., Chemale, F., Scherer, C., Guadagnin, F., Pereira, C., Santos, J.O.S., 2021. Paleogeographic constraints on source area and depositional systems in the Neoproterozoic Irecê Basin, São Francisco Craton. J. South Am. Earth Sci. 109, 103330.

Sauro, F., De Waele, J., Onac, B.P., Galli, E., Dublyansky, Y., Baldoni, E., Sanna, L., 2014. Hypogenic speleogenesis in quartzite: The case of Corona ’e Sa Craba Cave (SW Sardinia, Italy). Geomorphology 211, 77–88.

Shanmugan, G., Higgins, J.B., 1988. Porosity enhancement from chert dissolution beneath Neocomian unconformity: Ivishak Formation, North Slope, Alaska. AAPG Bull. 72(5), 523–535.

Siever, R., 1962. Silica solubility, 0°C - 200°C, and the diagenesis of siliceous sediments. J. Geol. 70, 127-150.

Smeraglia, L., Giuffrida, A., Grimaldi, S., Pullen, A., La Bruna, V., Billi, A., Agosta, F., 2021. Fault-controlled upwelling of low-T hydrothermal fluids tracked by travertines in a fold-and-thrust belt, Monte Alpi, southern Apennines, Italy. J. Struct. Geol. 144, 104276.

Souza, V.H.P., Bezerra, F.H.R., Vieira, L.C., Cazarin, C.L., Brod, J.A., 2021. Hydrothermal silicification confined to stratigraphic layers: Implications for carbonate reservoirs. Mar. Pet. Geol. 124, 104818.

Spötl, C., Dublyansky, Y., Koltai, G., Cheng, H., 2021. Hypogene speleogenesis and paragenesis in the Dolomites. Geomorphology 382, 107667.

Teixeira, J.B.G., Misi, A., Silva, M.G., 2007. Supercontinent evolution and the Proterozoic metallogeny of South America. Gondw. Res. 11, 346–361.

Terzaghi, R.D., 1965. Source of error in joint surveys. Geotechnique 15(3), 287–304.

Tsykin, R.A., 1989. Paleokarst of the Union of Soviet Socialistic Republics. In: Bosák, P., Ford, D.C., Głazek, J., Horáček, I. (Eds.), Paleokarst: A Systematic and Regional Review. Vidala Academia, Praha, 253–295.

Van Golf-Racht, T., 1982. Fundamentals of Fractured Reservoir Engineering. Elsevier, Amsterdam, pp. 732.

Wray, R. A., Sauro, F., 2017. An updated global review of solutional weathering processes and forms in quartz sandstones and quartzites. Earth-Sci. Rev. 171, 520-557.

Wu, M.B., Wang, Y., Zheng, M.L., Zhang, W.B., Liu, C.Y., 2007. The hydrothermal karstification and its effect on Ordovician carbonate reservoir in Tazhong uplift of Tarim Basin, Northwest China. Science in China Series D: Earth Science, 50(2), 103-113.

Xu, X., Chen, Q., Chu, C., Li, G., Liu, C., Shi, Z., 2017. Tectonic evolution and paleo- karstification of carbonate rocks in the Paleozoic Tarim Basin. Carb. & Evap. 32, 487–496.

You, D., Han, J., Hu, W., Qian, Y., Chen, Q., Xi, B., Ma, H., 2018. Characteristics and formation mechanisms of silicified carbonate reservoirs in well SN4 of the Tarim Basin. Energy Explor. Exploit. 36, 820–849.

Zambrano, M., Tondi, E., Korneva, I., Panza, E., Agosta, F., Janiseck, J.M., Giorgioni, M., 2016. Fracture properties analysis and discrete fracture network modelling of faulted tight limestones, Murge Plateau. Italy. Ital. J. Geosci. 135, 55–67.

Zhao, X., Jin, F., Zhou, L., Wang, Q., Pu, X., 2018. Re-exploration Programs for Petroleum-Rich Sags in Rift Basins. Gulf Professional Publishing, 642 pp.

Zhang, J.J., 2019. Rock physical and mechanical properties, in: Applied Petroleum Geomechanics. Elsevier, pp. 29–83.

Zheng, J., Wang, X., Lü, Q., Sun, H., Guo, J., 2020. A new determination method for the permeability tensor of fractured rock masses. J. Hydrol. 585, 124811.

Zhou, X., Chen, D., Qing, H., Qian, Y., Wang, D., 2014. Submarine silica-rich hydrothermal activity during the earliest Cambrian in the Tarim basin, northwest China. Int. Geol. Rev. 56, 1906–1918.

3.2

Published in Basin Research (2023)

https://doi.org/10.1111/bre.12748

Hydrothermal silicification and hypogene dissolution of an exhumed Neoproterozoic carbonate sequence in Brazil: Insights from fluid inclusion microthermometry and silicon-oxygen isotopes

Luca PISANI[1*], Gabriella KOLTAI[2], Yuri DUBLYANSKY[2], Barbara I. KLEINE[3,4], Martin J. WHITEHOUSE[5], Etienne SKRZYPEK[6], Cristina CARBONE[7], Christoph SPÖTL[2], Marco ANTONELLINI[1], Francisco H. BEZERRA[8], Jo DE WAELE[1]

1 Bologna University, Department of Biological, Geological and Environmental Sciences, Italy. lucapiso94@gmail.com; m.antonellini@unibo.it; jo.dewaele@unibo.it

2 Institute of Geology, University of Innsbruck, Austria. Gabriella.Koltai@uibk.ac.at; Yuri.Dublyansky@uibk.ac.at; Christoph.Spoetl@uibk.ac.at

3 Nordic Volcanological Center, Institute of Earth Sciences, University of Iceland. barbarak@hi.is

4 GeoZentrum Nordbayern, Friedrich-Alexander Universität Erlangen-Nürnberg, Erlangen, Germany

5 Swedish Museum of Natural History, Stockholm, Sweden, martin.whitehouse@nrm.se

6 Institute of Earth Sciences, NAWI Graz Geozentrum, Petrology and Geochemistry, University of Graz, Austria. etienne.skrzypek@uni-graz.at

7 DISTAV, Dipartimento di Scienze della Terra, dell'Ambiente e della Vita, Università di Genova, Italy. cristina.carbone@unige.it

8 Programa de Pós-Graduação em Geodinâmica e Geofísica, Federal University of Rio Grande Do Norte, Natal, Brazil. hilario.bezerra@ufrn.br

* Corresponding author

Abstract

Hypogene dissolution-precipitation processes strongly affect the petrophysical properties of carbonate rocks and fluid migration pathways in sedimentary basins. In many deep carbonate reservoirs, hypogene cavernous voids are often associated with silicified horizons. The diagenesis of silica in carbonate sequences is still a poorly-investigated research topic. Studies exploring the complexity of silica dissolution-precipitation patterns in hypogene cave analogues are therefore fundamental to unravel the diagenetic and speleogenetic processes that may affect this kind of reservoir. In this work, we investigated an exhumed and silicified Neoproterozoic carbonate sequence in Brazil hosting a 1.4 km-long cave. Quartz mineralization and silicified textures were analyzed with a multidisciplinary approach combining petrography, fluid inclusion microthermometry, silicon-oxygen stable isotope analyses and U-Th-Pb dating of monazite crystals. We found that an early silicification event caused the replacement of the dolostone layers with micro-crystalline quartz forming chert nodules. This event was likely associated with mixing fluids (ancient Neoproterozoic seawater and hydrothermal solutions sourced from the underlying Mesoproterozoic basement) at relatively low temperatures (ca. 50–100°C) and shallow depth. After the tectonic deformation produced by the Brasiliano orogeny, silica dissolution was promoted by high temperature and alkaline hydrothermal solutions rising from the quartzite basement along deep-rooted structures. Hypogene hydrothermal alteration promoted the dissolution of the cherty layers and the precipitation of chalcedony and megaquartz. Homogenization temperatures from primary fluid inclusions in megaquartz cement indicate minimum formation temperatures of 165–210°C. Similar temperature estimates (110–200°C) were obtained from the $\delta^{30}Si$ and $\delta^{18}O$ isotope systematics of quartz precipitated from hydrothermal solutions. The dissolved salts in the fluid inclusions were evaluated as $NaCl + CaCl_2$ from microthermometric data combined with cryogenic Raman spectroscopy, corresponding to salinity ranging between 17 and 25 wt.%. No reliable age constraints for hydrothermal silica dissolution-precipitation phases were obtained from monazite U-Th-Pb dating. However, our results, interpreted in the regional context of the São Francisco Craton, suggest that the Cambrian tectono-thermal events could have been amongst the possible drivers for this hypogene process in the basin.

Key words

Silicified reservoirs; fluid flow; hydrothermal karst; silica dissolution

3.2.1. Introduction

Although the solubility of silica under most surface or shallow crustal conditions is low (Rimstidt, 1997), dissolution (karstic) features including caves and cave systems are known in quartz-dominated rocks (Sauro et al., 2014; Wray & Sauro, 2017). Solutional voids and karstic vugs are commonly found in quartzites and silicified (cherty) carbonates in many hydrocarbon reservoirs in sedimentary basins, such as North Slope in Alaska (e.g. Shanmugan & Higgins, 1988), offshore

Brazil (De Luca et al., 2017; Fernández-Ibáñez, Jones, et al., 2022; Lima et al., 2020) and Tarim Basin in China (Dong et al., 2018; Wei et al., 2021; You et al., 2018).

Karst features in deep reservoirs are commonly attributed to hypogene dissolution (hypogene speleogenesis) resulting from upwelling and migration of thermal groundwaters (Andreychouk et al., 2009; Dublyansky, 1990; Klimchouk, 2007, 2019). Hydrothermal alteration in carbonate reservoirs resulting in cavernous vugs and non-matrix permeability is a common phenomenon, especially along fault and fracture zones (Álvaro, 2013; Fernández-Ibáñez, Jones, et al., 2022; Strugale & Cartwright, 2022; Zhou et al., 2014). These hypogene karst processes generate non-fabric-selective interconnected pore systems, resulting in heterogeneous porosity and highly anisotropic rock permeability (Fernández-Ibáñez, Jones, et al., 2022; Trice, 2005), which has implications not only for hydrocarbon exploration but also for the characterization of geothermal resources and groundwater reserves (Audra et al., 2022; Goldscheider et al., 2010; Montanari et al., 2017).

Exhumed hypogene caves accessible from the surface represent analogues of deep-seated conduit systems, where parameters of cave-forming environments can be reconstructed by studying mineralogical and geochemical footprints (Klimchouk, 2019). Studies of such features-analogues of deep-seated conduits are indispensable for interpreting data from drilling and geophysical surveys and building accurate conceptual models.

An increasing number of publications have documented the development of hypogene caves and karst features in silicified carbonate rocks (Bertotti et al., 2020; La Bruna et al., 2021; Pisani et al., 2022; Sauro et al., 2014; Souza et al., 2021). Cavernous, sometimes mineralized solutional voids attributed to hydrothermal speleogenesis have been described in quartzites and skarns in Kyrgyzstan (Kornilov, 1978; Leven, 1961), USA (Colorado; Lovering et al., 1978) and Ukraine (Tsykin, 1989). Silicified reservoirs are typical of the lower Cretaceous pre-salt sequences of the Campos and Santos basins in Brazil (Lima et al., 2020; Lima & De Ros, 2019), the Kwanza-Congo Basins of Africa (Poros et al., 2017; Teboul et al., 2019) and the Parkland gas field in Canada (Packard et al., 2001). On the basis of petrographic, isotopic and fluid inclusion studies, pervasive silicification and porosity enhancement processes in these basins were ascribed to the circulation of high-temperature fluids (De Luca et al., 2017; Girard & San Miguel, 2017; Lima et al., 2020; Poros et al., 2017; Teboul et al., 2019). However, the link between silicification and hypogene karst dissolution, and their evolution in space and time, are still poorly understood.

The study of secondary minerals lining or filling solutional (karstic) cavities is a powerful tool that can be combined with geomorphological observations to build accurate speleogenetic and minerogenetic models (Onac & Forti, 2011). Understanding the properties and origin of hydrothermal mineralizations (e.g. by studying fluid inclusions, stable isotopes and trace elements) may provide new insights into the characterization of hypogene conduit networks associated with ore deposit emplacement, hydrocarbon reservoirs and geothermal resources.

In this paper, we present the results of the study of an inactive hypogene cave system (Calixto Cave) developed in the Neoproterozoic rocks of the Una-Utinga Basin in northeastern Brazil. Using a multidisciplinary approach comprising petrographic, stratigraphic, structural and geomorphological observations, Pisani et al. (2022) documented quartz-rich mineral deposits partially filling solutional pores and fractures in the silicified rocks that host the main corroded high-permeability zones of the sedimentary sequence.

Since various processes may be involved in the formation of quartz-rich mineralization and silicified layers in marine carbonate units, a detailed characterization of quartz textures and mineral-forming fluid properties is needed to understand the character and evolution of fluid circulation, fluid–rock interaction and silica dissolution-precipitation.

To unravel the origin of silica dissolution-precipitation processes, we combined petrographic observations with fluid-inclusion studies and silicon ($\delta^{30}Si$) and oxygen ($\delta^{18}O$) isotope analyses of quartz, chalcedony and highly silicified chert samples from Calixto Cave, and quartzite samples from the underlying Mesoproterozoic basement (Chapada Diamantina Group). These analyses were integrated with the U-Th-Pb dating of monazite grains found in association with quartz-rich mineralization, attempting to constrain the age for fluid circulation, speleogenesis and mineral deposition. Lastly, the Si and O isotope composition of studied materials was compared with different genetic mechanisms using an isotope modelling approach (Kleine et al., 2018; Stefánsson et al., 2017).

3.2.2. Geological setting

The Calixto Cave is located in the São Francisco Craton (northeastern Brazil, Figure 1a). This hypogene karst system comprises 1.4 km of passages located between 420 and 475 m a.s.l. and is developed in the Neoproterozoic carbonates of the Salitre Formation (Fm), Una-Utinga Basin.

The São Francisco Craton is the western portion of a large crustal block segmented during the breakup of Pangea (Almeida et al., 2000; Misi et al., 2011). The Neoproterozoic rocks of the Una

Group (Misi et al., 2007, 2011) overlay the Archean-Paleoproterozoic basement, comprised of metamorphic and igneous rocks and the mainly siliciclastic Mesoproterozoic sequences of the Chapada Diamantina Group, rich in quartzites and ortho-quartzites (Magalhães et al., 2016) (Figure 1b). The Una-Utinga and the Irecê basins resulted from the rifting of the Rodinia supercontinent between ca. 900 to 600 Ma (Misi et al., 2007, 2011; Misi & Veizer, 1998). This extensional stage was responsible for the sedimentation of glaciogenic and marine carbonate mega-sequences of the Una Group.

Sedimentation in these basins was partially coeval with the geodynamic and tectonic events of the Brasiliano orogeny, which occurred in this area from ca. 740 to 540 Ma with a peak at 600 Ma (Bento dos Santos et al., 2015; Brito Neves et al., 2014; Santana et al., 2021; Sial et al., 2016). A first rifting event and a subsequent collisional stage determined the present structural configuration of the basins, with thrust faults, strike-slip (or oblique-slip) faults and folded belts (Brito Neves et al., 2014; D'Angelo et al., 2019). The late orogenic stages (540–510 Ma) involved magmatism, hydrothermal activity and large-scale fluid migration along faults and shear zones (Almeida et al., 2000; Guimarães et al., 2011; Trindade et al., 2004).

The lower units of the Salitre Fm are interpreted as the product of the accumulation of sediments in an intra-cratonic basin during rifting of the passive northern margin of the craton (Misi et al., 2007; Misi & Veizer, 1998; Santana et al., 2021). The upper part of the Salitre Fm is considered by some authors as a foreland basin filled with mega-sequences deposited during the Brasiliano orogeny ca. 600 Ma ago (Misi et al., 2007, 2011; Santana et al., 2021). The maximum depositional age determined from detrital zircons in the basal portion of the Salitre Fm is 669 ± 14 Ma (Santana et al., 2021; Sial et al., 2016).

The Salitre Fm hosts hundreds of karst systems, some of which are amongst the longest-known in South America (Auler, 2017). Most of these caves have a hypogene origin and were interpreted as the result of hydrothermal alteration by rising acidic solutions migrating through the fractured basement (Balsamo et al., 2020; Klimchouk et al., 2016; Pontes et al., 2021).

Some caves in the São Francisco Craton are also associated with silicification (Bertotti et al., 2020; La Bruna et al., 2021; Souza et al., 2021) or contain hydrothermal minerals, e.g. quartz and chalcedony filling veins and vugs (Cazarin et al., 2019). Furthermore, in several sites of the Una-Utinga and Irecê basins, hydrothermal mineral assemblages of quartz, sphalerite, barite and galena form Mississippi Valley Type (MVT) ore bodies (Caird et al., 2017; Cazarin et al., 2021; Kyle & Misi, 1997; Misi et al., 2012).

Amongst these caves, Calixto Cave represents a close analogue for karstified and silicified hydrocarbon reservoirs. The middle portion of the cave (middle storey; Figure 2) is a sub-horizontal and stratigraphically confined network of conduits mostly developed within silicified dolostone layers with a SiO_2 content up to 80–85 wt.% (unit B1, Figure 2b; Pisani et al., 2022). These silica-rich layers have a high permeability due to a combination of high fracture density and early-stage hypogene processes involving silica dissolution and precipitation (Pisani et al., 2022).

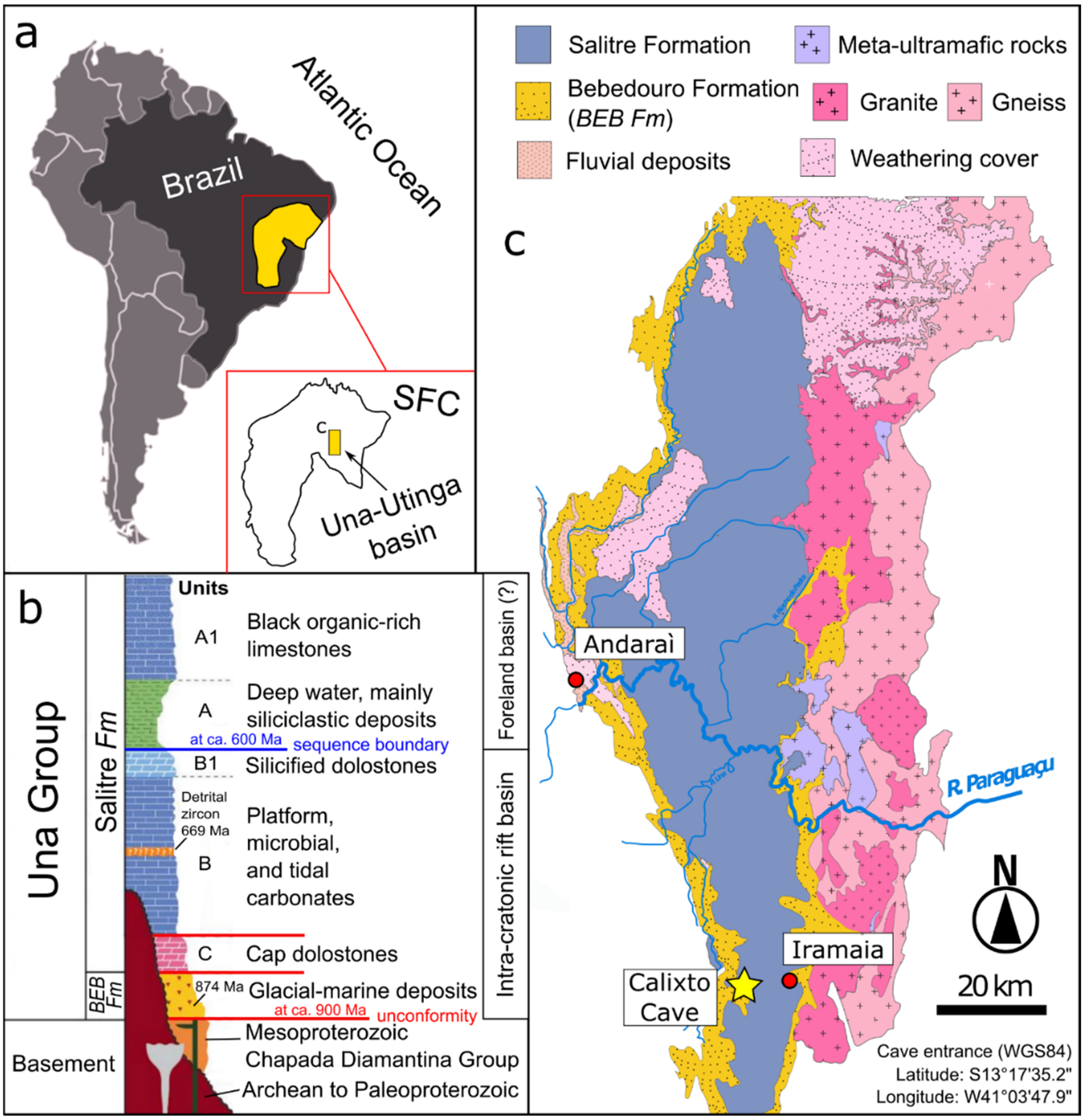

Figure 1. Geological setting: a) Location of the Una-Utinga basin in the São Francisco Craton (SFC) in northeastern Brazil; b) Conceptual stratigraphic column (not to scale) of the Una Group and the underlying basement rocks (modified from Misi et al., 2007 and Santana et al., 2021); c) Geological map of the Una-Utinga basin (Brazil), with the location of the Calixto Cave (modified from Pisani et al., 2022).

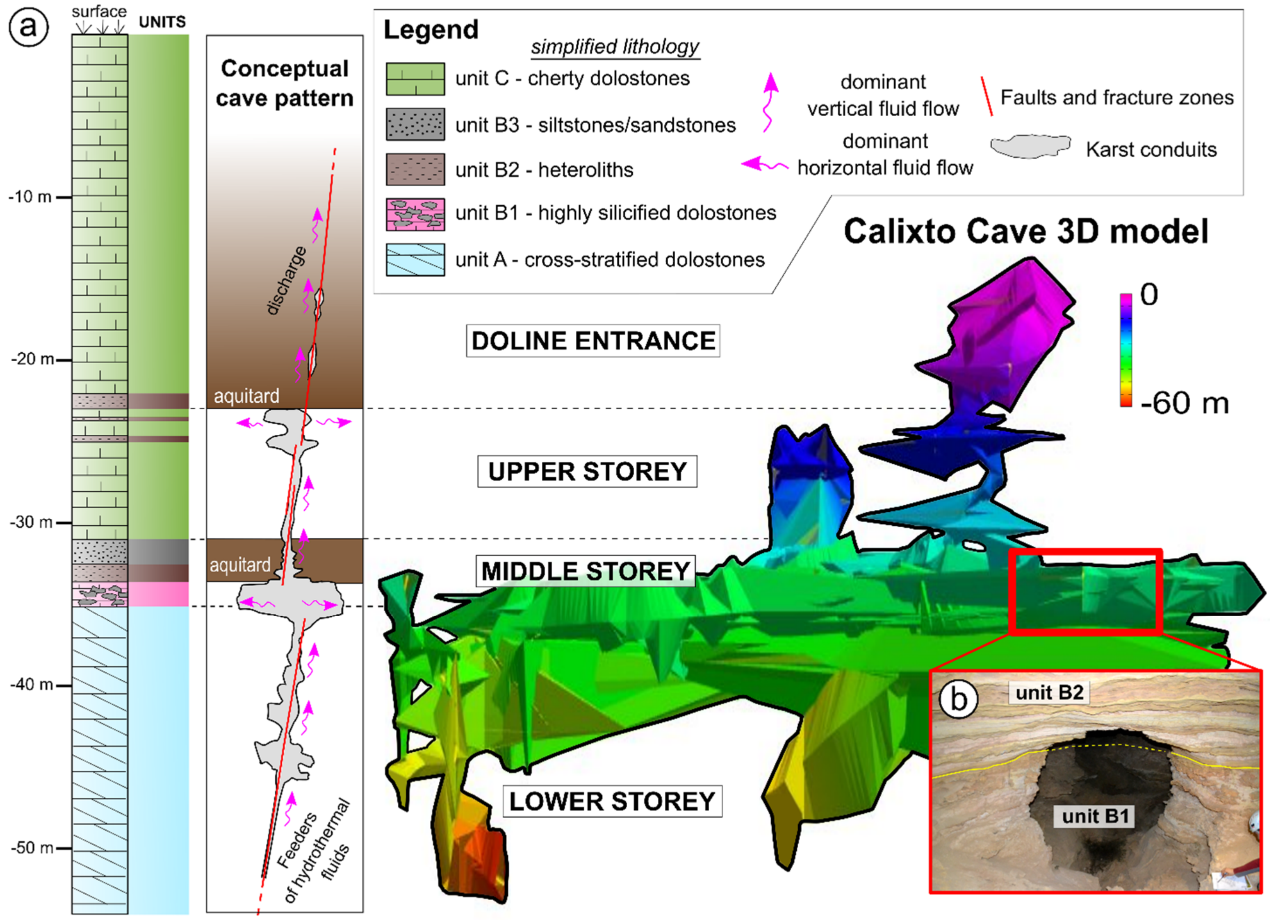

Figure 2. a) Lithostratigraphic log and schematic conceptual model of Calixto Cave conduit network. A 3D model of the cave is also shown (modified after Pisani et al., 2022). b) example of a master conduit in the middle storey, mostly localized in the sedimentary unit B1 (highly silicified dolostones).

3.2.3. Material and methods

To assess the origin of silica dissolution-precipitation processes in the Calixto Cave, we studied samples consisting of megaquartz (euhedral quartz crystals larger than 100 µm, generally up to 1–2 mm; Marin-Carbonne et al., 2014; Teboul et al., 2019), chalcedony and chert (lithotype composed of microcrystalline quartz). Quartzite samples from the Chapada Diamantina Group (Figure 1b) were analyzed for comparison.

3.2.3.1. Quartz and fluid inclusion petrography

Thirty-one thin sections were prepared and examined using a petrographic microscope to identify their main textural and petrographic characteristics. Five ca. 100 µm-thick doubly polished sections were prepared and examined for the presence of fluid-inclusion assemblages (FIAs) using a petrographic microscope. FIAs are defined as petrographically discriminated, cogenetic groups of fluid inclusions (Goldstein, 2003; Goldstein & Reynolds, 1994), which record the physical and chemical conditions of the fluid system at the time of trapping, assuming inclusions did not re-equilibrate (Bodnar, 2003). Roedder's criteria for FIAs classification according to the timing of entrapment were used (Goldstein & Reynolds, 1994; Roedder, 1984). FIAs were classed as primary (P), secondary (S), pseudosecondary (PS), or undetermined (U; no clear relationships with crystal growth could be established).

First-order features supporting the primary origin of FIAs are their occurrence in tridimensional clusters or their association with crystal growth zones. Different modes of occurrence of primary inclusions have been observed: FIAs associated with well-defined crystal growth zones (P1), isolated 3D clusters of inclusions of well-developed negative-crystal shapes (P2), or isolated 3D clusters of inclusions of elongated or irregular shapes (P3).

After identifying the main petrographic and textural characteristics of fluid inclusions, seven small fragments of the thick sections (up to 5 mm in diameter) were prepared for microthermometric measurements.

3.2.3.2. Fluid inclusion microthermometry

Microthermometric characteristics of fluid inclusions were determined using a Linkam THMS600 heating-freezing stage mounted on an Olympus BX41 microscope, using a 40× objective and a condenser lens at the University of Innsbruck. The stage was calibrated using H_2O-CO_2 synthetic fluid inclusions. The accuracy of the calibration is ±0.1°C.

Homogenization temperatures (T_h) were determined on the FIAs by heating the samples at room temperature using the cycling technique described by Goldstein and Reynolds (1994). Freezing experiments were performed after measuring T_h. Inclusions were cooled to −180°C and then slowly heated to detect the potential formation of solid phases (e.g. clathrates, salt hydrates, ice). Volume fractions of individual fluid inclusions (ratios of the vapour to liquid phases, V:L) were estimated visually at room temperature.

3.2.3.3. Fluid inclusion Raman spectrometry

The composition of representative individual inclusions was determined using Raman spectroscopy at room temperature and at cryogenic temperatures (Bakker, 2004; Bodnar, 2003; Goldstein & Reynolds, 1994; Samson & Walker, 2000; see Appendix C for further details). Raman analyses were performed at the University of Innsbruck with a Horiba Jobin-Yvon Labram-HR800 spectrometer, equipped with a 532.18 nm laser and a Linkam THMS600 heating/freezing stage. Two to three accumulations were used during spectral acquisitions. Raman spectra were processed with LabSpec software (ver. 6.6.2.7). Calibration was performed using a standard Si-wafer with known reference Si-Si vibration at 520.7 cm^{-1}.

3.2.3.4. $\delta^{18}O$ and $\delta^{30}Si$ analyses

Oxygen ($\delta^{18}O$) and silicon ($\delta^{30}Si$) isotope values were analyzed using an in-situ secondary ion mass spectrometry (SIMS) technique (Abraham et al., 2011; Kleine et al., 2018) at the NordSIMS laboratory of the Swedish Museum of Natural History. Two individual grains for each silica sample (0.2 to 1 mm in size) were embedded in epoxy along with the quartz standard UNIL-Q1 (Seitz et al., 2017). The sample mounts were polished to 1 µm and gold coated.

Each grain was chemically characterized using a scanning electron microscope (SEM) Tescan Vega 3 LMU equipped with an energy dispersive spectroscopy (EDS) Apollo-X SDD detector at 20 kV accelerating voltage, 1.2 nA beam current and 5–10 µm beam diameter, at the Earth Sciences Department of the University of Genova. EDS spectra and back-scattered electron (BSE) images (see Supplemental Materials online) were acquired to identify the most suitable locations (e.g. almost pure SiO_2 phase) for in-situ isotope analyses. One to two analyses for each SiO_2 grain were performed for silicon and oxygen isotopes.

The isotope values are reported relative to V-SMOW and NBS28 using the standard delta notation. Errors associated with the stable isotopes data range between ±0.13‰ and ±0.20‰ for $\delta^{30}Si$ and from ±0.19‰ to ±0.38‰ for $\delta^{18}O$.

Geochemical modelling of $\delta^{30}Si$ and $\delta^{18}O$ isotope systematics was carried out assuming an open system-type Rayleigh model for the simulation of quartz precipitation as a result of cooling/boiling hydrothermal fluids, burial diagenesis at different temperatures and fluid mixing. Rayleigh distillation curves were calculated following the procedure of Kleine et al. (2018). Further details on the adopted calculations and reference equations are reported in the Appendix C.

3.2.3.5. U-Th-Pb dating

Quantitative analyses of selected monazite grains were performed at the University of Graz using a JEOL JXA-8530F Plus electron microprobe equipped with five wavelength-dispersive spectrometers (radius of the Rowland circle = 140 mm). Operating conditions were 15 kV accelerating voltage, 150 nA beam current and 1 µm beam diameter. The X-ray lines, counting times, calibration materials and interference corrections are listed in the Supplementary Materials online (Table S1), together with the data for monazite reference materials measured to assess the accuracy of Th-U-total Pb dates. Matrix correction follows the method of Bence and Albee (1968) with α-factors after Kato (2005). The full data on monazite analyses are presented in the Supplementary Materials online (Table S2).

3.2.4. Results

3.2.4.1. Petrographic observations

Silica deposits studied in thin and thick sections were classified based on their petrographic and textural characteristics in five facies, defined as micro-crystalline quartz (qtz-mc), chalcedony and “jigsaw” mosaic quartz (qtz-C), early-stage megaquartz (qtz-I), late-stage megaquartz (qtz-II) and quartz-rich hydraulic breccias (qtz-br).

Qtz-mc replaces the precursor dolomite forming silicified zones, where the main sub-horizontal conduits of the cave are concentrated (Figure 2; middle storey; Pisani et al., 2022). Qtz-mc is organized in nodules and bands (namely chert) sometimes hosting patches of residual dolomite (Figure 3). The latter shows a grain size of 5–40 µm, with predominantly sub-euhedral crystal structures. Enlarged fractures, solutional vugs and cavernous voids up to several millimetres in size (classified as mesopores in the range of 4–32 mm, based on the definition by Choquette & Pray, 1970) are common in these silicified rocks observed at the thin-section scale. Occasionally, larger irregular mega-pores are observed at the hand sample scale, reaching up to 4–5 cm in their larger axes. Examples of representative vugs, cavernous voids and corrosion features in the cherts are shown in the Appendix C.

Small crystals (<10–20 µm) of Fe- and Fe-Ti oxides (less commonly, pyrite) are associated with qtz-mc. Fe hydroxides occur primarily as overgrowths of Fe oxides and sulfides or pseudomorphs after them.

Qtz-C consists of chalcedony (Figure 3b) or ‘jigsaw’ mosaic quartz (Moncada et al., 2012) filling micro-veins and solutional vugs in the chert nodules and at the transition zone with megaquartz crystals (Figure 3c,d). Sometimes, qtz-C is found in the core of the larger quartz crystals (Figure 4c). The transition between qtz-C and qtz-I is usually gradual and diffuse (Figure 5). Chalcedony fibres are typically aligned in a parallel or spherulitic fashion and have a ‘feathery’ appearance.

Qtz-I consists of megaquartz crystals with cloudy cores and colloform-plumose textures (Moncada et al., 2012; Sander & Black, 1988; Saunders, 1994; Figures 4a,b and 5a,b). Such textures commonly occur in the inner zones of qtz-I crystals (Figure 5b).

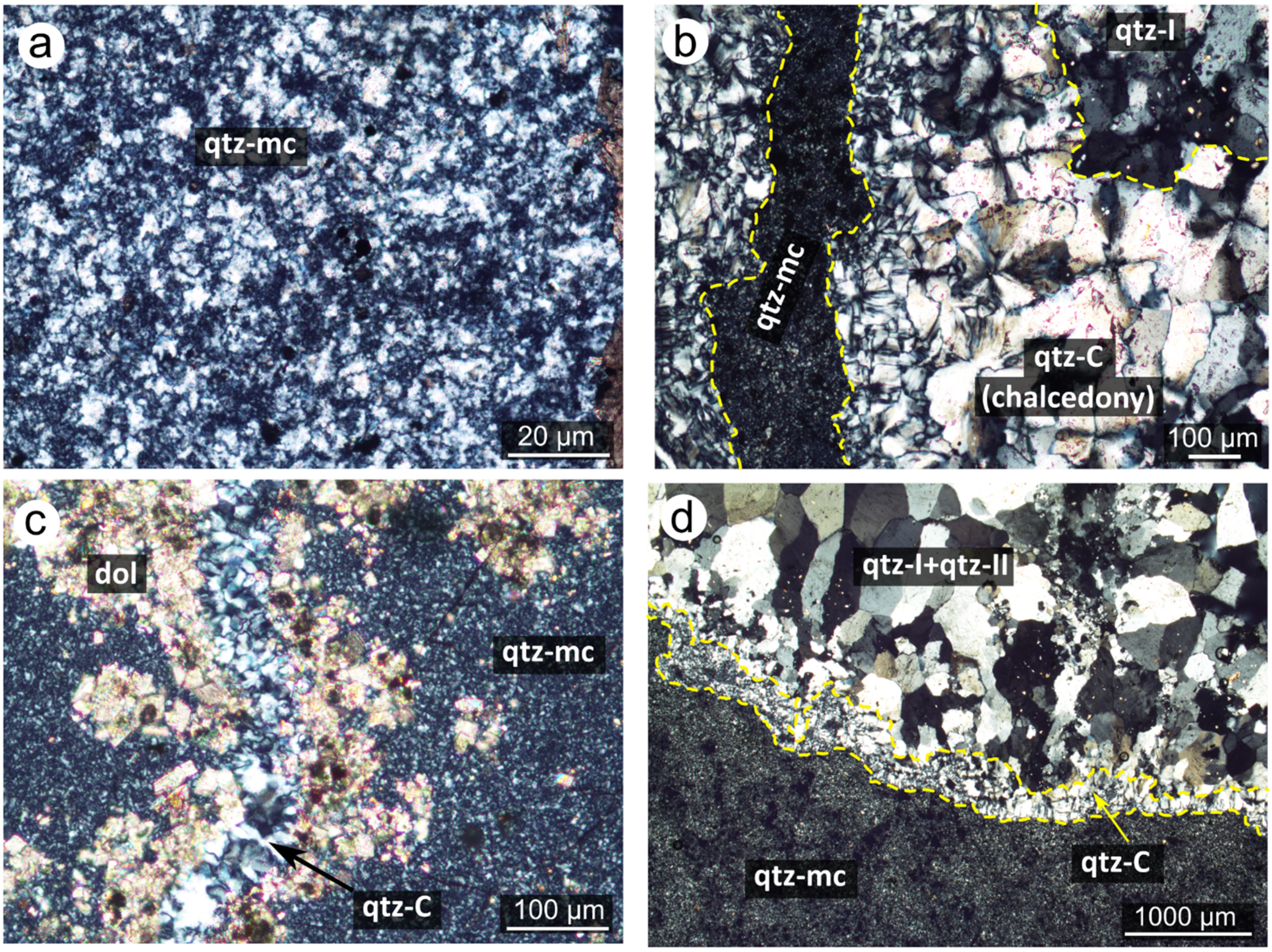

Figure 3. a) Microcrystalline quartz (qtz-mc) replacing the original dolomite and forming chert nodules. b) Qtz-mc, chalcedony (qtz-C), and early stage megaquartz (qtz-I) in the upper right corner. c) Residual dolomite (dol), qtz-mc and jigsaw quartz (qtz-C). d) Transition between qtz-mc and a solutional macro-pore in it, lined with qtz-C, qtz-I and qtz-II. Photographs at cross-polarized light. The yellow dashed lines mark the transition between silica facies.

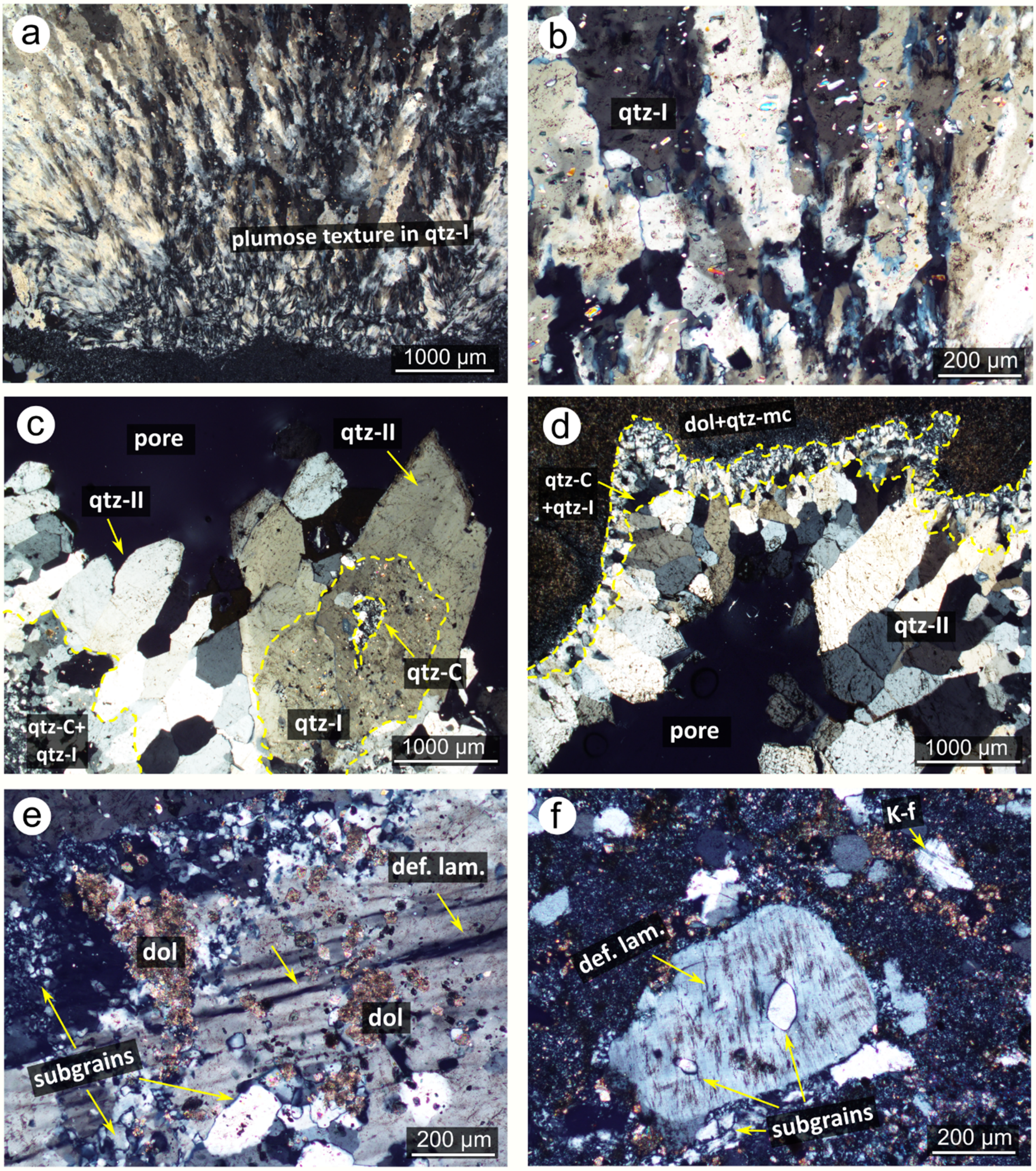

Figure 4. a) Megaquartz with plumose texture (qtz-I). b) Mineral inclusions with high interference colours (mostly anhydrite, barite and muscovite) in early-stage megaquartz (qtz-I). c) Late-stage megaquartz crystals (qtz-II) partially filling a solutional macro-pore. Note cores composed of qtz-C and qtz-I in a large qtz-II crystal. d) Residual dolomite partially replaced by silica (dol+qtz-mc), and the paragenetic sequence comprising qtz-C, qtz-I and qtz-II filling a solutional macro-pore. e, f) Deformation lamellae (def. lam.) and recrystallized subgrains in qtz-II. Photographs at cross-polarized light. dol, dolomite; K-f, K-feldspar. The yellow dashed lines mark the transition between silica facies.

The second facies of megaquartz (qtz-II) represents the final episode of crystallization in the paragenetic sequence (Figure 5a). It shows zonal or massive textures and a large crystal size variability (0.2 to 5 mm; Figures 4c,d and 5c,d). Both qtz-I and qtz-II show undulose extinction, deformation lamellae and recrystallization textures like interfingering subgrain boundaries (Passchier & Trouw, 2005), indicating crystal lattice deformation acquired at depth (Figure 4e,f).

Another type of quartz mineralization found in the Calixto Cave is qtz-br, which consists of subhedral or anhedral quartz fragments with breccia-like textures (Figure 5e), usually associated with abundant K-feldspar with sericitic alteration. This facies is commonly found along bedding interfaces and lamination of the heterolith layers overlying the main cave passages in the middle and upper storeys (Figure 2). Brecciation is represented by angular clasts of silica and K-feldspar in a matrix of fine-grained detrital grains with heterolithic composition. Alteration halos rich in muscovite and altered K-feldpsar are common in the matrix associated with the brecciated textures, spanning from hundreds of μm to a few mm around the quartz-rich zones (Pisani et al., 2022). Besides K-feldspar and muscovite, the halos host disseminated sulfides, Fe oxides and Fe hydroxide stains (up to 200–250 μm in size) and monazite grains (Pisani et al., 2022).

Solid inclusions (ca. 5–50 μm in size) of anhydrite, barite, K-feldspar, muscovite, sulfides, Fe-Ti oxides and apatite (Pisani et al., 2022) are abundant in early qtz-I and often found in qtz-C and qtz-br.

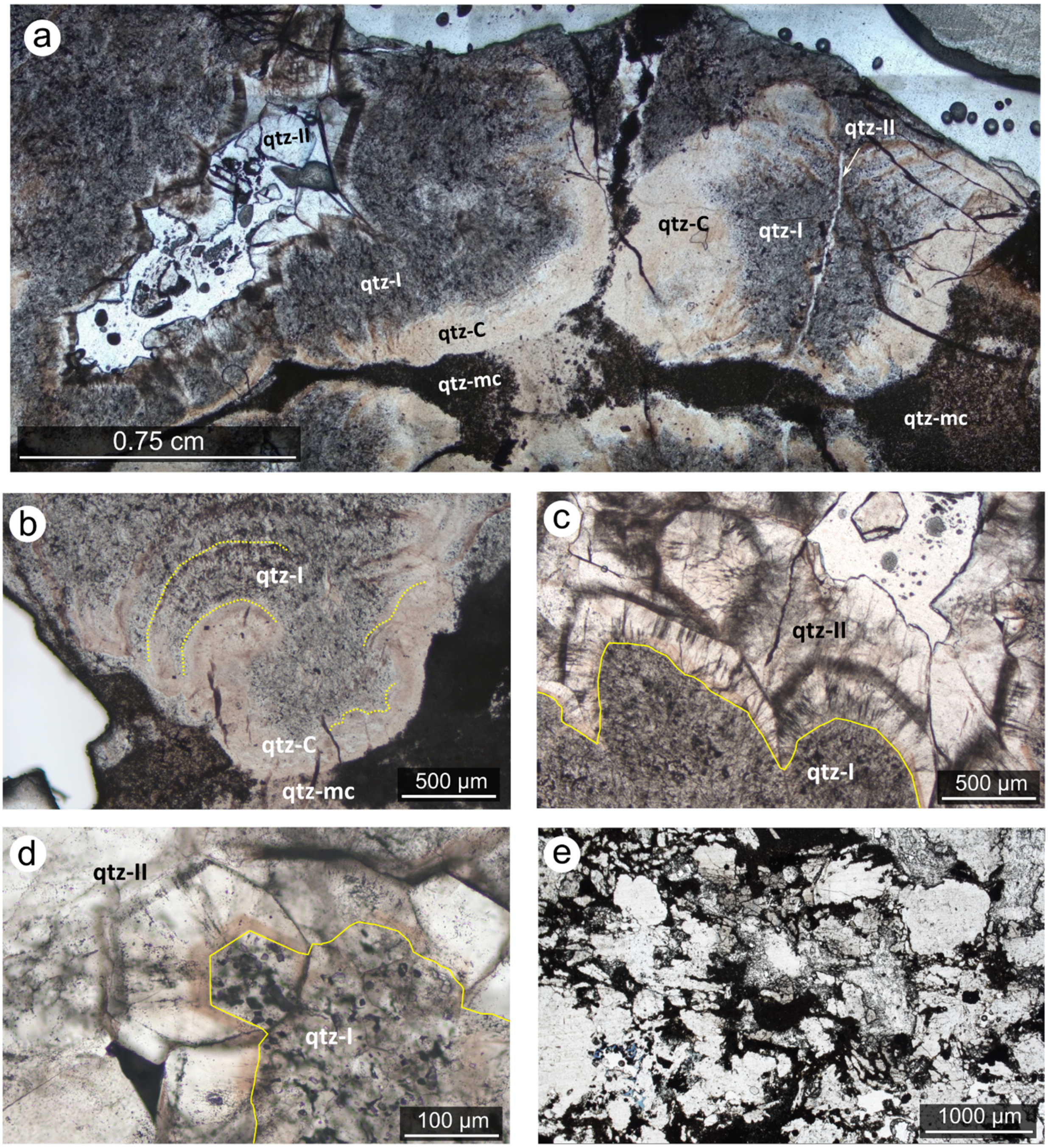

Figure 5. a) Paragenetic sequence of quartz facies from chert (qtz-mc) to (in order of growth) qtz-C (chalcedony), qtz-I (colloform-plumose quartz with cloudy cores), and qtz-II (massive or zonal euhedral megaquartz crystals). b) Contact between qtz-mc and qtz-C/qtz-I facies. Yellow dotted lines highlight colloform quartz bands. c) Qtz-I showing cloudy cores with randomly distributed inclusions, followed by qtz-II showing well-developed growth zones rich in primary fluid inclusions. Yellow solid lines highlight the transition between qtz-I and qtz-II. d) Detail of a qtz-I/qtz-II transition followed by defined growth zones parallel to crystal boundaries. Yellow solid lines highlight the transition between qtz-I and qtz-II. e) Breccia microtexture (qtz-br) in a heterolith layer, with fragmented clasts of silica and K-feldspar surrounded by a matrix of fine-grained detrital clasts.

3.2.4.2. Fluid inclusion petrography

Most of the fluid inclusions were found in qtz-I and qtz-II facies (Figures 5 and 6). Qtz-I possesses cloudy cores (Figure 5a) whose cloudy appearance is due to abundant mineral inclusions, randomly distributed two-phase liquid–vapour (L + V) inclusions (<10 µm in size) with inconsistent V:L ratios (Figure 6e) and dark large monophase (V) inclusions with shapes approaching negative-crystal (e.g. inclusions with surfaces resembling crystal faces; Goldstein & Reynolds, 1994) (Figure 6f).

The transition between qtz-I and qtz-II usually features well-developed growth zones with trails of primary two-phase L + V inclusions (Figures 5c,d and 6a). In qtz-II, growth zones with trails of primary two-phase FIAs are common (Figure 6a,b). Inclusions in these FIAs have sizes of 5–10 µm and show visually consistent V:L ratios (0.10–0.15). Other primary FIAs are associated with 3D clusters of large intracrystalline inclusions (up to 10–15 µm in size), often having negative-crystal shapes (Figure 6c). The boundaries between the quartz crystals commonly host irregular and imperfectly healed microfractures. Occasionally, dark single-phase (V) inclusions were observed in this type of quartz; no compelling evidence of their primary origin was recognized.

The qtz-mc and qtz-C facies show no recognizable FIAs due to the small size of the crystals. Abundant negative-crystal-shaped microcavities (ghosts of rhombohedral dolomite grains; Figure 6d) and relicts of the pristine dolostone rock are present (Figure 4d).

The qtz-br facies shows the coexistence of 3D clusters of large intracrystalline L + V inclusions (up to 20 µm in size) with consistent V:L ratios (0.10–0.15) and solid inclusions. Irregular-shaped dark single-phase (V) inclusions are also present in these facies.

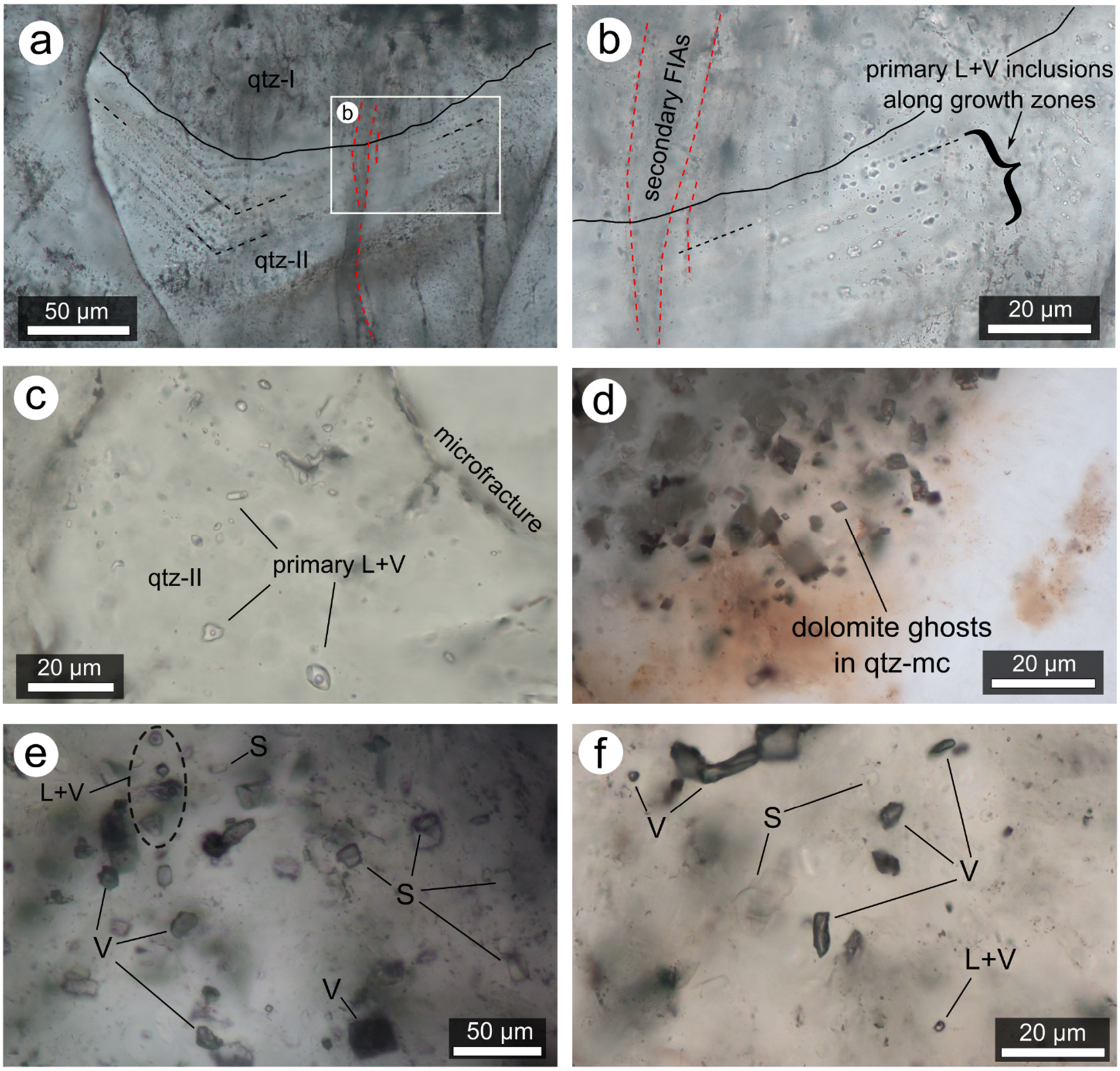

Figure 6. a) Trails of primary fluid inclusions (highlighted with black dashed lines) aligned parallel to qtz-II crystal faces. Black solid line marks the transition between qtz-I (cloudy core) and qtz-II (megaquartz with zonal texture). b) Close-up of inset in 'a': Primary two-phase (L+V) inclusions and trails of secondary inclusions, cross-cutting the primary FIAs (highlighted with red dashed lines). c) 3D cluster of primary fluid inclusions in qtz-II. Most of the inclusions have negative-crystal shapes. d) Rhombohedral dark cavities (ghosts of dolomite grains) in the qtz-mc facies. e-f) Coexisting two-phase (L+V), single-phase (V) fluid and solid (S) inclusions in the cloudy cores of qtz-I.

3.2.4.3. Fluid inclusion microthermometry

Four selected samples of qtz-II and one sample of qtz-br were studied to obtain microthermometric data from 57 FIAs (236 individual inclusions). The only phase transition observed during the heating runs was homogenization, which always occurred in the liquid phase. For most of the primary FIAs, T_h was consistent (according to the criteria of Goldstein & Reynolds, 1994). Figure 7a shows the cumulative frequency histogram of the entire dataset (*n* = 210) without three FIAs showing inconsistent T_h data (see Appendix C for the whole dataset). About 95% of the primary FIAs homogenize in the 175–210°C interval. The bimodal distribution has two well-defined peaks centred at 185 and 200°C.

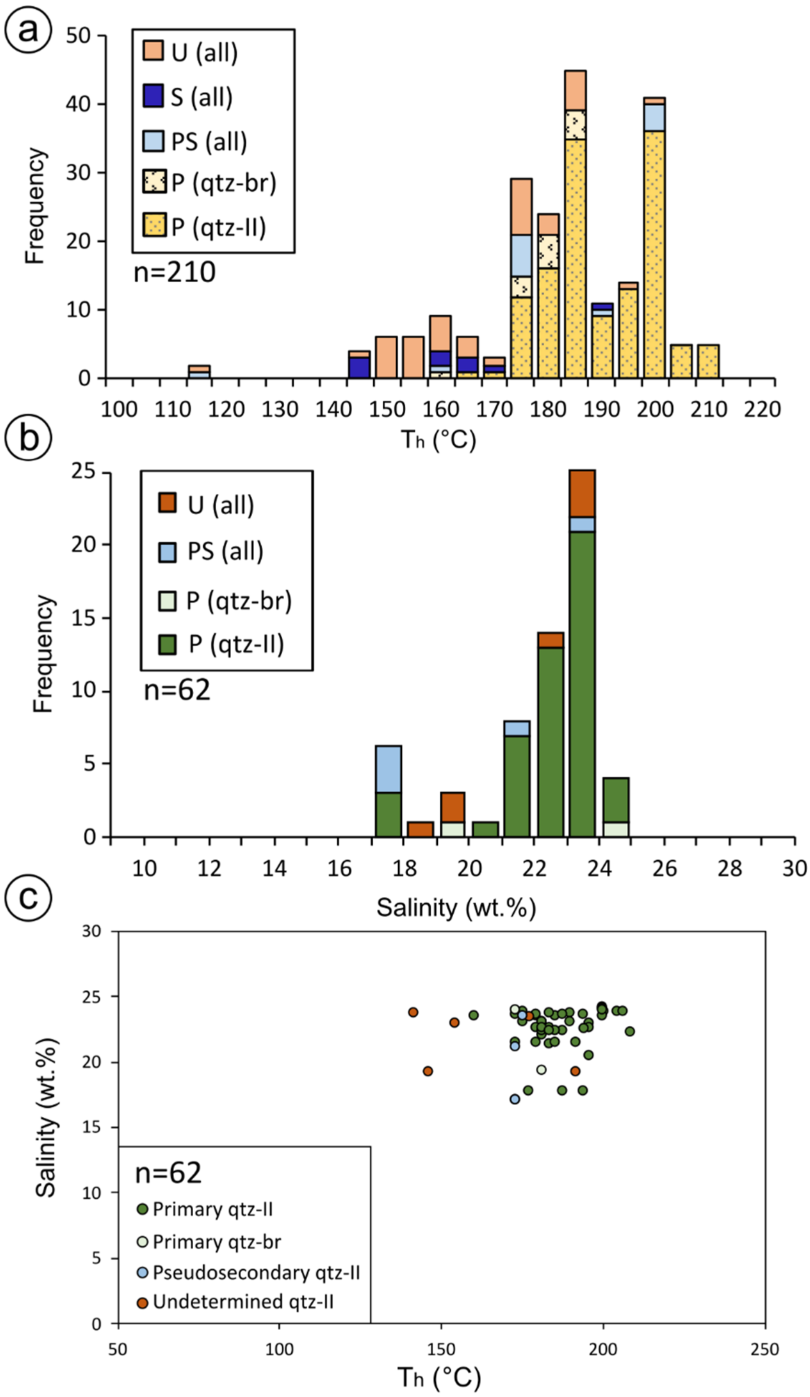

Figure 7. a) Frequency histogram of the homogenization temperatures (T_h) for the whole dataset (n = 210), excluding three FIAs (n = 26) that showed inconsistent results (according to the criteria of Goldstein & Reynolds, 1994). Undetermined (U), pseudo-secondary (PS) and secondary (S) assemblages are plotted in single groups, whilst quartz facies differentiate primary (P) assemblages. b) Frequency histogram of estimated salinity (NaCl-$CaCl_2$-equivalent) for all FIAs studied at low temperature (n = 62). c) T_h-salinity plot for the fluid inclusions where both T_h and salinity data were acquired (n = 62).

After the heating runs, freezing measurements were used to assess the salt composition of representative FIAs. Due to the very small size of most of the inclusions, phase changes during cooling runs were recognized only in a limited subset of FIAs (*n* = 62; Figure 7b). The two-phase aqueous inclusions were completely frozen (dark or brownish mosaic of crystals) at around −70° to −60°C. During slow heating, several phase transitions were observed between −60°C and room temperature. Most inclusions showed a clear first melting between −52 and −47°C. With progressive heating, an intermediate melting temperature between −28 and −26°C was observed in most of the FIAs with the sudden disappearance of the darkish, granular solid phase (likely small hydrohalite crystals), leaving the inclusions with only rounded and larger crystals, liquid and vapour phases. The final melting of the last solid phase (T_m) occurred between −26 and −15°C. About 90% of the primary inclusions have T_m values between −25 and −20°C (median at −23°C).

3.2.4.4. Raman spectrometry of fluid inclusions

As no gases were determined during microthermometry (e.g. melting of a carbonic phase or clathrate formation during the freezing experiments), Raman spectroscopy analyses were performed on a set of representative FIAs (samples 1094A-5, 1094B-3). Aqueous fluid inclusions hosted in qtz-I, qtz-II and qtz-br show a very broad peak at the characteristic wavenumbers of liquid H_2O (ca. 3400–3500 cm^{-1}) and occasional peak at the wavenumber characteristic of HCO_3^- solute (1017 cm^{-1}). These peaks were determined as weak in all spectra; no other gas phases (e.g. CO_2, H_2S, SO_2, CH_4) were detected. Such spectroscopic determinations are consistent with the lack of microthermometric evidence of a carbonic phase or clathrate formation during the freezing experiments (Dubessy et al., 2001; Marchesini et al., 2019).

Raman spectra were also acquired at −170 and −100°C, as well as at any observed phase transitions to detect the presence of ice, hydrohalite and salts in the spectral range of 2700 to 3550 cm^{-1} (Bakker, 2004; Baumgartner & Bakker, 2010; Samson & Walker, 2000). Most of the frozen inclusions showed Raman spectra with poorly defined peaks. However, few representative primary inclusions that were analyzed during progressive heating present broad peaks indicating the presence of a mixture of ice, NaCl hydrate (hydrohalite) and $CaCl_2$ hexahydrate (antarcticite). These solid phase peaks disappeared from the Raman spectra at the observed melting temperatures, as expected by the phase behaviour typical of the H_2O-NaCl-$CaCl_2$ system at low temperatures (see Appendix C for further details).

3.2.4.5. Oxygen and Silicon isotopes

The results of oxygen and silicon stable isotope analyses for Calixto Cave samples (*n* = 26) and quartzites from the Chapada Diamantina basement (*n* = 4) are summarized in Figure 8 and Table 1. The $\delta^{30}Si$ values of the Calixto Cave samples range from −3.6‰ to 2.6‰, whilst the Chapada Diamantina basement quartzites have $\delta^{30}Si$ values of 0.1‰ to 0.4‰ (Figure 8a). The $\delta^{18}O$ values of the cave samples range between 22.1‰ and 29.7‰, whereas those from the basement quartzites cluster around 13‰ (Figure 8b).

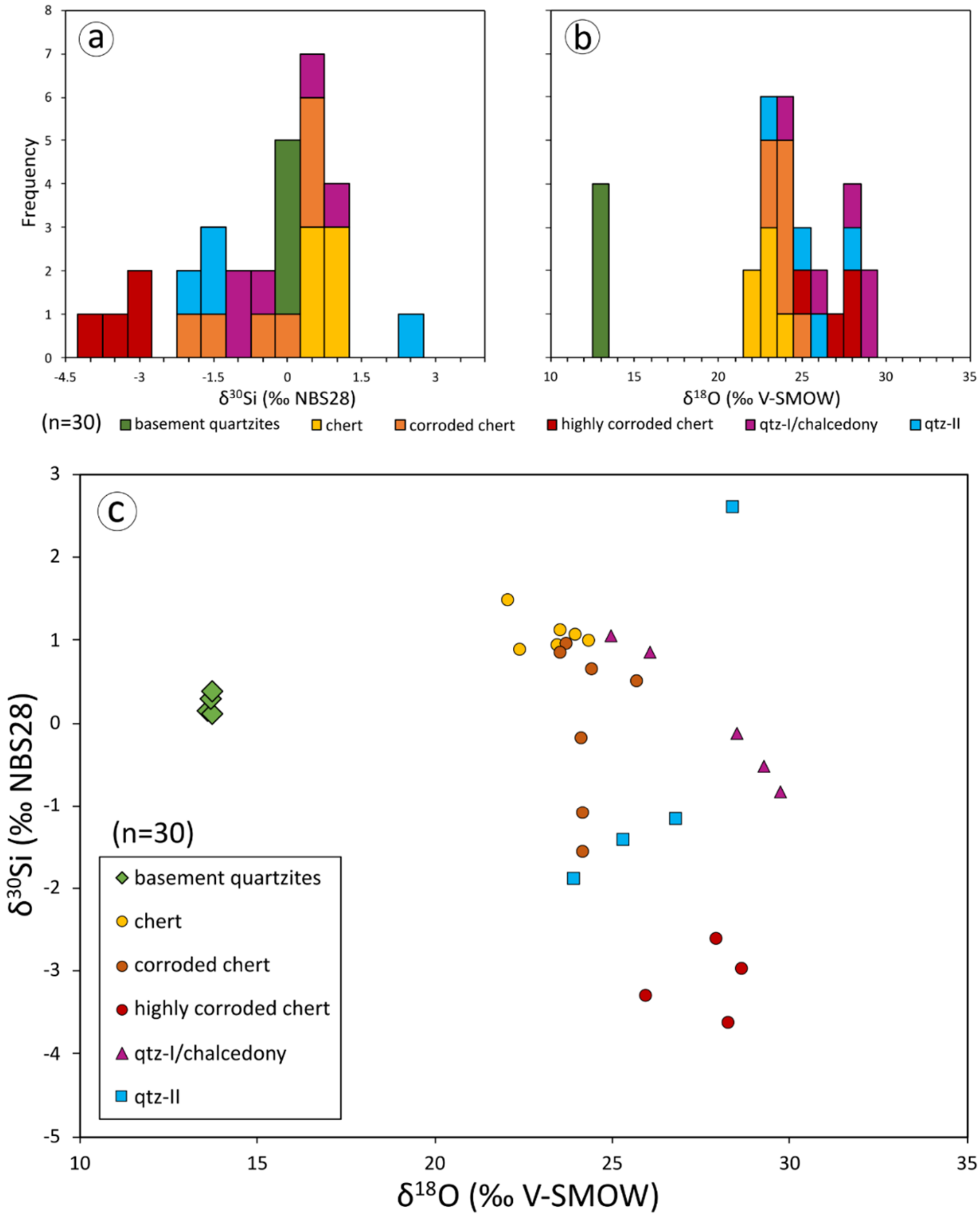

Figure 8. a) Frequency histogram of $\delta^{30}Si$ data of silica samples from Calixto Cave and Chapada Diamantina basement quartzites. b) Frequency histogram of $\delta^{18}O$ data of the silica samples from Calixto Cave and Chapada Diamantina basement quartzites. c) The $\delta^{18}O$-$\delta^{30}Si$ data.

The $\delta^{30}Si$ values of cherts found in Calixto Cave define a general trend toward more negative values going from the “pristine” or scarcely corroded cherts (0.9‰ to 1.5‰) to the highly corroded ones (−2.6‰ to −3.6‰) (Figure 8c). This trend is associated with an increase in the $\delta^{18}O$ values (by up to 7‰).

Table 1. $\delta^{30}Si$ and $\delta^{18}O$ isotope results with associated uncertainties (1σ).

Locality	Sample ID	Silica facies	Grain ID	$\delta^{30}Si$ (‰ NBS28)		$\delta^{18}O$ (‰ V-SMOW)	
Chapada Diamantina basement	CARB-1040	quartzite bedrock	16A	0.15	±0.17	13.58	±0.20
			16A-b1	0.12	±0.18	13.71	±0.19
			16B	0.30	±0.17	13.68	±0.18
			16B-b2	0.40	±0.19	13.73	±0.18
Calixto Cave	CARB-1081	qtz-I/chalcedony	19A	1.06	±0.17	24.95	±0.19
			19B	-0.52	±0.17	29.27	±0.20
	CARB-1063A	corroded chert	20A	0.95	±0.17	23.75	±0.20
			20B	-1.57	±0.20	24.18	±0.20
	CARB-1063B	qtz-I/chalcedony	21A	0.86	±0.18	26.05	±0.20
			21B	-0.12	±0.18	28.49	±0.19
	CARB-1098	chert	22A	0.98	±0.17	24.36	±0.27
			22A-b1	0.93	±0.14	23.47	±0.36
			22B	1.12	±0.20	23.56	±0.32
			22B-b2	1.07	±0.13	23.99	±0.38
	CARB-1085	chert	23A	1.48	±0.17	22.10	±0.36
			23B	0.88	±0.20	22.42	±0.36
	CARB-1094B	qtz-II	25A	-1.90	±0.18	23.95	±0.19
		corroded chert	25B	0.84	±0.19	23.55	±0.19
	CARB-1094D	corroded chert	27A	0.49	±0.17	25.70	±0.36
			27B	0.65	±0.17	24.43	±0.37
	CARB-1094E	corroded chert	28A	-0.19	±0.20	24.14	±0.21
			28B	-1.09	±0.17	24.19	±0.19
	CARB-1094F	qtz-I/chalcedony	29B	-0.83	±0.17	29.72	±0.19
		qtz-II	29A	-1.40	±0.18	25.30	±0.20
	CARB-1094G	qtz-II	30A	-1.17	±0.17	26.84	±0.36
			30B	2.60	±0.17	28.41	±0.36
	CARB-1094H	highly corroded chert	31A	-2.98	±0.17	28.66	±0.36
			31A-b1	-2.63	±0.20	27.95	±0.38
			31B	-3.64	±0.17	28.29	±0.38
			31B-b2	-3.30	±0.18	25.98	±0.36

Diagnostic textural features of the early-stage megaquartz (qtz-I) and qtz-C were hardly distinguishable in SEM observations. Therefore, they were classified into a single group. Samples from the middle-storey megaquartz and chalcedony deposits have heterogeneous values (Figure 8a, b), with the $\delta^{30}Si$ between −1.9‰ and 2.6‰, and the $\delta^{18}O$ between 23.9‰ and 29.7‰.

3.2.4.6. Monazite geochronology

Thirty-two U-Th-Pb analyses were performed on fourteen monazite grains (Table 2 and Figure 9). All grains were smaller than ca. 10 µm, had highly irregular shapes and were commonly crosscut by cracks and microfractures. The Th-U-total Pb dates range from ca. 2550 to 0 (Pb content below detection limit) Ma and four different groups were distinguished. The first and youngest group (group 1 in Table 2) is represented by 3 analyses of the same grain (siteD3-Mnz2) that cluster at 626 ± 17 Ma and have intermediate Y contents (Y_2O_3 = 1.25 wt.%). A second group comprising five analyses (group 2 in Table 2) of Y- and mostly Th-U-poor grains (Y_2O_3 = 0.51 wt.%) yielded dates between 1700 and 1100 Ma. The dominant and oldest group (group 3 in Table 2) at ca. 2000 Ma (one spot at 2500, twelve between 2200–1900 Ma) is relatively rich in Y (average Y_2O_3 = 1.89 wt.%), Th (ThO_2 = 6.37 wt.%) and Ca (CaO = 0.85 wt.%). The last group of analyses (not shown in Table 2 and Figure 9) comprises Y- and Th-U-poor analyses (Y_2O_3 < 0.10 wt.%; ThO_2 < 1.65 wt.%; U below detection limit) with Pb below the detection limit (around ca. 150 ppm; Montel et al., 1996). No reliable dates were calculated for this group.

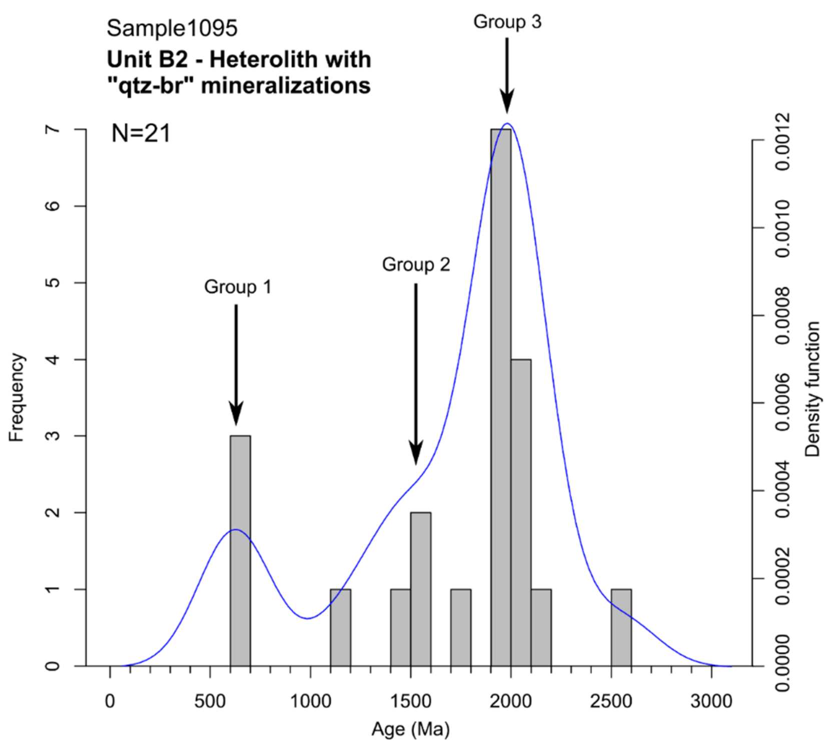

Figure 9. Frequency histogram and probability density distribution of the Th-U-total Pb dates for monazite grains in the heterolith unit with qtz-br mineralization (cf. Fig.2, unit B2).

Table 2. Th-U-total Pb dates obtained from electron microprobe dating of monazite.

ID site	number of analyses per site	calculated date (Ma)	2σ (Ma)	group
SiteD3-Mnz2	3	644	26	1
		604	34	
		619	31	
SiteA-Mnz1	2	1716	3	2
		(1402)	(7)	
SiteC-Mnz1	1	1186	46	
SiteMatrix4	2	1526	32	
		1508	82	
SiteA-Mnz2	2	2554	5	3
		2188	6	
SiteA-Mnz3	2	1973	5	
		1983	5	
SiteMatrix1	2	2006	20	
		1933	20	
SiteMatrix4	1	1942	30	
SiteMatrix3	6	2005	4	
		1994	4	
		1982	4	
		2010	4	
		2006	4	
		1962	5	

Note: (Date in brackets) = analysis with a low total.

3.2.5. Discussion

Hypogene caves and solutional karst porosity found in the carbonates of the Salitre Fm (Bertotti et al., 2020; Cazarin et al., 2019; Klimchouk et al., 2016; Pisani et al., 2022) and the nearby Chapada Diamantina Group (La Bruna et al., 2021; Souza et al., 2021) are often associated with silicified layers or hydrothermal mineralization containing quartz.

Silicification of marine carbonates is commonly the result of diagenetic processes (Maliva & Siever, 1989). The most representative silica crystallization sequence associated with increasing temperature during diagenesis is: (1) amorphous silica or opal-A; (2) cristobalite-tridymite (CT) opal; (3) microcrystalline quartz; (4) chalcedony; (5) megaquartz (Maliva & Siever, 1989; Marin, 2009; Marin-Carbonne et al., 2014; Sander & Black, 1988). This sequence is often observed in marine carbonates, where calcite/dolomite grains are replaced by opal or microcrystalline quartz (e.g. forming chert nodules). The other quartz textures occur preferentially in large voids and open fractures (Hesse, 1989), representing either late-stage silica deposition at elevated temperature or recrystallization of micro-quartz/chalcedony.

It is important to note that the behaviour of silica during the diagenetic evolution of carbonate sediments is more complex than the simple paragenetic sequence listed above. Various sediment-water interactions may act as either silica sinks or sources, for example: biodegradation of organic matter (Bennett et al., 1988), transformation of clay minerals, devitrification of volcanic ash (Siever, 1962; Siever & Woodford, 1973), or circulation of hydrothermal fluids (Wei et al., 2021). Chert with a predominantly volcanic silica source is recognizable by its high alkali, Al and Ti contents, ghosts of volcanic glass shards and associated volcaniclastic sediments (Maliva & Siever, 1989; Pollock, 1987). Another source could be direct precipitation from silica-rich seawater (Ledevin et al., 2019; Maliva & Siever, 1989), which could be expected for ancient Precambrian basins (Marin-Carbonne et al., 2014).

Based on the petrographic, textural and stratigraphic evidence from Calixto Cave (Pisani et al., 2022 and this study) and the entire São Francisco Craton (Bertotti et al., 2020; Cazarin et al., 2019; Klimchouk et al., 2016; Kyle & Misi, 1997; La Bruna et al., 2021; Souza et al., 2021), two main sources may be invoked to explain the widespread silica precipitation associated with karst development in the study area: (i) Si-enriched hydrothermal solutions rising through the fractured basement and (ii) Neoproterozoic connate (pore)water during burial diagenesis. Based on petrographic, mineralogical and speleogenetic observations, most of the works cited above interpreted silicification and karst development in the São Francisco Craton as a product of hydrothermal (hypogene) fluid circulation, even though no analytical data on quartz (e.g. stable isotopes, fluid inclusions, trace element composition) were reported so far.

In the following sections, the possible sources of silicification and silica dissolution-precipitation in Calixto Cave are discussed in the framework of the diagenetic evolution of the sequence.

3.2.5.1. Petrographic and microthermometric characteristics of silica

Like many Precambrian cherts (Maliva et al., 2005; Marin-Carbonne et al., 2014), no evidence of amorphous silica, opal-A, or opal-CT precipitated via biotic processes was found in the Calixto Cave sequence. The petrographic and textural characteristics of the chert nodules indicate that the first episodes of silica precipitation involved the replacement of the precursor carbonate with microcrystalline quartz. This process was likely related to early diagenetic (shallow burial) conditions, as supported by the ubiquitous cross-cutting relations between cherts and all tectonic and diagenetic features (like burial-related fractures and bedding-parallel stylolites) found in the cave, as described by Pisani et al. (2022). Furthermore, evidence of intense dissolution prevails in the qtz-mc facies, with cavernous vugs, solution-enlarged fractures and pores lined by qtz-C followed by megaquartz. Undulose extinction and deformation lamellae in megaquartz crystals also suggest that these crystals were subject to deformation after their deposition (Figure 4e,f).

Megaquartz and chalcedony in marine carbonate sequences are usually products of silica recrystallization and cementation in a deep-burial setting or due to later hydrothermal/metamorphic processes (Marin-Carbonne et al., 2013; Teboul et al., 2019). In Calixto Cave, the colloform-plumose textures and the coexisting solid (S), two-phase (V + L) and single-phase (V) primary inclusions are diagnostic features of hydrothermal processes, possibly associated with boiling solutions (Albinson et al., 2001; Moncada et al., 2017; Roedder & Bodnar, 1997). These features were mainly described in epithermal Au-Ag and precious ore deposits (Camprubí & Albinson, 2007; Dong et al., 1995; Moncada et al., 2012; Palinkaš et al., 2018; Sander & Black, 1988; Saunders, 1994; Shimizu, 2014).

In the Calixto Cave, colloform and plumose textures are typical of qtz-I facies, which represent the first crystallization stage of megaquartz in the paragenetic sequence (Figure 5, Table 3). Jigsaw mosaic quartz and chalcedony are also associated with the dissolution-recrystallization processes of microcrystalline quartz (Bobis, 1994; Moncada et al., 2012; Sander & Black, 1988; Shimizu, 2014). They are mainly associated with a gradually increasing crystal size, as usually observed at the transition between qtz-C and megaquartz and the rims of the solutional pores in the cherts (Figure 3b,c). The presence of spherulitic/fibrous chalcedony, which is a 'rapid' growth texture implying recrystallization of silica, suggests that the fluid was not at high temperature during the formation of this facies (< ca. 150°C; Marin-Carbonne et al., 2014).

Boiling and resultant quartz textures in epithermal systems (especially colloform quartz) are commonly related to upwelling fluids associated with open channels and accessory ore minerals precipitation (Hedenquist et al., 2000; Moncada et al., 2012; Simmons et al., 2005). Furthermore, silica-rich brecciated textures (like qtz-br facies) are considered a proxy for fluid overpressurization and hydraulic fracturing (Grare et al., 2018; Saunders, 1994).

Solid inclusions compatible with high temperature (likely >200°C) parental solutions were found mostly in the early-stage megaquartz (Figures 4b and 6e). Most of these inclusions consist of sulfates (anhydrite and barite), sulfides (pyrite and sphalerite), Fe- or Fe-Ti oxides, K-feldspar, muscovite and apatite (Pisani et al., 2022). Sericitic alteration of K-feldspar associated with sulfide precipitation, as observed in the alteration halos of qtz-br, is typical of high-temperature hydrothermal solutions, close to 200–350°C (Parry et al., 2002). Furthermore, penecontemporaneous precipitation of sulfides and sulfates may occur at a temperature range of 100 to 500°C and in alkaline or neutral (pH 7–10) solutions (Rye, 2005; Zhang, 1986). Alkaline (pH >8–9) conditions and high temperatures are also invoked to explain significant silica dissolution, as evidenced by the widespread karst features in the cherts (Andreychouk et al., 2009; Cui et al., 2017; Dove, 1995; Dove & Nix, 1997; Mitsiuk, 1974; Pisani et al., 2022; Siever, 1962).

The late-stage euhedral megaquartz (qtz-II) is characterized by massive or zonal textures (Figure 5c,d), typical of cooling aqueous solutions (Moncada et al., 2012, 2017; Sander & Black, 1988). During the low-temperature measurements, evidence of first melting below −40°C and last melting below the eutectic point of NaCl (−21.2°C) suggest the presence of antarcticite ($CaCl_2 \cdot 6H_2O$) in the frozen inclusions (Goldstein & Reynolds, 1994; Oakes et al., 1990). Considering the observed phase changes and Raman results at cryogenic temperatures (see Section 3.2.4.4. and Appendix C), we selected the H_2O-NaCl-$CaCl_2$ composition as the most likely approximation to assess the salinity for the studied inclusions. Estimated salinity values (Figure 7b) were calculated from the measured intermediate melting temperature (T_{int}) and final melting temperature (T_m) using the *Excel* spreadsheet provided by Steele-MacInnis et al. (2011). The salinity values are clustered in a narrow range of 17–25 wt.% with only a few individual inclusions showing values <20 wt.%.

Minimum formation temperature estimates were obtained from primary FIAs homogenization temperatures. Since no independent data on the burial-thermal history are available for the Salitre Fm, we cannot apply a pressure correction (Goldstein & Reynolds, 1994) to the homogenization temperatures. Qtz-II shows primary FIAs with T_h of 165–210°C and high salinity (17–25 wt.%, Figure 7b). No significant relations have been identified between salinity and T_h (Figure 7c).

The high salinity and the NaCl–$CaCl_2$ composition of the primary two-phase FIAs suggest extensive fluid–rock interactions, with an enrichment in $CaCl_2$ likely derived from the interaction with the carbonate-rich strata (Goldstein & Reynolds, 1994; You et al., 2018). Furthermore, the presence of solid inclusions of sulfates, hematite-ilmenite, pyrite, sphalerite and K-rich silicate (K-feldspar and muscovite), entrapped in the cloudy cores of qtz-I (Figures 5 and 6e), suggest that the estimated H_2O + NaCl + $CaCl_2$ composition is likely representative of the latest stages of crystallization, with the earlier being characterized by enrichment in other cations (e.g. Fe, Ba, K, Ti), H_2S and/or SO_4^{2-}.

Table 3. Summary of the silica facies at Calixto Cave with associated T_h and salinity values obtained from primary FIAs.

Silica facies	Texture	Primary inclusions T_h	Primary inclusions salinity (wt.%)	Description
qtz-mc	Microcrystalline quartz	*n.d.*	*n.d.*	Dolomite replacement; chert nodules and irregular bands; highly porous
qtz-C	Chalcedony or jigsaw mosaic quartz	*n.d.*	*n.d.*	Silica recrystallization texture; lining fractures and solutional vugs; gradual transition into qtz-I
qtz-br	Quartz-rich hydraulic breccias	160–185°C	19–25	Quartz + K-feldspar + sericitic alteration involving overpressurization and hydraulic fracturing
qtz-I	Plumose-colloform megaquartz	*n.d.*	*n.d*	Early stage of megaquartz precipitation, entrapping high temperature solid inclusions
qtz-II	Massive or zonal megaquartz	165–210°C	17–25	Late stage of megaquartz precipitation

Note: abbreviation *n.d.* = not determined.

3.2.5.2. Stable isotope modelling and the origin of silicification

Stable isotope modelling (Kleine et al., 2018; Stefánsson et al., 2017; and references therein) is a common tool used to assess the origin of fluids, chemical reactions and associated isotope fractionations for various processes occurring in the Earth's crust, including fluid–rock interaction, fluid phase separation (boiling) and cooling.

Silicon isotopes ($\delta^{30}Si$) are excellent proxies to trace hydrothermal activity and reconstruct paleoenvironments. Generally, the variation range of silicon isotopes during fractionation is very small. For example, the variation of $\delta^{30}Si$ in ancient sedimentary cherts goes from −5‰ to 5‰, whilst quartz cement range between −5‰ and 1‰ (Kleine et al., 2018), with negative $\delta^{30}Si$ values typical of hydrothermal silica precipitation (Abraham et al., 2011; Robert & Chaussidon, 2006).

In this paper, a Rayleigh-type model (see Section 3.2.3.4, Appendix C and editable Table S3 in the Supplementary Materials online for further details on the adopted calculations) was applied to simulate equilibrium and kinetic effects on silicon and oxygen isotope variations measured in cherts and quartz deposits in the course of: (1) quartz precipitation from boiling and cooling of hydrothermal fluids; (2) direct quartz precipitation from marine-derived pore water during burial diagenesis; (3) quartz precipitation from mixing of hydrothermal fluids and seawater.

As shown in Figure 10, most of the values from Calixto Cave quartz deposits are characterized by relatively negative δ^{30}Si values (−2‰ to 1‰) and relatively positive δ^{18}O values (23‰ to 29‰). The range of measured isotopes for most of the samples is consistent with silica precipitation upon boiling and cooling of Si-rich hydrothermal fluids at temperatures between 110 and 200°C. The isotopic signature of the hypothetic hydrothermal fluid (δ^{30}Si = 6.44‰, δ^{18}O = −0.21‰) was derived from the Chapada Diamantina basement rocks (in isotopic equilibrium with the fluid at ca. 300°C). The temperatures assessed for the scenario of boiling/cooling hydrothermal fluids (T = 140–200°C) for late-stage megaquartz (qtz-II) are also consistent with the T_h measured for this quartz facies (T_h = 165–210°C) (Table 3).

On the contrary, the "pristine" (non-corroded) chert cluster shows positive δ^{30}Si (>0.1‰, mean of 1‰) and δ^{18}O values ranging from 22 to 25‰; literature data (Abraham et al., 2011; Chakrabarti et al., 2012; Teboul et al., 2019; van den Boorn et al., 2010) consider these values as a possible indicator of direct precipitation from marine-derived pore water during diagenesis. High values of δ^{18}O in silica (>20‰–25‰) are usually interpreted in the context of diagenetic fluids (Marin-Carbonne et al., 2014; Teboul et al., 2019), whereas depleted δ^{18}O is considered to reflect either a mantle or a meteoric source (Hemond et al., 1993; Kleine et al., 2018). Hydrothermal-derived quartz and silica usually show more dispersed δ^{18}O values, in the range of 13%–36% (Clayton et al., 1972; Liu et al., 2022).

The values from uncorroded cherts of the unaltered host rock, clustering in a restricted area (Figure 10), are inconsistent with the modelled cooling/boiling systematics of hydrothermal fluids. A slightly higher shift in the δ^{30}Si (around +1‰) means that this cluster falls outside the predicted domain, suggesting a different parental fluid composition.

Furthermore, a clear trend towards more-depleted δ^{30}Si values is observed between the pristine chert and the corroded cherts, showing solutional (vuggy) porosity at the micro-scale. Values of corroded and highly corroded cherts represent samples collected in the middle storey (Figure 2b), where karstification was stronger and associated with the main conduits of the cave (Pisani et al., 2022).

Fluid–rock interaction resulting in modifications of the pristine isotope ratios of cave walls is a common phenomenon in hypogene speleogenesis (Plan et al., 2012; Spötl et al., 2021; Temovski et al., 2022). The most commonly observed pattern of isotopic alteration in carbonate rocks is the lowering of the bedrock $\delta^{18}O$ values near the cave wall because of the interaction with low-$\delta^{18}O$ high-temperature meteoric waters, as well as the lowering of bedrock $\delta^{13}C$ values due to interaction with dissolved inorganic carbon with lower $\delta^{13}C$ values (Dublyansky, 1995; Temovski et al., 2022). Interaction of low-$\delta^{30}Si$ and high-temperature thermal solutions with silica material would result in changes in the Si isotopic ratio, usually towards lower $\delta^{30}Si$ values (Chakrabarti et al., 2012). Many authors, however, suggested that, despite the highly uncertain effect of silica dissolution-recrystallization reactions on Si and O isotopic fractionation, early diagenetic cherts are less susceptible to pervasive post-depositional changes (Chakrabarti et al., 2012; Heck et al., 2011; Knauth, 1979).

In contrast to this assumption, the corroded chert samples in Calixto Cave show evidence of intense post-depositional isotopic alteration ($\delta^{30}Si$ depletion by up to 3‰–4‰; $\delta^{18}O$ increase by up to 6‰–7‰) that we interpret as the consequence of qtz-mc interacting with deep-seated hydrothermal solutions at high temperature and alkaline conditions, as supported also by textural and petrographic observations (see Section 3.2.5.1.).

To discuss a possible origin for the early-diagenetic cherts, simulation of isotope systematics for silica precipitated from pore (sea)water during diagenesis has been modelled adopting Rayleigh-type fractionation curves (see Appendix C). Trends corresponding to incremental steps of 30°C in burial temperatures were plotted in dashed red colour in Figure 10, ascribing a region of extremely positive $\delta^{30}Si$ and $\delta^{18}O$ values. Since no data are available for the burial-thermal history of the Salitre Fm, these burial temperatures were set arbitrarily to evaluate the consistency of the measured data with the model isotope systematics. Most of the cherts and chalcedony/qtz-I plot in the simulated isotopic range that would imply burial diagenesis reaching temperatures of 120–150°C (Figure 10). In the case of a hypothetical maximum burial temperature of around 150°C, a cumulative overburden of 4–6 km would be required above the Salitre Fm, assuming an average geothermal gradient of 25–35°C/km (Peters et al., 2012). Nevertheless, such high temperatures would reflect an unrealistic burial depth, exceeding the one estimated for the entire region (Japsen et al., 2012; Klimchouk et al., 2016).

A study by Japsen et al. (2012) based on apatite fission track data showed that prior to the Campanian the Chapada Diamantina Group (west of the study area) was buried to a depth of no more than 2–3 km. This cover was completely removed during episodic uplift between ca. 80 and 15 Ma (Japsen et al., 2012). However, it is unknown if the Una-Utinga basin was ever buried to the same (or different) depth after the deposition of the Calixto Cave sequence. Hypothesizing a thickness of around 500–1000 m for the Salitre Fm (Klimchouk et al., 2016; Misi & Veizer, 1998), a maximum burial between 2 and 2.5 km could be expected and related to peak temperatures of no more than 60–90°C under typical geothermal gradients (Peters et al., 2012). These values are not supported by the measured isotopes in the cherts and present a discrepancy in temperatures of about 60°C. Another possibility to fit the isotopic values and predicted temperatures for chert formation with low-burial thickness (up to ca. 2.5 km) requires an anomalously high geothermal gradient of 50–60°C/km.

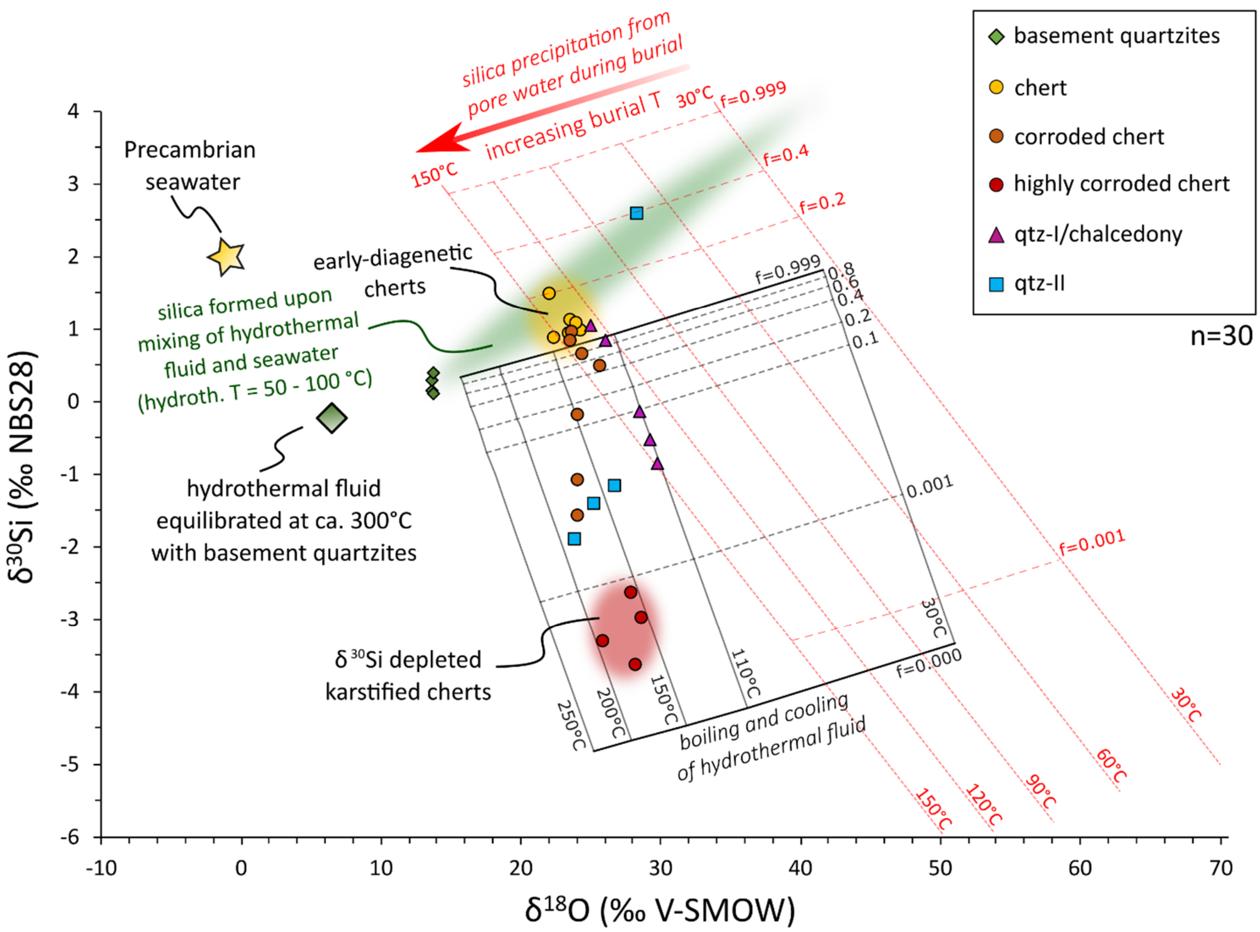

Figure 10. Predicted isotope systematics of quartz formed upon: (1) boiling/cooling of hydrothermal fluids (black grid), (2) burial diagenesis (red grid) and (3) mixing of Precambrian seawater with hydrothermal fluids (green shadowed area). The isotopic signature of the hydrothermal fluid is assumed to have been equilibrated with Chapada Diamantina quartzites at a temperature of 300°C. Composition of the Precambrian seawater from Robert and Chaussidon (2006) and Marin-Carbonne et al. (2014). f, fraction of remaining H_4SiO_4 in the aqueous fluid (following the adopted fractionation curves shown in the Supplementary Materials).

Since both scenarios seem geologically unlikely, we interpret the early diagenetic chert as the product of precipitation from Precambrian seawater mixed with hydrothermal solutions coming from the basement at relatively low temperature (ca. 50–100°C; Figure 10). This process could explain the slightly higher $\delta^{30}Si$ values that characterize the cherts, shifted towards the $\delta^{30}Si$ of Precambrian seawater, as predicted by the isotope values modelled for the mixing process (green region in Figure 10). Most of the values of uncorroded cherts plot close to the lower border of the green shadowed area in the model of Figure 10, which represent the predicted isotopes for silica precipitation from Precambrian oceanic seawater mixed with low-temperature hydrothermal fluids (T = 50°C). The upper border of the green area represents the predicted isotope systematics of silica precipitated from the same process, but with a hydrothermal fluid temperature reaching 100°C. This hypothesis is also consistent with the early-diagenetic petrographic characteristics of the cherts (Pisani et al., 2022).

3.2.5.3. Diagenetic evolution of the Salitre Formation and speleogenetic implications

The diagenetic, petrographic and karstic features in the studied Neoproterozoic sequence indicate a complex succession of processes that played a major role during (and after) the burial of the Salitre Fm sediments. The conceptual model of the main diagenetic and speleogenetic processes is presented in Figure 11 and discussed below.

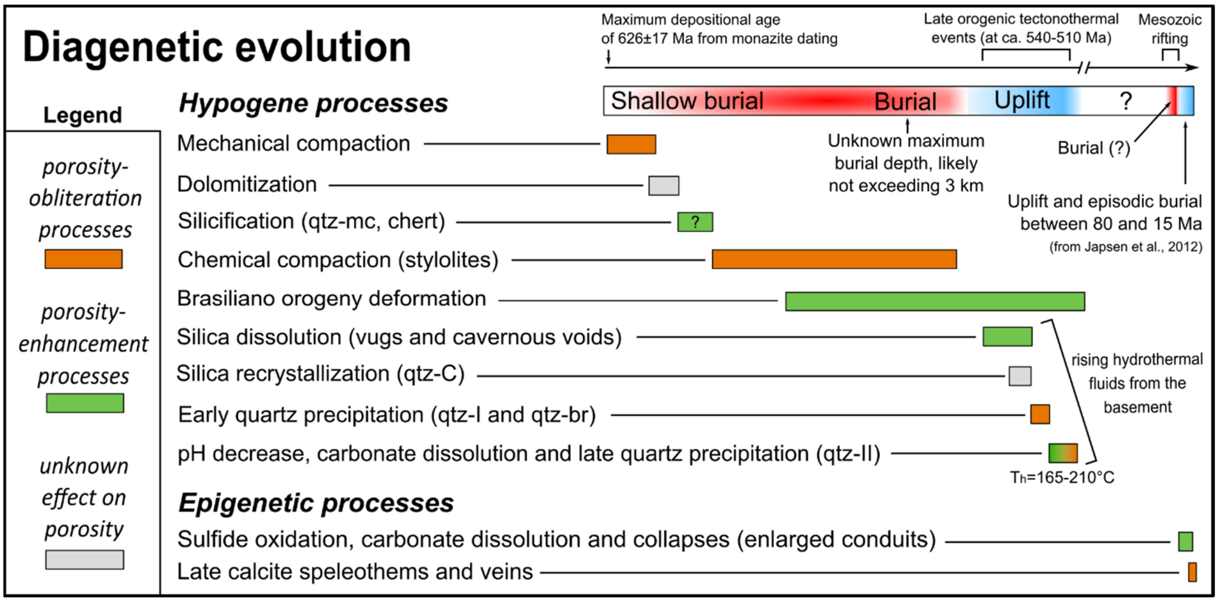

Figure 11. Conceptual scheme of the main diagenetic processes affecting the Calixto Cave sedimentary sequence in relation to the key geodynamic events that occurred in the São Francisco Craton. The main phases of silica dissolution-precipitation are here interpreted as the result of hydrothermal fluid circulation during the Cambrian tectono-thermal events (ca. 540–510 Ma).

During the shallow burial, following mechanical compaction of the sediments, primary calcite constituents were replaced by dolomite. The origin of diffuse dolomitization in the sequence is beyond the scope of this work; however, the subhedral shapes of the dolomite crystals suggest low temperatures and shallow burial conditions (Sibley & Gregg, 1987).

Chert (qtz-mc) in the dolostone layers is interpreted to have formed during a diffuse silicification episode at shallow depth and relatively low temperature (ca. 50–100°C), by precipitation from ancient seawater mixed with thermal water, sourced from the underlying quartzites of the Chapada Diamantina Group. This process was followed by progressive burial and chemical compaction to form bedding-parallel stylolites.

The process of hydrothermal silicification of carbonates plays an important role in modifying the original petrophysical properties of the rock. Although this effect on porosity is still debated, recent studies on Brazilian pre-salt hydrocarbon reservoirs (Fernández-Ibáñez, Nolting, et al., 2022) revealed an increase in porosity up to around 10% thanks to the hypogene dissolution of mineral grains and the brittle behaviour of silica. The localization of fractures in the stiff chert nodules has been observed also in Calixto Cave (Pisani et al., 2022) and contributed to significantly increased porosity and permeability.

Around ca. 600 Ma, the basin was involved in the Brasiliano orogeny, and the depositional environment changed from an intracratonic gulf-like basin to a foreland basin (Santana et al., 2021). Continued burial and tectonic deformation produced a large set of faults and fractures during a prolonged period and the reactivation of basement-rooted structures (D'Angelo et al., 2019). Crustal thickening, continental collision and uplift were marked by an intense magmatic activity, represented by numerous plutons and batholiths that intruded the basement in the orogenic belts surrounding the craton (Ferreira et al., 1998; Sial & Ferreira, 2016). In the Borborema Province (north of the study area), the ages of the plutons fall into two intervals of 640–610 and 590–530 Ma (Ferreira et al., 2021; Guimarães et al., 2004; Neves et al., 2015, 2022). The latest orogenic events in the Cambrian (540–510 Ma) were characterized by hydrothermalism and large-scale fluid migration in the craton (Almeida et al., 2000; Trindade et al., 2004). Deep-rooted deformation zones represented permeability pathways for the localized upwelling of thermal solutions from the underlying basement rocks (Bertotti et al., 2020; Klimchouk et al., 2016; Pisani et al., 2022).

Evidence of high temperature and alkaline parental solutions explain the widespread dissolution of silica observed in Calixto Cave middle storey, with the development of high solutional porosity and permeability. Bulk permeability in the silicified and karstified layers at Calixto Cave reached 10^3 mD, as reported by Pisani et al. (2022), with rock plugs permeability that can reach up to 200–250 mD (2 to 3 orders of magnitude higher than surrounding carbonates) and porosity up to 16%. The formation of pervasive cavernous porosity-permeability in silica is common in many hydrocarbon reservoirs affected by hydrothermal silicification (De Luca et al., 2017; Lima et al., 2020; Packard et al., 2001; Poros et al., 2017; Teboul et al., 2019; Wei et al., 2021). These reservoirs show incredibly complex porosity-permeability heterogeneities, fault- and fracture-controlled conduit systems, secondary mineralization and reactive fronts associated with vuggy pore space.

Our observations support the previous work of Pisani et al. (2022), who hypothesized that a deep-seated hydrothermal alteration in the cherts caused an increase in porosity and permeability at the micro-scale, which paved the way for the later speleogenetic processes. The combination of high fracture intensity that characterizes the silicified dolostones (Pisani et al., 2022) and early dissolution of silica was crucial for the definition of preferential flow pathways and favourable conditions for hypogene speleogenesis, which ultimately lead to the development of macro-scale conduit-type porosity.

Hydrothermal fluids rising from the underlying Chapada Diamantina Group along faults or fracture zones were the main drivers for hypogene speleogenetic processes in deep-seated confined settings; they determined the formation of extensive networks of conduits in the Salitre Fm, mostly of stratiform and multi-storey type and commonly associated with silica-rich mineralizations (Balsamo et al., 2020; Bertotti et al., 2020; Cazarin et al., 2019; Klimchouk et al., 2016; Pisani et al., 2022; Pontes et al., 2021). In this context, the dissolution of carbonate and silicified layers to form the main conduit networks required specific (and almost opposite) conditions, with the carbonate dissolution promoted by acidic and low-temperature conditions and the silica dissolution promoted by alkaline and/or high-temperature conditions (Andreychouk et al., 2009; Cui et al., 2017; Klimchouk, 2019). High-temperature aqueous solutions enlarged and connected the vuggy pores in chert nodules, producing micro-scale solutional cavernous voids. Water cooling and/or a gradual decrease in pH caused the switch from silica-dominant dissolution to carbonate-dominant dissolution and quartz precipitation.

Euhedral megaquartz (qtz-II) filling fractures and vuggy pores mark the final crystallization stages of the hydrothermal fluids at a minimum temperature range (from homogenization temperatures) of 165–210°C (Figure 7a). The decrease in pH towards more acidic conditions is supported not only by the dissolution of the carbonates in the sequence (Pisani et al., 2022) but also by the occurrence of HCO_3^- Raman peaks found in some primary fluid inclusions.

Hypogene karstification to produce the main macro-scale void-conduit systems must have been the result of prolonged dissolution in confined settings, with the formation of a three-dimensional pattern of conduits controlled by the main lateral and vertical heterogeneity in the distribution of flow-conducting fractures and, in turn, high- versus low-permeability zones (Klimchouk et al., 2016; Pisani et al., 2022).

3.2.5.4. Possible timing of hydrothermal dissolution-precipitation in the Salitre Formation

To constrain the possible age of the hydrothermal dissolution-precipitation phases, monazite grains associated with silicification were dated. The obtained ages (Figure 9, Table 2) point toward a detrital origin, with ages ranging from Paleoproterozoic (groups 2 and 3) to Neoproterozoic (group 1) source rocks. The maximum depositional age of the Salitre Fm was constrained by the age of the youngest zircon grain at 669 ± 14 Ma by Santana et al. (2021). Our youngest monazite grain (626 ± 17 Ma) further constrains the maximum depositional age of the Calixto Cave sequence to the Ediacaran. In addition, eleven analyses in the same sample are characterized by low Th, U and Pb contents (see Section 3.2.4.6.). This group of monazites, from which no reliable ages could be calculated, might represent detrital grains which have been hydrothermally altered during fluid circulation at the basin scale (Poitrasson et al., 2000) or new (authigenic) hydrothermal crystals. A widespread resetting of the U–Pb isotopic system triggered by hydrothermal fluid circulation was documented by Trindade et al. (2004) in the Salitre Fm carbonates and dated to the Cambrian (around ca. 520 Ma). The same tectono-thermal event could be related to the hypogene speleogenetic phase affecting the basin, as also suggested by Klimchouk et al. (2016) for the northern sector of the Irecê basin (ca. 330 km north of the study area). There, a giant cave system with similar characteristics to the Calixto Cave has been described (Balsamo et al., 2020; Cazarin et al., 2019; Klimchouk et al., 2016). However, we cannot attribute any definite geochronological constraint to the hydrothermal events affecting the Calixto Cave sequence.

The Cambrian tectono-thermal events recognized in the whole São Francisco and Congo Cratons (Almeida et al., 2000; Misi et al., 2005; Trindade et al., 2004) were regarded by several authors as the source of the Pb-Zn sulfide mineralization in the Salitre Fm (Gomes et al., 2000; Kyle & Misi, 1997; Moraes Filho & Leal, 1990; Silva et al., 2006; Teixeira et al., 2007, 2010), and as a possible driver of hypogene (hydrothermal) karst development (Bertotti et al., 2020; Klimchouk et al., 2016). The study of primary fluid inclusions in sphalerites of the Nova Redenção Pb-Zn sulfide deposit (about 20 km to the east of Andaraì city, Figure 1c) revealed the presence of saline (ca. 24–25 wt.%)

aqueous solutions formed mainly by H_2O-NaCl, possibly with dissolved salts of Ca, K or Mg, and minimum trapping temperatures of 140–190°C (Gomes et al., 2000). This economic ore deposit is in the same basin (Una-Utinga) and is associated with dolostones characterized by silicification and quartz-ferruginous breccias. Primary fluid inclusions in sphalerites from Fe-Zn-Pb ore deposits in the nearby Irecê basin (Kyle & Misi, 1997) point to minimum formation temperatures ranging from 140 to 200°C. All these ore deposits with gangue quartz mineralization were interpreted as the consequence of hydrothermal fluid circulation in the Salitre Fm during the late phases of the Brasiliano orogeny in the Cambrian. Such observations, reported from different sectors of the craton, are compatible with the petrographic and microthermometric data obtained from the Calixto Cave quartz deposits.

Despite a lack of geochronological constraints, which require additional research, we hypothesize that hypogene silica dissolution (and reprecipitation) likely occurred during the late-orogenic Cambrian tectono-thermal events (Figure 11). The presence of undulose extinction and deformation lamellae in megaquartz (Figure 4e,f) is also consistent with this interpretation, suggesting that megaquartz precipitation occurred before the Ordovician tectonic stabilization of the cratonic block (Almeida et al., 2000). Another possibility proposed by Klimchouk et al. (2016) is that rifting associated with the Pangea break-up (Triassic–Cretaceous) and its related fluid migration events could be a possible driver for the main phase of hypogene speleogenesis in the Salitre Fm.

If either of these interpretations is correct, the development of solutional (karst) porosity in the silicified rocks of Calixto Cave would be amongst the oldest studied on Earth (Auler, 2017; Klimchouk et al., 2016).

3.2.6. Conclusions

Our petrographic, microthermometric and stable isotope data suggest that the quartz deposits in the silicified layers of Calixto Cave resulted from interactions with high-temperature hydrothermal solutions. Associated processes involved chert dissolution, chalcedony/quartz reprecipitation lining fractures and vuggy pores in the sequence. Hydrothermal alteration of the cherts caused a $\delta^{30}Si$ decrease by up to 3‰–4‰ in the silicified cherty layers. The isotopic composition of the early diagenetic cherts is explained by precipitation from Neoproterozoic seawater mixed with thermal fluids derived from the quartzites of the Chapada Diamantina basement at an estimated temperature range of 50–100°C. Chalcedony and megaquartz formed by precipitation from high-temperature hydrothermal fluids show an isotopic signature compatible with boiling/cooling solutions derived from the basement quartzites in the range of 110–200°C. Further constraints were obtained from microthermometric measurements, which indicate that late-stage megaquartz precipitation happened at a minimum temperature range of 165–210°C. The dissolved salts in primary FIAs were identified as $NaCl$-$CaCl_2$ by low-temperature microthermometric measurements supported by cryogenic Raman spectroscopy. The salinity of the mineral-forming fluids was estimated at 17–25 wt.%. Similar values were also obtained for the quartz-rich hydraulic breccias in the sedimentary units sealing the main conduit system.

The documented dissolution and reprecipitation of silica in Calixto Cave demonstrate the role of hypogene (hydrothermal) processes that drastically modified the petrophysical properties of host rocks considered to have very low solubility at typical near-surface conditions (e.g. chert, quartzite, silicified carbonate). Hydrothermal silicification followed by the circulation of high-temperature aqueous fluids in fractured sub-surface systems may promote the formation of high-permeability zones (subsequently filled by chalcedony and mega-quartz). Such peculiar and underestimated processes may have important implications for the development of high porous chert/silicified reservoirs and, potentially, favourable conditions for hypogene speleogenetic processes (e.g. macroscale void-conduit formation).

Despite the high variability of silica sources in sedimentary basins, integrating geochemical, petrographic, and field observations in caves representing analogues of deep-seated conduits is a first-order tool to expand our knowledge of hypogene speleogenetic and minerogenetic processes. The research conducted in Calixto Cave may help to clarify the origin of silica dissolution-precipitation in other carbonate reservoirs where silicification and karst development are closely associated.

Acknowledgments

This research was carried out in association with the ongoing R&D project registered as ANP 20502-1, '*Processos e Propriedades em Reservartorios Carbonaticos Fraturados e Carstificados—POROCARSTE 3D' (UFRN/UNB/UFRJ/UFC/Shell Brasil/ANP*)—Porokarst—Processes and Properties in Fractured and Karstified Carbonate Reservoirs, sponsored by Shell Brasil under the ANP R&D levy as '*Compromisso de Investimento com Pesquisa e Desenvolvimento*'. Cave map data were kindly provided by *Grupo Pierre Marin de Espeleologia* (GPME). Cave sampling was performed through SISBIO permit 63178/1. We sincerely thank the Iramaia municipality (State of Bahia) and the Brazilian Federal Environmental Agency (*Instituto Chico Mendes*) for providing access to the cave and the special permission for collecting rock samples. We thank Bastian Joachim-Mrosko for providing the access to the Raman Spectroscopy Laboratory at the University of Innsbruck and for his valuable help. We also thank Jürgen Konzett for the early discussions on monazite dating and Augusto Auler for the help during fieldwork. We finally thank the Editor Atle Rotevatn for handling the manuscript and the reviewers Marjan Temovski, Cathy Hollis and Alexander Klimchouk for their suggestions and comments that helped to improve our paper. This article is the NordSIMS published contribution n. 726.

References

Abraham, K., Hofmann, A., Foley, S.F., Cardinal, D., Harris, C., Barth, M.G., Andre, L., 2011. Coupled silicon–oxygen isotope fractionation traces Archaean silicification. Earth and Planetary Science Letters 301, 222–230.

Albinson, T., Norman, D.I., Cole, D., Chomiak, B., 2001. Controls on formation of low-sulfidation epithermal deposits in Mexico; constraints from fluid inclusion and stable isotope data. Special Publication of the Society of Economic Geologists (U.S.) 8, 1–32.

Almeida, F.F.M., Brito Neves, B.B., Dal Rè Carneiro, C., 2000. The origin and evolution of the South American Platform. Earth-Science Reviews 50, 77–111.

Álvaro, J., 2013. Late Ediacaran syn-rift/post-rift transition and related fault-driven hydrothermal systems in the Anti-Atlas Mountains, Morocco. Basin Research 25, 348–360.

Andreychouk, V., Dublyansky, Y.V., Ezhov, Y., Lisenin, G., 2009. Karst in the Earth's Crust: Its Distribution and Principal Types. University of Silezia — Ukrainian Institute of Speleology and Karstology, Sosnovec–Simferopol, 72 pp.

Audra, P, Laurent, J.Y., Cailhol, N., Bigot, J.Y., Laurent, D., Vanara, N., Cailhol, D., Cazenave, G., 2022. Hydrodynamic model for independent cold and thermo-mineral twin springs in a stratified continental karst aquifer, Camou, Arbailles Massif, Pyrénées, France. International Journal of Speleology 51, 81-91.

Auler, A.S., 2017. Hypogene caves and karst of South America. In: In: Klimchouk, A., Palmer, A.N., De Waele, J., Auler, A.S., Audra, P. (Eds.), Hypogene Karst Regions and Caves of the World, Cave and Karst Systems of the World, vol. 2017 Springer International Publishing, Cham.

Bakker, R.J., 2004. Raman spectra of fluid and crystal mixtures in the systems H_2O, H_2O-NaCl and H_2O-$MgCl_2$ at low temperatures: Applications to fluid-inclusion research. Canadian Mineralogist 42, 1283–1314.

Balsamo, F., Bezerra, F.H.R., Klimchouk, A.B., Cazarin, C.L., Auler, A.S., Nogueira, F.C., Pontes, C., 2020. Influence of fracture stratigraphy on hypogene cave development and fluid flow anisotropy in layered carbonates, NE Brazil. Marine and Petroleum Geology 114, 104207.

Baumgartner, M., Bakker, R.J., 2010. Raman spectra of ice and salt hydrates in synthetic fluid inclusions. Chemical Geology 275, 58– 66.

Bence, A.E., Albee, A.L., 1968. Empirical correction factors for the electron microanalysis of silicates and oxides. Journal of Geology 76, 382–403.

Bennett, P.C., Melcer, M.E., Siegel, D.I., Hassett, J.P., 1988. The dissolution of quartz in dilute aqueous solutions of organic acids at 25°C. Geochimica et Cosmochimica Acta 52, 1521–1530.

Bento dos Santos, T.M., Tassinari, C.C.G., Fonseca, P.E., 2015. Diachronic collision, slab break-off and long-term high thermal flux in the Brasiliano–Pan-African orogeny: Implications for the geodynamic evolution of the Mantiqueira Province. Precambrian Research 260, 1–22.

Bertotti, G., Audra, P., Auler, A., Bezerra, F.H., de Hoop, S., Pontes, C., Prabhakaran, R., Lima, R., 2020. The Morro Vermelho hypogenic karst system (Brazil): Stratigraphy, fractures, and flow in a carbonate strike-slip fault zone with implications for carbonate reservoirs. AAPG Bulletin 104, 2029–2050.

Bobis, R.E., 1994. A review of the description, classification and origin of quartz textures in low sulphidation epithermal veins. Journal of the Geological Society of the Philippines 49, 15–39.

Bodnar, R.J., 2003. Reequilibration of Fluid Inclusions. In: Samson, I., Anderson, A., and Marshall, D. (Eds.), Fluid inclusions: Analysis and Interpretation. Mineralogical Association of Canada, 213–230.

Brito Neves, B.B., Fuck, R.A., Martins, M., 2014. The Brasiliano collage in South America: a review. Brazilian Journal of Geology 44, 493–518.

Caird, R.A., Pufahl, P.K., Hiatt, E.E., Abram, M.B., Rocha, A.J.D., Kyser, T.K., 2017. Ediacaran stromatolites and intertidal phosphorite of the Salitre Formation, Brazil: Phosphogenesis during the Neoproterozoic Oxygenation Event. Sedimentary Geology 350, 55–71.

Camprubí, A., Albinson, T., 2007. Epithermal deposits in México - Update of current knowledge and an empirical reclassification. Special Paper of the Geological Society of America 422, 377–415.

Cazarin, C.L., Bezerra, F.H.R., Borghi, L., Santos, R.V., Favoreto, J., Brod, J.A., Auler, A.S., Srivastava, N.K., 2019. The conduit-seal system of hypogene karst in Neoproterozoic carbonates in northeastern Brazil. Marine and Petroleum Geology 101, 90–107.

Cazarin, C.L., van der Velde, R., Santos, R.V., Reijmer, J.J.G., Bezerra, F.H.R., Bertotti, G., La Bruna, V., Silva, D.C.C., de Castro, D.L., Srivastava, N.K., Barbosa, P.F., 2021. Hydrothermal activity along a strike-slip fault zone and host units in the São Francisco Craton, Brazil – Implications for fluid flow in sedimentary basins. Precambrian Research 365, 106365.

Chakrabarti, R., Knoll, A.H., Jacobsen, S.B., Fischer, W.W., 2012. Si isotope variability in Proterozoic cherts. Geochimica et Cosmochimica Acta 91, 187–201.

Choquette, P.W., Pray, L.C., 1970. Geologic Nomenclature and Classification of Porosity in Sedimentary Carbonates. AAPG Bulletin 54, 207-250.

Clayton, R.N., O'Neil, J.R., Mayeda, T.K., 1972. Oxygen isotope exchange between quartz and water. Journal of Geophysical Research 77, 3057–3067

Cui, H., Kaufman, A.J., Xiao, S., Zhou, C., Liu, X.M., 2017. Was the Ediacaran Shuram Excursion a globally synchronized early diagenetic event? Insights from methane-derived authigenic carbonates in the uppermost Doushantuo Formation, South China. Chemical Geology 450, 59–80.

D'Angelo, T., Barbosa, M.S.C., Danderfer Filho, A., 2019. Basement controls on cover deformation in eastern Chapada Diamantina, northern São Francisco Craton, Brazil: Insights from potential field data. Tectonophysics 772, 228231.

De Luca, P.H.V., Matias, H., Carballo, J., Sineva, D., Pimentel, G.A., Tritlla, J., Esteban, M., Loma, R., Alonso, J.L.A., Jiménez, R.P., Pontet, M., Martinez, P.B., Vega, V., 2017. Breaking barriers and paradigms in presalt exploration: The Pão de Açúcar discovery (Offshore Brazil). AAPG Memoir 113, 177–193.

Dong, G., Morrison, G., Jaireth, S., 1995. Quartz textures in epithermal veins, Queensland - classification, origin, and implication. Economic Geology 90, 1841–1856.

Dong, S., You, D., Guo, Z., Guo, C., Chen, D., 2018. Intense silicification of Ordovician carbonates in the Tarim Basin: constraints from fluid inclusion Rb–Sr isotope dating and geochemistry of quartz. Terra Nova 30, 406–413.

Dove, P.M., 1995. Kinetic and thermodynamic controls on silica reactivity in weathering environments. In: White A. F., Brantley S. L. (Eds.), Reviews in Mineralogy 31, Chemical Weathering Rates of Silicate Minerals, Berlin, De Gruyter & Co., 235-291.

Dove, P.M., Nix, C.J., 1997. The influence of the alkaline earth cations, magnesium, calcium, and barium on the dissolution kinetics of quartz. Geochimica et Cosmochimica Acta 61(16), 3329–3340.

Dubessy, J., Buschaert, S., Lamb, W., Pironon, J., Thiéry, R., 2001. Methane-bearing aqueous fluid inclusions: Raman analysis, thermodynamic modelling and application to petroleum basins. Chemical Geology 173, 193–205.

Dublyansky, Y.V., 1990. Zakonomernosti formirovaniya i modelirovaniye gidrotermokarsta (Particularities of the development and modeling of hydrothermal karst). Nauka, Novosibirsk, 151 pp.

Dublyansky, Y.V., 1995. Speleogenetic history of the Hungarian hydrothermal karst. Environmental Geology 25, 24–35.

Fernández-Ibáñez, F., Jones, G.D., Mimoun, J.G., Bowen, M.G., Simo, J.A.T., Marcon, V., Esch, W.L., 2022. Excess permeability in the Brazil pre-Salt: Non matrix types, concepts, diagnostic indicators, and reservoir implications. AAPG Bulletin 106, 701–738.

Fernández-Ibáñez, F., Nolting, A., Breithaupt, C.I., Darby, B., Mimoun, J., Henares, S., 2022. The properties of faults in the Brazil pre-salt: A reservoir characterization perspective. Marine and Petroleum Geology 146, 105955.

Ferreira, V.P., Sial, A.N., Jardim de Sà, E.F., 1998. Geochemical and isotopic signatures of Proterozoic granites in terranes of the Borborema structural province, northeast Brazil. Journal of South American Earth Sciences 11(5), 439–455.

Ferreira, A.C., Dantas, E.L., Fuck, R.A., Nedel, I.M., Reimold, W.U., 2021. Multiple stages of migmatite generation during the Archean to Proterozoic crustal evolution in the Borborema Province, Northeast Brazil. Gondwana Research 90, 314-334.

Girard, J.P., San Miguel, G., 2017. Evidence of high temperature hydrothermal regimes in the pre-salt series, Kwanza Basin, offshore Angola. In: American Association of Petroleum Geologists Annual Convention and Exhibition (Houston, Texas, USA, Abstracts).

Goldscheider, N., Mádl-Szőnyi, J., Erőss, A., Schill, E., 2010. Thermal water resources in carbonate rock aquifers. Hydrogeology Journal 18, 1303–1318.

Goldstein, R.H., 2003. Petrographic analysis of fluid inclusions. In: Samson, I., Anderson, A., and Marshall, D. (Eds.), Fluid inclusions: Analysis and Interpretation, Mineralogical Association of Canada, 1–45.

Goldstein, R.H., Reynolds, T.J., 1994. Systematics of Fluid Inclusions in Diagenetic Minerals. Soc. Sed. Geol. Short Course 31, 199 pp.

Gomes, A.S.R., Coelho, C.E.S., Misi, A., 2000. Fluid Inclusion Investigation of the Neoproterozoic Lead-Zinc Sulfide Deposit of Nova Redenção, Bahia, Brazil. Revista Brasileira de Geociências 30, 315–317.

Grare, A., Lacombe, O., Mercadier, J., Benedicto, A., Guilcher, M., Trave, A., Ledru, P., Robbins, J., 2018. Fault zone evolution and development of a structural and hydrological barrier: The quartz breccia in the Kiggavik area (Nunavut, Canada) and its control on uranium mineralization. Minerals 8, 1–28.

Guimarães, I.P., Da Silva Filho, A.F., Almeida, C.N., Van Schmus, W.R., Araújo, J.M.M., Melo, S.C., Melo, E.B., 2004. Brasiliano (Pan-African) granitic magmatism in the Pajeú-Paraíba belt, Northeast Brazil: an isotopic and geochronological approach. Precambrian Research 135, 23–53.

Guimarães, J.T., Misi, A., Pedreira, A.J., Dominguez, J.M.L., 2011. The Bebedouro formation, Una Group, Bahia (Brazil). Geological Society of London Memoirs 36, 503–508.

Heck, P.R., Huberty, J.M., Kita, N.T., Ushikubo, T., Kozdon, R., Valley, J.W., 2011. SIMS analyses of silicon and oxygen isotope ratios for quartz from Archean and Paleoproterozoic banded iron formations. Geochimica et Cosmochimica Acta 75, 5879-5894.

Hedenquist, J.W., Arribas, R.A., Gonzalez-Urien, E., 2000. Exploration for epithermal gold deposits. Reviews in Economic Geology 13, 245–277.

Hemond, C., Arndt, N.T., Lichtenstein, U., Hofmann, A.W., Oskarsson, N., Steinthorsson, S., 1993. The heterogeneous Iceland plume: Nd Sr O isotopes and trace element constraints. Journal of Geophyscal Research: Solid Earth 98, 15833-15850.

Hesse, R., 1989. Silica diagenesis: origin of inorganic and replacement cherts. Earth-Science Reviews 26, 253–284.

Japsen, P., Bonow, J.M., Green, P.F., Cobbold, P.R., Chiossi, D., Lilletveit, R., Magnavita, L.P., Pedreira, A.J., 2012. Episodic burial and exhumation history of NE Brazil after opening of the south Atlantic. GSA Bulletin 124, 800–816.

Kato, T., 2005. New accurate Bence-Albee α-factors for oxides and silicates calculated from the PAP correction procedure. Geostandards and Geoanalytical Research 29, 83–94.

Kleine, B.I., Stefánsson, A., Halldórsson, S.A., Whitehouse, M.J., Jónasson, K., 2018. Silicon and oxygen isotopes unravel quartz formation processes in the Icelandic crust. Geochemical Perspectives Letters 7, 5–11.

Klimchouk A., 2007. Hypogene speleogenesis: hydrogeological and morphometric perspective. Carlsbad, National Cave and Karst Research Institute, 106 pp.

Klimchouk, A., 2019. Speleogenesis, hypogenic. In: White, W.B., Culver, D.C., Pipan, T. (Eds.), Encyclopedia of Caves, 3rd edition. Academic Press, New York, 974–988.

Klimchouk, A., Auler, A.S., Bezerra, F.H.R., Cazarin, C.L., Balsamo, F., Dublyansky, Y.V., 2016. Hypogenic origin, geologic controls, and functional organization of a giant cave system in Precambrian carbonates, Brazil. Geomorphology 253, 385–405.

Knauth, L.P., 1979. A model for the origin of chert in limestone. Geology 7(6), 274–277.

Kornilov, V.F., 1978. The temperature regime of formation of the mercury–antimony mineralization (Southern Kirghizia). In: Ermakov, N.P. (Ed.), Thermobarogeochemistry of the Earth's Crust. Nauka, Moscow, 155–161.

Kyle, J.R., Misi, A., 1997. Origin of Zn-Pb-Ag sulfide mineralization within upper proterozoic phosphate-rich carbonate strata, Irêce Basin, Bahia, Brazil. International Geology Review 39, 383–399.

La Bruna, V., Bezerra, F.H.R., Souza, V.H.P., Maia, R.P., Auler, A.S., Araújo, R.E.B., Cazarin, C.L., Rodrigues, M.A.F., Vieira, L.C., Sousa, M.O.L., 2021. High-permeability zones in folded and faulted silicified carbonate rocks – Implications for karstified carbonate reservoirs. Marine and Petroleum Geology 128, 105046.

Ledevin, M., Arndt, N., Chauvel, C., Jaillard, E., Simionovici, A., 2019. The sedimentary origin of black and white banded cherts of the Buck Reef, Barberton, South Africa. Geosciences 9, 17–24.

Leven, J.A., 1961. Problems of origin of optical-quality fluorite from deposits of the Zeravshan–Gissar Mountains. Trans. Samarkand Univ. 16, 35–51.

Lima, B.E.M., De Ros, L.F., 2019. Deposition, diagenetic and hydrothermal processes in the Aptian Pre-Salt lacustrine carbonate reservoirs of the northern Campos Basin, offshore Brazil. Sedimentary Geology 383, 55–81.

Lima, B.E.M., Tedeschi, L.R., Pestilho, A.L.S., Santos, R.V., Vazquez, J.C., Guzzo, J.V.P., De Ros, L.F., 2020. Deep-burial hydrothermal alteration of the Pre-Salt carbonate reservoirs from northern Campos Basin, offshore Brazil: evidence from petrography, fluid inclusions, Sr, C and O isotopes. Marine and Petroleum Geology 113, 104143.

Liu, C., Ma, J., Zhang, L., Wang, C., Liu, J., 2022. Protracted formation of nodular cherts in marine platform: new insights from the Middle Permian Chihsian carbonate successions, South China. Carbonates and Evaporites 37, 1–19.

Lovering, T.S., Tweto, O., Loweing, T.G., 1978. Ore deposits of the Gilman District, Eagle Country, Colorado. U.S. Geological Survey Professional Paper, 1017, 90 pp.

Magalhães, A.J.C., Raja Gabaglia, G.P., Scherer, C.M.S., Bállico, M.B., Guadagnin, F., Bento Freire, E., Silva Born, L.R., Catuneanu, O., 2016. Sequence hierarchy in a Mesoproterozoic interior sag basin: from basin fill to reservoir scale, the Tombador Formation, Chapada Diamantina Basin, Brazil. Basin Research 28, 393–432.

Maliva, R.G., Siever, R., 1989. Nodular Chert Formation in Carbonate Rocks. Journal of Geology 97, 421–433.

Maliva, R.G., Knoll, A.H., Simonson, B.M., 2005. Secular change in the Precambrian silica cycle: Insights from chert petrology. GSA Bulletin 117, 835–845.

Marchesini, B., Garofalo, P.S., Menegon, L., Mattila, J., Viola, G., 2019. Fluid-mediated, brittle-ductile deformation at seismogenic depth - Part 1: Fluid record and deformation history of fault veins in a nuclear waste repository (Olkiluoto Island, Finland). Solid Earth 10, 809–838.

Marin, J., 2009. Composition isotopique de l'oxygène et du silicium dans les cherts Précambriens: Implications Paléo-environnementales. PhD thesis. Institut National Polythechnique de Lorraine, 402 pp.

Marin-Carbonne, J., Faure, F., Chaussidon, M., Jacob, D., Robert, F., 2013. A petrographic and isotopic criterion of the state of preservation of Precambrian cherts based on the characterization of the quartz veins. Precambrian Research 231, 290–300.

Marin-Carbonne, J., Robert, F., Chaussidon, M., 2014. The silicon and oxygen isotope compositions of Precambrian cherts: A record of oceanic paleo-temperatures? Precambrian Research 247, 223–234.

Misi, A., Veizer, J., 1998. Neoproterozoic carbonate sequences of the Una Group, Irêce Basin, Brazil: chemostratigraphy, age and correlations. Precambrian Research 89, 87–100.

Misi, A., Iyer, S.S.S., Coelho, C.E.S., Tassinari, C.C.G., Franca-Rocha, W.J.S., Cunha, I.D.A., Gomes, A.S.R., de Oliveira, T.F., Teixeira, J.B.G., Filho, V.M.C., 2005. Sediment hosted lead–zinc deposits of the Neoproterozoic Bambuí Group and correlative sequences, São Francisco craton, Brazil: a review and a possible metallogenic evolution model. Ore Geology Reviews 26, 263–304.

Misi, A., Kaufman, A.J., Veizer, J., Powis, K., Azmy, K., Boggiani, P.C., Gaucher, C., Teixeira, J.B.G., Sanches, A.L., Iyer, S.S., 2007. Chemostratigraphic correlation of Neoproterozoic successions in South America. Chemical Geology 237, 22–45.

Misi, A., Kaufman, A.J., Azmy, K., Dardenne, M.A., 2011. Neoproterozoic successions of the São Francisco craton, Brazil: The Bambuí, Una, Vazante and Vaza Barris/Miaba groups and their glaciogenic deposits. Geological Society of London Memoirs 36, 509–522.

Misi, A., Batista, J., Teixeira, G., 2012. Mapa Metalogenético Digital do Estado da Bahia e Principais Províncias Minerais. Série Publicações Especiais 11.

Mitsiuk, B.N., 1974. Vzaimodeistvie kremnezema s vodoy v hydrotermalnych usloviach (Interaction between silica and water in hydrothermal conditions). In: Naukova Dumka, Kiev, 86 pp.

Moncada, D., Mutchler, S., Nieto, A., Reynolds, T.J., Rimstidt, J.D., Bodnar, R.J., 2012. Mineral textures and fluid inclusion petrography of the epithermal Ag–Au deposits at Guanajuato, Mexico: Application to exploration. Journal of Geochemical Exploration 114, 20–35.

Moncada, D., Baker, D., Bodnar, R.J., 2017. Mineralogical, petrographic and fluid inclusion evidence for the link between boiling and epithermal Ag-Au mineralization in the La Luz area, Guanajuato Mining District, México. Ore Geology Reviews 89, 143–170.

Montanari, D., Minissale, A., Doveri, M., Gola, G., Trumpy, E., Santilano, A., Manzella, A., 2017. Geothermal resources within carbonate reservoirs in western Sicily (Italy): A review. Earth-Science Reviews 169, 180–201.

Montel, J. M., Foret, S., Veschambre, M., Nicollet, C., Provost, A., 1996. Electron microprobe dating of monazite. Chemical Geology 131(1-4), 37-53.

Moraes Filho, O., Leal, R.A., 1990. Lead-zinc-silver search in the municipal district of Nova Redenção (BA). In: Anais 36° Congresso Brasileiro de Geologia, 1990, Natal, 1487-1501.

Neves, S.P., Lages, G.A., Brasilino, R.G., Miranda, A.W.A., 2015. Paleoproterozoic accretionary and collisional processes and the build-up of the Borborema Province (NE Brazil): Geochronological and geochemical evidence from the Central Domain. Journal of South American Earth Sciences 58, 165–187.

Neves, S.P., Teixeira, C.M.L., Silva, V.L., Bruguier, O., 2022. Protracted (>60 Myrs) thermal evolution of a Neoproterozoic metasedimentary sequence from eastern Borborema Province (NE Brazil): Thermal and rheological implications for orogenic development. Precambrian Research 377, 106709.

Oakes, C.S., Bodnar, R.J., Simonson, J.M., 1990. The system $NaCl–CaCl_2–H_2O$: I. The ice liquidus at 1 atm total pressure. Geochimica et Cosmochimica Acta 54, 603–610.

Onac, B.P., Forti, P., 2011. Minerogenetic mechanisms occurring in the cave environment: An overview. International Journal of Speleology 40, 79–98.

Packard, J.J., Al-Aasm, I., Samson, I., 2001. A Devonian hydrothermal chert reservoir: The 225 bcf Parkland field, British Columbia, Canada. AAPG Bulletin 85(1), 51–84.

Palinkaš, S.S., Hofstra, A.H., Percival, T.J., Šoštarkć, S.B., Palinkaš, L., Bermanec, V., Pecskay, Z., Boev, B., 2018. Comparison of the Allchar Au-As-Sb-Tl Deposit, Republic of Macedonia, with Carlin-Type Gold Deposits. In: John L. Muntean (Ed.), Diversity in Carlin-Style Gold Deposits, Reviews in Economic Geology vol. 20, Society of Economic Geologists, Littleton, USA, 353-363.

Parry, W.T., Jasumback, M., Wilson, P.N., 2002. Clay Mineralogy of Phyllic and Intermediate Argillic Alteration at Bingham, Utah. Economic Geology 97(2), 221–239.

Passchier, C.W., Trouw, R.A., 2005. Microtectonics. Springer Science & Business Media.

Peters, K.E., Curry, D.J., Kacewicz, M., 2012. An overview of basin and petroleum system modeling: Definitions and concepts. In: K.E. Peters, D.J. Curry, & M. Kacewicz (Eds.), Basin modeling: New horizons in research and applications (Vol. 4, pp. 1– 16). AAPG Hedberg Series.

Pisani, L., Antonellini, M., Bezerra, F.H.R., Carbone, C., Auler, A.S., Audra, P., La Bruna, V., Bertotti, G., Balsamo, F., Pontes, C.C.C., De Waele, J., 2022. Silicification, flow pathways, and deep-seated hypogene dissolution controlled by structural and stratigraphic variability in a carbonate-siliciclastic sequence (Brazil). Marine and Petroleum Geology, 139, 105611.

Plan, L., Tschegg, C., De Waele, J., Spötl, C., 2012. Corrosion morphology and cave wall alteration in an Alpine sulfuric acid cave (Kraushöhle, Austria). Geomorphology 169–170, 45–54.

Poitrasson, F., Chenery, S., Shepherd, T.J., 2000. Electron microprobe and LA-ICP-MS study of monazite hydrothermal alteration: Implications for U-Th-Pb geochronology and nuclear ceramics. Geochimica et Cosmochimica Acta 64, 3283–3297.

Pollock, S.G., 1987. Chert formation in an Ordovician volcanic arc. Journal of Sedimentary Petrology 57(1), 75-87.

Pontes, C.C.C., Bezerra, F.H.R., Bertotti, G., La Bruna, V., Audra, P., De Waele, J., Auler, A.S., Balsamo, F., De Hoop, S., Pisani, L., 2021. Flow pathways in multiple-direction fold hinges: implications for fractured and karstified carbonate reservoirs. Journal of Structural Geology 146, 104324.

Poros, Z., Jagniecki, E., Luczaj, J., Kenter, J., Gal, B., Correa, T.S., Ferreira, E., McFadden, K.A., Elifritz, A., Heumann, M., Johnston, M., Matt, V., 2017. Origin of silica in pre-salt carbonates, Kwanza Basin, Angola. In: American Association of Petroleum Geologists Annual Convention and Exhibition, Houston, Texas (USA).

Rimstidt, J.D., 1997. Quartz solubility at low temperatures. Geochimica et Cosmochimica Acta 61, 2553–2558.

Robert, F., Chaussidon, M., 2006. A palaeotemperature curve for the Precambrian oceans based on silicon isotopes in cherts. Nature 443, 969–972.

Roedder, E., 1984. Fluid inclusions. In: Reviews in Mineralogy 12, ed. Mineralogical Society of America, 646 pp.

Roedder, E., Bodnar, R.J., 1997. Fluid inclusion studies of hydrothermal ore deposits. In: Barnes, H.L. (Ed.), Geochemistry of Hydrothermal Ore Deposits. Wiley, New York, 657–697.

Rye, R.O., 2005. A review of the stable-isotope geochemistry of sulfate minerals in selected igneous environments and related hydrothermal systems. Chemical Geology 215, 5–36.

Samson, I.M., Walker, R.T., 2000. Cryogenic raman spectroscopic studies in the system $NaCl$-$CaCl_2$-H_2O and implications for low-temperature phase behavior in aqueous fluid inclusions. Canadian Mineralogist 38, 35–43.

Sander, M. V., Black, J.E., 1988. Crystallization and recrystallization of growth-zoned vein quartz crystals from epithermal systems; implications for fluid inclusion studies. Economic Geology 83, 1052–1060.

Santana, A., Chemale, F., Scherer, C., Guadagnin, F., Pereira, C., Santos, J.O.S., 2021. Paleogeographic constraints on source area and depositional systems in the Neoproterozoic Irecê Basin, São Francisco Craton. Journal of South American Earth Sciences 109, 103330.

Saunders, J.A., 1994. Silica and gold textures in bonanza ores of the sleeper deposit, Humboldt County, Nevada: Evidence for colloids and implications for epithermal ore-forming processes. Economic Geology 89, 628–638.

Sauro, F., De Waele, J., Onac, B.P., Galli, E., Dublyansky, Y.V., Baldoni, E., Sanna, L., 2014. Hypogenic speleogenesis in quartzite: The case of Corona ’e Sa Craba Cave (SW Sardinia, Italy). Geomorphology 211, 77–88.

Seitz, S., Baumgartner, L.P., Bouvier, A.S., Putlitz, B., Vennemann, T., 2017. Quartz Reference Materials for Oxygen Isotope Analysis by SIMS. Geostandards and Geoanalytical Research 41, 69–75.

Shanmugan, G., Higgins, J.B., 1988. Porosity enhancement from chert dissolution beneath Neocomian unconformity: Ivishak Formation, North Slope, Alaska. AAPG Bulletin 72(5), 523–535.

Shimizu, T., 2014. Reinterpretation of quartz textures in terms of hydrothermal fluid evolution at the Koryu Au-Ag deposit, Japan. Economic Geology 109, 2051–2065.

Sial, A.N., Ferreira, V.P., 2016. Magma associations in Ediacaran granitoids of the Cachoeirinha–Salgueiro and Alto Pajeú terranes, northeastern Brazil: Forty years of studies. Journal of South American Earth Sciences 68, 113–133.

Sial, A.N., Gaucher, C., Misi, A., Boggiani, P.C., De Alvarenga, C.J.S., Ferreira, V.P., Pimentel, M.M., Pedreira, J.A., Warren, L.V., Fernández-Ramírez, R., Geraldes, M., Pereira, N.S., Chiglino, L., Dos Santos Cezario, W., 2016. Correlations of some Neoproterozoic carbonate-dominated successions in South America based on high-resolution chemostratigraphy. Brazilian Journal of Geology 46(3), 439-388.

Sibley, D.F., Gregg, J.M., 1987. Classification of dolomite rock textures. Journal of Sedimentary Research 57, 967–975.

Siever, R., 1962. Silica solubility, 0°C - 200°C, and the diagenesis of siliceous sediments. Journal of Geology 70, 127-150.

Siever, R., Woodford, N., 1973. Sorption of silica by clay minerals. Geochimica et Cosmochimica Acta 37, 1851-1880.

Silva, M.G., Neves, J.P., Klein, E., Bento, R.V., Dias, V.M., 2006. Principais processos envolvidos na gênese das mineralizações de Sn, Au, Ba, quartzo rutilado e diamante, na região do Espinhaço-Chapada Diamantina, Bahia. In: Anais 43° Congresso Brasileiro de Geologia, 2006, Aracaju, 381 pp.

Simmons, S.F., White, N.C., John, D.A., 2005. Geological characteristics of epithermal precious and base metal deposits. In: J.W., Hedenquist, J.F.H., Thompson, R.J., Goldfarb, J.P. Richards (Eds.), Economic Geology: One Hundredth Anniversary Volume 1905–2005, Society of Economic Geologists, 485–522.

Souza, V.H.P., Bezerra, F.H.R., Vieira, L.C., Cazarin, C.L., Brod, J.A., 2021. Hydrothermal silicification confined to stratigraphic layers: Implications for carbonate reservoirs. Marine and Petroleum Geology 124, 104818.

Spötl, C., Dublyansky, Y., Koltai, G., Cheng, H., 2021. Hypogene speleogenesis and paragenesis in the Dolomites. Geomorphology 382, 107667.

Steele-MacInnis, M., Bodnar, R.J., Naden, J., 2011. Numerical model to determine the composition of H_2O–NaCl–$CaCl_2$ fluid inclusions based on microthermometric and microanalytical data. Geochimica et Cosmochimica Acta 75, 21–40.

Stefánsson, A., Hilton, D.R., Sveinbjörnsdóttir, Á.E., Torssander, P., Heinemeier, J., Barnes, J.D., Ono, S., Halldórsson, S.A., Fiebig, J., Arnórsson, S., 2017. Isotope systematics of Icelandic thermal fluids. Journal of Volcanology and Geothermal Research 337, 146–164.

Strugale, M., Cartwright, J., 2022. Tectono-stratigraphic evolution of the rift and post-rift systems in the Northern Campos Basin, offshore Brazil. Basin Research 34 (5), 1655-1687.

Teboul, P.A., Durlet, C., Girard, J.P., Dubois, L., San Miguel, G., Virgone, A., Gaucher, E.C., Camoin, G., 2019. Diversity and origin of quartz cements in continental carbonates: Example from the Lower Cretaceous rift deposits of the South Atlantic margin. Applied Geochemistry 100, 22–41.

Teixeira, J.B.G., Misi, A., Silva, M.G., 2007. Supercontinent evolution and the Proterozoic metallogeny of South America. Gondwana Research 11, 346–361.

Teixeira, J.B.G., da Silva, M.D.G., Misi, A., Cruz, S.C.P., da Silva Sá, J.H., 2010. Geotectonic setting and metallogeny of the northern São Francisco craton, Bahia, Brazil. Journal of South American Earth Sciences 30, 71– 83.

Temovski, M., Rinyu, L., Futó, I., Molnár, K., Túri, M., Demény, A., Otoničar, B., Dublyansky, Y., Audra, P., Polyak, V., Asmerom, Y., Palcsu, L., 2022. Combined use of conventional and clumped carbonate stable isotopes to identify hydrothermal isotopic alteration in cave walls. Scientific Reports 12, 9202.

Trice, R., 2005. Challenges and insights in optimising oil production form Middle Eastern karst reservoirs. In: SPE Middle East Oil and Gas Show and Conference, Kingdom of Bahrain, March 2005, SPE-93679-MS.

Trindade, R.I.F., D'Agrella-Filho, M., Babinski, M., Neves, B.B., 2004. Paleomagnetism and geochronology of the Bebedouro cap carbonate: evidence for continental scale Cambrian remagnetization in the São Francisco Craton, Brazil. Precambrian Research 128, 83-103.

Tsykin, R.A., 1989. Paleokarst of the Union of Soviet Socialistic Republics. In: Bosák, P., Ford, D.C., Głazek, J., Horáček, I. (Eds.), Paleokarst: A Systematic and Regional Review. Vidala Academia, Praha, 253–295.

van den Boorn, S.H.J.M., van Bergen, M.J., Vroon, P.Z., de Vries, S.T., Nijman, W., 2010. Silicon isotope and trace element constraints on the origin of ∼3.5 Ga cherts: Implications for Earth Archaean marine environments. Geochimica et Cosmochimica Acta 74, 1077-1103.

Wei, D., Gao, Z., Fan, T., Niu, Y., Guo, R., 2021. Volcanic events-related hydrothermal dolomitisation and silicification controlled by intra-cratonic strike-slip fault systems: Insights from the northern slope of the Tazhong Uplift, Tarim Basin, China. Basin Research 33, 2411–2434.

Wray, R. A., Sauro, F., 2017. An updated global review of solutional weathering processes and forms in quartz sandstones and quartzites. Earth-Science Reviews 171, 520-557.

You, D., Han, J., Hu, W., Qian, Y., Chen, Q., Xi, B., Ma, H., 2018. Characteristics and formation mechanisms of silicified carbonate reservoirs in well SN4 of the Tarim Basin. Energy Exploration and Exploitation 36, 820–849.

Zhang, R., 1986. Sulfur Isotopes and Pyrite-Anhydrite Equilibria in a Volcanic Basin Hydrothermal System of the Middle to Lower Yangtze River Valley. Economic Geology 81, 32-45.

Zhou, X., Chen, D., Qing, H., Qian, Y., Wang, D., 2014. Submarine silica-rich hydrothermal activity during the earliest Cambrian in the Tarim basin, northwest China. International Geology Reviews 56, 1906–1918.

4. Conclusions

4.1. Concluding remarks and implications

The main outcomes of this research and their implications to geofluids management and karstification are synthesized below. The concluding remarks are presented in two separated chapters dealing with the research lines that were carried out during the PhD project.

4.1.1. Section 1: Hypogene dissolution in fractured and folded carbonates

We have studied two different settings of deformed carbonate units where hypogene speleogenesis produced networks of solutional conduits: i) the Majella Massif (chapter 2.1.) and ii) the Irecê and Una-Utinga basins in the São Francisco Craton (Brazil) (chapter 2.2.). The major conclusions of the research can be summarized in the following points:

- In tight carbonates with low primary porosity and permeability, fracture networks are the main controlling elements for flow pathways and dissolution. Fractures as joints and veins are highly corroded and the main persistent deformation zones (e.g., fracture clusters, fracture corridors) control the orientation and the spatial distribution of solutional conduit development.
- In the Majella Massif fault zones consist of barrier-conduit structures with high-permeability domains localized in the pervasively fractured damage zones and along slip surfaces. On the contrary, fault cores characterized by recrystallization and/or cataclastic processes act as low-permeability domains (barriers) for fluid flow, whereas fault cores with pervasive fragmentation or composite chaotic breccia (reactivation of inherited cataclastic fabric) may enhance porosity and act as conduits for fluid flow. Deep-rooted and sub-vertical strike-slip faults (associated with the early orogenic phase) channelized the ascending hypogenic solutions from depth. The damage zones of the wider faults, with through-going fracture clusters or completely fragmented textures formed high-permeability domains for fault-parallel flow. Linkage and intersection of these faults by splay fracture systems and pre-orogenic normal faults permitted ascending fluids to reach multiple recharge points (feeders) of the karst system.

- In the São Francisco Craton (Brazil), vast hypogene caves are mainly developed following fracture corridors along orthogonal fold hinges and fault zones. Feeders and high dissolution zones are located at the intersection of different sets of fractures. Fracture corridors are formed along fold hinges related to two different contractional events associated with the Brasiliano orogeny. They are formed also in gentle folds with a bedding dip of less than ~10°.
- The vertical profile of the cave passages shows an ellipsoidal shape/geometry due to the textural variation that provides different karstification levels. Almost pure carbonate layers with low content of detrital minerals and high content of pyrite are more karstified and acted as preferential horizontal flow paths for rising fluids (e.g., thanks to oxidation of pyrite boosting acidification). On the other hand, carbonate layers with a coarser grain size and higher detrital minerals content (e.g., marly limestones) hindered the karstification. These layers often acted as seals/buffers to rising fluid flow.
- Rising hypogenic solutions interacted with the shallower aquifers with lateral flow and dissolution focused along bedding interfaces and through-going fracture cluster zones/fracture corridors following anticline hinges. The localization of deformation in through-going structures, rather than background (strata bound) fractures, exerts the main control on flow pathways and dissolution. Our results in both study areas suggest that hinge-related deformation zones in folded carbonates may represent a potential driver for lateral migration of hypogenic fluids and karstification, which can be inferred from maximum curvature maps and seismic profiles.
- The exhaustive interpretation of cave morphologies has proven to be an invaluable tool that must be accompanied by comprehensive structural, geological, and petrographic observations. The spatial-morphological patterns of the cave systems reflect the hydro-dynamic setting involved, the configuration of the fracture network, and the evolution of the landscape. Sulfuric acid speleogenesis driven by ascending H_2S-rich fluids in a highly faulted setting resulted in a sub-horizontal karst system with gentle variations in altitude and an angular pattern of master conduits, reflecting the evolving position of the water table (e.g., as a consequence of uplift). In the presence of multiple intersecting fault systems, various sub-vertical karst channels acting as discharge feeders can be expected. On the contrary, hypogene dissolution linked to rising hydrothermal fluids in the Irecê and Una-Utinga Basins, affected by multi-phase folding events, generated maze networks of interconnected

conduits following the most persistent and deep-rooted fracture systems associated with fault zones and hinge-related deformation (e.g., fracture corridors).

- Sub-seismic flow pathways and hypogene karst conduit development in deformed geological settings can be inferred by accurate structural analysis. Anticline hinge-related deformation and deep-rooted fault zones proved to be primary controlling elements for the development of hypogene void-conduit systems. Independently from the overall tectonic setting, the structural and karstic events documented in the two study areas can be applicable to other faulted and folded carbonate reservoirs or geothermal fields characterized by hypogene processes. Scaling-laws and models to quantify the intensity, distribution and persistence of fractures associated to fault growth mechanisms and folding are needed to predict the hydraulic conductivity of deformation zones in such reservoirs. These models could be used to infer the potential occurrence of hypogene cavernous voids in the subsurface and their spatial organization.

4.1.2. Section 2: Hydrothermal silicification, silica dissolution, and hypogene speleogenesis in mixed carbonates-siliciclastic

We studied a mixed carbonate-siliciclastic Neoproterozoic sequence affected by silicification hosting a km-long cave (Calixto Cave; chapters 3.1. and 3.2.). The main conclusions of the study can be summarized in the following points:

- Geomorphological, mineralogical, and geochemical ($\delta^{30}Si$ - $\delta^{18}O$) features suggest a multi-stage history of dissolution-precipitation in the Neoproterozoic sequence. The early stages are related to hypogene (hydrothermal) processes.
- Early diagenetic silicification caused by mixing of Neoproterozoic pore (sea)water and low temperature hydrothermal fluids (T = ca. 50-100 °C), sourced from buried quartzite units, led to the replacement of the carbonate constituents with microcrystalline quartz, forming silicified cherty carbonates with up to 80-85 wt.% of SiO_2 content. Brittle deformation is localized in chert nodules, causing a high intensity of open-mode fractures that contributed to high permeability and conductivity.
- Alkaline, high temperature and high salinity hydrothermal fluids caused silica dissolution followed by chalcedony and quartz re-precipitation at minimum formation temperatures of 165-210 °C. Silica dissolution and karstification are manifested by widespread solutional features at the µm- to cm-scale, as well as the alteration in the $\delta^{30}Si$ and $\delta^{18}O$ isotopic

composition of the pristine host rock. Highly silicified carbonate layers in the sequence have porosities up to 16% and permeability up to 250 mD. EPM permeability combining the effect of fractures and matrix components in the silicified (chert) unit is 2 to 3 orders of magnitude higher than the heterolithic and carbonate units. Abundant mineral inclusions in quartz are compatible with the hydrothermal genesis. Alteration and dissolution of the chert unit produced cavernous and high-permeability zones that contributed to the localization of late-stage speleogenetic processes.

- Late-stage processes in deep-seated conditions involved hypogene speleogenesis producing macro-scale karst conduits organized in a 3D multistorey system that reflects the structural and stratigraphic variability in the layered sequence. Through-going fracture zones and faults in the lower sector of the cave focused rising fluids along vertical permeability pathways. Sedimentary units composed of heteroliths, marly dolostones, and fine-grained siliciclastic rocks represent a low-permeability seal/buffer unit that stopped/buffered vertical fluid flow. The silicified and high-permeability layers favored lateral migration of the fluids in the middle storey of the cave. Through-going fracture zones locally breached these units, allowing vertical discharge and providing interconnectivity among the different sedimentary units. After the exhumation of the sedimentary sequence, supergene and epigene karst processes, as well as gravitational collapses, further amplified the cave conduit dimensions.
- Early silica dissolution promoted by high temperature and alkaline conditions led to the formation of a stratigraphically-controlled inception horizon in the silicified carbonates of the middle storey of the cave. The main karstification phase was due to multiple alternating silica- and carbonate-dominant dissolution phases driven by hydrothermal solutions, as well as the precipitation of chalcedony and quartz filling pore space and fractures. Hydrothermal silicification and hypogene dissolution may be typical of mixed sedimentary sequences with buried sources of Si-rich thermal fluids (e.g., deep basinal fluids interacting with quartzites or quartz-arenitic units). Karstification in hypogene setting to produce the main macro-scale void-conduit systems must have been the result of prolonged dissolution in confined settings, with formation of a three-dimensional pattern of conduits controlled by the main lateral and vertical heterogeneity in distribution of flow-conducting fractures.
- Silica paragenesis was accurately characterized by the combined use of petrography, SEM-EDS, microthermometry, and $\delta^{30}Si$ - $\delta^{18}O$ stable isotope analyses. Cavernous voids and high-permeability zones localized in the silicified layers present close similarities with solutional

void-conduit features found in many silicified/chert reservoirs worldwide. The documented dissolution and reprecipitation of silica in Calixto Cave demonstrate the role of hypogene (hydrothermal) processes that drastically modified the petrophysical properties of host rocks considered to have very low solubility at typical shallow or near-surface conditions. Such peculiar and underestimated process may have important implications for the development of highly porous chert/silicified unconventional reservoirs. Our findings may shed new light on the process of hydrothermal silicification and high permeability zones development in many of these poorly studied reservoirs.

- Enhanced porosity and permeability caused by hypogene silica dissolution and the mechanical behavior of stiff chert nodules (localizing deformation) are efficient processes that can lead to stratigraphically controlled super-permeability (super-K) zones in silicified/chert reservoirs. Such super-K zones may be characteristic of deep reservoirs within hydrothermally altered carbonates thanks to rising high temperature aqueous solutions along through-going fracture zones or faults. Major 3D conduit networks can be expected, with the main sub-vertical channels that are guided by fractures, and the main sub-horizontal conduits guided by the interplay between super-K units confined by low-K seal/buffer layers (even with sub-seismic thickness).

4.2. Suggestions for future research

The conceptual geological models obtained within this research are first-order tools that can be used in the applied industrial geofluid sector (e.g., hydrocarbon and geothermal reservoirs, aquifers, ore deposits, CO_2 injection and storage, etc.) to predict the spatial-morphological organization of hypogene karst features in carbonate, silicified, and mixed sequences. However, the integration of such results in quantitative models is still lacking and a daunting task.

The integration of karstification effects on fracture enlargement and transmissivity in deterministic or stochastic discrete fracture network (DFN) models is still an under-investigated topic. In fact, enlargement of fracture aperture due to karst dissolution might increase the network transmissivities by several orders of magnitude, greatly impacting fluid flow properties and reservoir productivity (Bourdon et al., 2004). Despite their relevance in the hydrocarbon and geothermal industry, karstic features are currently largely ignored in the development of reservoir models due to the complexity and variability of their geometries (Burchette, 2012), causing considerable uncertainty in predictive models (Medekenova and Jones, 2014).

Attempts to fill this knowledge gap have been proposed recently by Lopes et al. (2022), with the computation of DFN+K (karst) models. Despite their innovative approach, such models are only referred to a 2D space, and they lack in evaluating the real complexity of void-conduit spatial organization in relation to hypogene solutional mechanisms. Given the 3D nature of Calixto Cave, and the presence of multiple lithologies, from pure carbonates to heteroliths and silicified cherty carbonates, we believe that our results may be of interest to expand the current input of DFN+K models based on a real sub-seismic hypogene cave-analogue scenario with both fracture- and stratigraphic- controlled karst features.

Furthermore, future research should be pointed towards the study and comparison of other (potential) hypogene caves developed in association with silicified/chert lithotypes to unravel similarities or differences in the diagenetic and speleogenetic history that affected the Calixto Cave. The use of combined $\delta^{30}Si$ and $\delta^{18}O$ isotopes on chert and quartz samples, here used for the first time to unravel the possible effect of (karstic) alteration in a hypogene system, may be used to trace dissolution-precipitation patterns in other settings, especially in unconventional silicified reservoirs such as the recently discovered pre-Salt fields of Africa (Teboul et al. 2017, 2019) and Brazil (Lima and De Ros, 2019; Lima et al., 2020).

References

Bourdon, L., Coca, S., Alessio, L., 2004. Karst Identification and Impact on Development Plan. SPE Asia Pacific Oil and Gas Conference and Exhibition, Perth, Australia, October 2004.

Burchette, T.P., 2012. Carbonate rocks and petroleum reservoirs: a geological perspective from the industry. Geological Society of London Special Publication 370, 17–37.

Lima, B.E.M., De Ros, L.F., 2019. Deposition, diagenetic and hydrothermal processes in the Aptian Pre-Salt lacustrine carbonate reservoirs of the northern Campos Basin, offshore Brazil. Sediment. Geol. 383, 55–81.

Lima, B.E.M., Tedeschi, L.R., Pestilho, A.L.S., Santos, R.V., Vazquez, J.C., Guzzo, J.V.P., De Ros, L.F., 2020. Deep-burial hydrothermal alteration of the Pre-Salt carbonate reservoirs from northern Campos Basin, offshore Brazil: Evidence from petrography, fluid inclusions, Sr, C and O isotopes. Mar. Pet. Geol. 113, 104143.

Lopes, J.A.G., Medeiros, W.E., La Bruna, V., de Lima, A., Bezerra, F.H.R., Schiozer, D.J., 2022. Advancements towards DFKN modelling: Incorporating fracture enlargement resulting from karstic dissolution in discrete fracture networks. J. Pet. Sci. Eng. 209, 109944.

Medekenova, A., Jones, G.D., 2014. Characterization and Modeling Challenges Associated with Fracture and Karst (Non-Matrix) in the Margin Area of a Carbonate Reservoir. SPE Annual Caspian Technical Conference and Exhibition, Astana, Kazakhstan, November 2014.

Teboul, P.A., Kluska, J.M., Marty, N.C.M., Debure, M., Durlet, C., Virgone, A., Gaucher, E.C., 2017. Volcanic rock alterations of the Kwanza Basin, offshore Angola - insights from an integrated petrological, geochemical and numerical approach. Mar. Pet. Geol. 80, 394–411.

Teboul, P.A., Durlet, C., Girard, J.P., Dubois, L., San Miguel, G., Virgone, A., Gaucher, E.C., Camoin, G., 2019. Diversity and origin of quartz cements in continental carbonates: Example from the Lower Cretaceous rift deposits of the South Atlantic margin. Applied Geochemistry 100, 22–41.

Appendices

Appendix A: supplementary materials of chapter 2.1.

Bitumen-impregnated speleothems in the Cavallone-Bove cave system

Speleothems with a blackish or dark-brown color are common in the entire Cavallone-Bove cave system, especially in association with fault damage zones. They usually occur in close association with active percolation of black viscous materials, at a first sight hypothesized to be tar or bitumen (Fig. A1). Two representative samples of carbonaceous material from a blackish calcite speleothem collected in Bove Cave and a limestone from Bolognano Fm have been characterized at the University of Almería to unravel their nature and origin.

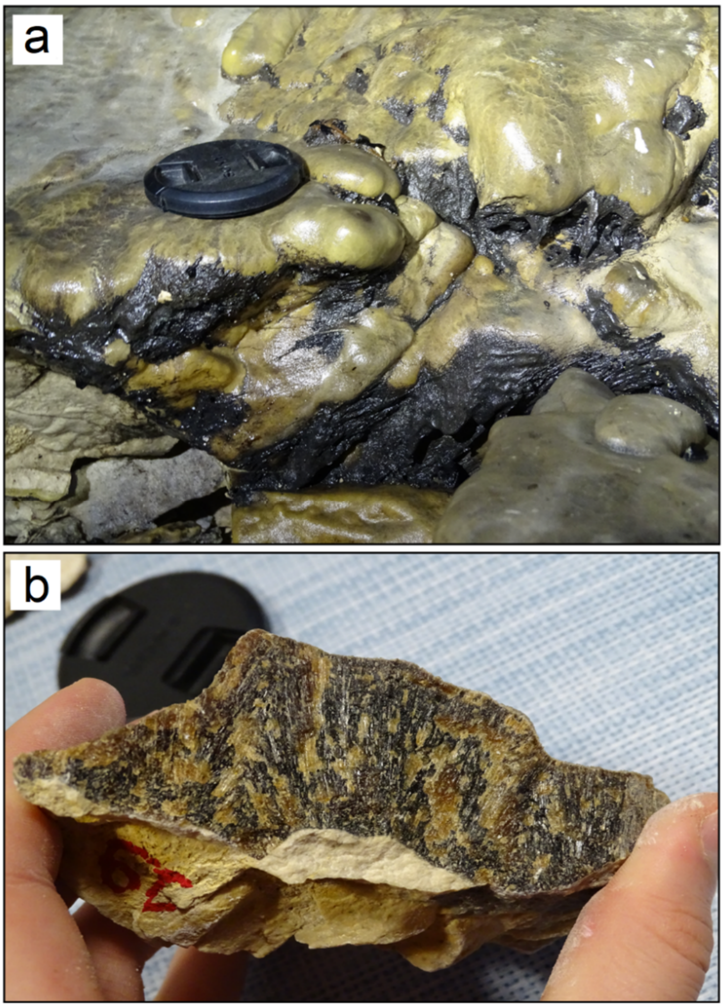

Figure A1. a) speleothem in the Bove cave with active percolation of a black organic viscous material; b) section of a broken speleothem. Note the blackish/dark brownish color of the calcite crystals.

Fourier-transform infrared spectroscopy (FTIR) and $\delta^{13}C$ (‰ V-PDB) analyses were carried out after a HCl treatment to remove the lithic material and leave only the organic carbon, using the procedures described in Gazquez et al. (2012).

The organic matter was isolated from the powdered samples using a separation method based on acid digestion. Five grams for each sample reacted with excess HCl (12 M) over 24 hours at ambient temperature, maintaining an acid pH in the solution. The solutions were neutralized with NaOH (1 M) and centrifuged; then, the residues were rinsed several times in distilled water and dried.

For $\delta^{13}C$ analyses, a combustion module (CM) coupled to a CRDS System (G2201-i Analyzer, Picarro) was used. Powdered samples collected in tin capsules (~1.25 mg) were loaded into the CM by an autosampler (Costech Analytical Technologies, Valencia, CA, US), achieving complete combustion at 1200 °C. The released CO_2 passed through a water filter, a GC column and then transferred to a Picarro Liaiso A0301 interface. The system assembly uses ultra-high purity (UHP) N_2 as the carrier gas and pure O_2 for combustion. Four replicates per sample were analyzed and the mean $\delta^{13}C$ isotope values were reported in the Vienna PeeDee Belemnite (V-PDB) standard notation.

For the FTRIR analyses, measurements were obtained using a BRUKER Raman-FTIR instrument (model Vertex 70) equipped with a DLATGS detector and a Michelson interferometer (model RocksolidTM at 60°). FTIR measurements have a spectral resolution of 0.4 cm^{-1}.

Most of the FTIR spectra for the analyzed samples (Fig. A2 and A3) are consistent with the typical FTIR absorption signals of bitumen (Weigel and Stephan, 2018).

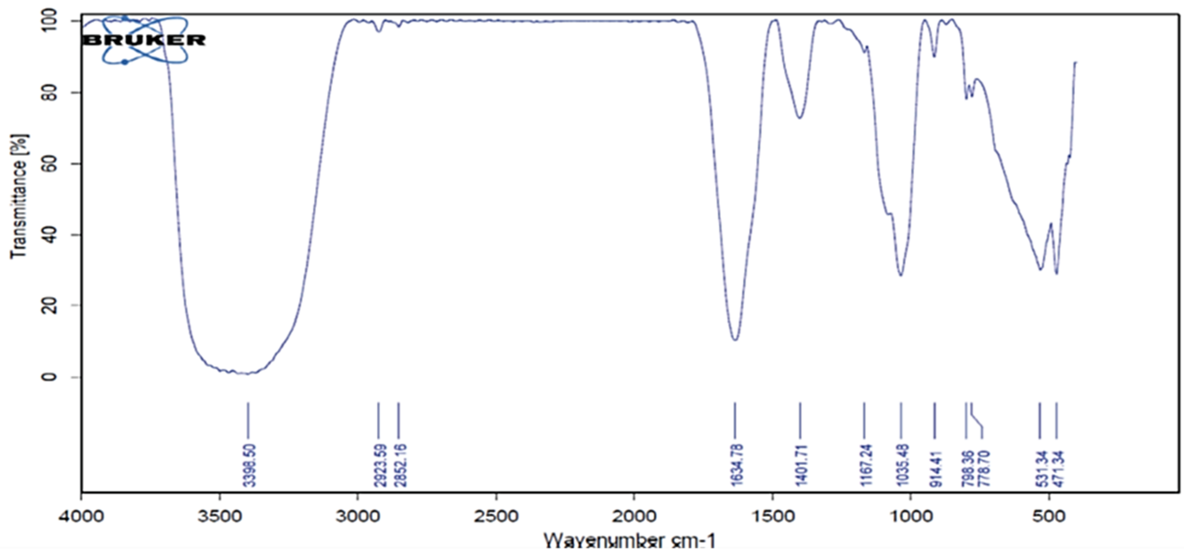

Figure A2. FTIR spectra of the HCl-treated limestone sample from Bolognano Fm.

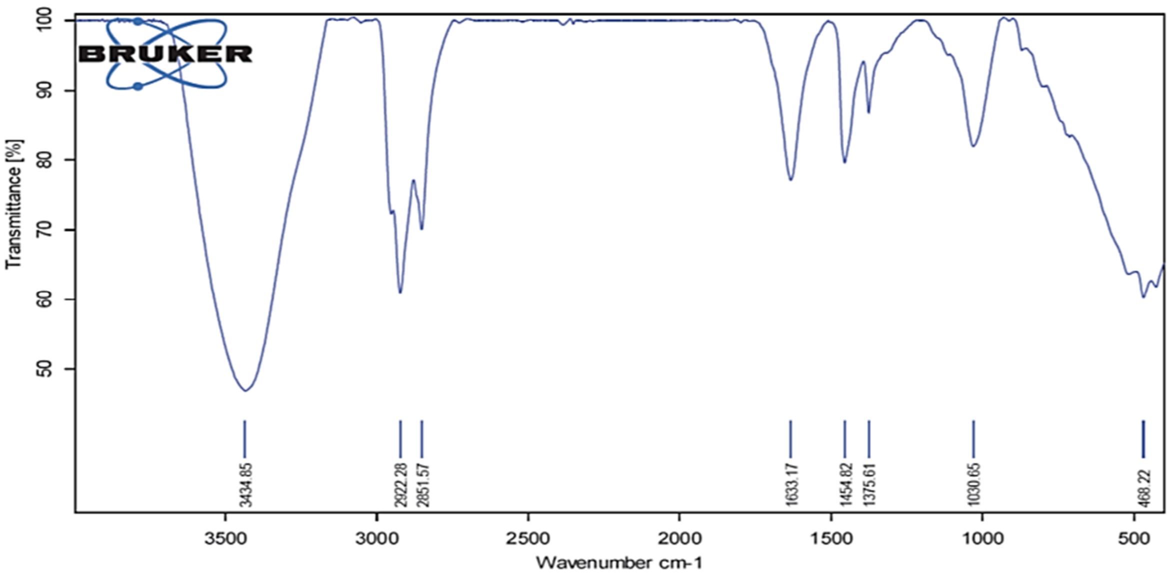

Figure A3. FTIR spectra of the HCl-treated speleothem sample.

The broad peak present in both spectra and centered at around 3350-3450 cm^{-1} is typical of the stretching vibration of the O-H bond in water. Characteristic signals of organic compounds, such as those at 2923 cm^{-1}, 2851-2852 cm^{-1}, and around 1350-1450 cm^{-1} relate to stretching and bending vibrations of the C-H bonds in aliphatic CH_2 and CH_3 organic compounds (Gazquez et al., 2012; Weigel and Stephan, 2018). The strong peaks at around 1633-1634 cm^{-1} could be attributed to C-C stretching vibration of aromatic compounds, whereas the ones at 1030-1035 cm^{-1} indicate stretching S-O bonds. Disulfides and polysulfides S-S stretching vibrations are also indicated by several absorption peaks in the region between 430 and 530 cm^{-1} (Weigel and Stephan, 2018; Nandiyanto et al., 2019). The peaks at 914, 778 and 798 cm^{-1}, represented only in the bitumen sample (Fig. A2) are typical of C-H bending vibrations in aromatic compounds (Nandiyanto et al., 2019).

The characteristic bitumen peaks in both FTIR spectra, combined with the similar $\delta^{13}C$ isotopic composition of the analyzed materials (Table A1), suggest that the black-impregnated speleothems found in the Cavallone-Bove cave system are related to the entrapment of organic compounds (mostly bitumen) that is commonly found as accumulation within the Bolognano Fm carbonates in the Majella Massif (Lipparini et al., 2018).

Table A1. Carbon ($\delta^{13}C$) stable isotope composition of analyzed samples. Values of limestones from Santo Spirito Fm and Bolognano Fm are also reported for comparison (data from Auer et al. 2015, Cornacchia et al., 2018).

Samples	**$\delta^{13}C_{V-PDB}$**
Bitumen in Bolognano Fm	-28.81 ± 0.01 ‰
Organic matter in the speleothem	-27.69 ± 0.12 ‰
Santo Spirito Fm limestones (from literature)	-1 to 2 ‰
Bolognano Fm limestones (from literature)	0.5 to 2 ‰

Appendix B: supplementary materials of chapter 3.1.

EPM (Equivalent Porous Media) calculations

From Darcy's law, given that:

$$Q = -K \frac{dH}{dL} A$$

We applied the parallel-plate model (Taylor et al., 1999) for modeling discharge in single isolated fractures. The fracture is approximated as having sub-parallel walls. Q_f is the volumetric flow rate, w the fracture width perpendicular to the flow direction, dH/dL is the head gradient along which the flow takes place, and b is the hydraulic aperture (calculated considering the effect of fracture roughness, see chapter 3.1.3.2.).

$$Q_f = \frac{b^3 \rho g}{12\mu} \left(\frac{dH}{dL}\right) w$$

This relationship, commonly referred to as the "cubic law for joint flow", results in:

$$K_f = \frac{b^2}{12}$$

To approximate the material as an Equivalent Porous Media (EPM), we modelled an elementary cubic volume of 1 m^3 (W=1 m) combining the discharge related to both matrix (K_m) and fracture (K_f) permeability. In this model, fractures sets are approximated to be normal to bedding, and bedding is sub-horizontal.

Two values of EPM permeability were computed, considering two end-members where flow is exactly parallel to the main fracture sets (K_P) or normal to the main fracture sets (K_N).

$$K_P = \sum_{i=1}^{n} \frac{K_i d_i}{W}$$

$$K_N = \frac{W}{\sum_{i=1}^{n} \frac{d_i}{K_i}}$$

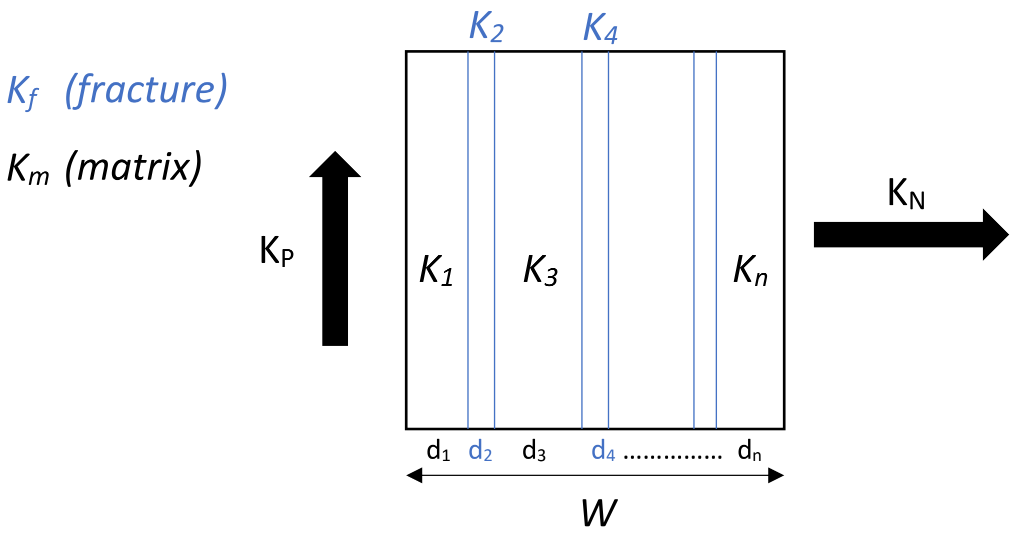

Figure B1. schematized bi-dimensional diagram illustrating the elements used for the calculations.

Where K_i is the contribution to permeability deriving from each individual element in the cell (see the Fig. B1 for a graphic illustration). For fractures, K_i is calculated from the equation of K_f and the number of fractures n depends on fracture set spacing. For matrix permeability contribution, it is extracted from rock plugs petrophysical properties calculations (see chapter 3.1.4.4. in the full article). Bedding-normal (vertical) matrix permeability was used for calculations of K_P, and bedding-parallel (horizontal) matrix permeability was used for calculation of K_N. d_i is the width of each element (for fractures we used the mean hydraulic aperture of each set).

Appendix C: supplementary materials of chapter 3.2.

Cryogenic Raman spectroscopy

Cryogenic Raman spectroscopy was used to evaluate the possible presence of dissolved salts in primary fluid inclusions. After freezing the sample, Raman spectra were acquired at -170 °C, -100 °C, and at any observed phase transitions (Fig. C1) in order to detect the presence of ice, hydrohalite and salts in the spectral range of 2700 to 3550 cm^{-1} (Samson and Walker, 2000; Bakker, 2004; Baumgartner and Bakker, 2010). Spectra with well-defined hydrate peaks at low temperatures (-170 °C) could not have been obtained even using slow cooling rates of 10–15 °C/min (Bakker, 2004), also after thawing and re-freezing the inclusions (Samson and Walker, 2000). In such conditions, the spectra were marked by intense background noise. Every analyzed inclusion showed a main peak generally occurring between 3107 and 3118 cm^{-1} (interpreted as ice) and a weak to intense broad peak, centered at approximately 3430 to 3450 cm^{-1}. Sometimes, a broad bulge has been observed at ca. 3300–3320 cm^{-1} that could be attributed to the formation of amorphous ice (Klug et al. 1987, Tulk et al. 1998; Samson and Walker, 2000). With a fast optical comparison with the spectra reported in Samson and Walker (2000), these broad peaks likely indicate the presence of a mixture of frozen H_2O, NaCl hydrate (hydrohalite), and $CaCl_2$ hexahydrate (antarcticite). Alternatively, the broad peak at 3430–3450 cm^{-1} may represent O–H stretching vibrations of liquid H_2O, which generally form a broad asymmetrical peak centered at ca. 3450 cm^{-1} (Walrafen 1964, 1972; Bakker, 2004). With increasing salinity, the shape of this band becomes more symmetric but remains centered at ca 3450 cm^{-1} as the intensities of the lower-frequency peaks diminish (Walrafen 1962, Mernagh and Wilde 1989).

The position and shape of the broad band in our spectra acquired at -170 °C is, therefore, more consistent with the presence of a mixture of not-perfectly formed hydrate crystals, rather than an aqueous solution. Other broad peaks typical of ice (at ca. 3090 cm^{-1} and 3250 cm^{-1}) were sometimes observed, whereas the peak of hydrohalite (3536 cm^{-1}) was rarely present. At the measured first melting temperatures (-52 °C to -47 °C), the position of the main peak of ice shifted towards higher values (cf. Dubessy et al., 1982; Bakker, 2004) and only one well-defined peak was observed. This is likely related to a mixture of small hydrohalite crystals (band centered at ca. 3428 cm^{-1}). Spectra acquired after slow heating above the intermediate melting temperature (-26 °C in the example of Fig. C1) are characterized by the disappearance of the hydrohalite peaks and the shift of the ice peak towards progressively higher values. The final ice melting (T_m) occurred between -26 °C and -23 °C.

In Raman spectra it was reflected by the disappearance of the ice peak and the very broad and asymmetric water peak in the range of 3400–3500 cm^{-1}.

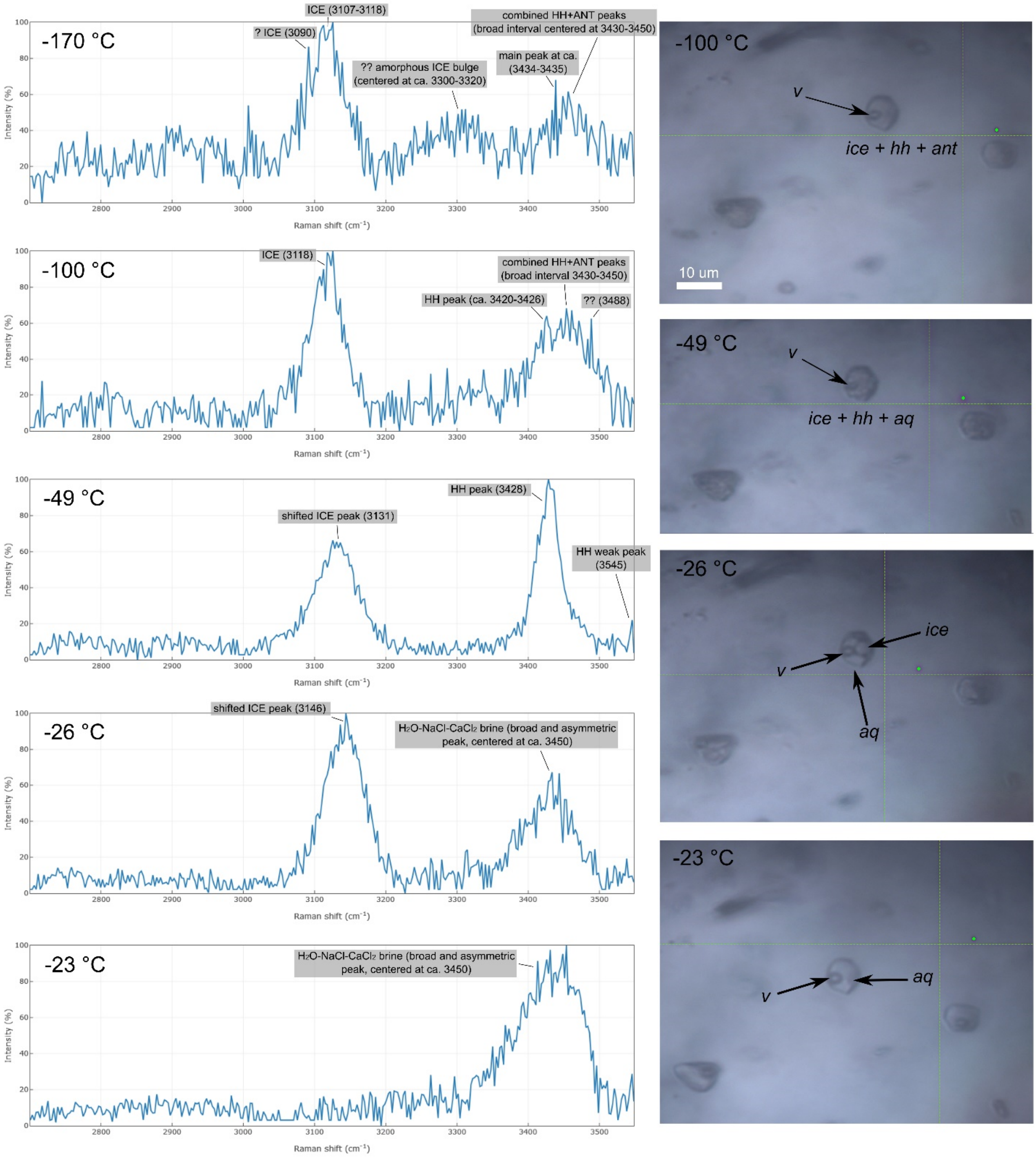

Figure C1. Sequence of normalized Raman spectra in the range of 2700 to 3550 cm^{-1} acquired during heating from -170 to -23°C of a primary inclusion (sample CARB-1094A.5). Labels explanation: HH=hydrohalite, ANT=antarcticite, aq=aqueous solution, v=vapor.

Stable isotope modelling

Stable isotopes modelling approaches (Stefánsson et al., 2017, and references therein) are common proxies to assess the origin of fluids, chemical reactions, and associated isotope fractionation for various processes in the Earth's crust. An open system-type Rayleigh model, where the back reaction is considered non-reactive, was assumed for the simulation of quartz precipitation upon cooling/boiling of hydrothermal fluids, burial diagenesis at different temperatures, and fluid mixing. We calculated Rayleigh distillation curves for: 1) precipitation of quartz upon boiling and cooling of hydrothermal fluids, 2) assuming direct quartz precipitation from pore (sea)water during burial diagenesis, and 3) quartz precipitation resulting from fluid mixing between hydrothermal fluids and seawater to assess the change in δ^{30}Si and δ^{18}O of aqueous (H_4SiO_4, H_2O) and solid species (quartz) as a function of reaction progress in the temperature range of 30-300°C (see Table S3 in the Supplementary Materials online for an editable *Excel* spreadsheet).

The initial hydrothermal fluid composition was approximated by a solution that had equilibrated at 300°C with the basement quartzites of the Chapada Diamantina Group (δ^{30}Si = 0.24 ± 0.13‰ and δ^{18}O = 13.68 ± 0.07‰). The resulting initial δ^{30}Si and δ^{18}O values of the Si-rich hydrothermal fluid were -0.21‰ and 6.44‰, respectively.

For the initial composition of ancient Neoproterozoic seawater, an average δ^{30}Si composition was extracted from the list of the Neoproterozoic chert samples reported in the extensive review by Robert and Chaussidon (2006), assuming the criteria that cherts with a δ^{18}O value satisfying the equation $\delta^{18}O_{KL} < \delta^{18}O < \delta^{18}O_{KL}$-6‰ (see Knauth and Lowe, 1978, Robert and Chaussidon, 2006 and Marin-Carbonne et al., 2014 for further discussions), preserve the original isotopic δ^{30}Si composition of the solution from where they precipitated (Table S3). For the δ^{18}O composition, we assumed the estimated value of pre-Cambrian oceanic water (-1‰) reported in Marin-Carbonne et al. (2014) and Kleine et al. (2018), based on the works of Gregory (1991) and Holmden and Muehlenbachs (1993).

The fractionation factors used in the modeling calculations for δ^{30}Si and δ^{18}O are based on fitting reported equilibrium fractionation factors to a smooth temperature function (following the methods described in Kleine et al., 2018; Fig. C2). Best fits equations for the fractionation curves between mineral and fluid for silicon and oxygen isotopes are summarized in Table C1.

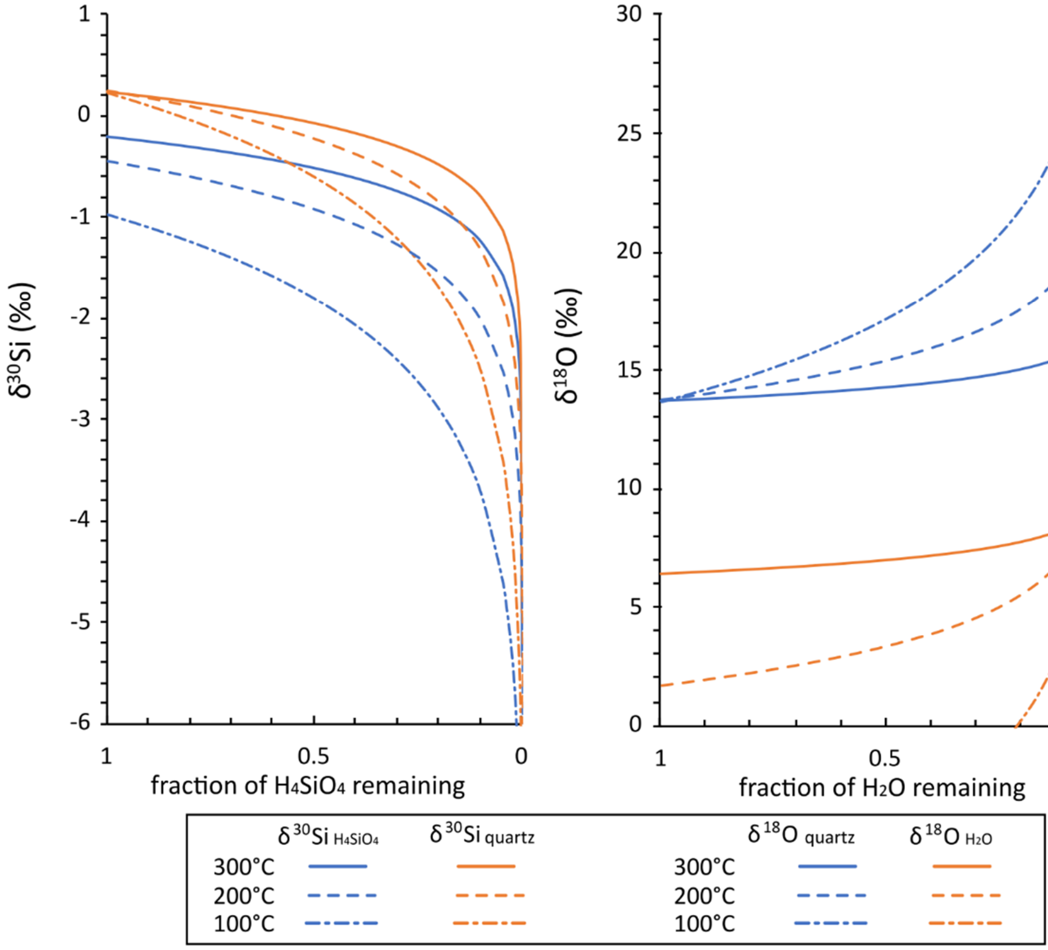

Figure C2. Rayleigh fractionation model simulating the $\delta^{30}Si$ and $\delta^{18}O$ systematics between quartz and the H_4SiO_4 and $H_2O(lq)$ fluid species calculated at different temperatures upon quartz precipitation from a boiling/cooling hydrothermal fluid.

Table C1. Best fit fractionation curves and associated references used in the isotope modelling.

Reaction	T range (°C)	$10^3\ln\alpha$ (best fit fractionation curve)	References
$\delta^{30}Si$			
quartz-H_4SiO_4	0 - ∞	$0.005\times(10^6/T^2)^2+0.132\times(10^6/T^2)$	Kleine et al. (2018) based on Dupuis et al. (2015), Pollington et al. (2016)
$\delta^{18}O$			
quartz-H_2O	0 - 1000	$0.377-3.48\times10^3/T+4.25\times10^6/T^2$	Kleine et al. (2018) based on Clayton et al. (1972); Bottinga and Javoy (1973); Clayton et al. (1989); Ligang et al. (1989); Hu and Clayton (2003)
$H_2O(v)$-$H_2O(lq)$	0-374	$7.685-6.7123\times10^3/T+1.6664\times10^6/T^2-0.35041\times10^9/T^3$	Horita and Wesolowski (1994)

Multi-scale representative solutional features in the silicified carbonates

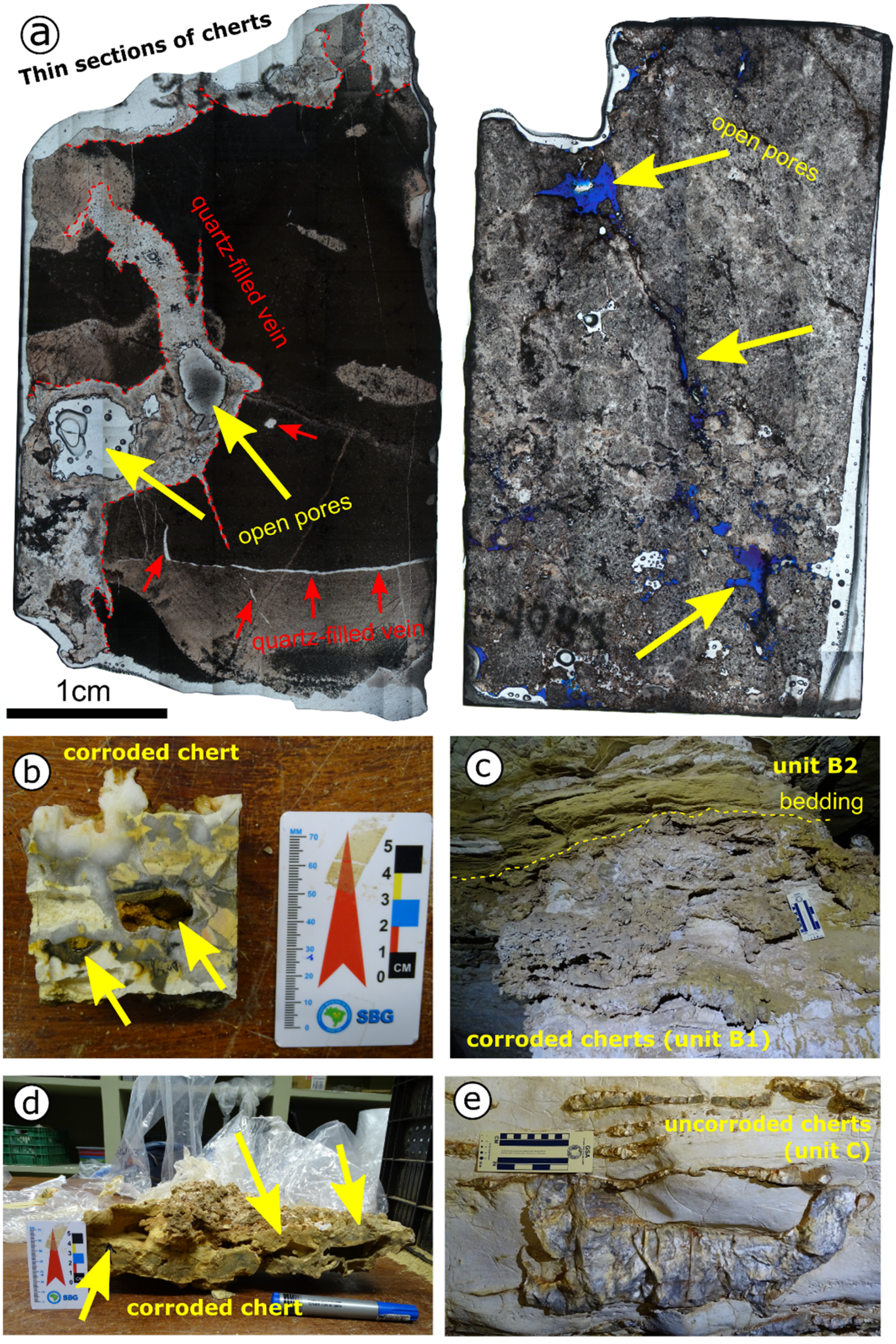

Figure C3. a) thin sections with high solutional porosity. Open pore space is pointed by yellow arrows; red arrows indicate quartz/chalcedony-filled veins; b) hand-sample of a corroded silicified dolostone *collected in the middle storey unit B2; c) example of dissolution features characterizing the irregular, corroded and "spongy" texture of the cherts in unit B2, middle storey; d) example of a representative corroded chert layer collected in the unit B2; e) example of uncorroded chert nodules in the upper unit C.*

Full dataset of the microthermometric measurements

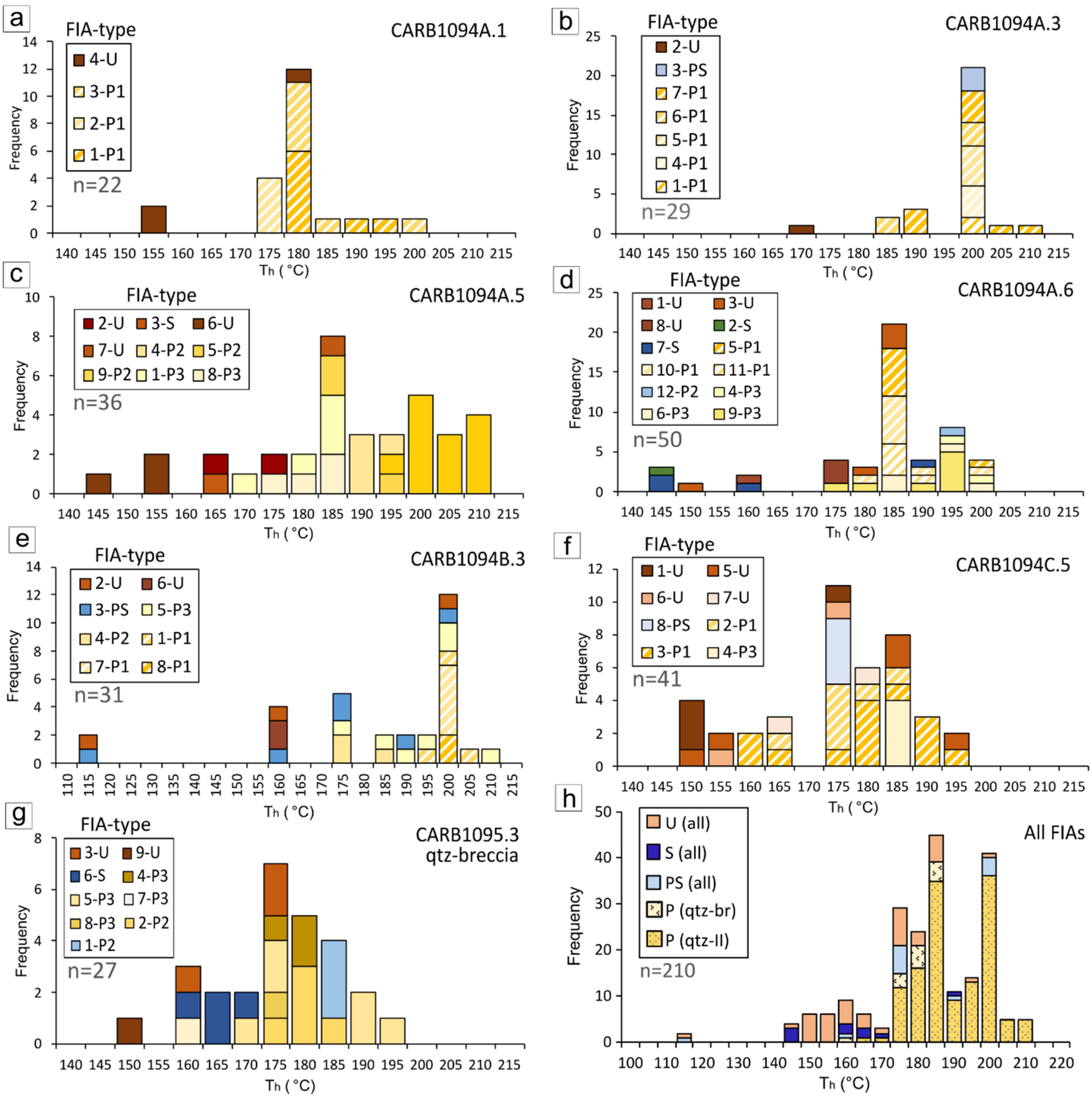

Figure C4. Full T_h data of the analyzed FIAs. Panel 'h' shows the cumulative frequency histogram of the dataset.

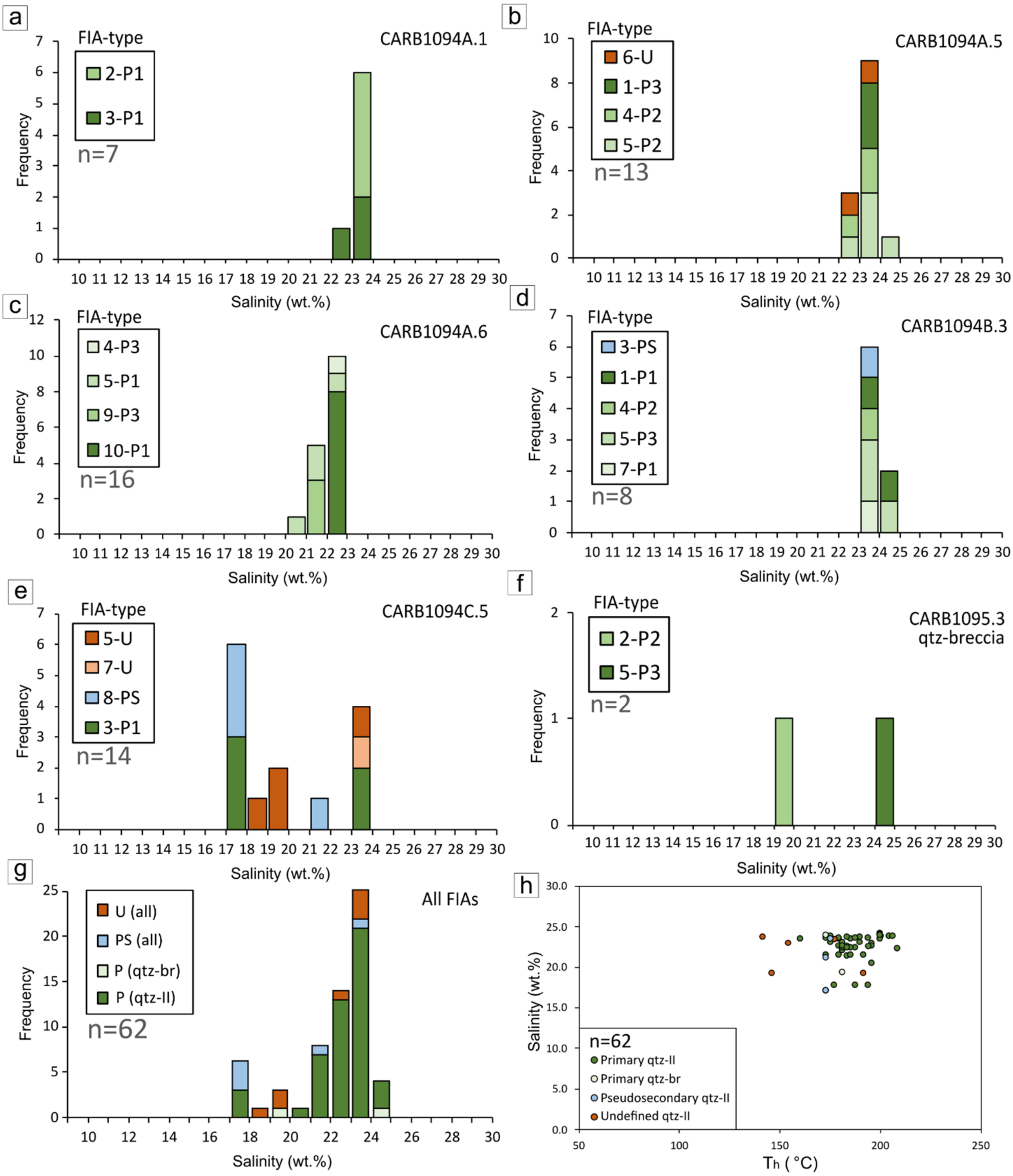

Figure C5. Full dataset of salinity measured in the analyzed FIAs. Panel (h) shows the T_h-salinity plot for the whole dataset.

Appendices references

Auer, G., Piller, W.E., Reuter, M., Harzhauser, M., 2015. Correlating carbon and oxygen isotope events in early to middle Miocene shallow marine carbonates in the Mediterranean region using orbitally tuned chemostratigraphy and lithostratigraphy. Paleoceanography 30, 332–352.

Bakker, R.J., 2004. Raman spectra of fluid and crystal mixtures in the systems H_2O, H_2O-NaCl and H_2O-$MgCl_2$ at low temperatures: Applications to fluid-inclusion research. Canadian Mineralogist 42(5), 1283–1314.

Baumgartner, M., Bakker, R.J., 2010. Raman spectra of ice and salt hydrates in synthetic fluid inclusions. Chemical Geology 275(1–2), 58–66.

Bottinga, Y., Javoy, M., 1973. Comments on oxygen isotope geothermometry. Earth and Planetary Science Letters 20, 250-265.

Clayton, R.N., O'Neil, J.R., Mayeda, T.K., 1972. Oxygen isotope exchange between quartz and water. Journal of Geophysical Research 77(17), 3057–3067.

Clayton, R.N., Goldsmith, J.R., Mayeda, T.K., 1989. Oxygen isotope fractionation in quartz, albite, anorthite and calcite. Geochimica et Cosmochimica Acta 53, 725-733.

Cornacchia, I., Brandano, M., Raffi, I., Tomassetti, L., Flores, I., 2018. The Eocene–Oligocene transition in the C-isotope record of the carbonate successions in the Central Mediterranean. Glob. Planet. Change 167, 110–122.

Dubessy, J., Audeoud, D., Wilkins, R., Kosztolanyi, C., 1982. The use of the Raman microprobe mole in the determination of the electrolytes dissolved in the aqueous phase of fluid inclusions. Chemical Geology 37, 137-150.

Dupuis, R., Benoit, M., Nardin, E., Méheut, M., 2015. Fractionation of silicon isotopes in liquids: the importance of configurational disorder. Chemical Geology 396, 239-254.

Gázquez, F., Calaforra, J.M., Rull, F., Forti, P., García-Casco, A., 2012. Organic matter of fossil origin in the amberine speleothems from El Soplao Cave (Cantabria, Northern Spain). Int. J. Speleol. 41, 113–123.

Gregory, R.T., 1991. Oxygen isotope history of seawater revisited: timescales for boundary event changes in the oxygen isotopic composition of sea water. In: Stable Isotopic Geochemistry: A Tribute to Samuel Epstein, Geochem. Soc. Spec. Publ.

Holmden, C., Muehlenbachs, K., 1993. The $^{18}O/^{16}O$ ratio of 2-billion-year-old sea- water inferred from ancient oceanic crust. Science 259, 1733–1736.

Horita, J., Wesolowski, D.J., 1994. Liquid-vapor fractionation of oxygen and hydrogen isotopes of water from the freezing to the critical temperature. Geochimica et Cosmochimica Acta 58, 3425-3437.

Hu, G., Clayton, R.N., 2003. Oxygen isotope salt effects at high pressure and high temperature and the calibration of oxygen isotope geothermometers. Geochimica et Cosmochimica Acta 67, 3227-3246.

Kleine, B. I., Stefánsson, A., Halldórsson, S. A., Whitehouse, M. J., Jónasson, K., 2018. Silicon and oxygen isotopes unravel quartz formation processes in the Icelandic crust. Geochemical Perspectives Letters 7, 5–11.

Klug, D.D., Mishima, O., Whalley, E., 1987. High-density amorphous ice. IV. Raman spectrum of the uncoupled O–H and O–D oscillators. The Journal of Chemical Physics 86, 5323-5328.

Knauth, L.P., Lowe, D.R., 1978. Oxygen isotope geochemistry of cherts from Onverwacht Group (3.4 billion years), Transvaal, South Africa with implications for secular variations in the isotopic compositions of cherts. Earth and Planetary Science Letters 41, 209–222.

Ligang, Z., Jingxiu, L., Huanbo, Z., Zhensheng, C., 1989. Oxygen isotope fractionation in the quartz-water-salt system. Economic Geology 84, 1643-1650.

Marin-Carbonne, J., Robert, F., Chaussidon, M., 2014. The silicon and oxygen isotope compositions of Precambrian cherts: A record of oceanic paleo-temperatures? Precambrian Research 247, 223–234.

Mernagh, T.P., Wilde, A.R., 1989. The use of the laser Raman microprobe for the determination of salinity in fluid inclusions. Geochimica et Cosmochimica Acta 53, 765-771.

Nandiyanto, A.B.D., Oktiani, R., Ragadhita, R., 2019. How to Read and Interpret FTIR Spectroscope of Organic Material. Indones. J. Sci. Technol. 4, 97–118.

Pollington, A.D., Kozdon, R., Anovitz, l.M., Georg, R.B., Spicuzza, M.J., Valley, J.W., 2016. Experimental calibration of silicon and oxygen isotope fractionations between quartz and water at 250° C by in situ microanalysis of experimental products and application to zoned low δ^{30}Si quartz overgrowths. Chemical Geology 421, 127-142.

Samson, I.M., Walker, R.T., 2000. Cryogenic raman spectroscopic studies in the system $NaCl-CaCl_2-H_2O$ and implications for low-temperature phase behavior in aqueous fluid inclusions. Canadian Mineralogist 38(1), 35–43.

Stefánsson, A., Hilton, D.R., Sveinbjörnsdóttir, Á.E., Torssander, P., Heinemeier, J., Barnes, J.D., Ono, S., Halldórsson, S.A., Fiebig, J., Arnórsson, S., 2017. Isotope systematics of Icelandic thermal fluids. Journal of Volcanology and Geothermal Research 337, 146–164.

Taylor, W.L., Pollard, D.D., Aydin, A., 1999. Fluid flow in discrete joint sets: Field observations and numerical simulations. J. Geophys. Res. Solid Earth 104, 28983–29006.

Tulk, C.A., Klug, D.D., Branderhorst, R., Sharpe, P., Ripmeester, J.A., 1998. Hydrogen bonding in glassy liquid water from Raman spectroscopic studies. The Journal of Chemical Physics 109, 8478-8484.

Walrafen, G.E., 1962. Raman spectral studies of the effects of electrolytes on water. The Journal of Chemical Physics 36, 1035-1042.

Walrafen, G.E., 1964. Raman spectral studies of water structure. The Journal of Chemical Physics 40, 3249-3256

Walrafen, G.E., 1972. Raman and infrared spectral investigations of water structure. In: Water, a Comprehensive Treatise, 1. The Physics and Physical Chemistry of Water (F. Franks, ed.). Plenum Press, New York, 151-214.

Weigel, S., Stephan, D., 2018. Bitumen Characterization with Fourier Transform Infrared Spectroscopy and Multivariate Evaluation: Prediction of Various Physical and Chemical Parameters. Energy & Fuels 32, 10437–10442.

Author’s declaration

List of Publications on IF journals

1) Pisani, L., Antonellini, M., Angeli, I.M.D., Waele, J. De, 2021. Structurally controlled development of a sulfuric hypogene karst system in a fold-and-thrust belt (Majella Massif, Italy). J. Struct. Geol. 145, 104305. https://doi.org/10.1016/j.jsg.2021.104305
2) Pontes, C.C.C., Bezerra, F.H.R., Bertotti, G., La Bruna, V., Audra, P., De Waele, J., Auler, A.S., Balsamo, F., Hoop, S.D., Pisani, L., 2021. Flow pathways in multiple-direction fold hinges: Implications for fractured and karstified carbonate reservoirs. J. Struct. Geol. 146, 104324. https://doi.org/10.1016/j.jsg.2021.104324
3) Pisani, L., Antonellini, M., Bezerra, F.H.R., Carbone, C., Auler, A.S., Audra, P., La Bruna, V., Bertotti, G., Balsamo, F., Pontes, C.C.C., De Waele, J., 2022. Silicification, flow pathways, and deep-seated hypogene dissolution controlled by structural and stratigraphic variability in a carbonate-siliciclastic sequence (Brazil). Mar. Pet. Geol. 105611. https://doi.org/10.1016/J.MARPETGEO.2022.105611
4) Pisani, L., Koltai, G., Dublyansky, Y., Kleine, B.I., Whitehouse, M.J., Skrzypek, E., Carbone, C., Spötl, C., Antonellini, M., Bezerra, F.H., De Waele, J., 2023. Hydrothermal silicification and hypogene dissolution of an exhumed Neoproterozoic carbonate sequence in Brazil: Insights from fluid inclusion microthermometry and silicon-oxygen isotopes. Basin Res. https://doi.org/10.1111/BRE.12748

This declaration states the independent research contribution of the PhD candidate for each paper compiled in the thesis.

Paper n	**Title and bibliographic reference**		
Paper 1	Pisani, L., Antonellini, M., Angeli, I.M.D., Waele, J. De, 2021. Structurally controlled development of a sulfuric hypogene karst system in a fold-and-thrust belt (Majella Massif, Italy). J. Struct. Geol. 145, 104305. https://doi.org/10.1016/j.jsg.2021.104305		
Role of PhD candidate	**Type of contribution**	**Overall contribution (%)**	**Signature of PhD candidate and supervisor**
First author, corresponding author	Conceptualization, methodology, investigation, formal analyses, validation, data curation, writing original draft, writing review-editing.	75-90 %	

Paper n	**Title and bibliographic reference**		
Paper 2	Pontes, C.C.C., Bezerra, F.H.R., Bertotti, G., La Bruna, V., Audra, P., De Waele, J., Auler, A.S., Balsamo, F., Hoop, S.D., Pisani, L., 2021. Flow pathways in multiple-direction fold hinges: Implications for fractured and karstified carbonate reservoirs. J. Struct. Geol. 146, 104324. https://doi.org/10.1016/j.jsg.2021.104324		
Role of PhD candidate	**Type of contribution**	**Overall contribution (%)**	**Signature of PhD candidate and supervisor**
Co-author	Investigation, validation, writing review-editing.	10-25 %	

Paper n	Title and bibliographic reference		
Paper 3	Pisani, L., Antonellini, M., Bezerra, F.H.R., Carbone, C., Auler, A.S., Audra, P., La Bruna, V., Bertotti, G., Balsamo, F., Pontes, C.C.C., De Waele, J., 2022. Silicification, flow pathways, and deep-seated hypogene dissolution controlled by structural and stratigraphic variability in a carbonate-siliciclastic sequence (Brazil). Mar. Pet. Geol. 105611. https://doi.org/10.1016/J.MARPETGEO.2022.105611		
Role of PhD candidate	**Type of contribution**	**Overall contribution (%)**	**Signature of PhD candidate and supervisor**
First author, corresponding author	Conceptualization, methodology, investigation, formal analyses, validation, data curation, writing original draft, writing review-editing.	75-90 %	

Paper n	Title and bibliographic reference		
Paper 4	Pisani, L., Koltai, G., Dublyansky, Y., Kleine, B.I., Whitehouse, M.J., Skrzypek, E., Carbone, C., Spötl, C., Antonellini, M., Bezerra, F.H., De Waele, J., 2023. Hydrothermal silicification and hypogene dissolution of an exhumed Neoproterozoic carbonate sequence in Brazil: Insights from fluid inclusion microthermometry and silicon-oxygen isotopes. Basin Res. https://doi.org/10.1111/BRE.12748		
Role of PhD candidate	**Type of contribution**	**Overall contribution (%)**	**Signature of PhD candidate and supervisor**
First author, corresponding author	Conceptualization, methodology, investigation, formal analyses, validation, data curation, writing original draft, writing review-editing.	70-80 %	

Acknowledgments

First, I would like to thank my supervisors Jo De Waele and Marco Antonellini for their help and guidance during these three years of research. This thesis would have not been possible without their support. I also want to thank Francisco Hilario Bezerra, Vincenzo La Bruna, Cayo Pontes, Lorenna Oliveira, Philippe Audra, Augusto Auler, Giovanni Bertotti and Fabrizio Balsamo for their time and assistance during my research periods in Brazil. I also want to acknowledge and thank Alexander Klimchouk (National Academy of Science of Ukraine) and Fabrizio Agosta (Università della Basilicata) for kindly accepting to review this thesis.

I thank my friends and companions from Gruppo Speleologico Bolognese – Unione Speleologica Bolognese (GSB-USB) for all the emotions and discoveries shared together underground during these years. Special thanks to Gabriella Koltai, Tanguy Racine, Charlotte Honiat and Lukas Plan for their support during my period in Austria and the time spent together in the mountains or in caves. I will always remember it with caring.

Thanks to Alessia Nannoni, Andrea Columbu, Matteo Meli and Sabrina Napoleoni, with whom I shared most of my working time in our dark hole-office, and to Michele Sivelli from Biblioteca F. Anelli for the frequent talks on caves and speleology.

Thanks and cheers to my bands' mates: Giorgino, Lupo, Matte, Guato, Germi, Liuc. Music helped to make bad periods less scaring.

Finally, a special mention goes to my family and loved ones: my parents Elena and Roberto, my brothers Giulio and Matteo, and Francesca Golfieri for their constant encouragement and support during these frenetic years. A last (but not least) gratitude goes to Marianna Coltelli for her contagious curiosity, love and all the special moments shared together.